Technische Universität München

Fakultät für Medizin

Data-driven host-directed antiviral drug repurposing against emerging pathogens

Valter Bergant

Vollständiger Abdruck der von der **Fakultät für Medizin der Technischen Universität München** zur Erlangung des akademischen Grades eines

Doktors der Naturwissenschaften (Dr. rer. nat.)

genehmigten Dissertation.

Vorsitz: Prof. Dr. Dirk H. Busch

Prüfer*innen der Dissertation:

1. Prof. Dr. Andreas Pichlmair, Ph.D.
2. Prof. Dr. Danny Nedialkova
3. Prof. Jernej Ule, Ph.D.

Die Dissertation wurde am 08.11.2022 bei der Technischen Universität München eingereicht und durch die Fakultät für Medizin am 21.03.2023 angenommen.

Data-driven host-directed antiviral drug repurposing against emerging pathogens

Abstract

The emergence[1] of severe acute respiratory distress syndrome coronavirus 2 (SARS-CoV-2) requires an in-depth understanding of functions of viral proteins on the molecular level, as well as their interactions with the host proteins. Multiple individual omics studies so far extended our knowledge of coronavirus disease 2019 (COVID-19) pathophysiology. Integration of such datasets would allow to obtain a broader view of virus-host interface as well as to better define the pathogenic properties of the virus. This, however, is limited by the heterogeneity of the used experimental systems. We conducted a concurrent multi-omics study of SARS-CoV-2 and SARS-CoV. Using state-of-the-art proteomics on human lung-derived cell line, we investigated the interactomes of both viruses and their influence on transcriptome, proteome, ubiquitinome and phosphoproteome. Mapping the gathered findings onto the network of cellular signaling revealed a prominent crosstalk between the infection-induced perturbations occurring at different layers. Notably, we identified both unique and common molecular mechanisms contributing to the life cycle and pathogenicity of these closely related coronaviruses.

We leveraged[2] both direct acting (DAAs) and host-directed (HDAs) antiviral drugs to inhibit the activity of SARS-CoV-2 viral cap 2'-O-ribose methyltransferase (MTase) NSP16. Notably, we demonstrated that the activity of the host cap 2'-O-ribose methyltransferase MTr1 (also known as CMTR1, FTSJD2) promotes virus replication by compensating for loss or lack of activity of NSP16. Concomitant inhibition of both MTr1 and NSP16 allowed to efficient suppression of SARS-CoV-2. By using *in silico* target-based drug discovery we identified a bispecific MTr1/NSP16 inhibitor. This inhibitor is highly antiviral against SARS-CoV-2 both *in vitro* and *in vivo*, however, has unfavorable side effects and activities. To maintain their activity, S-adenosylmethionine(SAM)-dependent MTases depend on metabolic homeostasis facilitated by the host SAM-cycle. Strikingly, inhibiting independent stages of the SAM-cycle by either small molecules or genetic ablation is antiviral against SARS-CoV-2. Most notably, the inhibitor of adenosylhomocysteinase (AHCY) DZNep is antiviral *in vitro*, *ex vivo* and *in vivo*, as well as synergizes with existing and approved COVID-19 treatments. Beyond antiviral efficacy, DZNep exhibited a favorable immunomodulatory effect by curbing hyperinflammation and reducing lung fibrosis markers *ex vivo*.

---

[1] Paragraph adapted from my own writing published in Stukalov, Girault, Grass, Karayel, Bergant, Urban, Haas, Huang et al., 2021

[2] Paragraph adapted from my own writing published in Bergant, Yamada et al., EMBO, 2022

Datengestützte Identifizierung antiviraler Medikamente gegen neu auftretende Krankheitserreger

Zusammenfassung

Das weltweite Auftreten[3] von SARS-CoV-2 erfordert dringend ein tiefgreifendes Verständnis der molekularen Funktionen der viralen Proteine und ihrer Wechselwirkungen mit dem Wirtsproteom. Mehrere einzelne Omics-Studien haben unser Wissen über die Pathophysiologie von COVID-19 erweitert. Die Integration solcher Datensätze, um ein ganzheitliches Bild der Virus-Wirt-Interaktionen zu erhalten und die pathogenen Eigenschaften von SARS-CoV-2 zu definieren, wird durch die Heterogenität der experimentellen Systeme eingeschränkt. Wir haben daher die erste vergleichende Multi-omics-Studie von SARS-CoV-2 und SARS-CoV durchgeführt. Mithilfe modernster Proteomik konnten wir das Interaktom beider Viren sowie deren Einfluss auf Transkriptom, Proteom, Ubiquitinom und Phosphoproteom in einer aus der Lunge stammenden menschlichen Zelllinie charakterisieren. Die Projektion dieser Daten auf das globale Netzwerk zellulärer Interaktionen offenbarte die Veränderungen, welche bei Infektionen mit SARS-CoV-2 und SARS-CoV auf verschiedenen Ebenen auftreten, und identifizierte virus spezifische und Pan-Coronavirus-vermittelte molekulare Mechanismen.

Darüber hinaus nutzten[4] wir sowohl direkt wirkende als auch wirtsgerichtete antivirale Wirkstoffe, um die SARS-CoV-2 cap 2'-O-Ribose-Methyltransferase (MTase) NSP16 pharmakologisch zu hemmen. Insbesondere konnte gezeigt werden, dass die wirtseigene Cap-2'-O-Ribose-Methyltransferase MTr1 die Virusreplikation erleichtert, indem sie für den Verlust von NSP16 kompensiert. Die gleichzeitige Hemmung von MTr1 und NSP16 unterdrückt effizient die Replikation von SARS-CoV-2. Bei der zielgerichteten Arzneimittelentdeckung *in silico* wurde ein bispezifischer MTr1/NSP16-Inhibitor identifiziert, der *in vitro* und *in vivo* antiviral gegen SARS-CoV-2 wirkt, aber ungünstige Nebenwirkungen hat. SAM-abhängige MTasen hängen entscheidend von der Metaboliten-Homöostase ab, die durch den SAM-Zyklus des Wirts aufrechterhalten wird. Inhibitoren, die auf unabhängige Stadien des SAM-Zyklus abzielen, wirken antiviral. Vor allem der Adenosylhomocysteinase (AHCY)-Inhibitor DZNep ist *in vitro*, *ex vivo* und in einem Mausinfektionsmodell antiviral und wirkt synergistisch mit bestehenden COVID-19-Behandlungen. Darüber hinaus zeigte DZNep eine starke immunmodulatorische Wirkung, indem es die infektionsinduzierte Hyperinflammation eindämmte und *ex vivo* die Lungenfibrosemarker reduzierte.

---

[3] Paragraph adapted from my own writing published in Stukalov, Girault, Grass, Karayel, Bergant, Urban, Haas, Huang et al., 2021

[4] Paragraph adapted from my own writing published in Bergant, Yamada et al., EMBO, 2022

Data-driven host-directed antiviral drug repurposing against emerging pathogens

Short abstract

We conducted a multi-omics study of SARS-CoV-2 and SARS-CoV and profiled their interactomes and their influence on host transcriptome, proteome, ubiquitinome and phosphoproteome. We further discovered both direct acting and host-directed antivirals that concomitantly inhibit both viral and host methyltransferases, which we demonstrate is required to efficiently suppress SARS-CoV-2 replication.

Datengestützte Identifizierung antiviraler Medikamente gegen neu auftretende Krankheitserreger

Kurze Zusammenfassung

Wir führten eine Multi-omics-Studie von SARS-CoV-2 und SARS-CoV durch und erstellten Profile ihrer Interaktome sowie ihres Einflusses auf das Transkriptom, Proteom, Ubiquitinom und Phosphoproteom des Wirts. Darüber hinaus entdeckten wir sowohl direkt wirkende als auch auf wirtsgerichtete Virostatika, die gleichzeitig sowohl virale als auch Wirts-Methyltransferasen hemmen, was nachweislich erforderlich ist, um die Replikation von SARS-CoV-2 effizient zu unterdrücken.

Table of contents

Acknowledgements

First of all, I want to thank my supervisor Prof. Dr. Andreas Pichlmair, who supported and guided me during my PhD studies. He enabled me to work on most exciting biological topics and encouraged me to explore scientific questions in different fields. I highly value his advice and appreciate his genuine enthusiasm for science.

I am also very thankful to all the current and past members of the Pichlmair lab with whom it was a great privilege to work with. I am in particular grateful for all the patience and advice I received from Dr. Alexey Stukalov.

Furthermore, I want to thank all the members of my thesis committee: Prof. Dr. Mark Schmidt-Supprian, Prof. Dr. Jernej Ule, and Prof. Dr. Danny Nedialkova.

I also want to acknowledge our collaborators, with whom we had very productive collaborations. I am most thankful for their contributions, the opportunity to work with and learn from them.

Finally, I want to thank my wife Eva and my son Kilian, my family and my friends for ongoing support and encouragement.

Disclosure statements

Parts of this thesis have been published in:

Valter Bergant*, Shintaro Yamada*, Vincent Grass, Yuta Tsukamoto, Teresa Lavacca, Karsten Krey, Maria-Teresa Mühlhofer, Sabine Wittmann, Armin Ensser, Alexandra Herrmann, Anja vom Hemdt, Yuriko Tomita, Shutoku Matsuyama, Takatsugu Hirokawa, Yiqi Huang, Antonio Piras, Constanze A. Jakwerth, Madlen Oelsner, Susanne Thieme, Alexander Graf, Stefan Krebs, Helmut Blum, Beate M. Kümmerer, Alexey Stukalov, Carsten B. Schmidt-Weber, Manabu Igarashi, Thomas Gramberg, Andreas Pichlmair[§], Hiroki Kato[§]. **Attenuation of SARS-CoV-2 replication and associated inflammation by concomitant targeting of viral and host cap 2'-O-ribose methyltransferases.** *EMBO*, 2022.
doi: 10.15252/embj.2022111608

Open access publication, Creative Commons Attribution 4.0 Unported License (CC BY) summary: *“Under CC BY, users are free to share (copy, distribute and transmit) and to adapt (edit, rewrite or remix) the contribution including for commercial purposes, but with formal attribution. Users must attribute the contribution in the manner specified by the author or licensor.”*

Alexey Stukalov*, Virginie Girault*, Vincent Grass*, Ozge Karayel*, **Valter Bergant***, Christian Urban*, Darya A. Haas*, Yiqi Huang*, Lila Oubraham, Anqi Wang, M. Sabri Hamad, Antonio Piras, Fynn M. Hansen, Maria C. Tanzer, Igor Paron, Luca Zinzula, Thomas Engleitner, Maria Reinecke, Teresa M. Lavacca, Rosina Ehmann, Roman Wölfel, Jörg Jores, Bernhard Kuster, Ulrike Protzer, Roland Rad, John Ziebuhr, Volker Thiel, Pietro Scaturro, Matthias Mann & Andreas Pichlmair. **Multilevel proteomics reveals host perturbations by SARS-CoV-2 and SARS-CoV.** *Nature*, 2021. doi: 10.1038/s41586-021-03493-4

Springer Nature Limited Author reuse permissions (excerpt): *“Authors have the right to reuse their article’s Version of Record, in whole or in part, in their own thesis. Additionally, they may reproduce and make available their thesis, including Springer Nature content, as required by their awarding academic institution.”*

These two publications are appended to this thesis as permitted by the respective publishers according to the publishing contracts. In this regard, an acknowledgement of the reference publication is required, which is clearly provided above.

Parts of this thesis result from collaborations and are acknowledged accordingly.

Competing interests statement

Valter Bergant is a co-inventor of multiple patent applications related to the content of this thesis (see section **List of patents**).

List of first-author publications

1. **Valter Bergant***, Shintaro Yamada*, Vincent Grass, Yuta Tsukamoto, Teresa Lavacca, Karsten Krey, Maria-Teresa Mühlhofer, Sabine Wittmann, Armin Ensser, Alexandra Herrmann, Anja vom Hemdt, Yuriko Tomita, Shutoku Matsuyama, Takatsugu Hirokawa, Yiqi Huang, Antonio Piras, Constanze A. Jakwerth, Madlen Oelsner, Susanne Thieme, Alexander Graf, Stefan Krebs, Helmut Blum, Beate M. Kümmerer, Alexey Stukalov, Carsten B. Schmidt-Weber, Manabu Igarashi, Thomas Gramberg, Andreas Pichlmair§, Hiroki Kato§. **Attenuation of SARS-CoV-2 replication and associated inflammation by concomitant targeting of viral and host cap 2'-O-ribose methyltransferases.** *EMBO*, 2022
2. Alexey Stukalov*, Virginie Girault*, Vincent Grass*, Ozge Karayel*, **Valter Bergant***, Christian Urban*, Darya A. Haas*, Yiqi Huang*, Lila Oubraham, Anqi Wang, M. Sabri Hamad, Antonio Piras, Fynn M. Hansen, Maria C. Tanzer, Igor Paron, Luca Zinzula, Thomas Engleitner, Maria Reinecke, Teresa M. Lavacca, Rosina Ehmann, Roman Wölfel, Jörg Jores, Bernhard Kuster, Ulrike Protzer, Roland Rad, John Ziebuhr, Volker Thiel, Pietro Scaturro, Matthias Mann & Andreas Pichlmair. **Multilevel proteomics reveals host perturbations by SARS-CoV-2 and SARS-CoV.** *Nature*, 2021

List of other publications

3. Liu H, **Bergant V**, Frishman G, Ruepp A, Pichlmair A, Vincendeau M, Frishman D. **Influenza A Virus Infection Reactivates Human Endogenous Retroviruses Associated with Modulation of Antiviral Immunity.** *Viruses*, 2022
4. Pei J, Beri NR, Zou AJ, Hubel P, Dorando HK, **Bergant V**, Andrews RD, Pan J, Andrews JM, Sheehan KCF, Pichlmair A, Amarasinghe GK, Brody SL, Payton JE, Leung DW. **Nuclear-localized human respiratory syncytial virus NS1 protein modulates host gene transcription.** *Cell Rep.*, 2021
5. Manček-Keber M, Hafner-Bratkovič I, Lainšček D, Benčina M, Govednik T, Orehek S, Plaper T, Jazbec V, **Bergant V**, Grass V, Pichlmair A, Jerala R. **Disruption of disulfides within RBD of SARS-CoV-2 spike protein prevents fusion and represents a target for viral entry inhibition by registered drugs.** *FASEB J.*, 2021
6. Lainšček D, Fink T, Forstnerič V, Hafner-Bratkovič I, Orehek S, Strmšek Ž, Manček-Keber M, Pečan P, Esih H, Malenšek Š, Aupič J, Dekleva P, Plaper T, Vidmar S, Kadunc L, Benčina M, Omersa N, Anderluh G, Pojer F, Lau K, Hacker D, Correia BE, Peterhoff D, Wagner R, **Bergant V**, Herrmann A, Pichlmair A, Jerala R. **A Nanoscaffolded Spike-RBD Vaccine Provides Protection against SARS-CoV-2 with Minimal Anti-Scaffold Response.** *Vaccines (Basel)*, 2021
7. Gebhardt A, **Bergant V**, Schnepf D, Moser M, Meiler A, Togbe D, Mackowiak C, Reinert LS, Paludan SR, Ryffel B, Stukalov A, Staeheli P, Pichlmair A. **The alternative cap-binding complex is required for antiviral defense in vivo.** *PLoS Pathog.*, 2019
8. Hubel P, Urban C, **Bergant V**, Schneider WM, Knauer B, Stukalov A, Scaturro P, Mann A, Brunotte L, Hoffmann HH, Schoggins JW, Schwemmle M, Mann M, Rice CM, Pichlmair A. **A protein-interaction network of interferon-stimulated genes extends the innate immune system landscape.** *Nat Immunol.*, 2019

List of patents

1. **Valter Bergant**, Vincent Grass, Andreas Pichlmair (Technische Universität München). **Treatment of coronavirus infections using SAM cycle inhibitors.** WO2022189379A1

List of abbreviations

COVID-19	Coronavirus disease 2019 (disease)
DAAs	Direct-acting antivirals (antiviral compounds)
DZNep	3-Deazaneplanocin A (an antiviral compound)
HDAs	Host-directed antivirals (antiviral compounds)
ISGs	Interferon stimulated genes (set of genes)
KD	Knock-down (method in biotechnology)
KO	Knock-out (method in biotechnology)
MTases	Methyltransferases (enzymes)
NHBEs	Normal human bronchial epithelial cells (primary cells)
SAH	S-Adenosylhomocysteine (endogenous metabolite)
SAM	S-Adenosylmethionine (endogenous metabolite)
SARS-CoV	Severe acute respiratory syndrome coronavirus (virus)
SARS-CoV-2	Severe acute respiratory syndrome coronavirus 2 (virus)
SCIs	SAM-cycle inhibitors (compounds inhibiting the SAM-cycle)

Introduction

Over 20 highly divergent virus families are known to cause a wide variety of human diseases ranging in severity from common cold caused by e.g. rhinoviruses to hemorrhagic fevers caused by e.g. filoviruses. New viral etiologic agents of human diseases are continuously emerging and are being identified[1,2]. Despite a variety of pathogens causing significant detrimental impact on societies around the globe, approved antivirals center around treating only a handful of viral diseases[3–6] caused by "the big four" viruses: HIV (ca. 50% of approvals), HCV (ca. 20% of approvals), herpesviruses (ca. 15% of approvals) and HBV (ca. 10% of approvals). The discrepancy in approvals is a clear reflection of imbalance in funding for research favoring a small selection of viruses over a large number of neglected pathogens. This has led to significant gaps in knowledge that hinder responses to new pathogens such as coronaviruses.

Treatment of virus infections represents a complex 3-body problem, where the host, the virus and the drug each interact and interface with one another (Figure 1). These interfaces take place at multiple molecular levels that facilitate cellular signal transduction (Figure 1). The ultimate goal of applied antiviral research is to find drugs with molecular activity that would counter molecular disease determinants that lead to pathological manifestations and/or promote virus clearance, thus ultimately favoring host survival.

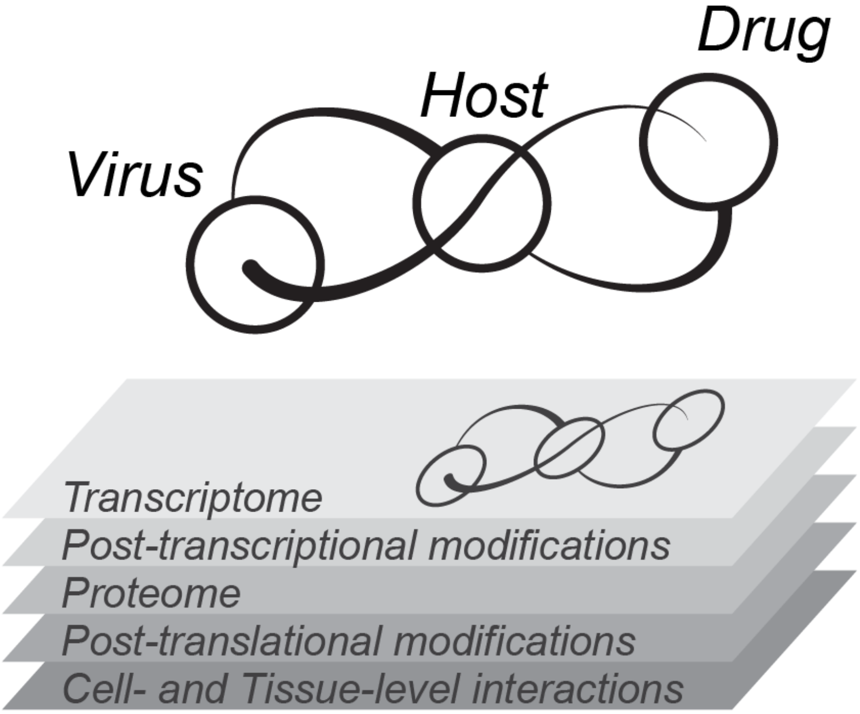

Figure 1 | Schematic representation of the 3-body problem of antiviral treatment development.

Direct-acting and host-directed antivirals

Antiviral compounds can be divided according to their targets into direct-acting antivirals (DAAs, ca. 85% of approvals) and host-directed antivirals (HDAs, ca. 15% of approvals)[5]. DAAs are compounds that target virus-specific events, most commonly inhibiting enzymatic functions of viral polymerases (ca. 40% of approvals) or viral proteases (ca. 25% of approvals)[5] in virus infected cells (virocells) (Figure 2). DAAs aim to prevent virus replication and facilitate virus clearance, but do not explicitly tackle other detrimental effects associated with virus infection such as inflammation, fibrosis or tissue damage.

HDAs are compounds that target host proteins and in particular either inhibit host factors or activate restriction factors[7]. Host factors are host proteins that are required for, or promote, virus proliferation (e.g. surface receptors), and restriction factors are host proteins that inhibit or attenuate virus proliferation (e.g. interferons and various interferon stimulated genes (ISGs)). HDAs thereby modulate host properties to make host cells more refractive to infection by a viral pathogen or a virocell to propagate the virus less efficiently (Figure 2). Vast majority of currently approved HDAs are biological treatments aiming to stimulate cell-intrinsic innate immunity (e.g. interferons[5,8,9]), which in turn promotes virus clearance. Some host-directed drugs, exemplified by dexamethasone used against COVID-19[10], are not antiviral per se, but are used in stand-alone manner or in conjunction with DAAs to curb detrimental host responses to the virus infection.

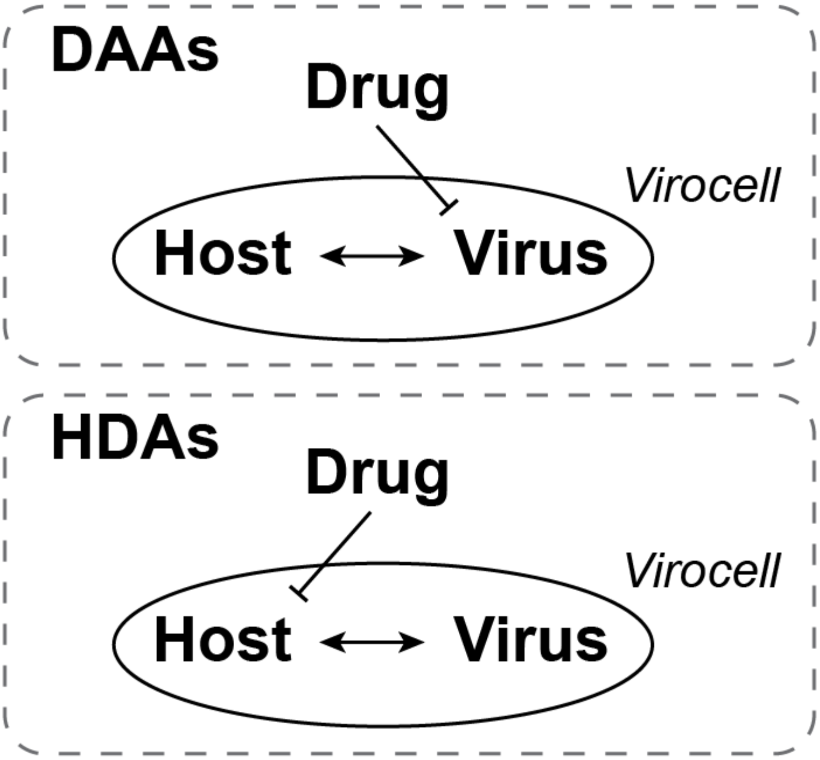

Figure 2 | Schematic representation of activities of DAAs and HDAs.

Data-driven HDA repurposing

The manuscripts appended to this thesis deal with data-driven[11,12] and in part hypothesis-driven[12] antiviral drug repurposing, wherein multi-omics analyses were used first and foremost towards identification of novel host-factors that can be pharmaceutically targeted to exert an antiviral effect. Multi-omics analyses represent an attractive option of gathering sufficiently deep biological information for bottom-up drug repurposing, but are hindered by the lack of data analysis and integration methodology. In our work, we aimed to overcome this lack of methodology by introducing and incorporating multiple innovative wet lab and computational methods into a unified we-dry-animal-lab workflow[11,12].

To identify potential druggable host factors required for virus replication, we performed multi-omics analysis that included both investigation of the effects of individual virus proteins (i.e. interactomics and effectomics) as well as their concerted activity in the context of infection on multiple signal transduction layers (i.e. transcriptomics, proteomics, phosphoproteomics and ubiquitinomics). Integrative analysis of these approaches allowed us to infer causal relationships between the activity of viral proteins and modulation of host signaling occurring in the infected setting (Figure 3). Although yet untapped, the inferred causal relationships may be used as a basis for DAA development.

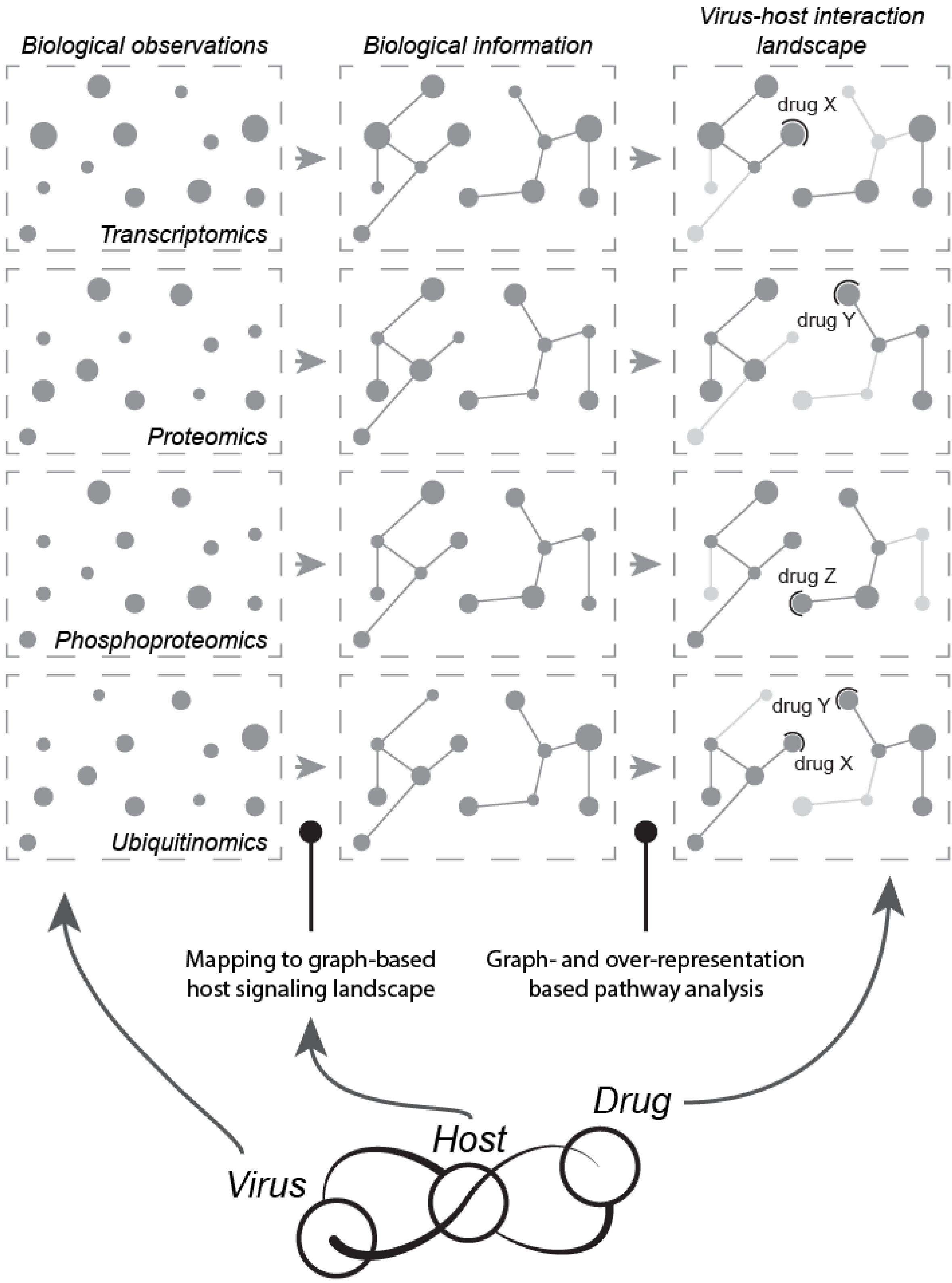

Figure 3 | Schematic representation of our multi-omics based data-driven host-directed antiviral drug repurposing approach: layer-centric data analysis and interpretation.

SARS-CoV-2 and the viral MTases

Recent pandemics, such as 2009 influenza A, 2016 Zika and the ongoing COVID-19, highlight the requirement for rapid development of antiviral treatments in addition to vaccines. Clinical studies and market prognosis predict a significant number of COVID-19 cases in the future, against which currently no effective antiviral treatment exists. COVID-19 patients commonly suffer from acute and persistent lung fibrosis[13], coagulation disorders[14] and other post-COVID conditions. Antiviral treatments that target the virus as well as improve tissue repair are urgently needed to control the pandemic and re-install a productive socioeconomic state.

Viral MTases[5] | S-adenosylmethionine (SAM) dependent methyltransferases (MTases) transfer a methyl group from SAM onto a variety of substrates. Notably, mature mRNA from both human and coronaviruses has two particular methylations at their 5' end. The cap N7 methylation allows for association of mRNA with cap-binding proteins (e.g. the nuclear cap-binding complex) that is pivotal for its transport and translation[15,16]. In addition, 2'O methylation of cap-proximal ribose moieties is needed by the virus in order to evade innate immunity, in particular from sensing by the pattern recognition receptors (PRRs) RIG-I[17] and MDA5[18] or sequestered by the interferon (IFN) response effector protein IFIT1[19–21]. Two viral MTases are encoded on the SARS-CoV-2 genome: the non-structural proteins (NSP) 14 and 16, which are a cap N7 MTase with proofreading exoribonuclease (ExoN) activity[22,23], and a cap 2'O-ribose MTase[24,25], respectively. NSP14 and NSP16 were thought to be the only MTases required for the viral mRNA maturation. Therefore, they were both considered critically required for virus replication as well as highlighted as potential targets for development of antiviral therapies[22,24]. The activity of NSP16 was in particular shown to be required for resistance to interferon response as well as the virulence of SARS and MERS coronaviruses[26,27]. Despite structural insights gained in the past few years, specific targeting of MTases in general remains challenging[25,28–31].

SAM-cycle and inhibitors thereof

One-carbon metabolism[5], and the SAM-cycle in particular, is required for sustaining the enzymatic activity of SAM-dependent MTases. The main metabolic output of the SAM-cycle is SAM, the universal methyl-group donor. The SAM-cycle furthermore recycles the S-adenosylhomocysteine (SAH), which is a potent product-inhibitor of all SAM-dependent MTases[32]. The SAM-cycle (Figure 4) is composed of four enzymatic interconversions: SAM biosynthesis, SAH hydrolysis, methionine biosynthesis and SAM-dependent methylation of substrates. Three of these steps (Figure 4) rely on host enzymes and may be inhibited by known small molecules, while SAM-dependent methylation is facilitated by numerous highly similar MTases that remain very challenging to target specifically.

---

[5] Paragraph adapted from my own writing published in Bergant, Yamada et al., EMBO, 2022

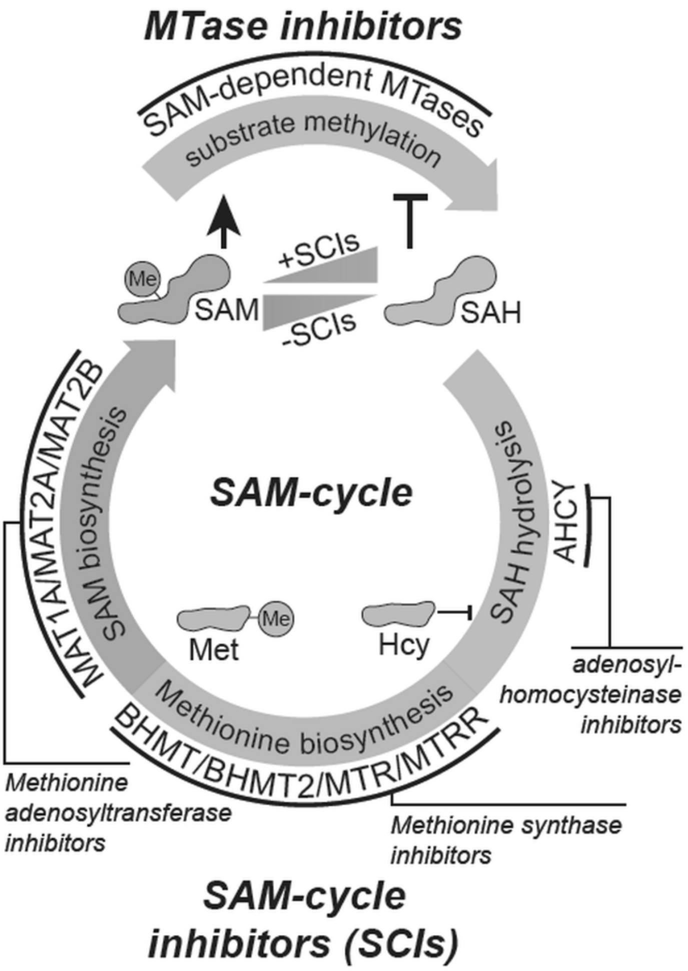

Figure 4 | Schematic representation of the SAM-cycle, metabolites, enzymatic components and inhibitors thereof. Figure adapted from my own publication[12].

SAM-cycle inhibitors (SCIs), DZNep[6] | SAM-cycle inhibitors impair the methylation homeostasis in cells by negatively influencing key metabolic biomarkers, i.e. they downregulate levels of SAM, upregulate the levels of SAH and/or reduce the SAM to SAH abundance ratio[33–35]. This ultimately leads to a broad spectrum inhibition of both host and viral MTases such as coronavirus NSP16[36] via substrate insufficiency and/or product-inhibition. Pharmaceutical inhibition of the SAM-cycle at multiple distinct stages is a treatment option in development for a number of cancers[37–39], and was shown to be well tolerated in mice[39,40]. Inhibition of the enzyme AHCY by DZNep was shown to be antiviral against multiple highly pathogenic viruses, among others, Ebola virus in mice[41,42] (WO 2016/022563 A1, WO 2016/051396 A1). DZNep, however, was ineffective in reducing lung SARS-CoV titer in mice[43]. Recently, DZNep was shown to be antiviral against coronaviruses including SARS-CoV-2 *in vitro* and Infectious bursitis virus (IBV) *in ovo*[44]. In this case, DZNep was shown to cause defects in viral RNA m6A methylation and cap maturation and impair viral protein production[44].

---

[6] Paragraph adapted from my own writing published in Bergant, Yamada et al., EMBO, 2022

DZNep and EZH2 - collateral benefits[7] | In human, over a hundred SAM-dependent MTases are involved in a multitude of diverse biological processes. Particularly notable is their engagement in epigenetic regulation of gene expression via histone H3K27 methylation. H3K27 methylation is a repressive chromatin mark (downregulating gene expression) and its deposition is facilitated by the polycomb repressive complex 2 (PRC2). PRC2 and H3K27 methylation were previously linked to numerous disease-relevant processes such as tissue fibrosis[45] and innate immune responses[46,47]. Indirect inhibition of the enhancer of zeste 2 (EZH2), the MTase subunit of the PRC2 complex, by DZNep was shown to impair the TGF-β1 induced transformation of human lung fibroblasts into myofibroblasts as well as to attenuate the pulmonary fibrosis induced by bleomycin in mice[45]. It was moreover associated with impairment of the NF-kB-dependent responses through upregulation of TNFAIP3/A20 and NFKBIA[48], both endogenous NF-kB inhibitors, and upregulation of the IFN response[49,50]. NF-kB pathway is highly active upon infection of cells by SARS-CoV-2 as well as in COVID-19 patients, where it contributes to the disease immunopathology[51]. SARS-CoV-2 is potently inhibited by the type-I IFN signaling, however, multiple viral proteins actively inhibit the activation of this pathway on multiple signaling levels[11,52]. Inhibition of EZH2 could in the context of COVID-19 therefore reduce lung fibrosis and in part relieve cytokine imbalance, both in the past associated with negative disease outcomes, and thereby promote to the resolution of acute and long-lasting effects of this disease.

Formulations of DZNep *in vivo* | In animal models, DZNep was commonly dissolved in saline and administered intravenously (i.v.)[40,53] or subcutaneously (s.c.)[41,42], although a PEGylated liposome carrier based formulation was also reported[54]. Notably, this formulation was shown to increase the area under the plasma concentration curve by 138-fold, potentially offering a major reduction in treatment doses. We further successfully implemented intranasal administration in mice, which is a highly attractive non-invasive delivery option[12]. Bioavailability of DZNep is poor and inconsistent upon oral administration[55].

In vivo toxicity of DZNep | Toxicity of DZNep was previously investigated in mice[53,56,57] and rats[40]. From these studies, Lhussier et al. used a treatment regimen closest to our current preclinical antiviral regimen[12,57]. In short, the study involved administration of 2 mg/kg DZNep, 3-times weekly for 8 weeks in 8 weeks old NMRI mice. In contrast to a previous study that looked at dose-dependent toxicity in single-treatment regimen[53], no kidney function abnormalities were found, indicating that renal toxicity may be Cmax-driven. The authors report signs of toxicity in spleen, bone marrow and testes, which are likely AUC-driven and manifest upon multiple administrations of the drug.

---

[7] Paragraph adapted from my own writing published in Bergant, Yamada et al., EMBO, 2022

Objectives

This thesis deals with data-driven[11,12] and hypothesis-driven[12] antiviral drug repurposing, wherein multi-omics analyses were used towards identification of novel host-factors that can be pharmaceutically targeted to exert an antiviral effect. Multi-omics analyses represent an attractive option of gathering sufficiently deep biological information for bottom-up drug repurposing, but are hindered by the lack of data analysis and integration methodology. In our work, we aimed to overcome this lack of methodology by introducing and incorporating multiple innovative wet lab and computational methods into a unified wet-dry-animal-lab workflow[11,12].

Materials and methods - part 1

This methods section describes in detail my own methodological contribution in investigations presented in the following publication, and is adapted from it:

Valter Bergant*, Shintaro Yamada*, Vincent Grass, Yuta Tsukamoto, Teresa Lavacca, Karsten Krey, Maria-Teresa Mühlhofer, Sabine Wittmann, Armin Ensser, Alexandra Herrmann, Anja vom Hemdt, Yuriko Tomita, Shutoku Matsuyama, Takatsugu Hirokawa, Yiqi Huang, Antonio Piras, Constanze A. Jakwerth, Madlen Oelsner, Susanne Thieme, Alexander Graf, Stefan Krebs, Helmut Blum, Beate M. Kümmerer, Alexey Stukalov, Carsten B. Schmidt-Weber, Manabu Igarashi, Thomas Gramberg, Andreas Pichlmair[§], Hiroki Kato[§]. **Attenuation of SARS-CoV-2 replication and associated inflammation by concomitant targeting of viral and host cap 2'-O-ribose methyltransferases.** *EMBO*, 2022.
doi: 10.15252/embj.2022111608

Cell lines and reagents

HEK293T, A549-ACE2 and Vero E6 (CRL-1586, ATCC) cell lines, and their respective culturing conditions, were described previously[11]. NHBE cells (CC-2540, Thermo Fisher Scientific) were cultured as described previously[58]; in short, the cells were grown until reaching 80% confluence. To avoid gene expression changes or influence on virus growth induced by growth factors in the BEGM medium (Lonza), cells were rested in basal medium (BEBM, Lonza) for 24 h before the start of the experiment. A549-RFP-ACE2 cell line was generated through lentiviral transduction of A549-ACE2 cell line and blasticidin selection, leading to expression of nuclear localized mRFP – plasmid pHIV-H2BmRFP was a gift from Bryan Welm & Zena Werb (Addgene plasmid #18982; http://n2t.net/addgene:18982; RRID:Addgene_18982)[59]. In preparation of KO cell lines, the following sequences were used in multiplexed manner for cloning of gRNA templates into pLentiCRISPRv2 plasmid: STAT1 (GGTGGCAAATGAAACATCAT; GAGGTCATGAAAACGGATGG; CAGGAGGTCATGAAAACGGA), NTC[60] (AACCGGATCGCCACGCGTCC; TCCGGAGCTTCTCCAGTCAA; TGCAAAGTTCAGGGTAATGG), AHCY (TTTCCTCCCGTAGCCGACAT; CCAGGCAGCCAGGCCGATGT; TCCCGTAGCCGACATCGGCC), MAT2A (CTGGAATGATCCTTCTTGCT; TGGAATGATCCTTCTTGCTG; TGCTGTTGACTACCAGAAAG). pLentiCRISPRv2 was a gift from Feng Zhang (Addgene plasmid #52961; http://n2t.net/addgene:52961; RRID:Addgene_52961)[60]. Lentiviruses production, transduction of cells and antibiotic selection for KO preparation were performed as described previously[11]. In brief, A549-ACE2 cells were transduced using puromycin resistance carrying lentiviruses encoding Cas9 and gRNAs and grown for 4 days using medium, supplemented with 3 µg/mL puromycin, before being used for further experiments. MTr1 KO cells (clone number: H1) were generated by transducing the parental A549 cells with plasmid encoding gRNA (CCTCAACGATGTCCTTCCGACCC), Cas9 and mCherry (kindly provided by Martin Schlee). After FACS-sorting for mCherry positive cells, clonal colonies were isolated, expanded and validated for the loss of MTr1 by Western blotting and genome sequencing (CTR cell line was selected from clones with intact MTr1 locus and expression). All cell lines were tested to be mycoplasma-free.

For the stimulation of cells, recombinant human IFN-α was a kind gift from Peter Stäheli. The following inhibitors were used: Tubercidin (Sigma-Aldrich, T0642), 3-deazaneplanocin A (Sigma-Aldrich, 5060690001, and Biozol, SEL-S7120), D-eritadenine (Biomol, Cay21747-1), Remdesivir (Hölzel biotech, CS-0028115), FIDAS-5 (MAT2A Inhibitor II, FIDAS-5 – Calbiochem, Sigma-Aldrich, 5041730001), MAT2A inhibitor 1 (Hölzel Diagnostika, HY-112131), PF-9366 (Hölzel Diagnostika, HY-107778), CBHcy (S- (4-Carboxybutyl)-D,L-homocysteine, BioTrend, AOB2142), Tazemetostat (EPZ-6438, biomol, Cay16174-1), Dexamethasone (Sigma-Aldrich, D1756), Marimastat (Sigma-Aldrich, M2699), Prinomastat (Sigma-Aldrich, PZ0198), Ipatasertib (GDC-0068, 18412, Cayman chemical) and Chloroquine (Chloroquine diphosphate salt, Sigma-Aldrich, C6628).

For detection of protein abundance by western blotting, ACTB-HRP (Santa Cruz; sc-47778; 1:5000 dilution), and SARS-CoV-2/SARS-CoV N protein (Sino Biological; 40143-MM05; 1:1000 dilution) antibodies were used. Secondary antibody detecting mouse IgG (Cell Signaling; 7076; 1:5000 dilution) was horseradish peroxidase (HRP)-coupled. Alexa Fluor 488 conjugated goat anti-mouse antibody (Abcam, ab150113) was used for protein abundance detection by immunofluorescence. WB imaging was performed as described previously[11].

Virus strains, stock preparation and in vitro infection

SARS-CoV-Frankfurt-1[61], SARS-CoV-2-MUC-IMB-1[62], SARS-CoV-2 Alpha (B.1.1.7)[63], SARS-CoV-2 Delta (B.1.617.2)[64] and SARS-CoV-2-GFP[11] strains were produced as described previously[11]. The SARS-CoV-2 Beta variant (B.1.351) was isolated in Bonn from a throat swab of a patient on and propagated on Caco-2 cells cultured in DMEM medium (10% FCS, 100 µg/ml streptomycin, 100 U/ml penicillin and 2.5 µg/ml Amphotericin B). For in vivo experiments, the virus was passaged once on Caco-2 cells in DMEM medium (10% FCS, 100 µg/ml streptomycin, 100 U/ml penicillin) at an MOI of 0.001 and harvested at 3 days post infection. Virus in the cleared supernatant (200 g, 10 min, 4°C) was stored at -80°C. Viral titers of the stocks were determined on Vero E6 cells using a carboxymethylcellulose overlay as described previously[65]. Recombinant SARS-CoV-2 NSP16mut virus was generated via plasmid pBeloCoV harboring the inactivating mutations D130A, K170A in the coding sequence of NSP16 (pBeloCoV-NSP16mut), which was cloned through Red recombination (manuscript by T. Gramberg in preparation). The virus was further amplified in CaCo-2 cells (1 passage, 72 hours) and quantified in cleared and purified supernatants by RT-qPCR. Recombinant YFV 17D and YFV 17D NS5 E218A (YFV E218A) were generated via electroporation of an infectious cDNA clone-derived in vitro mRNA transcript into BHK-J cells and a single passage on BHK-J cells; titers was determined by plaque assays using BHK-J cells as described previously[66]. Recombinant Vesicular stomatitis virus (VSV) Indiana strain encoding EGFP in position 5 of the genome (VSV-GFP) was recovered from BSR T7/5 cells infected with VACV WR vTF7.3 and transfected with pVSV1 (+) P5_EGFP, pL, pP, and pN as described previously[67]. It was further propagated in BSR T7/5 cells, and virus titers determined by plaque assay using Vero cells.

Cells were pretreated with inhibitors by medium (containing any indicated inhibitor) exchange at 6 h (unless stated otherwise) prior to addition of infectious inoculum containing SARS-CoV-2 at MOI 3 (SARS-CoV-2-MUC-IMB-1, unless stated otherwise) with medium replacement 1 h post infection where indicated. Infection with YFV 17D wt and YFV NS5 E218A was performed in PBS containing 1% FBS for 1h, followed by 2xPBS and 1xMEM wash and medium replacement.

At the time of sample harvest, the cells were washed once with 1x PBS buffer and lysed in LBP (Macherey-Nagel), 1x SSB lysis buffer (62.5 mM Tris HCl pH 6.8; 2% SDS; 10% glycerol; 50 mM DTT; 0.01% bromophenol blue) or freshly prepared SDC buffer (100 mM Tris HCl pH 8.5; 4% SDC) for RT-qPCR, western blot or LC-MS/MS analyses, respectively. The samples were heat-inactivated and frozen at -80°C until further processing. Sampled supernatants were stored frozen at -80°C until further processing.

Antiviral assays using SARS-CoV-2-GFP

A549-ACE2 cells were seeded into 96-well plates in DMEM medium (10% FCS, 100 µg/ml Streptomycin, 100 IU/ml Penicillin) one day before infection. Six hours before infection, the medium was replaced with 125 µl of DMEM medium containing either the compound (s) of interest or their respective vehicle (s) as control. Infection was performed by adding 10 µl of SARS-CoV-2-GFP (MOI 3, unless otherwise stated) per well and plates were placed in the IncuCyte S3 Live-Cell Analysis System where images of phase, green and red (when using A549-RFP-ACE2 cell line) channels were captured at regular time intervals at 4x (whole-well) or 20x magnification. Cell viability was assessed as the cell confluence per well (Phase area). Virus growth was assessed as GFP integrated intensity normalized to cell confluence per well (GFP integrated intensity/Phase area) or GFP area normalized to cell confluence per well (GFP area/Phase area) or GFP area normalized to RFP-positive nuclei count (when using A549-RFP-ACE2 cell line). Basic image analysis and image export was performed using IncuCyte S3 Software (Essen Bioscience; version 2019B Rev2). Statistical analysis and visualization was performed using R version 4.0.2. Three parameter logistic function fitting was performed using R package drc (version 3.0-1).

Quantification of gene expression in cell lines by RT-qPCR

Total cellular RNA, or RNA content of the supernatants, were harvested and isolated using MACHEREY-NAGEL NucleoSpin RNA mini kit according to manufacturer instructions. Reverse transcription was performed using Takara PrimeScript RT reagent kit with gDNA eraser according to manufacturer instructions.

RT-qPCR was performed using primers targeting SARS-CoV-2 N (fw: 5’-TTACAAACATTGGCCGCAAA-3’; rev: 5’-GCGCGACATTCCGAAGAA-3’), SARS-CoV-2 E (Figure 1c, i, Figure EV1d) (fw: 5’-ACAGGTACGTTAATAGTTAATAGCGT-3’; rev: 5’-ATATTGCAGCAGTACGCACACA-3’), SARS-CoV-2 E (Figure EV1g) and MERS-CoV N were described previously[68], SARS-CoV N was described previously[69], VSV N (fw: 5’-GGAGTATCGGATGCTTCCAGAACCA-3’; rev: 5’-ACGACCTTCTGGCACAAGAGGTT-3’), MAT2A (fw: 5’-CTTCGTAAGGCCACTTCCGC-3’; rev: 5’-TCTGGTAGCAACAGCAGCTC-3’), AHCY (fw: 5’-AACTGCCCTACAAAGTCGCC-3’; rev: 5’-ATGGTCCTGGGTGGAGAAGA-3’) and RPLP0 (unless stated otherwise the housekeeper control, fw: 5'-GGATCTGCTGCATCTGCTTG-3'; rev: 5'-GCGACCTGGAAGTCCAACTA-3') using PowerUp SYBR Green (Thermo Fisher, A25778), and SARS-CoV-2 RdRp (fw: 5'-GTGAAATGGTCATGTGTGGCGG-3'; rev: 5'-CAAATGTTAAAAACACTATTAGCATA-3'; VIC -CAGGTGGAACCTCATCAGGAGATGC- BMN-Q535), Eukaryotic 18S rRNA (Hs99999901_s1, Applied Biosystems), human IFNB1 (Hs01077958_s1, Applied Biosystems), human IFIT1 (ISG56) (Hs03027069_s1, Applied Biosystems), human MxA (Hs00895608_m1, Applied Biosystems) using TaqMan Fast Advanced Master Mix (Applied Biosystems). QuantStudio 3 Real-Time PCR system (Thermo Fisher) or Step One Plus Real-Time PCR System (Applied Biosystems) were used. Ct values, obtained using QuantStudio Design and Analysis Software v1.4.3, were averaged across technical replicates and -ΔCt values as a measure of gene expression were calculated as Ct (RPLP0) - Ct (N). -ΔΔCt values as a measure of change in gene expression between distinct KOs and NTC were calculated as –ΔCt (KO) – (–ΔCt (NTC)). For display of highly divergent values, one replicate of vehicle treated samples was assigned a relative expression value of 10^6. Viral RNA copy was calculated from the standard curve using serial diluted cDNA with known copy number. Statistical analysis and visualization was performed using R version 4.0.2.

Protein abundance quantification by Western blotting

At the time of sample harvest, the cells were washed with PBS, lysed in SSB buffer (62.5 mM Tris HCl from 1 M stock solution with pH 6.8, 2% SDS, 10% Glycerol, 50 mM DTT and 0.01% Bromophenol Blue in distilled water) and protein concentrations measured using Pierce 660-nm Protein Assay with an addition of Ionic detergent compatibility kit (Thermo Fischer Scientific) according to manufacturer instructions. Protein concentrations were equalized and up to 10 micrograms of proteins were loaded in NuPAGE Bis-Tris, 1 mm, 4-12% gels (Thermo Fisher Scientific). Protein separation was performed according to gel manufacturer instructions and proteins transferred to 0.22µm nitrocellulose membrane (1h at 100 V in 25 mM Trizma base, 0.192 M Glycine, pH 8.3). The membranes were blocked for 1h in 5% skim milk in TBS-T buffer (0.25% Tween-20 in phosphate buffered saline solution) with gentle agitation. The antibodies listed in the section above (cell lines and reagents) were diluted in 5% skim milk (TBS-T); the membranes were washed 5x for 5 minutes with TBS-T between and after incubations with primary and secondary antibodies. Western Lightning ECL Pro (PerkinElmer) was used for band detection according to manufacturer instructions. Normalization of band signals was performed using Image Lab Software (Bio-Rad, version 6.0.1 build 34).

Viral protein detection and quantification by immunofluorescence

For detection of viral protein expression using immunofluorescence, the cells were washed 3x with phosphate buffered saline (PBS), fixed for 15 minutes with 4% formaldehyde in PBS, washed again and permeabilized using 0.1% Triton-X in 4% BSA (PBS) for 15 min. They were further blocked for 1h using 4% BSA in PBS. The antibodies listed in the section above (cell lines and reagents) were diluted in 4% BSA (PBS); the cells were washed 5x for 1 minute with PBS between and after incubations with primary and secondary antibodies. Stained cells were imaged using IncuCyte S3 Live-Cell Analysis System. Whole-well images of GFP and Phase channels were captured at 4x magnification. Cell viability and virus growth were assessed as the cell confluence per well (Phase area) and GFP integrated intensity normalized to cell confluence per well (GFP integrated intensity/Phase area) respectively using IncuCyte S3 Software (Essen Bioscience; version 2019B Rev2). Analysis and visualization was performed using R version 4.0.2.

Quantification of secreted cytokines by ELISA

For detection of human IL-6 and IP-10, commercially available ELISA kits were used (Human IL-6 ELISA Set, BD OptEIA, 555220; Human IP-10 ELISA Set, BD OptEIA, 550926) according to manufacturer instructions. Basal medium, used for NHBE culturing at time of treatment and infection, was used as blank control. Statistics (Figure 4e) were calculated using paired Student's two-sided t-test on log-transformed values between indicated conditions before donor-wise normalization to vehicle-treated mock controls.

Mass spectrometry sample preparation and analysis

For the determination of proteome changes, A549-ACE2 cells were pretreated for 6 h with vehicle (PBS) or 0.75 µM DZNep and infected with SARS-CoV-2 and SARS-CoV at MOI 3 for 24 h. Experiment involving Tubercidin was performed and analyzed in an analogous manner with the following experimental modifications: 1 µM Tubercidin was used with DMSO as vehicle, 3 h pre-treatment, SARS-CoV-2 MOI 0.1, SARS-CoV MOI 0.01. Cells were then lysed in SDC lysis buffer (100 mM Tris HCl pH 8.5; 4% SDC). The following conditions were considered: vehicle-treated uninfected (3 replicates, 4 in Tubercidin treatment), DZNep-treated uninfected (4 replicates), vehicle-treated SARS-CoV-2 infected (4 replicates), DZNep-treated SARS-CoV-2 infected (4 replicates), vehicle-treated SARS-CoV infected (4 replicates), DZNep-treated SARS-CoV infected (4 replicates). For the determination of proteome changes in NHBEs, pretreated for 6 h with vehicle (PBS) or 1.5 µM DZNep and infected with SARS-CoV-2 and SARS-CoV at MOI 3 for 24 h, cells were lysed in SDC lysis buffer (100 mM Tris HCl pH 8.5; 4% SDC). The following conditions were considered: vehicle-treated uninfected, DZNep-treated uninfected, vehicle-treated SARS-CoV-2 infected, DZNep-treated SARS-CoV-2 infected, vehicle-treated SARS-CoV infected, DZNep-treated SARS-CoV infected. Cells from 4 distinct donors were used. Sample preparation was performed as described previously[3]. In brief, protein concentrations of cleared lysates were normalized and 50 µg were used for further processing. To reduce and alkylate proteins, samples were incubated for 5 min at 45 °C with TCEP (10 mM) and CAA (40 mM). Samples were digested overnight at 37 °C using trypsin (1:100 w/w, enzyme/protein, Sigma-Aldrich) and LysC (1:100 w/w, enzyme/protein, Wako). Resulting peptide solutions were desalted using SDB-RPS StageTips (Empore). Samples were diluted with 1% TFA in isopropanol to a final volume of 200 µl and loaded onto StageTips, subsequently washed with 200 µl of 1% TFA in isopropanol and 200 µl 0.2% TFA/ 2% ACN. Peptides were eluted with 75 µl of 1.25% Ammonium hydroxide (NH4OH) in 80% ACN and dried using a SpeedVac centrifuge (Eppendorf, Concentrator plus). Next, the peptides were reconstituted in buffer A* (0.2% TFA/ 2% ACN) prior to LC-MS/MS analysis. Peptide concentrations were measured optically at 280 nm (Nanodrop 2000, Thermo Scientific) and subsequently equalized using buffer A*. 1µg peptide was subjected to LC-MS/MS and protein groups quantified (MaxQuant version 1.6.10.43) with LFQ normalization (A549s) and without LFQ normalization (NHBEs) as described previously[11].

The analysis of MS data sets was performed using R version 4.0.2. LFQ values were $\log_2$-transformed and protein groups only identified by site, reverse matches and potential contaminants excluded from the analysis. Additionally, protein groups quantified by a single peptide or not detected in all replicates of at least one condition were excluded from further analysis. In NHBE dataset, LFQ values were normalized for donor-specific effects on protein abundance. In short, the protein $\log_2$-intensities were compared across conditions in a donor-wise manner, and systematic deviations across conditions subtracted in order to get normalized LFQ values.

The imputation of missing $\log_2$-intensity values was done similarly to the method implemented in Perseus[70]: the mean and the standard deviation of $\log_2$-intensities were calculated for each dataset, and missing values were replaced by sampling from the normal distribution with the following parameters: 0.3 * standard deviation, mean – 1.8 * standard deviation. In addition, effect scaling was performed using Gaussian generalized linear modeling approach (core function glm) to allow for quantitative comparison between virus infections and treatments in different contexts. In short, the following experiment design was used: norm. $\log_2$-LFQ ~ virus + virus:treatment, where virus refers to infection with mock, SARS-CoV or SARS-CoV-2, and treatment refers to vehicle or DZNep treatment. Median absolute values of significant effects ($p<0.01$) originating from virus and virus:treatment coefficients were calculated and divided by median of SARS-CoV-2 and mock:DZNep, respectively, resulting in coefficient 1 +/- 0.15 that were used in downstream analysis as coefficients in experimental design matrix.

The following experiment design was used for LASSO-based differential protein abundance analysis: LFQ ~ virus + virus:treatment, where virus refers to infection with mock-, SARS-CoV or SARS-CoV-2, and treatment refers to vehicle or DZNep treatment. The following effects were thus estimated: effect of SARS-CoV infection, effect of SARS-CoV-2 infection, effect of DZNep treatment of mock-infected cells, effect of DZNep treatment of SARS-CoV infected cells and the effect of DZNep treatment of SARS-CoV-2 infected cells. The estimation of LASSO model parameters was performed using R package glmnet[88] (version 4.0.2) with thresh=1e-28, maxit=1e7 and nfolds=11. The exact model coefficients and lambda value at cross-validation minimum (lambda.min) were extracted and used for p-value estimation by fixed-lambda LASSO inference using R package selectiveInference[71] version 1.2.5. Default parameters were used with the following modifications: tol.beta=0.025, alpha=0.1, tailarea_rtol=0.1, tol.kkt=0.1 and bits=100. The bits parameter was set to 300 or 500 if the convergence was not reached. The sigma was explicitly estimated using function estimateSigma from the same package. No multiple hypothesis p-value correction was performed since that is facilitated by the choice of lambda. The following thresholds were applied to LASSO analysis results to identify statistically significant effects (log2 fold-changes): $p < 10^{-5}$ and abs (log2 fold change) > 0.5 for the NHBE data, and $p < 10^{-4}$ and abs (log2 fold change) > 0.2 for A549 data. If a protein reached significance in one infected condition, or one treated condition, and not others, the significance thresholds for the other conditions were relaxed to: $p < 10^{-2}$ and abs (log2 fold chage) > 0.2, in order to avoid over-estimating differences among similar infections or drug treatments.

Protein GO-term annotations were retrieved using R package biomaRt[72] (version 2.45.5). Fisher's exact test was employed, and FDR-adjusted p-values were used to identify the terms that are significantly enriched among the changing proteins (threshold: $p < 10^{-2}$).

Proteins, significantly changing in the same direction (up- or down-regulated) upon DZNep treatment of SARS-CoV and SARS-CoV-2 infected NHBEs as determined by the above described analysis (marked in grey and dark-grey in Figure 4b) were used in network diffusion analysis. Network diffusion analysis was performed using ReactomeFI network v2019[73]. Random walk with restart kernel (R) was computed for this network in undirected manner, with restart probability of 0.4 according to the following equation: $R = alpha * (I- (1-alpha)*W)^{-1}$, where I is the identity matrix and W is the weight matrix computed as $W = D^{-1} * A$, where D is degree diagonal matrix and A is adjacency matrix for ReactomeFI graph. The diagonal values of the R matrix, representing restart- and feedback-flows, were excluded from subsequent analysis and set to 0. The significant hits from MS-data analysis were mapped to genes in the ReactomeFI network by matching gene names or their synonyms (from the biomaRt_hsapiens gene ensemble dataset) with the gene names in ReactomeFI. Nodes with significant flows originating from nodes representing hits in individual analyses were estimated using a randomization based approach. All hits and non-hits of the analysis were attributed equal weight (1 and 0, respectively) in subsequent statistical analysis. Flows to all nodes in the network were computed by multiplying the R matrix with the vector of hits described above. Furthermore, nodes in the network were assigned to 8 bins of approximately equal size according to the node degree. The same procedure of calculating inbound flows to all network nodes was repeated for 2500 iterations, each time using the same number of randomly selected decoy hits from sets of nodes with 1 bin higher node degree (on per-hit basis). The p-values describing the significance of functional connectivity to input hits were computed for each node according to the following formula: p = N (iteration with equal or higher inbound flux)/N (iterations). For visualization purposes, the ReactomeFI network was filtered for nodes that were either representing input proteins or proteins with $p < 0.005$ and further trimmed by removing non-hit nodes with degree equal to 1.

Virus adaptation and competition assays

Vero E6 cells were seeded in T-175 flasks at 15 million cells per flask 24 hours before the standard culturing medium was exchanged to one including treatments of choice (0.025% DMSO, 1.25 µM DZNep or 2.5 µM FIDAS-5). 6 hours post treatment, the cultures were inoculated with SARS-CoV-2-MUC-IMB-1 (P0) at MOI 0.01. 48 hours post inoculation, the supernatant was harvested, spun at 1.000 g for 5 minutes, and further processed for RNA isolation and titration of infectious viral particle content as described above. Deduced titers were used to inoculate freshly prepared Vero E6 cells as described for P0. The process was repeated until reaching passage 10 and is schematically depicted in Figure 5a. Isolated viral genomic RNA was reverse transcribed as described above and submitted for sequencing (described below).

For pairwise comparison of replication fitness (competition assay), Vero E6 cells were seeded in 12-well plate at a density of 0.2 million cells per well 24 hours before the standard culturing medium was exchanged for one containing treatments of choice (0.025% DMSO, 1.25 µM DZNep or 2.5 µM FIDAS-5). 6 hours post treatment, the cultures were inoculated with 1 to 1 mixture (according to infectious particle content) of 1.) DMSO P10 and DZNep P10, 2.) DMSO P10 and FIDAS-5 P10, and 3.) DMSO P10 and P0, at MOI 0.01. A part of the inoculum was saved for sequencing analysis. 48 hours post infection, the culture supernatant was harvested and its RNA content isolated, which was further reverse transcribed as described above and submitted for sequencing (described below).

For sequencing, SARS-CoV-2 genomes were prepared from amplicon pools, generated with a balanced primer pool according to ARTICv3 protocol[91]. Amplicons were converted to barcoded Illumina sequencing libraries with the NexteraXT kit (Illumina, San Diego, USA) in a miniaturized version using a Mantis dispenser (Formulatrix, Bedford, USA) and sequenced on an Illumina NextSeq1000. The obtained sequence reads were demultiplexed and aligned to the SARS-CoV-2 reference genome (NC 045512.2) with BWA-MEM[74]. The read depth along the reference genome was calculated with samtools depth. Variants were called using Freebayes[75] using a ploidy of 1 (-p 1). The effects of genetic variants on amino acid sequences were predicted with SnpEff[75]. The pileups files were generated using samtools[76] and used for consensus sequence generation within the iVar[77] package with default settings. Multiple sequence alignments of the consensus sequences were calculated using MAFFT (v7.475)[78] which were passed to IQ-TREE2 (v.2.1.2)[79] to calculate the newick tree.

Ratios between viral isolates in virus competition assay were calculated using mutations depicted in Figure EV5g according to the following formulas, assuming no adaptation events during the course of virus competition assay:

$$Svf \ = \ X \times A_{vf} + Y \times B_{vf}$$

$$X + Y = 1$$

Where S_{vf}, A_{vf} and B_{vf} are measured variation frequencies of particular mutation in sample of interest, isolate A used in inoculum and isolate B used in inoculum, respectively. X and Y describe the ratios of isolate A and isolate B in the sample, respectively, and in sum equal to unity. X and Y can be deduced from equations above in the following manner:

$$X = \frac{S_{vf} - B_{vf}}{A_{vf} - B_{vf}}$$

$$Y \ = \ 1 - X$$

Quantitative analysis of co-treatments

Viral inhibition assays utilizing DZNep and Remdesivir (or IFN-α) co-treatment and SARS-CoV-2-GFP virus were performed as described above. For Remdesivir, A549-RFP-ACE2 cell line was used and a number of RFP-positive cell nuclei was used for normalization of virus reporter signal (instead of phase based cell confluence used for IFN-α). The calculations of combination indexes for mutually exclusive drugs were performed as described previously[80]. In short, fractions of system affected and unaffected (f_a and f_u, respectively) were calculated for means of normalized GFP integrated intensities (NGII) originating from individual treatment conditions according to the following equation:

$$f_a = 1 - f_u = 1 - \frac{NGII\,(c_{DZNep}, c_{Remdesivir})}{NGII\,(vehicle, vehicle)}$$

Half maximal effective concentrations (EC50) and Hill-type coefficients (m) were calculated by performing linear modelling of vehicle co-treated data according to the following equations:

$$log_2\,(\frac{f_a\,(c_{DZNep}, vehicle)}{1-f_a\,(c_{DZNep}, vehicle)}) = m \times log_2 c_{DZNep} - m \times log_2 EC50_{DZNep}$$

$$log_2\,(\frac{f_a\,(vehicle, c_{Remdesivir})}{1-f_a\,(vehicle, c_{Remdesivir})}) = m \times log_2 c_{Remdesivir} - m \times log_2 EC50_{Remdesivir}$$

Combination index (CI) was further calculated according to the following equations:

$$D^t_{DZNep} = EC50_{DZNep} \times \left(\frac{f_a}{1-f_a}\right)^{1/m_{DZNep}}$$

$$D^t_{Remdesivir} = EC50_{Remdesivir} \times \left(\frac{f_a}{1-f_a}\right)^{1/m_{Remdesivir}}$$

$$IC = \frac{c_{DZNep}}{c^t_{DZNep}} + \frac{c_{Remdesivir}}{c^t_{Remdesivir}}$$

Quantification of virus transcripts in mouse lung material by RT-qPCR

At 2 days post infection, lungs of infected mice were harvested and homogenized in TRIzol (Invitrogen) using gentle MACS Octo Dissociator (Miltenyi Biotec). RNA was extracted from the homogenates following the manufacturer’s protocol. cDNA was generated using High-Capacity cDNA Reverse Transcription Kit (Applied Biosystems). To quantify the viral RNA, real-time quantitative PCR was performed by Step One Plus Real-Time PCR System (Applied Biosystems) using Fast SYBR Green Master Mix (Applied Biosystems) and TaqMan Fast Advanced Master Mix (Applied Biosystems) (for transcripts M, E and 18s rRNA), and by QuantStudio 3 Real-Time PCR system (Thermo Fisher) using PowerUp SYBR Green (Thermo Fisher) (for transcripts N and Actb). RT-qPCR primers were designed for SARS-CoV-2 genes as below: 5'-TGTGACATCAAGGACCTGCC-3'; 5'-CTGAGTCACCTGCTACACGC -3' for SARS-CoV-2 M and 5'-ACAGGTACGTTAATAGTTAATAGCGT-3'; 5'-ATATTGCAGCAGTACGCACACA-3' for SARS-CoV-2 E and 5’-TTACAAACATTGGCCGCAAA-3’; 5’-GCGCGACATTCCGAAGAA-3’ for SARS-CoV-2 N. Levels of viral transcripts M and E were normalized with 18s rRNA levels using the TaqMan probe for eukaryotic 18s rRNA (Hs99999901_s1, Applied Biosystems). Levels of viral transcript N were normalized with Actb levels (RT-qPCR primers: 5’-CTCTGGCTCCTAGCACCATGAAGA-3’; 5’-GTAAAACGCAGCTCAGTAACAGTCCG-3’).

Materials and methods - part 2

This methods section describes my own methodological contribution in investigations presented in the following publication, and is adapted from it:

Alexey Stukalov*, Virginie Girault*, Vincent Grass*, Ozge Karayel*, **Valter Bergant***, Christian Urban*, Darya A. Haas*, Yiqi Huang*, Lila Oubraham, Anqi Wang, M. Sabri Hamad, Antonio Piras, Fynn M. Hansen, Maria C. Tanzer, Igor Paron, Luca Zinzula, Thomas Engleitner, Maria Reinecke, Teresa M. Lavacca, Rosina Ehmann, Roman Wölfel, Jörg Jores, Bernhard Kuster, Ulrike Protzer, Roland Rad, John Ziebuhr, Volker Thiel, Pietro Scaturro, Matthias Mann & Andreas Pichlmair. **Multilevel proteomics reveals host perturbations by SARS-CoV-2 and SARS-CoV.** *Nature*, 2021. doi: 10.1038/s41586-021-03493-4

Cell lines and reagents

HEK293T, A549, Vero E6 and HEK293-R1 cells and their respective culturing conditions were described previously[81]. All cell lines were tested to be mycoplasma-free. Expression constructs for C-terminal HA tagged viral ORFs were synthesized (Twist Bioscience and BioCat) and cloned into pWPI vector as described previously[82] with the following modifications: starting ATG codon was added, internal canonical splicing sites were replaced with synonymous mutations and C-terminal HA-tag, followed by amber stop codon, was added to individual viral open reading frames. C-terminally hemagglutinin(HA)-tagged ACE2 sequence was amplified from an ACE2 expression vector (kindly provided by Stefan Pöhlmann)[83] into the lentiviral vector pWPI-puro. A549 cells were transduced twice, and ACE2-expressing A549 (A549-ACE2) cells were selected with puromycin. Lentiviruses production, transduction of cells and antibiotic selection were performed as described previously[84]. RNA-isolation (Macherey-Nagel NucleoSpin RNA plus), reverse transcription (TaKaRa Bio PrimeScript RT with gDNA eraser) and RT-qPCR (Thermo-Fisher Scientific PowerUp SYBR green) were performed as described previously[85]. RNA-isolation for NGS applications was performed according to manufacturer's protocol (Qiagen RNeasy mini kit, RNase free DNase set). For detection of protein abundance by western blotting, HA-HRP (Sigma-Aldrich), ACTB-HRP (Santa Cruz), MAP1LC3B, MAVS, HSPA1A, TGF-β and SQSTM1, phospho-p38 (T180/Y182), p38 (Cell Signaling), SARS-CoV-2/SARS-CoV N protein (Sino Biological) antibodies were used. For AP-MS and AP-WB applications, HA-beads (Sigma-Aldrich and Thermo Fisher Scientific) and Streptactin II beads (IBA Lifesciences) were used. Secondary antibodies: HRP and WB imaging was performed as described previously[16]. For the stimulation of cells in the reporter assay, recombinant human IFN-α was a kind gift from Peter Stäheli, recombinant human IFN-γ were purchased from PeproTech and IVT4 was produced as described before[86]. All compounds tested during the viral inhibitor assay are listed in Supplementary Table 9 in the appended manuscript.

Virus strains, stock preparation, plaque assay and in vitro infection

SARS-CoV-Frankfurt-1, SARS-CoV-2-MUC-IMB-1 and SARS-CoV-2-GFP strains[62] were produced by infecting Vero E6 cells cultured in DMEM medium (10% FCS, 100 ug/ml Streptomycin, 100 IU/ml Penicillin) for 2 days (MOI 0,01). Viral stock was harvested and spun twice (1000g/10min) before storage at -80°C. Titer of viral stock was determined by plaque assay. Confluent monolayers of VeroE6 cells were infected with serial five-fold dilutions of virus supernatants for 1 hour at 37 °C. The inoculum was removed and replaced with serum-free MEM (Gibco, Life Technologies) containing 0.5% carboxymethylcellulose (Sigma-Aldrich). Two days post infection, cells were fixed for 20 minutes at room temperature with formaldehyde directly added to the medium to a final concentration of 5%. Fixed cells were washed extensively with PBS before staining with H2O containing 1% crystal violet and 10% ethanol for 20 minutes. After rinsing with PBS, the number of plaques was counted and the virus titer was calculated.

A549-ACE2 cells were infected with either SARS-CoV-Frankfurt-1 or SARS-CoV-2-MUC-IMB-1 strains (MOI 2) for the subsequent experiments. At each time point, the samples were washed once with 1x TBS buffer and harvested in SDC lysis buffer (100 mM Tris HCl pH 8.5; 4% SDC) or 1x SSB lysis buffer (62.5 mM Tris HCl pH 6.8; 2% SDS; 10% glycerol; 50 mM DTT; 0.01% bromophenol blue) or RLT (Qiagen) for proteome-phosphoproteome-ubiquitinome, western blot, and transcriptome analyses, respectively. The samples were heat-inactivated and frozen at -80°C until further processing, as described in the following sections.

Affinity purification and mass spectrometric analyses of SARS-CoV-2, SARS-CoV and HCoV-229E/NL63 proteins expressed in A549 cells

To determine the interactomes of SARS-CoV-2 and SARS-CoV and the interactomes of an accessory protein (encoded by ORF4/ORF4a of HCoV-229E or ORF3 of HCoV-NL63) that presumably represents a homolog of the ORF3 and ORF3a proteins of SARS-CoV-2 and SARS-CoV, respectively, four replicate affinity purifications were performed for each HA-tagged viral protein. A549 cells (6×10^6 cells per 15-cm dish) were transduced with lentiviral vectors encoding HA-tagged SARS-CoV-2, SARS-CoV or HCoV-229E/NL63 proteins and protein lysates were prepared from cells harvested three days post-transduction. Cell pellets of two 15-cm dishes were lysed in lysis buffer (50 mM Tris-HCl pH 7.5, 100 mM NaCl, 1.5 mM $MgCl_2$, 0.2% (v/v) NP-40, 5% (v/v) glycerol, cOmplete protease inhibitor cocktail (Roche), 0.5% (v/v) 750 U/µl Sm DNAse) and sonicated (5 min, 4°C, 30 sec on, 30 sec off, low settings; Bioruptor, Diagenode SA). Following normalization of protein concentrations of cleared lysates, virus protein-bound host proteins were enriched by adding 50 µl anti-HA-agarose slurry (Sigma-Aldrich, A2095) with constant agitation for 3 hours at 4°C. Non-specifically bound proteins were removed by four subsequent washes with lysis buffer followed by three detergent-removal steps with washing buffer (50 mM Tris-HCl pH 7.5, 100 mM NaCl, 1.5 mM $MgCl_2$, 5% (v/v) glycerol). Enriched proteins were denatured, reduced, alkylated and digested by addition of 200 µl digestion buffer (0.6 M guanidinium chloride, 1 mM TCEP, 4 mM CAA, 100 mM Tris-HCl pH 8, 0.5 µg LysC (WAKO Chemicals), 0.5 µg trypsin (Promega) at 30°C overnight. Peptide purification on StageTips with three layers of C18 Empore filter discs (3M) and subsequent mass spectrometry analysis was performed as described previously[81,82]. Briefly, purified peptides were loaded onto a 20 cm reverse-phase analytical column (75 µm diameter; ReproSil-Pur C18-AQ 1.9 µm resin; Dr. Maisch) and separated using an EASY-nLC 1200 system (Thermo Fisher Scientific). A binary buffer system consisting of buffer A (0.1% formic acid in H_2O)

and buffer B (80% acetonitrile, 0.1% formic acid in H_2O) with a 90 min gradient (5-30% buffer B (65 min), 30-95% buffer B (10 min), wash out at 95% buffer B (5 min), decreased to 5% buffer B (5 min), and 5% buffer B (5 min)) was used at a flow rate of 300 nl per min. Eluting peptides were directly analysed on a Q-Exactive HF mass spectrometer (Thermo Fisher Scientific). Data-dependent acquisition included repeating cycles of one MS1 full scan (300–1.650 m/z, R = 60.000 at 200 m/z) at an ion target of 3×10^6, followed by 15 MS2 scans of the highest abundant isolated and higher-energy collisional dissociation (HCD) fragmented peptide precursors (R = 15.000 at 200 m/z). For MS2 scans, collection of isolated peptide precursors was limited by an ion target of 1 × 10e5 and a maximum injection time of 25 ms. Isolation and fragmentation of the same peptide precursor was eliminated by dynamic exclusion for 20 s. The isolation window of the quadrupole was set to 1.4 m/z and HCD was set to an normalized collision energy of 27%.

Proteome analyses of cells expressing SARS-CoV-2, SARS-CoV and HCoV-229E/NL63 proteins

For the determination of proteome changes in A549 cells expressing SARS-CoV-2, SARS-CoV or HCoV-229E/NL63 proteins, a fraction of 1×10^6 lentivirus-transduced cells from the affinity purification samples were lysed in guanidinium chloride buffer (6 M GdmCl, 10 mM TCEP, 40 mM CAA, 100 mM Tris-HCl pH 8), boiled at 95°C for 8 min and sonicated (10 min, 4°C, 30 sec on, 30 sec off, high settings). Protein concentrations of cleared lysates were normalized to 50 µg and proteins were pre-digested with 1 µg LysC at 37°C for 1 hour followed by a 1:10 dilution (100 mM Tris-HCl pH 8) and overnight digestion with 1 µg trypsin at 30°C. Peptide purification on StageTips with three layers of C18 Empore filter discs (3M) and subsequent mass spectrometry analysis was performed as described previously[81,82]. Briefly, 300 ng of purified peptides were loaded onto a 50 cm reversed phase column (75 µm inner diameter, packed in house with ReproSil-Pur C18-AQ 1.9 µm resin [Dr. Maisch GmbH]). The column temperature was maintained at 60°C using a homemade column oven. A binary buffer system, consisting of buffer A (0.1% formic acid (FA)) and buffer B (80% ACN, 0.1% FA), was used for peptide separation, at a flow rate of 300 nl/min. An EASY-nLC 1200 system (Thermo Fisher Scientific), directly coupled online with the mass spectrometer (Q Exactive HF-X, Thermo Fisher Scientific) via a nano-electrospray source, was employed for nano-flow liquid chromatography. Peptides were eluted by a linear 80 min gradient from 5% to 30% buffer B (0.1% v/v formic acid, 80% v/v acetonitrile), followed by a 4 min increase to 60% B, a further 4 min increase to 95% B, a 4 min plateau phase at 95% B, a 4 min decrease to 5% B and a 4 min wash phase of 5% B. To acquire MS data, the data-independent acquisition (DIA) scan mode operated by the XCalibur software (Thermo Fisher) was used. DIA was performed with one full MS event followed by 33 MS/MS windows in one cycle resulting in a cycle time of 2.7 seconds. The full MS settings included an ion target value of 3×10^6 charges in the 300 – 1650 m/z range with a maximum injection time of 60 ms and a resolution of 120.000 at m/z 200. DIA precursor windows ranged from 300.5 m/z (lower boundary of first window) to 1649.5 m/z (upper boundary of 33rd window). MS/MS settings included an ion target value of 3×10^6 charges for the precursor window with an Xcalibur-automated maximum injection time and a resolution of 30.000 at m/z 200.

To generate the proteome library for DIA measurements purified peptides from the first and the fourth replicates of all samples were pooled separately and 25 µg of peptides from each pool were fractionated into 24 fractions by high pH reversed-phase chromatography as described earlier[87]. During each separation, fractions were concatenated automatically by shifting the collection tube every 120 seconds. In total 48 fractions were dried in a vacuum centrifuge, resuspended in buffer A* (0.2% TFA, 2% ACN) and subsequently analyzed by a top12 data-dependent acquisition (DDA) scan mode using the same LC gradient and settings. The mass spectrometer was operated by the XCalibur software (Thermo Fisher). DDA scan settings on full MS level included an ion target value of 3 x 10^6 charges in the 300 – 1650 m/z range with a maximum injection time of 20 ms and a resolution of 60.000 at m/z 200. At the MS/MS level the target value was 10^5 charges with a maximum injection time of 60 ms and a resolution of 15.000 at m/z 200. For MS/MS events only, precursor ions with 2-5 charges that were not on the 20 s dynamic exclusion list were isolated in a 1.4 m/z window. Fragmentation was performed by higher-energy C-trap dissociation (HCD) with a normalized collision energy of 27eV.

qRT-PCR analysis

RNA isolation from SARS-CoV and SARS-CoV-2 infected A549-ACE2 cells was performed as described above (Qiagen). 500 ng total RNA was used for reverse transcription with PrimeScript RT with gDNA eraser (Takara). For relative transcript quantification PowerUp SYBR Green (Applied Biosystems) was used.

Co-immunoprecipitation and western blot analysis

HEK293T cells were transfected with pWPI plasmid encoding single HA-tagged viral proteins, alone or together with pTO-SII-HA expressing host factor of interest. 48 hours after transfection, cells were washed in PBS, flash frozen in liquid nitrogen and kept at -80°C until further processing. Co-immunoprecipitation experiments were performed as described previously[81,82]. Briefly, cells were lysed in lysis buffer (50 mM Tris-HCl pH 7.5, 100 mM NaCl, 1.5 mM $MgCl_2$, 0.2% (v/v) NP-40, 5% (v/v) glycerol, cOmplete protease inhibitor cocktail (Roche), 0.5% (v/v) 750 U/µl Sm DNAse) and sonicated (5 min, 4°C, 30 sec on, 30 sec off, low settings; Bioruptor, Diagenode SA). HA or Streptactin beads were added to cleared lysates and samples were incubated for 3 hours at 4°C under constant rotation. Beads were washed six times in the lysis buffer and resuspended in 1x SDS sample buffer 62,5 mM Tris-HCl pH 6.8, 2% SDS, 10% glycerol, 50 mM DTT, 0.01% bromophenol blue). After boiling for 5 minutes at 95°C, a fraction of the input lysate and elution were loaded on NuPAGE™ Novex™ 4-12% Bis-Tris (Invitrogen), and further submitted to western blotting using Amersham Protran nitrocellulose membranes. Imaging was performed by HRP luminescence (ECL, Perkin Elmer).

SARS-CoV-2 infected A549-ACE2 cell lysates were sonicated (10 min, 4°C, 30 sec on, 30 sec off, low settings; Bioruptor, Diagenode SA). Protein concentration was adjusted based on Pierce660 assay supplemented with ionic detergent compatibility reagent. After boiling for 5 min at 95°C and brief max g centrifugation, the samples were loaded on NuPAGE™ Novex™ 4-12% Bis-Tris (Invitrogen), and blotted onto

0,22 µm Amersham™ Protran® nitrocellulose membranes (Merck). Primary and secondary antibody stainings were performed according to the manufacturer's recommendations. Imaging was performed by HRP luminescence using Femto kit (ThermoFischer Scientific) or Western Lightning PlusECL kit (Perkin Elmer).

Viral inhibitor assay

A549-ACE2 cells were seeded into 96-well plates in DMEM medium (10% FCS, 100 ug/ml Streptomycin, 100 IU/ml Penicillin) one day before infection. Six hours before infection, or at the time of infection, the medium was replaced with 100µl of DMEM medium containing either the compounds of interest or DMSO as a control. Infection was performed by adding 10µl of SARS-CoV-2-GFP (MOI 3) per well and plates were placed in the IncuCyte S3 Live-Cell Analysis System where whole well real-time images of mock (Phase channel) and infected (GFP and Phase channel) cells were captured every 4 hours for 48 hours. Cell viability (mock) and virus growth (mock and infected) were assessed as the cell confluence per well (Phase area) and GFP area normalized on cell confluence per well (GFP area/Phase area) respectively using IncuCyte S3 Software (Essen Bioscience; version 2019B Rev2).

For comparative analysis of antiviral treatment activity against SARS-CoV and SARS-CoV-2, A549-ACE2 cells were seeded in 24-well plates, as previously described[81,82]. Treatment was performed for 6 hours with 0.5ml of DMEM medium containing either the compounds of interest or DMSO as a control, and infected with SARS-CoV-Frankfurt-1 or SARS-CoV-2-MUC-IMB-1 (MOI 1) for 24 hours. Total cellular RNA was harvested and analyzed by qRT-PCR, as previously described[81,82].

Publication results summary - part 1

Valter Bergant*, Shintaro Yamada*, Vincent Grass, Yuta Tsukamoto, Teresa Lavacca, Karsten Krey, Maria-Teresa Mühlhofer, Sabine Wittmann, Armin Ensser, Alexandra Herrmann, Anja vom Hemdt, Yuriko Tomita, Shutoku Matsuyama, Takatsugu Hirokawa, Yiqi Huang, Antonio Piras, Constanze A. Jakwerth, Madlen Oelsner, Susanne Thieme, Alexander Graf, Stefan Krebs, Helmut Blum, Beate M. Kümmerer, Alexey Stukalov, Carsten B. Schmidt-Weber, Manabu Igarashi, Thomas Gramberg, Andreas Pichlmair[§], Hiroki Kato[§]. **Attenuation of SARS-CoV-2 replication and associated inflammation by concomitant targeting of viral and host cap 2'-O-ribose methyltransferases.** *EMBO*, 2022.
doi: 10.15252/embj.2022111608

This publication was a result of a large-scale collaborative effort between multiple research groups. I contributed to conceptualization, experiments, analysis and writing of the manuscript and spearheaded the efforts of our group centered around SCIs (Fig. 3-5, EV2-5). With exception of BSL3 work and in consultation with coauthors, I planned, performed, analyzed and interpreted antiviral and other assays (e.g. Fig. 3, EV2, EV3, 5C-D) and LC-MS/MS experiments (Fig. 4, EV4). I also analyzed and interpreted the virus sequencing data (Fig. 5A-B, EV5A-G) and visualized the data (Fig. 3-5, EV2-5). With input from coauthors, I wrote the sections of manuscript dealing with SCIs.

Summary is adapted from the above stated publication.

Summary

We leveraged both direct acting and host-directed antiviral drug repurposing to explore the antiviral potential of pharmaceutical inhibition of SARS-CoV-2 cap 2'-O-ribose methyltransferase NSP16. Through *in silico* molecular docking we identified a set of drug candidates with the potential to inhibit MTase activity of NSP16. While the inhibitor Tubercidin (7-deazaadenosine) proved to be highly antiviral against SARS-CoV-2, other inhibitors with comparable or higher docking scores did not significantly affect virus replication. We show that genetically inflicted loss of function of NSP16 results in an unexpectedly mild attenuation of SARS-CoV-2, indicating that stand-alone inhibition of NSP16 is insufficient to impair the virus replication. Surprisingly, SARS-CoV-2 NSP16 mutant virus failed to replicate in cells that were depleted for the host cap 2’O-ribose MTase CMTR1 (MTr1, FTSJD2), suggesting that this host protein can compensate for the activity of its viral analog NSP16. Indicative of promiscuity, Tubercidin potently inhibited both NSP16 and MTr1 in vitro, further emphasizing that a concomitant inhibition of NSP16 and MTr1 is pivotal for effective antiviral treatment. The activity of MTr1 and NSP16 critically depends on the metabolite homeostasis maintained by the host SAM-cycle. We further explored the antiviral potential of host-directed SAM-cycle inhibitors (SCIs), which in an indirect manner induce a metabolic broad spectrum MTase inhibition. We show that targeting all three independent enzymatic steps of the SAM-cycle by unrelated small molecule inhibitors significantly reduces SARS-CoV-2 proliferation in vitro. Notably, the SAM-cycle inhibitor 3-deazaneplanocin A (DZNep), an inhibitor of AHCY, has especially potent and selective antiviral efficacy against SARS-CoV-2 in vitro, ex vivo and in a mouse infection model. In line with its known facilitative effect on tissue repair, DZNep treatment of primary human lung cells exhibited a strong immunomodulatory effect curbing infection-induced hyperinflammation and reduced lung fibrosis- and coagulopathy related markers. Moreover, we show that DZNep specifically synergizes with the current treatment options Remdesivir and Interferon alpha. These findings demonstrate that targeting the MTases involved in SARS-CoV-2 viral life cycle is a novel and therapeutically viable antiviral strategy for treatment of COVID-19.

Publication results summary - part 2

Alexey Stukalov*, Virginie Girault*, Vincent Grass*, Ozge Karayel*, **Valter Bergant***, Christian Urban*, Darya A. Haas*, Yiqi Huang*, Lila Oubraham, Anqi Wang, M. Sabri Hamad, Antonio Piras, Fynn M. Hansen, Maria C. Tanzer, Igor Paron, Luca Zinzula, Thomas Engleitner, Maria Reinecke, Teresa M. Lavacca, Rosina Ehmann, Roman Wölfel, Jörg Jores, Bernhard Kuster, Ulrike Protzer, Roland Rad, John Ziebuhr, Volker Thiel, Pietro Scaturro, Matthias Mann & Andreas Pichlmair. **Multilevel proteomics reveals host perturbations by SARS-CoV-2 and SARS-CoV.** *Nature*, 2021. doi: 10.1038/s41586-021-03493-4

This publication was a result of a large-scale collaborative effort between multiple research groups. I in part contributed to conceptualization, experiments, analysis and writing of the manuscript. In particular, I performed the biological interpretation of the multiomics (interactomics, effectomics) data presented in e.g. Fig. 1a-c, ED1b and ED2c-d (for SARS-CoV and SARS-CoV-2 NSP3, NSP14, ORF7a, ORF7b, ORF9b). I also contributed to the analysis and interpretation of the virus infection multiomics data and network diffusion analyses presented in Fig. 2a-d, Fig. 4a and elsewhere (transcriptomics, proteomics, ubiquitinomics and phosphoproteomics). I also contributed to visualization of the data and together with other coauthors wrote the manuscript.

Summary is adapted from the above stated publication.

Summary

The global emergence of SARS-CoV-2 urgently requires an in-depth understanding of molecular functions of viral proteins and their interactions with the host proteome. Several individual omics studies have extended our knowledge of COVID-19 pathophysiology. Integration of such datasets to obtain a holistic view of virus-host interactions and to define the pathogenic properties of SARS-CoV-2 is limited by the heterogeneity of the experimental systems. We therefore conducted the first-ever concurrent multi-omics study of SARS-CoV-2 and SARS-CoV. Using state-of-the-art proteomics, we profiled the interactome of both viruses, as well as their influence on transcriptome, proteome, ubiquitinome and phosphoproteome in a lung-derived human cell line. Projecting these data onto the global network of cellular interactions revealed crosstalk between the perturbations taking place upon SARS-CoV-2 and SARS-CoV infections at different layers and identified unique and common molecular mechanisms of these closely related coronaviruses. Among our findings, the TGF-β pathway, known for its involvement in tissue fibrosis, was specifically dysregulated by SARS-CoV-2 ORF8, as well as autophagy by SARS-CoV-2 ORF3. The extensive dataset presented here highlights hotspots that can be targeted by available drugs and rational design of virus- and host-directed therapies, which we exemplify by identifying kinase and MMPs inhibitors with potent antiviral effects against SARS-CoV-2.

Discussion

Similar to pandemics of the past century, tackling COVID-19 pandemic has so far been dominated by pharmaceutical and non-pharmaceutical preventive measures, i.e. vaccines and exposure prevention measures, respectively. While work on therapeutic antiviral drug candidates is underway, the primary treatment remains symptomatic, involving symptome management, supportive care and isolation.

There are currently more than 500 vaccine-unrelated single or combinatorial COVID-19 drug candidates in clinical trials. Vast majority of them are direct-acting antivirals (DAAs), such as fusion- (e.g. Camostat), protease- (e.g. Paxlovid) and polymerase (e.g. Remdesivir, Molnupiravir) inhibitors[88], which aim to limit virus replication. DAAs do not affect tissue processes, such as fibrosis or regeneration, per se. Minority of current drug candidates are host-directed (HD) and include immunosuppressants (e.g. anakinra), steroids (e.g. dexamethasone) and interferons (e.g. PEGinterferons).

Multifunctional antivirals, especially ones possessing antiviral and immunomodulatory functions, would be highly beneficial for treatment of acute viral infections such as COVID-19. To the best of our knowledge, there are currently no single drug candidates that could offer virus repression and collateral benefits, such as we demonstrate for DZNep. The main competitive therapies consist of combinatorial treatments involving DAAs and anti-inflammatory treatments (i.e. current standards of care for severe cases), e.g. Remdesivir/Molnupiravir + dexamethasone (alternatively + JAK inhibitors baricitinib/tofacitinib or + anti-IL6R mAbs tocilizumab/sarilumab), supplemented as necessary by symptomatic treatments (e.g. anticoagulants)

Our multi-omics investigation[8] of SARS coronaviruses, which we directly coupled to the host-directed antivirals' target validation, demonstrates the value of our multi-omics dataset. Further exploration of this rich dataset by the scientific community will substantially contribute to our molecular understanding of the biology and pathogenicity of coronaviruses such as the SARS-CoV-2. Moreover, this resource in conjunction with complementary approaches aims to streamline the repurposing and discovery of antiviral compounds. It may furthermore serve as the foundation towards rational design of combinatorial therapies that target the virus or the host from multiple synergistic trajectories.

We further leveraged[9] repurposing of both direct-acting and host-directed antivirals to evaluate the potential of inhibiting viral cap 2'-O-ribose MTase NSP16. We showed that, in this context, robust antiviral effect against SARS-CoV-2 critically requires concomitant inhibition of both the viral MTase NSP16 and the related novel host factor MTr1. Collectively, our findings demonstrate the potential of developing multifunctional host-directed antivirals, in the process of which the state of the art of both virus as well as host biology is used towards applied antiviral research. Notably, we showed that host-directed therapeutics that act at the virus-host metabolic interface and in particularly target the SAM-cycle have both antiviral as well as

---

[8] Paragraph adapted from my own writing published in Stukalov, Girault, Grass, Karayel, Bergant, Urban, Haas, Huang et al., 2021

[9] Paragraph adapted from my own writing published in Bergant, Yamada et al., EMBO, 2022

host-preserving functions. To the best of our knowledge, no single-drug therapy against COVID-19 is currently available that could tackle both the virus replication as well as the potentially long term lung damage and fibrosis[89–91]. DZNep is an excellent antiviral drug candidate for it combines these activities by repressing viral load, limiting the hyperinflammatory landscape in infected tissues and promoting cell intrinsic tissue repair programs.

References

1. Desselberger, U. Emerging and re-emerging infectious diseases. *J. Infect.* **40**, 3–15 (2000).
2. Bryan-Marrugo, O. L. *et al.* History and progress of antiviral drugs: From acyclovir to direct-acting antiviral agents (DAAs) for Hepatitis C. *Medicina Universitaria* **17**, 165–174 (2015).
3. De Clercq, E. Antivirals: past, present and future. *Biochem. Pharmacol.* **85**, 727–744 (2013).
4. De Clercq, E. & Li, G. Approved Antiviral Drugs over the Past 50 Years. *Clin. Microbiol. Rev.* **29**, 695–747 (2016).
5. Chaudhuri, S., Symons, J. A. & Deval, J. Innovation and trends in the development and approval of antiviral medicines: 1987–2017 and beyond. *Antiviral Research* vol. 155 76–88 Preprint at https://doi.org/10.1016/j.antiviral.2018.05.005 (2018).
6. Bule, M., Khan, F. & Niaz, K. Antivirals: Past, Present and Future. in *Recent Advances in Animal Virology* (eds. Malik, Y. S., Singh, R. K. & Yadav, M. P.) 425–446 (Springer Singapore, 2019).
7. Kaufmann, S. H. E., Dorhoi, A., Hotchkiss, R. S. & Bartenschlager, R. Host-directed therapies for bacterial and viral infections. *Nat. Rev. Drug Discov.* **17**, 35–56 (2018).
8. Kumar, N. *et al.* Host-Directed Antiviral Therapy. *Clin. Microbiol. Rev.* **33**, (2020).
9. Tripathi, D., Sodani, M., Gupta, P. K. & Kulkarni, S. Host directed therapies: COVID-19 and beyond. *Curr Res Pharmacol Drug Discov* **2**, 100058 (2021).
10. The RECOVERY Collaborative Group. Dexamethasone in Hospitalized Patients with Covid-19. *N. Engl. J. Med.* **384**, 693–704 (2021).
11. Stukalov, A. *et al.* Multilevel proteomics reveals host perturbations by SARS-CoV-2 and SARS-CoV. *Nature* **594**, 246–252 (2021).
12. Bergant, V. *et al.* Attenuation of SARS-CoV-2 replication and associated inflammation by concomitant targeting of viral and host cap 2’-O-ribose methyltransferases. *EMBO J.* e111608 (2022).
13. Gupta, A. *et al.* Extrapulmonary manifestations of COVID-19. *Nat. Med.* **26**, 1017–1032 (2020).
14. O’Sullivan, J. M., Gonagle, D. M., Ward, S. E., Preston, R. J. S. & O’Donnell, J. S. Endothelial cells orchestrate COVID-19 coagulopathy. *The Lancet. Haematology* vol. 7 e553–e555 (2020).
15. Muthukrishnan, S., Moss, B., Cooper, J. A. & Maxwell, E. S. Influence of 5’-terminal cap structure on the initiation of translation of vaccinia virus mRNA. *J. Biol. Chem.* **253**, 1710–1715 (1978).
16. Gebhardt, A. *et al.* The alternative cap-binding complex is required for antiviral defense in vivo. *PLoS Pathog.* **15**, (2019).
17. Schuberth-Wagner, C. *et al.* A Conserved Histidine in the RNA Sensor RIG-I Controls Immune Tolerance to N1-2’O-Methylated Self RNA. *Immunity* **43**, 41–51 (2015).
18. Züst, R. *et al.* Ribose 2′-O-methylation provides a molecular signature for the distinction of self and non-self mRNA dependent on the RNA sensor Mda5. *Nature Immunology* vol. 12 137–143 Preprint at https://doi.org/10.1038/ni.1979 (2011).
19. Daffis, S. *et al.* 2′-O methylation of the viral mRNA cap evades host restriction by IFIT family members. *Nature* **468**, 452–456 (2010).
20. Habjan, M. *et al.* Sequestration by IFIT1 impairs translation of 2’O-unmethylated capped RNA. *PLoS Pathog.* **9**, e1003663 (2013).
21. Abbas, Y. M. *et al.* Structure of human IFIT1 with capped RNA reveals adaptable mRNA binding and mechanisms for sensing N1 and N2 ribose 2?-O methylations. *Proc. Natl. Acad. Sci. U. S. A.* **114**, E2106–E2115 (2017).
22. Chen, Y. *et al.* Functional screen reveals SARS coronavirus nonstructural protein nsp14 as a novel cap N7 methyltransferase. *Proc. Natl. Acad. Sci. U. S. A.* **106**, 3484–3489 (2009).
23. Yan, L. *et al.* Coupling of N7-methyltransferase and 3′-5′ exoribonuclease with

SARS-CoV-2 polymerase reveals mechanisms for capping and proofreading. *Cell* **184**, 3474–3485.e11 (2021).
24. Decroly, E. *et al.* Coronavirus nonstructural protein 16 is a cap-0 binding enzyme possessing (nucleoside-2’O)-methyltransferase activity. *J. Virol.* **82**, 8071–8084 (2008).
25. Rosas-Lemus, M. *et al.* High-resolution structures of the SARS-CoV-2 2′-O-methyltransferase reveal strategies for structure-based inhibitor design. *Science Signaling* vol. 13 eabe1202 Preprint at https://doi.org/10.1126/scisignal.abe1202 (2020).
26. Menachery, V. D. *et al.* Attenuation and restoration of severe acute respiratory syndrome coronavirus mutant lacking 2’-o-methyltransferase activity. *J. Virol.* **88**, 4251–4264 (2014).
27. Menachery, V. D. *et al.* Middle East Respiratory Syndrome Coronavirus Nonstructural Protein 16 Is Necessary for Interferon Resistance and Viral Pathogenesis. *mSphere* **2**, (2017).
28. Chen, Y. *et al.* Biochemical and Structural Insights into the Mechanisms of SARS Coronavirus RNA Ribose 2′-O-Methylation by nsp16/nsp10 Protein Complex. *PLoS Pathog.* **7**, e1002294 (2011).
29. Ahmed-Belkacem, R. *et al.* Synthesis of adenine dinucleosides SAM analogs as specific inhibitors of SARS-CoV nsp14 RNA cap guanine-N7-methyltransferase. *Eur. J. Med. Chem.* **201**, 112557 (2020).
30. Vijayan, V. *et al.* Identification of promising drug candidates against NSP16 of SARS-CoV-2 through computational drug repurposing study. *J. Biomol. Struct. Dyn.* 1–15 (2020).
31. Aldahham, B. J. M. *et al.* Identification of naphthyridine and quinoline derivatives as potential Nsp16-Nsp10 inhibitors: a pharmacoinformatics study. *J. Biomol. Struct. Dyn.* 1–8 (2020).
32. Hoffman, D. R., Marion, D. W., Cornatzer, W. E. & Duerre, J. A. S-Adenosylmethionine and S-adenosylhomocystein metabolism in isolated rat liver. Effects of L-methionine, L-homocystein, and adenosine. *J. Biol. Chem.* **255**, 10822–10827 (1980).
33. Collinsova, M., Strakova, J., Jiracek, J. & Garrow, T. A. Inhibition of betaine-homocysteine S-methyltransferase causes hyperhomocysteinemia in mice. *J. Nutr.* **136**, 1493–1497 (2006).
34. Strakova, J. *et al.* Inhibition of betaine-homocysteine S-methyltransferase in rats causes hyperhomocysteinemia and reduces liver cystathionine β-synthase activity and methylation capacity. *Nutr. Res.* **31**, 563–571 (2011).
35. Aury-Landas, J. *et al.* The Antitumoral Effect of the S-Adenosylhomocysteine Hydrolase Inhibitor, 3-Deazaneplanocin A, is Independent of EZH2 but is Correlated with EGFR Downregulation in Chondrosarcomas. *Cell. Physiol. Biochem.* **53**, 731–745 (2019).
36. Aouadi, W. *et al.* Binding of the Methyl Donor S-Adenosyl-l-Methionine to Middle East Respiratory Syndrome Coronavirus 2’-O-Methyltransferase nsp16 Promotes Recruitment of the Allosteric Activator nsp10. *J. Virol.* **91**, (2017).
37. Uchiyama, N. *et al.* Identification of AHCY inhibitors using novel high-throughput mass spectrometry. *Biochem. Biophys. Res. Commun.* **491**, 1–7 (2017).
38. Hasan, T. *et al.* Disturbed homocysteine metabolism is associated with cancer. *Exp. Mol. Med.* **51**, 1–13 (2019).
39. Konteatis, Z. *et al.* Discovery of AG-270, a First-in-Class Oral MAT2A Inhibitor for the Treatment of Tumors with Homozygous MTAP Deletion. *J. Med. Chem.* (2021) doi:10.1021/acs.jmedchem.0c01895.
40. Sun, F. *et al.* Preclinical pharmacokinetic studies of 3-deazaneplanocin A, a potent epigenetic anticancer agent, and its human pharmacokinetic prediction using GastroPlus^{TM}. *Eur. J. Pharm. Sci.* **77**, 290–302 (2015).
41. Bray, M., Driscoll, J. & Huggins, J. W. Treatment of lethal Ebola virus infection in mice with a single dose of an S-adenosyl-L-homocysteine hydrolase inhibitor. *Antiviral Res.* **45**, 135–147 (2000).
42. Bray, M., Raymond, J. L., Geisbert, T. & Baker, R. O. 3-deazaneplanocin A induces massively increased interferon-alpha production in Ebola virus-infected mice. *Antiviral*

Res. **55**, 151–159 (2002).

43. Barnard, D. L. *et al.* Evaluation of immunomodulators, interferons and known in vitro SARS-coV inhibitors for inhibition of SARS-coV replication in BALB/c mice. *Antivir. Chem. Chemother.* **17**, 275–284 (2006).
44. Kumar, R. *et al.* S-adenosylmethionine-dependent methyltransferase inhibitor DZNep blocks transcription and translation of SARS-CoV-2 genome with a low tendency to select for drug-resistant viral variants. *Antiviral Res.* **197**, 105232 (2022).
45. Xiao, X. *et al.* EZH2 enhances the differentiation of fibroblasts into myofibroblasts in idiopathic pulmonary fibrosis. *Physiol Rep* **4**, (2016).
46. Chen, S. *et al.* Enhancer of Zeste Homolog 2 Is a Negative Regulator of Mitochondria-Mediated Innate Immune Responses. *The Journal of Immunology* **191**, 2614–2623 (2013).
47. Arbuckle, J. H. *et al.* Inhibitors of the Histone Methyltransferases EZH2/1 Induce a Potent Antiviral State and Suppress Infection by Diverse Viral Pathogens. *MBio* **8**, (2017).
48. Loong, K. T. EZH2 Mediates Resistance To Apoptosis In Nktl By Activating Nfkb Signaling Through Repression Of TNFAIP3/A20 By H3K27 Trimethylation. *Blood* **122**, 1278 (2013).
49. Wee, Z. N. *et al.* EZH2-Mediated Inactivation of IFN-γ-JAK-STAT1 Signaling Is an Effective Therapeutic Target in MYC-Driven Prostate Cancer. *Cell Rep.* **8**, 204–216 (2014).
50. Morel, K. L. *et al.* EZH2 inhibition activates a dsRNA–STING–interferon stress axis that potentiates response to PD-1 checkpoint blockade in prostate cancer. *Nature Cancer 2021 2:4* **2**, 444–456 (2021).
51. Leisman, D. E. *et al.* Cytokine elevation in severe and critical COVID-19: a rapid systematic review, meta-analysis, and comparison with other inflammatory syndromes. *The Lancet. Respiratory medicine* **8**, 1233–1244 (2020).
52. Miorin, L. *et al.* SARS-CoV-2 Orf6 hijacks Nup98 to block STAT nuclear import and antagonize interferon signaling. *Proc. Natl. Acad. Sci. U. S. A.* **117**, 28344–28354 (2020).
53. Peer, C. J. *et al.* A rapid ultra HPLC-MS/MS method for the quantitation and pharmacokinetic analysis of 3-deazaneplanocin A in mice. *J. Chromatogr. B Analyt. Technol. Biomed. Life Sci.* **927**, 142–146 (2013).
54. Sun, F., Li, J., Yu, Q. & Chan, E. Loading 3-deazaneplanocin A into pegylated unilamellar liposomes by forming transient phenylboronic acid-drug complex and its pharmacokinetic features in Sprague-Dawley rats. *Eur. J. Pharm. Biopharm.* **80**, 323–331 (2012).
55. Coulombe, R. A., Jr, Sharma, R. P. & Huggins, J. W. Pharmacokinetics of the antiviral agent 3-deazaneplanocin A. *Eur. J. Drug Metab. Pharmacokinet.* **20**, 197–202 (1995).
56. Gannon, O. M., Merida de Long, L., Endo-Munoz, L., Hazar-Rethinam, M. & Saunders, N. A. Dysregulation of the repressive H3K27 trimethylation mark in head and neck squamous cell carcinoma contributes to dysregulated squamous differentiation. *Clin. Cancer Res.* **19**, 428–441 (2013).
57. Lhuissier, E. *et al.* Evaluation of the impact of S-adenosylmethionine-dependent methyltransferase inhibitor, 3-deazaneplanocin A, on tissue injury and cognitive function in mice. *Oncotarget* **9**, 20698–20708 (2018).
58. Zissler, U. M. *et al.* Interleukin-4 and interferon-γ orchestrate an epithelial polarization in the airways. *Mucosal Immunol.* **9**, 917–926 (2016).
59. Welm, B. E., Dijkgraaf, G. J. P., Bledau, A. S., Welm, A. L. & Werb, Z. Lentiviral transduction of mammary stem cells for analysis of gene function during development and cancer. *Cell Stem Cell* **2**, 90–102 (2008).
60. Sanjana, N. E., Shalem, O. & Zhang, F. Improved vectors and genome-wide libraries for CRISPR screening. *Nat. Methods* **11**, 783 (2014).
61. Pfefferle, S. *et al.* Reverse genetic characterization of the natural genomic deletion in SARS-Coronavirus strain Frankfurt-1 open reading frame 7b reveals an attenuating

function of the 7b protein in-vitro and in-vivo. *Virol. J.* **6**, 131 (2009).

62. Thi Nhu Thao, T. *et al.* Rapid reconstruction of SARS-CoV-2 using a synthetic genomics platform. *Nature* **582**, 561–565 (2020).
63. Coronaviridae Study Group of the International Committee on Taxonomy of Viruses. The species Severe acute respiratory syndrome-related coronavirus: classifying 2019-nCoV and naming it SARS-CoV-2. *Nature microbiology* **5**, 536–544 (2020).
64. Mlcochova, P. *et al.* SARS-CoV-2 B.1.617.2 Delta variant replication and immune evasion. *Nature* **599**, 114–119 (2021).
65. Pa, K. *et al.* Structure-guided multivalent nanobodies block SARS-CoV-2 infection and suppress mutational escape. *Science* **371**, (2021).
66. Kümmerer, B. M. & Rice, C. M. Mutations in the yellow fever virus nonstructural protein NS2A selectively block production of infectious particles. *J. Virol.* **76**, 4773–4784 (2002).
67. Whelan, S. P., Ball, L. A., Barr, J. N. & Wertz, G. T. Efficient recovery of infectious vesicular stomatitis virus entirely from cDNA clones. *Proc. Natl. Acad. Sci. U. S. A.* **92**, 8388–8392 (1995).
68. Matsuyama, S. *et al.* The Inhaled Steroid Ciclesonide Blocks SARS-CoV-2 RNA Replication by Targeting the Viral Replication-Transcription Complex in Cultured Cells. *J. Virol.* **95**, (2020).
69. Corman, V. M. *et al.* Detection of a novel human coronavirus by real-time reverse-transcription polymerase chain reaction. *Euro Surveill.* **17**, (2012).
70. Tyanova, S. *et al.* The Perseus computational platform for comprehensive analysis of (prote)omics data. *Nature Methods 2016 13:9* **13**, 731–740 (2016).
71. Lee, J. D., Sun, D. L., Sun, Y. & Taylor, J. E. Exact post-selection inference, with application to the lasso. *Ann. Stat.* **44**, 907–927 (2013).
72. Durinck, S., Spellman, P. T., Birney, E. & Huber, W. Mapping identifiers for the integration of genomic datasets with the R/ Bioconductor package biomaRt. *Nat. Protoc.* **4**, 1184–1191 (2009).
73. Wu, G., Dawson, E., Duong, A., Haw, R. & Stein, L. ReactomeFIViz: a Cytoscape app for pathway and network-based data analysis. *F1000Res.* **3**, 146 (2014).
74. Li, H. Aligning sequence reads, clone sequences and assembly contigs with BWA-MEM. (2013).
75. Cingolani, P. *et al.* A program for annotating and predicting the effects of single nucleotide polymorphisms, SnpEff: SNPs in the genome of Drosophila melanogaster strain w1118; iso-2; iso-3. *Fly* **6**, 80–92 (2012).
76. Li, H. *et al.* The Sequence Alignment/Map format and SAMtools. *Bioinformatics* **25**, 2078–2079 (2009).
77. Grubaugh, N. D. *et al.* An amplicon-based sequencing framework for accurately measuring intrahost virus diversity using PrimalSeq and iVar. *Genome Biol.* **20**, (2019).
78. Katoh, K. & Standley, D. M. MAFFT multiple sequence alignment software version 7: improvements in performance and usability. *Mol. Biol. Evol.* **30**, 772–780 (2013).
79. Minh, B. Q. *et al.* IQ-TREE 2: New Models and Efficient Methods for Phylogenetic Inference in the Genomic Era. *Mol. Biol. Evol.* **37**, 1530–1534 (2020).
80. Chou, T. C. & Talalay, P. Quantitative analysis of dose-effect relationships: the combined effects of multiple drugs or enzyme inhibitors. *Adv. Enzyme Regul.* **22**, 27–55 (1984).
81. Hubel, P. *et al.* A protein-interaction network of interferon-stimulated genes extends the innate immune system landscape. *Nat. Immunol.* **20**, 493–502 (2019).
82. Scaturro, P. *et al.* An orthogonal proteomic survey uncovers novel Zika virus host factors. *Nature* **561**, 253–257 (2018).
83. Hoffmann, M. *et al.* SARS-CoV-2 Cell Entry Depends on ACE2 and TMPRSS2 and Is Blocked by a Clinically Proven Protease Inhibitor. *Cell* **181**, 271–280.e8 (2020).
84. Zhang, J.-Y. *et al.* Single-cell landscape of immunological responses in patients with COVID-19. *Nat. Immunol.* **21**, 1107–1118 (2020).
85. Ali, A. & Vijayan, R. Dynamics of the ACE2-SARS-CoV-2/SARS-CoV spike protein interface reveal unique mechanisms. *Sci. Rep.* **10**, 14214 (2020).
86. Goldeck, M., Schlee, M., Hartmann, G. & Hornung, V. Enzymatic synthesis and

purification of a defined RIG-I ligand. *Methods Mol. Biol.* **1169**, 15–25 (2014).
87. Kulak, N. A., Geyer, P. E. & Mann, M. Loss-less Nano-fractionator for High Sensitivity, High Coverage Proteomics. *Mol. Cell. Proteomics* **16**, 694–705 (2017).
88. Frediansyah, A., Tiwari, R., Sharun, K., Dhama, K. & Harapan, H. Antivirals for COVID-19: A critical review. *Clin Epidemiol Glob Health* **9**, 90–98 (2021).
89. Chitalia, V. C. & Munawar, A. H. A painful lesson from the COVID-19 pandemic: the need for broad-spectrum, host-directed antivirals. *Journal of Translational Medicine 2020 18:1* **18**, 1–6 (2020).
90. George, P. M., Wells, A. U. & Jenkins, R. G. Pulmonary fibrosis and COVID-19: the potential role for antifibrotic therapy. *The Lancet. Respiratory medicine* **8**, 807–815 (2020).
91. Feuillet, V., Canard, B. & Trautmann, A. Combining Antivirals and Immunomodulators to Fight COVID-19. *Trends in Immunology* vol. 42 31–44 Preprint at https://doi.org/10.1016/j.it.2020.11.003 (2021).

Article

SOURCE DATA
TRANSPARENT PROCESS
OPEN ACCESS

THE EMBO JOURNAL

Attenuation of SARS-CoV-2 replication and associated inflammation by concomitant targeting of viral and host cap 2'-O-ribose methyltransferases

Valter Bergant[1,], Shintaro Yamada[2,], Vincent Grass[1,], Yuta Tsukamoto[2,], Teresa Lavacca[1], Karsten Krey[1], Maria-Teresa Mühlhofer[1], Sabine Wittmann[3], Armin Ensser[3], Alexandra Herrmann[3], Anja vom Hemdt[4], Yuriko Tomita[5], Shutoku Matsuyama[5], Takatsugu Hirokawa[6 7 8], Yiqi Huang[1], Antonio Piras[1], Constanze A Jakwerth[9], Madlen Oelsner[9], Susanne Thieme[10], Alexander Graf[10], Stefan Krebs[10], Helmut Blum[10], Beate M Kümmerer[4,11], Alexey Stukalov[1], Carsten B Schmidt-Weber[9], Manabu Igarashi[12,13], Thomas Gramberg[3], Andreas Pichlmair[1,14,*] & Hiroki Kato[2,*]

Abstract

The SARS-CoV-2 infection cycle is a multistage process that relies on functional interactions between the host and the pathogen. Here, we repurposed antiviral drugs against both viral and host enzymes to pharmaceutically block methylation of the viral RNA 2'-O-ribose cap needed for viral immune escape. We find that the host cap 2'-O-ribose methyltransferase MTr1 can compensate for loss of viral NSP16 methyltransferase in facilitating virus replication. Concomitant inhibition of MTr1 and NSP16 efficiently suppresses SARS-CoV-2 replication. Using *in silico* target-based drug screening, we identify a bispecific MTr1/NSP16 inhibitor with anti-SARS-CoV-2 activity *in vitro* and *in vivo* but with unfavorable side effects. We further show antiviral activity of inhibitors that target independent stages of the host SAM cycle providing the methyltransferase co-substrate. In particular, the adenosylhomocysteinase (AHCY) inhibitor DZNep is antiviral in *in vitro*, in *ex vivo*, and in a mouse infection model and synergizes with existing COVID-19 treatments. Moreover, DZNep exhibits a strong immunomodulatory effect curbing infection-induced hyperinflammation and reduces lung fibrosis markers *ex vivo*. Thus, multispecific and metabolic MTase inhibitors constitute yet unexplored treatment options against COVID-19.

Keywords antivirals; COVID-19; host-directed; methyltransferase; SARS-CoV-2
Subject Categories Immunology; Microbiology, Virology & Host Pathogen Interaction
DOI 10.15252/embj.2022111608 | Received 8 May 2022 | Revised 23 June 2022 | Accepted 27 June 2022 | Published online 25 July 2022
The EMBO Journal (2022) 41: e111608

Introduction

S-adenosylmethionine (SAM)-dependent methyltransferases (MTases) facilitate the transfer of a methyl group to a variety of substrates.

---

1 Institute of Virology, School of Medicine, Technical University of Munich (TUM), Munich, Germany
2 Institute of Cardiovascular Immunology, Medical Faculty, University Hospital Bonn (UKB), Bonn, Germany
3 Institute of Clinical and Molecular Virology, Friedrich-Alexander University Erlangen-Nürnberg, Erlangen, Germany
4 Institute of Virology, Medical Faculty, University of Bonn, Bonn, Germany
5 Department of Virology III, National Institute of Infectious Diseases (NIID), Tokyo, Japan
6 Transborder Medical Research Center, University of Tsukuba, Tsukuba, Japan
7 Division of Biomedical Science, University of Tsukuba, Tsukuba, Japan
8 Cellular and Molecular Biotechnology Research Institute, National Institute of Advanced Industrial Science and Technology, Tokyo, Japan
9 Center for Allergy & Environment (ZAUM), Technical University of Munich (TUM) and Helmholtz Center Munich, German Research Center for Environmental Health, Member of the German Center for Lung Research (DZL), CPC-M, Munich, Germany
10 Laboratory for functional genome analysis (LAFUGA), Gene Centre, Ludwig Maximilian University of Munich (LMU), Munich, Germany
11 German Center for Infection Research (DZIF), Bonn-Cologne Partner Site, Bonn, Germany
12 International Collaboration Unit, International Institute for Zoonosis Control, Hokkaido University, Sapporo, Japan
13 Division of Global Epidemiology, International Institute for Zoonosis Control, Hokkaido University, Sapporo, Japan
14 German Center for Infection Research (DZIF), Munich partner site, Munich, Germany
*Corresponding author. Tel: +49 89 4140 9270; E-mail: andreas.pichlmair@tum.de
**Corresponding author. Tel: +49 228287 51425; E-mail: hkato@uni-bonn.de
[†] These authors contributed equally to this work as first authors
[‡] These authors contributed equally to this work as second authors

© 2022 The Authors. Published under the terms of the CC BY 4.0 license.

Notably, mature mRNA from both humans and SARS-CoV-2 carry two distinct methylation marks at the 5′ end. The cap N7 methylation facilitates mRNA association with cap-binding proteins, which are essential for mRNA transport and translation (Muthukrishnan *et al*, 1978; Gebhardt *et al*, 2019). In addition, cap 2’O-ribose methylation is required by the virus to evade cell-intrinsic immunity, specifically from being sensed by the cellular pattern recognition receptors RIG-I (Schuberth-Wagner *et al*, 2015) and MDA5 (Züst *et al*, 2011) and restricted by the interferon (IFN)-induced protein IFIT1 (Daffis *et al*, 2010; Habjan *et al*, 2013; Abbas *et al*, 2017). SARS-CoV-2 encodes two viral MTases, non-structural protein (NSP) 14, a cap N7 MTase with proofreading exoribonuclease (ExoN) activity (Chen *et al*, 2009*; Yan* et al, 2021), and NSP16, a cap 2’O-ribose MTase (Decroly *et al*, 2008; Rosas-Lemus *et al*, 2020). NSP14 and NSP16 were so far believed to be the sole MTases involved in their respective steps of viral RNA maturation. Therefore, both enzymes were considered pivotal for virus replication and recognized as potential targets for anti-SARS-CoV antiviral therapies (Decroly *et al*, 2008; Chen *et al*, 2009). In particular, the activity of NSP16 was shown to be required for IFN resistance and virulence of related SARS and MERS coronaviruses in an MDA5- and IFIT1-dependent manner (Menachery *et al*, 2014, 2017). Despite recent structural insights, specific targeting of viral MTases remains challenging (Chen *et al*, 2011; Rosas-Lemus *et al*, 2020; Ahmed-Belkacem *et al*, 2020; Vijayan *et al*, 2020; Aldahham *et al*, 2020).

In humans, more than 150 SAM-dependent MTases contribute to a plethora of biological processes. Of particular importance is their involvement in epigenetic gene regulation via histone H3K27 methylation, a repressive chromatin mark deposited by polycomb repressive complex 2 (PRC2), which has been linked to disease-relevant processes such as tissue fibrosis (Xiao *et al*, 2016) and innate immune responses (Chen *et al*, 2013; Arbuckle *et al*, 2017). Inhibition of the enhancer of zeste 2 PRC2 subunit (EZH2) was shown to reduce TGF-β1-induced human lung fibroblast-to-myofibroblast transformation and to attenuate bleomycin-induced pulmonary fibrosis in mice (Xiao *et al*, 2016). Moreover, it was also associated with reduction in NF-kB-dependent responses via upregulation of NF-kB inhibitors TNFAIP3/A20 and NFKBIA (Loong, 2013) and activation of the IFN response (Wee *et al*, 2014; Morel *et al*, 2021). Notably, NF-kB signaling is highly active in SARS-CoV-2-infected cells and in COVID-19 patients, thereby contributing to virus-induced immunopathology (Leisman *et al*, 2020). At the same time, SARS-CoV-2 is strongly inhibited by the antiviral functions invoked by type I IFN signaling but a number of viral proteins actively perturb this pathway at multiple levels (Miorin *et al*, 2020; Stukalov *et al*, 2021). Direct or indirect inhibition of MTase EZH2 could therefore lead to a reduction in lung fibrosis and relieve cytokine imbalance, both associated with negative disease outcomes, and thereby contribute to the resolution of acute and long-term effects of COVID-19.

One-carbon metabolism, and in particular the S-adenosylmethionine (SAM) cycle, is essential for maintaining the activity of SAM-dependent MTases. The SAM cycle produces the universal methyl group donor SAM and recycles the S-adenosylhomocysteine (SAH), which is a product inhibitor of SAM-dependent MTases (Hoffman *et al*, 1980). The SAM cycle can be subdivided into four enzymatic steps: the methionine biosynthesis, SAM biosynthesis, SAM-dependent methylation of substrates, and SAH hydrolysis. Of these steps, three rely on host metabolic enzymes and can be perturbed by host-targeting inhibitors, while SAM-dependent methylation is driven by distinct MTases, which are challenging to target specifically. The host metabolic enzymes involved in the SAM cycle are the methionine synthases (BHMT, BHMT2, and MTR together with the factor required for its regeneration MTRR), methionine adenosyltransferases (MAT1A, MAT2A, and associated regulator MAT2B), and adenosylhomocysteinase AHCY. Pharmaceutical targeting of the SAM cycle at different stages is a potential treatment option for a number of cancers (Uchiyama *et al*, 2017; Hasan *et al*, 2019; Ko*nteatis et al*, 2021) and was shown to be well tolerated in model organisms (Sun *et al*, 2015; Konteatis *et al*, 2021). Inhibitors of the SAM cycle enzymes negatively influence key cellular methylation capacity biomarkers, i.e., reduce the levels of SAM, increase the levels of SAH, and reduce the SAM-to-SAH ratio (Collinsova *et al*, 2006; Strakova *et al*, 2011; Aury-Landas *et al*, 2019), leading to broad-spectrum inhibition of SAM-dependent MTases through substrate starvation and product inhibition.

Drug repurposing is the most rapid antiviral drug development approach (Kaufmann *et al*, 2018; Garćа-Serradilla *et al*, 2019; Chitalia & Munawar, 2020). Host-directed antiviral drug repurposing is, in particular, attractive because it leverages a larger set of well-defined drugs used for treating non-infectious diseases and limits the risk to select for viral escape mutants. It allows for synergistic use of the state-of-the-art knowledge of both virus and host biology and has the potential for developing cross-functional and broad-spectrum antivirals. Targeting known disease-promoting factors, i.e., target-based host-directed drug repurposing, led to the discovery of the host protease inhibitor camostat (Kawase *et al*, 2012) and inosine-5′-monophosphate dehydrogenase (IMPDH) inhibitors ribavirin and VX-497 (Markland *et al*, 2000). Such approaches, often based on *in silico* screens, are of specific importance in tackling emerging and pandemic viruses and viral families for which extensive molecular characterization, otherwise serving as the basis for developing direct-acting antivirals, is incomplete or missing.

Herein, we leveraged both direct-acting and host-directed antiviral drug repurposing to explore the antiviral potential of pharmaceutical inhibition of SARS-CoV-2 cap 2’-O-ribose methyltransferase NSP16. Through *in silico* molecular docking, we identified a set of drug candidates with the potential to inhibit MTase activity of NSP16. While the inhibitor tubercidin (7-deazaadenosine) proved to be highly antiviral against SARS-CoV-2, other inhibitors with comparable or higher docking scores did not significantly affect the virus replication. In line with previous observations for SARS-CoV (Menachery *et al*, 2014), we show that genetically inflicted loss of function of NSP16 results in only moderate attenuation of SARS-CoV-2, indicating that stand-alone inhibition of NSP16 is insufficient to impair virus replication. Surprisingly, SARS-CoV-2 NSP16 mutant virus failed to replicate in cells that were depleted for the host cap 2’O-ribose MTase MTr1 (CMTR1, FTSJD2; Bélanger *et al*, 2010), suggesting that this host protein can compensate for the activity of its viral analog NSP16. Indicative of promiscuity, tubercidin potently inhibited both NSP16 and MTr1 *in vitro*, further emphasizing that a concomitant inhibition of NSP16 and MTr1 is pivotal for effective antiviral treatment. The activity of MTr1 and NSP16 critically depends on the metabolite homeostasis maintained by the host SAM cycle. We further explored the antiviral potential of host-directed SAM cycle inhibitors (SCIs), which in an indirect manner induce a

© 2022 The Authors

metabolic broad-spectrum MTase inhibition. We show that targeting all three independent enzymatic steps of the SAM cycle by unrelated small molecule inhibitors significantly reduces SARS-CoV-2 proliferation *in vitro*. Notably, the SAM cycle inhibitor 3-deazaneplanocin A (DZNep), an inhibitor of AHCY, has especially potent and selective antiviral efficacy against SARS-CoV-2 in *in vitro*, in *ex vivo*, and in a mouse infection model. In line with its known facilitative effect on tissue repair, DZNep treatment of primary human lung cells exhibited a strong immunomodulatory effect curbing infection-induced hyperinflammation and reduced lung fibrosis- and coagulopathy-related markers. Moreover, our data demonstrate that DZNep synergizes with the current treatment options remdesivir and interferon-alpha. These findings show that targeting the MTases involved in SARS-CoV-2 viral life cycle is a novel and therapeutically viable antiviral strategy for treatment of COVID-19.

Results

In silico screening identified NSP16 inhibitors with potent anti-SARS-CoV-2 activity

We employed a target-based drug repurposing approach aimed toward identification of potential novel NSP16 inhibitors. In particular, we utilized *in silico* screening of 4,991 unique DrugBank compounds for binding to the SAM-binding pocket of the SARS-CoV-2 NSP10/16 complex (PDB 6W4H; Fig 1A). As expected, SAM and SAH had the highest docking scores in our screen, followed by the SAM analog sinefungin (Krafcikova *et al*, 2020) and numerous other adenosine mimics (Dataset EV1). Based on the results of the *in silico* screen, we shortlisted 14 commercially available compounds (Fig 1B) and tested them for antiviral efficacy against SARS-CoV-2. Toward this, we pretreated human lung-derived cell line A549 complemented with the SARS-CoV-2 receptor angiotensin-converting enzyme 2 (A549-ACE2) with selected compounds at 1 μM concentration and infected them with SARS-CoV-2 at MOI 0.01. Twenty-four hours post-infection, RNA was isolated and the abundance of viral transcript encoding envelope protein (*E*) quantified by RT–qPCR. Surprisingly, most compounds did not exhibit antiviral activity with a notable exception of tubercidin, which was found to be highly potent under conditions used (Fig 1C). The *in silico* docking screen suggested that tubercidin binds to the SAM-binding pocket of NSP16 (Fig 1D), indicating that it may serve as a potential inhibitor of its cap 2’O-ribose MTase activity. We employed an *in vitro* MTase activity assay to experimentally test whether tubercidin influences the enzymatic activity of the NSP10/16 complex. Toward this, we used *in vitro*-transcribed cap0 RNA as the methyl group recipient and measured the MTase activity of recombinant NSP16/10 by quantifying the transferred tritium-labeled methyl groups from SAM[^{3}H]. While only mildly inhibiting unrelated Vaccinia virus MTase VP39, tubercidin significantly reduced the enzymatic activity of the MTase NSP10/16 (Fig 1E), indicating specificity in this assay.

To further explore the antiviral efficacy of tubercidin (Schultz *et al*, 2022), we pretreated A549-ACE2 cells with tubercidin at a range of concentrations 3 h prior to infection with SARS-CoV-2 and quantified SARS-CoV-2 nucleoprotein (N) accumulation by Western blot and immunostaining. In agreement with our previous findings, we observed a strong reduction of SARS-CoV-2 N accumulation in tubercidin-treated conditions as compared to control treatments (Figs 1F and EV1A). In an analogous experiment with SARS-CoV, we observe a similar trend, indicating that tubercidin is antiviral against both highly related coronaviruses (Fig EV1B and C). We further employed liquid chromatography coupled to tandem mass spectrometry (LC–MS/MS) analysis to evaluate abundance changes of viral proteins upon tubercidin or vehicle pretreatment of SARS-CoV or SARS-CoV-2-infected A549-ACE2 cells. We observed a prominent and highly significant tubercidin-dependent reduction in accumulation across all viral proteins (Fig 1G and Dataset EV2). We additionally observe a potent reduction in levels of viral RNA in SARS-CoV-2- or SARS-CoV-infected and tubercidin-treated A549-ACE2 cells as compared to vehicle-treated controls (Fig EV1D and E). Moreover, the production of infectious viral progeny (Figs 1H and EV1F) and viral RNA accumulation (Fig EV1G) was strongly reduced in the supernatants of tubercidin-treated SARS-CoV-2-, SARS-CoV-, or MERS-CoV-infected cells as compared to control treatments.

Next, we examined potential variability between antiviral efficacies of tubercidin against the different SARS-CoV-2 variants of concern. Toward this, we pretreated A549-ACE2 cells with 1 μM tubercidin and infected them with variants of concern alpha (B.1.1.7), beta (B.1.351), and delta (B.1.617.2) at MOI 0.01 for 24 h. For all viruses tested, we observed a comparable tubercidin-dependent reduction in viral RNA accumulation (Fig 1I). Taken together, employing target-based drug repurposing we identified tubercidin as a novel inhibitor of SARS-CoV-2 NSP16 with a potent antiviral efficacy against SARS-CoV-2 and other tested betacoronaviruses.

Concomitant inhibition of NSP16 and MTr1 is necessary for efficient suppression of SARS-CoV-2

NSP16 was previously proposed to be critical for SARS-CoV replication (Decroly *et al*, 2008) and was found to be required for IFN resistance and virulence of related SARS-CoV (Menachery *et al*, 2014) and MERS-CoV (Menachery *et al*, 2017). To assess the functional role of NSP16 in SARS-CoV-2 replication, we generated a mutant SARS-CoV-2 with the functionally deficient NSP16 harboring D130A K170A mutations (designated SARS-CoV-2 NSP16mut). These mutations abrogate NSP16 MTase activity (manuscript by T. Gramberg in preparation). To explore the effect of NSP16 deficiency, we monitored virus propagation levels in Calu-3 cell supernatants over a 6-day period. We observed only a minor loss in replication competency of SARS-CoV-2 NSP16mut compared with the wild-type (wt) SARS-CoV-2 (Fig 2A), indicating a prominent but not vital role of NSP16 in SARS-CoV-2 replication. An analogous observation was previously reported for SARS-CoV (Menachery *et al*, 2014). We hypothesized that the potent activity of tubercidin (Fig 1C and F–I) may be due to additional targeting of host factors that compensate for the loss of NSP16 activity. A potential host target of tubercidin is the cellular cap 2’O-ribose MTase MTr1, which is active on the host RNA. Notably, confocal imaging indicated nuclear and cytoplasmic localization of MTr1 in A549 cells, which is also in line with reports in public repositories (Williams *et al*, 2020). MTr1 expression is upregulated by IFN-α treatment (Williams *et al*, 2020; Fig EV1H). Nucleocytoplasmic fractionation of A549 cells further confirmed

© 2022 The Authors

cytoplasmic localization of MTr1 and increase in cytoplasmic MTr1 abundance upon IFN-β treatment (Fig EV1I). To evaluate whether tubercidin targets MTr1, we conducted molecular docking simulations, which indeed indicated that tubercidin can bind to the active site of MTr1 (Fig 2B). Moreover, tubercidin inhibited MTr1 function *in vitro* (manuscript in preparation by HK), potentially leading to concomitant inhibition of MTr1 and NSP16 in tubercidin-treated SARS-CoV-2-infected cells.

To assess the potential role of MTr1 in the SARS-CoV-2 life cycle, we tested to what extent MTr1-deficient A549-ACE2 cells (MTr1 KO) can support SARS-CoV-2 replication in comparison with controls. Toward this, we first characterized MTr1 KO cells in uninfected and infected conditions. Replication of a model virus (vesicular stomatitis virus, VSV) was not affected by the MTr1 KO (Fig 2C). In line with the literature (Williams *et al*, 2020), the basal and VSV-induced IFN-β mRNA levels were similar in mock- and virus-infected control and MTr1 knockout cells, respectively (Fig 2C). However, we unexpectedly observed a major impairment in SARS-CoV-2 protein and RNA accumulation in MTr1 KO cells as compared to non-targeting control cells (Figs 2D and EV1J). In addition, we could observe virus-induced cytopathic effects in control cells but not in MTr1 KO cells (Fig EV1K). Most notably, release of infectious SARS-CoV-2 NSP16mut was almost undetectable in MTr1 KO cells (Fig 2E). These data indicated that human MTr1 serves as a host

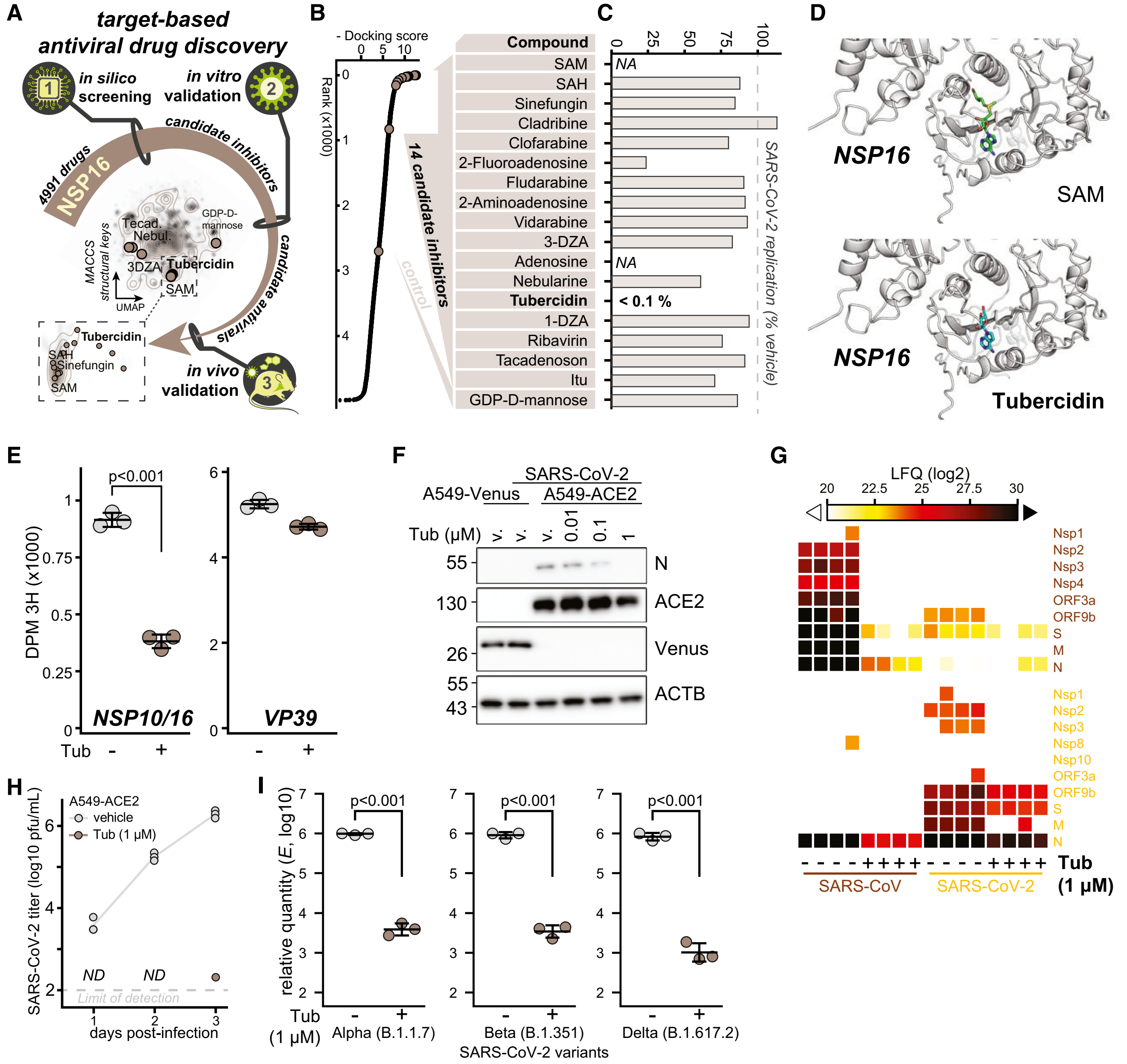

Figure 1.

Figure 1. ***In silico*** **screening identified NSP16 inhibitors with potent anti-SARS-CoV-2 activity.**

A Schematic representation of the target-based antiviral drug discovery pipeline employed herein. A total of 4,991 chemical compounds from DrugBank were docked to the SAM-binding pocket in the crystal structure of SARS-CoV-2 NSP16 (PDB ID: 6W4H), obtaining 14 commercially available compounds with high docking score that were used, along a control, in an *in vitro* antiviral assay. UMAP dimensionality reduction according to MACCS structural keys. Plots depict structural diversity of the shortlisted compounds alongside the compounds used in the *in silico* screen (contour lines), overlaid on the top of density distribution of ~800,000 bioactive small molecules (Duran-Frigola *et al*, 2020).

B Docking score from the *in silico* screen, depicted for all (black) and shortlisted (beige, table) compounds (full list provided in Dataset EV1).

C Results of *in vitro* antiviral assay for compounds according to (B). A549-ACE2 cells were pretreated with indicated compounds at 1 μM concentration for 3 h prior to infection with SARS-CoV-2 at MOI 0.01. Twenty-four hours post-infection, expression of SARS-CoV-2 transcript encoding envelope protein (*E*) was quantified by RT–qPCR as a measure of SARS-CoV-2 replication and is shown as a percent of vehicle-treated control. *NA*, not assayed.

D The docking poses of SAM (top) or tubercidin (bottom) in the SAM-binding pocket of SARS-CoV-2 NSP10/16 (PDB 6W4H).

E Disintegrations per minute (DPM 3H) originating from *in vitro*-transcribed cap0 RNA methylated by the NSP10/16 complex (left) or Vaccinia virus VP39 (right) with optional addition of 10 mM tubercidin. SAM[^{3}H] was provided as a substrate. Error bars correspond to mean ± SD of three reaction replicates; statistics were calculated using Student's two-sided *t*-test between indicated conditions.

F A549-ACE2 or control A549-Venus cells were pretreated with tubercidin or vehicle (DMSO) 3 h prior to infection with SARS-CoV-2 at MOI 0.1. After 24 h, the abundance of SARS-CoV-2 nucleoprotein (N), ACE2, Venus, and β-actin (ACTB, loading control) was visualized using Western blotting. The presented data are representative of three independent repeats.

G A549-ACE2 cells were pretreated with tubercidin or vehicle (DMSO) 3 h prior to infection with SARS-CoV (MOI 0.01) or SARS-CoV-2 (MOI 0.1). After 24 h, protein content of the cells was isolated and subjected to LC–MS/MS-based proteomics analysis. Label-free quantification (LFQ)-based abundance of detected viral proteins is depicted.

H A549-ACE2 cells were pretreated with tubercidin or vehicle (DMSO) 3 h prior to infection with SARS-CoV-2 at MOI 0.01. At 1 h post-infection, medium change was performed. At the indicated days post-infection, infectious viral progeny was quantified in the supernatants from three independently infected wells by plaque assay on Vero cells. *ND*, not detected. The measurements are representative of two independent repeats.

I A549-ACE2 cells were pretreated with tubercidin or vehicle (DMSO) 3 h prior to infection with indicated strains of SARS-CoV-2 at MOI 0.01. At 24 h post-infection, relative expression of SARS-CoV-2 *E* was quantified by RT–qPCR. Error bars correspond to mean ± SD of $n = 3$ independently infected wells, and the measurements are representative of two independent repeats; statistics were calculated using Student's two-sided *t*-test between indicated conditions.

Source data are available online for this figure.

factor in the absence of a functional viral 2'O methyltransferase. To test whether this was specific to SARS-CoV-2 or whether this phenotype can also be observed for other viruses that lack their 2'O methyltransferase activity, we infected wt and MTr1 knockout cells with wt yellow fever virus (YFV) and YFV with a mutation in its 2'O-ribose MTase (YFV-E218A; Zhou *et al*, 2007). Notably, both wt and mutant YFV grew to similar titers in wt and MTr1-deficient cells, indicating that YFV does not rely on cellular MTr1 (Fig 2F). We concluded that MTr1 is a SARS-CoV-2-specific host factor with a redundant or cooperative function to NSP16. These genetic observations further indicated that a concomitant pharmaceutical inhibition of viral NSP16 and host MTr1 is critical for the efficient suppression of SARS-CoV-2.

In order to assess whether tubercidin is antiviral against SARS-CoV-2 *in vivo*, we infected C57BL/6 mice with SARS-CoV-2 beta variant (B.1.351, 250 pfu intranasal) and treated the animals at the day (day 0) and 1 day after infection (day 1) with tubercidin (25 μg, intranasal application; Fig 2G). At day 2 post-infection, which represented the early acute stage of infection, the animals were sacrificed and lungs were harvested to quantify the viral load. We observed a significant reduction of the viral RNA level in the lungs of tubercidin-treated animals relative to the control (Fig 2H). However, we also observed significant weight loss of treated mice (Fig 2I), suggesting *in vivo* toxicity of this compound that may be prohibitive for its clinical application. Taken together, we identified MTr1 as a novel SARS-CoV-2 host factor with a redundant or cooperative activity to the viral MTase NSP16. We further showed that concomitant targeting of both NSP16 and MTr1 is critical for efficient repression of SARS-CoV-2 replication. While dual targeting of NSP16 and MTr1 may be a central property explaining the antiviral efficacy of tubercidin observed *in vitro* and *in vivo*, alternative targeting strategies are required to circumvent its toxicity.

SAM cycle enzymes are key host factors facilitating SARS-CoV-2 proliferation

We explored alternative strategies of concomitant inhibition of NSP16 and MTr1 that may be applicable for clinical settings. The activity of both NSP16 and MTr1 is influenced by the levels of their substrate S-adenosylmethionine (SAM) and product inhibitor S-adenosylhomocysteine (SAH). Homeostasis of both SAM and SAH is solely driven by the enzymes of the host SAM cycle (Fig 3A). Inhibition of the SAM cycle enzymes causes a metabolic broad-spectrum MTase inhibition through substrate starvation and product inhibition (Hoffman *et al*, 1980). This may exert an antiviral effect against SARS-CoV-2 mechanistically similar to tubercidin (Fig 3B). To explore the role of the SAM cycle enzymes in SARS-CoV-2 infection, we used CRISPR/Cas9 to genetically ablate MAT2A, the main methionine adenosyltransferase of extrahepatic tissues, and AHCY, the sole human adenosylhomocysteinase, in A549-ACE2 cells. We employed time-resolved live-cell fluorescent imaging to evaluate cell growth and proliferation of GFP-expressing SARS-CoV-2 reporter virus (SARS-CoV-2-GFP; Thi Nhu Thao *et al*, 2020; Stukalov *et al*, 2021). Cells lacking MAT2A or AHCY exhibited minor reduction in cell growth relative to non-targeting control cells (NTC; Fig EV2A and B). Notably, compared with NTC, targeting MAT2A and AHCY significantly restricted SARS-CoV-2 replication (Fig 3C).

We evaluated anti-SARS-CoV-2 efficacy of the inhibitor of methionine synthases BHMT/BHMT2 (CBHcy; Jiracek *et al*, 2006), inhibitors of methionine adenosyltransferases MAT1A/MAT2A/MAT2B (MI1 (Konteatis *et al*, 2018), FIDAS-5 (Zhang *et al*, 2013; Sviripa *et al*, 2014), and PF-9366 (Quinlan *et al*, 2017)), and inhibitors of adenosylhomocysteinase AHCY (DZNep (Glazer *et al*, 1986) and DER (Schanche *et al*, 1984)), collectively termed SAM cycle inhibitors (SCIs; Fig 3A). Notably, the inhibition of all SAM cycle

© 2022 The Authors

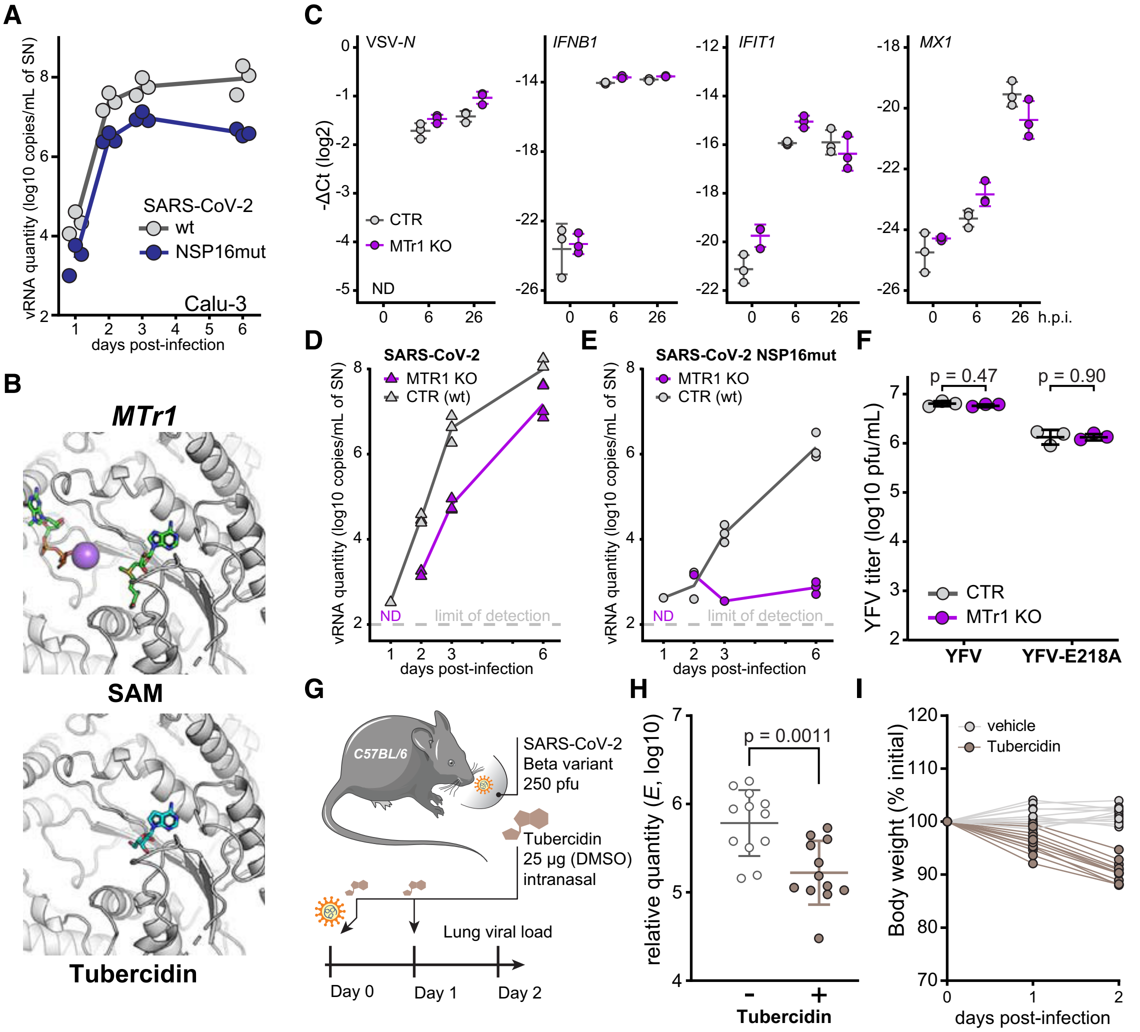

Figure 2. Concomitant inhibition of NSP16 and MTr1 is necessary for efficient suppression of SARS-CoV-2.

A Calu-3 cells were infected with SARS-CoV-2 or SARS-CoV-2 NSP16mut at 5,000 RNA copies/well. At indicated times post-infection, RNA from the supernatants from $n = 3$ independently infected wells was isolated and RT–qPCR used to quantify the presence of viral RdRp encoding RNA.

B The docking poses of SAM (top) or tubercidin (bottom) in the SAM-binding pocket of human MTr1 (PDB 4N49).

C CTR or MTr1 KO A549-ACE2 cells were infected with VSV-GFP at MOI 1 or mock (0 h post-infection, h.p.i.). At indicated times post-infection, depicted transcript abundance was quantified by RT–qPCR (relative to 18S rRNA). Error bars correspond to mean ± SD of $n = 3$ independently infected wells.

D, E Control (CTR) or MTr1 knockout (KO) A549-ACE2 cells were infected with SARS-CoV-2 (D) or SARS-CoV-2 NSP16mut (E) at 5,000 RNA copies/well. At indicated times post-infection, RNA from the supernatants from $n = 3$ independently infected wells was isolated and RT–qPCR used to quantify the presence of viral RNA targeting RdRp coding region. Dotted line—not detected.

F CTR or MTr1 KO A549-ACE2 cells were infected with YFV or YFV-E218A at MOI 0.1. At 2 days post-infection, infectious viral progeny was quantified in the supernatants by plaque assay on Vero cells. Error bars correspond to mean ± SD of $n = 3$ independently infected wells.

G Schematic representation of the *in vivo* antiviral assay employing a murine infection model.

H, I C57BL/6 mice were infected with SARS-CoV-2 beta variant (250 pfu, intranasal) and treated at D0 and D1 with tubercidin (25 µg, intranasal). Forty-eight hours post-infection, lungs of infected mice were isolated. The presented data were pooled from two independent experiments. (H) Abundance of SARS-CoV-2 transcript *E* was quantified in the lung samples by RT–qPCR as a measure of lung viral load. Mean ± SD of $n = 12$ animals per condition is shown; statistics were calculated using Student's two-sided *t*-test as indicated. (I) Animal body weight, depicted as percentage of initial weight, measured at indicated times post-infection.

enzymes exhibited a significant antiviral effect against SARS-CoV-2 (Figs 3D and EV2C–G). While most inhibitors showed significant antiviral effects at μM concentrations, DZNep, an AHCY inhibitor, was most potent and led to a significant reduction in SARS-CoV-2 growth in the nM range (Fig 3D and E). In contrast to tubercidin (Figs 3F and G, and EV2H), treatment with SCIs had minor-to-no impact on cell proliferation for most compounds (Figs 3E and EV2C–G), indicating that the observed antiviral effect for those compounds was not due to altered cellular viability or growth rates. To corroborate these findings, we evaluated the antiviral efficacy of DZNep, FIDAS-5 and CBHcy in Vero E6 cells. Toward this, we pretreated Vero E6 cells with SCIs at different concentrations, infected them with wild-type (wt) SARS-CoV-2, and after 48 h quantified the amount of released viral progeny in the supernatant by plaque

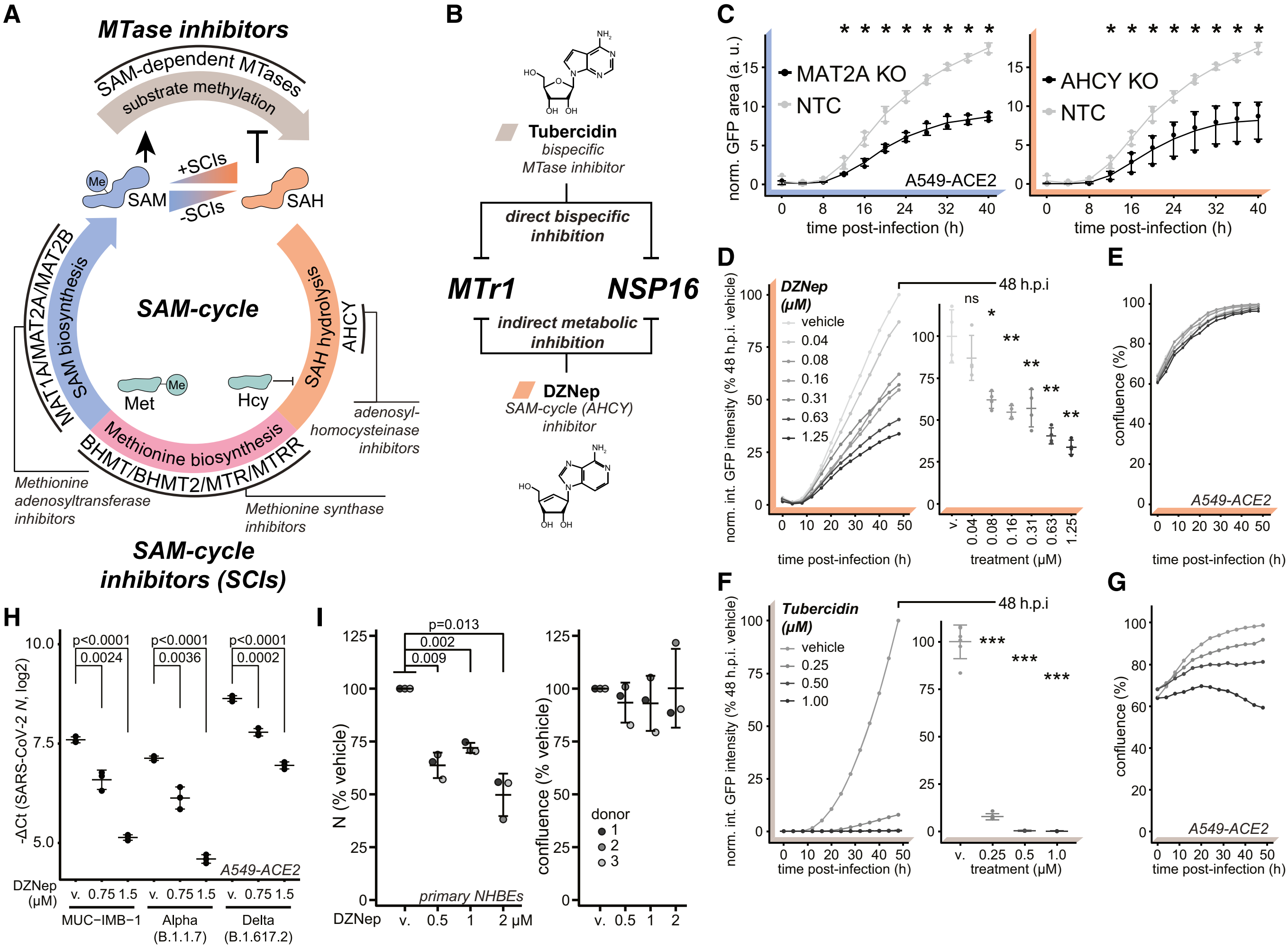

Figure 3. SAM cycle enzymes are key host factors facilitating SARS-CoV-2 proliferation.

A Schematic representation of the SAM cycle, metabolites, enzymatic components, and inhibitors thereof.

B Schematic representation of the two orthogonal mechanisms allowing for concomitant inhibition of MTases NSP16 and MTr1.

C AHCY KO, MAT2A KO, or non-targeting control (NTC) A549-ACE2 cells were infected with SARS-CoV-2-GFP at MOI 3 and normalized GFP area plotted over time as a measure of reporter virus growth. Error bars correspond to mean ± SD of $n = 3$ independently infected wells. Statistics were calculated using Student's two-sided *t*-test between individual KOs and NTC at indicated times post-infection. ns $P > 0.05$, * $P < 0.05$.

D–G The effect of the SAM cycle inhibitor DZNep and bispecific MTase inhibitor tubercidin on cell and virus growth. A549-ACE2 cells were pretreated for 6 h with indicated concentrations of (D, E) DZNep or (F, G) tubercidin and infected with SARS-CoV-2-GFP at MOI 3. Normalized integrated GFP intensity and confluence are depicted as a measure of virus replication and cell growth, respectively. Error bars correspond to mean ± SD of (D, E) $n = 4$ and (F, G) $n = 6$ independently infected wells; the measurements are representative of three independent repeats. Statistics were calculated using Student's two-sided *t*-test between indicated treatment concentrations and respective vehicle controls (v., DZNep—PBS; tubercidin—DMSO). ns $P > 0.05$, * $P < 0.05$, ** $P < 0.01$, *** $P < 0.001$.

H A549-ACE2 cells were pretreated for 6 h with indicated concentrations of DZNep or vehicle (v., PBS) and infected with indicated variants of SARS-CoV-2 at MOI 3 for 24 h. Graph shows *N* mRNA expression normalized to housekeeping gene (*RPLP0*); error bars represent mean ± SD of $n = 3$ independently infected wells. *P*-values were calculated using Student's two-sided *t*-test as indicated.

I NHBEs derived from three independent donors were pretreated for 6 h with indicated concentrations of DZNep or vehicle and infected with SARS-CoV-2 for 24 h. Cells were fixed, and the abundance of SARS-CoV-2 N was quantified by immunofluorescent staining. Shown are vehicle-normalized integrated anti-N fluorescent intensity and cell confluence; error bars represent mean ± SD of $n = 3$ donors. Statistics were calculated using one sample Student's two-sided *t*-test.

Source data are available online for this figure.

assay. In line with the reporter virus assays, we observed dose-dependent suppression of the wt SARS-CoV-2 for the tested SCIs (Fig EV3A–C). Interestingly, while DZNep, an inhibitor of AHCY, proved the most efficacious in the reporter virus assay, CBHcy, an inhibitor of BHMT/BHMT2, exhibited the highest antiviral effect in this setting (Fig EV3C).

DZNep was previously shown to have antiviral activity against some viruses but not against others (Tseng *et al*, 1989; Chen *et al*, 2013; Arbuckle *et al*, 2017). We first explored the antiviral effect of DZNep against the early clinical isolate SARS-CoV-2-MUC-IMB-1, the alpha (B.1.1.7) and the delta (B.1.617.2) SARS-CoV-2 variants. The reduction of SARS-CoV-2 *N* mRNA levels as a proxy for antiviral efficacy of DZNep against the tested variants was comparable (Fig 3H), indicating that they are similarly susceptible to AHCY inhibition. DZNep was shown to be ineffective in reducing SARS-CoV lung titer in a murine infection model (Barnard *et al*, 2006). We employed a Western blot-based readout to compare antiviral efficacy against SARS-CoV-2 and SARS-CoV. In agreement with our previous findings, we observed a reduction in SARS-CoV-2 N accumulation in DZNep-treated conditions (Fig EV3D). However, in contrast to tubercidin but in line with the literature (Barnard *et al*, 2006), we observed no clear effect of DZNep on SARS-CoV N accumulation under the tested conditions (Fig EV3E).

In order to explore whether DZNep treatment impairs virus replication or an earlier process such as virus entry, we compared SARS-CoV-2-GFP reporter virus growth curves upon treatment of A549-ACE2 cells with DZNep, IFN-α, or neutralizing antisera (Lainšček *et al*, 2021). While antisera, which reduces virus infection rates, delayed onset of virus replication by 3–4 h, it did not affect the overall increase in GFP signal over time (Fig EV3F, left). In contrast, IFN-α treatment restricts virus replication at multiple levels downstream of viral entry, which is characterized by reduced maximal virus proliferation rate and a tilted slope in GFP signal (Fig EV3F, middle). Notably, SARS-CoV-2 reporter virus growth rates in DZNep-treated cells did not delay onset of virus replication but were comparable to growth rates obtained in IFN-α-treated cells (Figs 3D and EV3F, right). To further corroborate these findings, we treated A549-ACE2 cells with DZNep 4 h prior, at the time of, and 4 h post-infection. We detected no major differences in its antiviral efficacy (Fig EV3G), indicating that inhibition of viral entry is not the main driver of antiviral efficacy of DZNep but that a post-entry process is affected by DZNep.

DZNep was shown to be highly efficacious against Ebolavirus infection *in vivo* (Bray *et al*, 2000, 2002), in the context of which it strongly stimulated type I IFNs (Bray *et al*, 2002). To explore the contribution of the IFN response to antiviral efficacy of DZNep against SARS-CoV-2, we used a STAT1-deficient A549-ACE2 cell line and compared its response with that of DZNep relative to the NTC with optional IFN-α co-treatment (Fig EV3H). As expected, treatment of NTC cells with IFN-α significantly attenuates virus growth (Mantlo *et al*, 2020), as did treatment of NTC cells with DZNep. Interestingly, co-treatment with DZNep and IFN-α led to further reduction in virus propagation, suggesting that IFN-α may potentiate antiviral efficacy of DZNep. In line with our observations from IFN-deficient Vero E6 cells, IFN-α was no longer active in STAT1-deficient cells, while DZNep retained its antiviral activity (Fig EV3H).

DZNep was previously shown to invoke depletion of H3K27 trimethylation in cancer cells (Tan *et al*, 2007; Miranda *et al*, 2009), suggesting inhibitory activity on the MTase EZH2, the enzymatic component of the PRC2 complex. It is possible that SCIs, due to their related mode of action, in general confer EZH2 inhibition and subsequently deplete H3K27 trimethylation levels. We used tazemetostat (Knutson *et al*, 2014), a potent and selective competitive inhibitor of EZH2 approved for treatment of epithelioid sarcoma, to explore the antiviral potential of stand-alone EZH2 inhibition against SARS-CoV-2. We observed a moderate tazemetostat-dependent decrease in virus proliferation (Fig EV3I), suggesting that EZH2 inhibition may partially contribute to the antiviral efficacy of DZNep against SARS-CoV-2.

In order to corroborate our *in vitro* findings, we employed primary normal human bronchial epithelial cells (NHBEs) as a highly relevant lung-derived *ex vivo* infection model. Toward this, we pretreated NHBEs with various concentrations of DZNep, infected them with SARS-CoV-2 at MOI 3 for 24 h and quantified viral N accumulation by immunofluorescence analysis. In line with observations in cell lines, DZNep treatment mediated a significant decrease in abundance of N in human primary cells (Fig 3I). Collectively, this shows that the SAM cycle enzymes are key host factors for SARS-CoV-2 replication that can be pharmaceutically targeted to exert an antiviral effect.

DZNep treatment modulates tissue and immune processes

In order to explore the effect of DZNep as antiviral SCI on host and viral protein expression, we employed LC–MS/MS analysis. In particular, we evaluated protein abundance changes upon DZNep or vehicle pretreatment of mock-, SARS-CoV- or SARS-CoV-2-infected A549-ACE2 cells and NHBEs (Fig 4A, and Datasets EV3 and EV4). We quantified abundance of 5,957 and 6,129 proteins in A549-ACE2s and NHBEs, respectively, and evaluated the effect of SARS-CoV and SARS-CoV-2 infection, as well as drug treatment using the LASSO statistical model (Figs 4A and EV4A). In both A549-ACE2 and NHBEs, SARS-CoV-2 and SARS-CoV infections, as well as treatment in distinct conditions, elicited comparable proteome changes (Figs 4B and EV4B–E). Consistent with our previous findings, we show DZNep-dependent inhibition of SARS-CoV-2 but not of SARS-CoV, as determined by abundance changes of N and spike (S) proteins (Fig 4C). In NHBEs, we observed infection-dependent upregulation of proteins associated with innate immunity, which was further amplified by DZNep treatment and which may contribute to the antiviral activity of DZNep (Fig EV4E). Interestingly, we also observed DZNep-dependent upregulation of numerous SAM-dependent MTases, in A549-ACE2 cells (e.g., NSUN2, NOP2, METTL3, CMTR2, NTMT1, and FTSJ1; Fig EV4D) and in NHBEs (NSUN2, NOP2, and CMTR2; Fig EV4E). This expression pattern may reflect host regulatory processes to compensate for the loss in activity of MTases, broadly inhibited by the activity of DZNep.

In order to explore the cellular functions perturbed by DZNep in NHBEs, we analyzed pathways associated with proteins, significantly regulated by DZNep in SARS-CoV-2- and SARS-CoV-infected conditions. We applied a network diffusion approach, which allows to highlight clusters of functionally related host proteins and pathways, which may be implicated in DZNep-induced perturbations (Wu *et al*, 2014). Among the significantly enriched subnetworks was a cluster of genes functionally interacting with STAT3 and NF-KB1 (Fig EV4F and G). In particular, this cluster can be subdivided into two distinct parts containing proteins related to biological processes governing fibrosis and blood coagulation, and inflammation (Fig EV4F). In line with these findings, we observed that DZNep treatment led to a reduction in pulmonary fibrosis biomarkers (e.g., COL4A1, MMP14, and SERPINE1) and upregulation of factors counteracting fibrotic processes (e.g., ELAFIN, SLPI, and ECM1; Fig 4D). Furthermore, it led to reduction in factors of the extrinsic coagulation cascade (e.g., F3 and TFPI2) and plasminogen activation system (e.g., PAI1, PLAT, PLAU), which were upregulated by SARS-CoV-2 (O'Sullivan *et al*, 2020; Jha *et al*, 2021; FitzGerald *et al*, 2021; Fig 4D). We also observed DZNep-dependent changes in

© 2022 The Authors

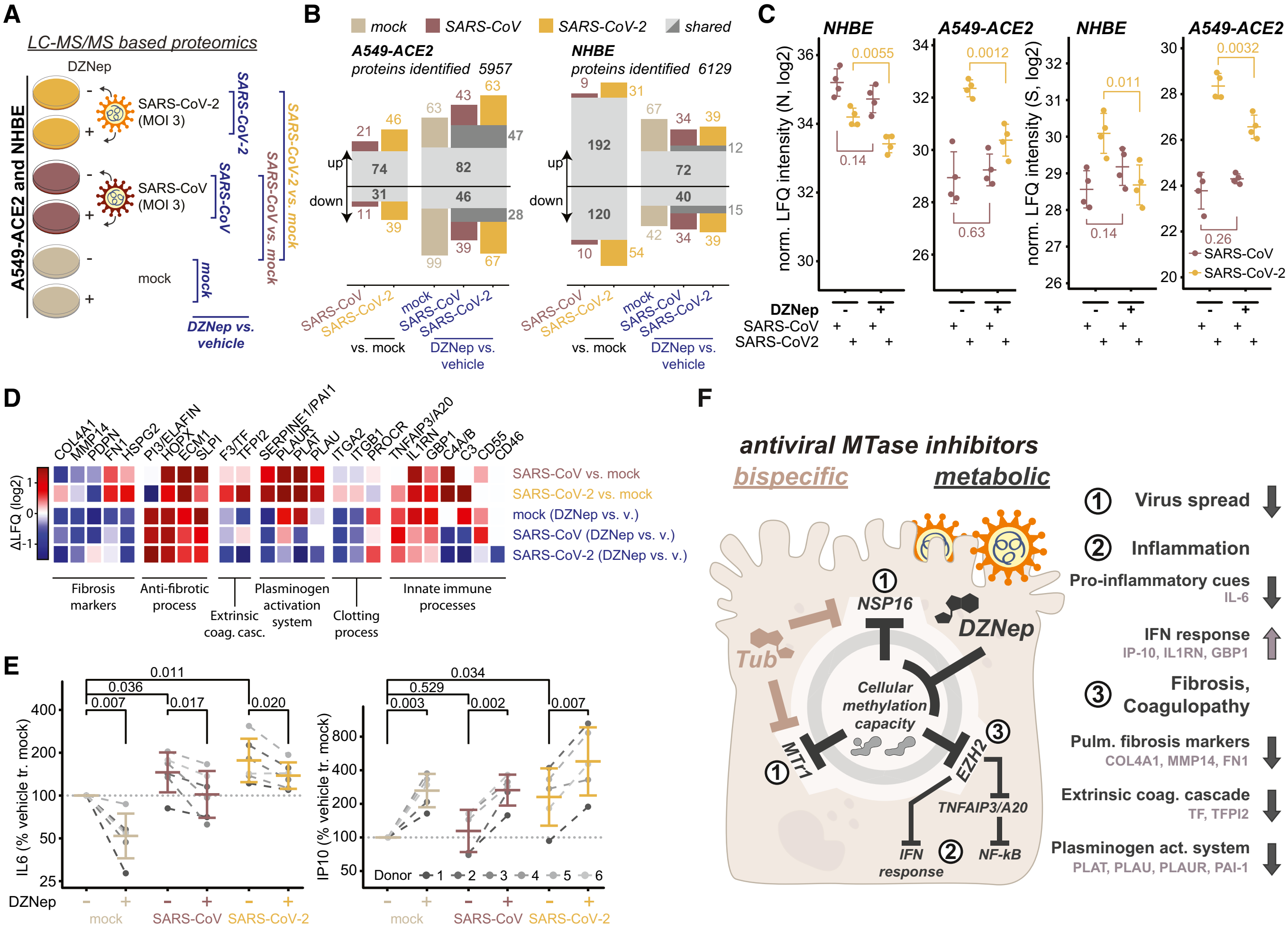

Figure 4. DZNep treatment modulates tissue and immune processes.

A–D Mass spectrometry-based analysis of cells treated with DZNep and infected with SARS-CoV-2 and SARS-CoV. (A) Schematic representation of LC–MS/MS experiments. A549-ACE2s and NHBEs were pretreated for 6 h with 0.75 and 1.5 μM DZNep, respectively, or vehicle (PBS), and infected with SARS-CoV-2 or SARS-CoV at MOI 3 for 24 h (A549-ACE2) or 36 h (NHBEs). Changes in protein abundance were analyzed according to the depicted scheme using LASSO-based linear model followed by fixed LASSO inference-based p-value estimation as described in the Materials and Methods section. (B) Number of significantly up- or downregulated proteins in indicated comparisons according to (A). (C) Donor-normalized LFQ abundance of viral nucleoprotein (N) and spike (S) in the indicated conditions. Error bars represent mean ± SD of $n = 4$ donors (NHBE) or $n = 4$ independently infected A549-ACE2 cultures. Statistics were calculated using Student's two-sided t-test as indicated. (D) Expression patterns according to (A) of a selection of genes related to the disease-relevant pathways as annotated.

E NHBEs (six independent donors) were pretreated for 6 h with 0.75 μM DZNep or vehicle and infected with SARS-CoV or SARS-CoV-2 at MOI 3. Twenty-four hours later, accumulation of IL-6 and IP-10 was measured in the supernatant by ELISA. Donor-wise IL-6 and IP-10 secretion, normalized to vehicle-treated uninfected controls (as further described in Materials and Methods), is shown.

F Schematic representation of the proposed disease-relevant functions of DZNep in the context of COVID-19 alongside the model of their molecular origin.

abundance of innate immunity-related factors (e.g., IL-1RN, C3, and TNFAIP3/A20; Fig 4D). In particular, TNFAIP3/A20 was previously shown to be upregulated by DZNep, leading to taming of NF-kB signaling (Loong, 2013).

These findings prompted us to explore the impact of DZNep treatment on cell-intrinsic immunity *ex vivo*. Of particular relevance for infection-associated pathology are the overshooting pro-inflammatory cytokine secretion (i.e., cytokine storm; Blanco-Melo *et al*, 2020; Leisman *et al*, 2020) and blunted type I interferon signaling (Acharya *et al*, 2020; Hadjadj *et al*, 2020), which is inhibited by SARS-CoV-2 through multiple mechanisms (Miorin *et al*, 2020; Stukalov *et al*, 2021). Toward this, we quantified secretion of the IRF3-dependent cytokine IP-10 and the NF-kB-dependent cytokine IL-6 by ELISA. As expected and reported previously (Leisman *et al*, 2020; Blanco-Melo *et al*, 2020), we observed a SARS-CoV and SARS-CoV-2 infection-dependent increase in IL-6 secretion in NHBEs (Fig 4E). Interestingly, DZNep treatment significantly reduced IL-6 secretion in all tested conditions (Fig 4E), which may be explained by its upregulation of TNFAIP3/A20 (Loong, 2013; Yang *et al*, 2020). In contrast to IL-6 and in line with MS-based observations concerning interferon-induced proteins (e.g., upregulation of IL-1RN and GBP1), IP-10 secretion was enhanced after DZNep treatment (Fig 4E). Collectively, these analyses indicate that DZNep treatment of SARS-CoV-2-infected primary human NHBEs not only inhibits virus proliferation but also elicits favorable immunomodulatory and antifibrotic effects (Fig 4F). Notably, the combination of multiple beneficial activities could provide the required synergy for effective treatment of COVID-19 and its symptoms.

SCIs treatment does not select for escape mutants in viral methyltransferases

Plasticity of SARS-CoV-2 genome was previously demonstrated *in vitro* upon treatment with remdesivir (Szemiel *et al*, 2021). SCIs include inhibitors of both SAM biosynthesis and SAH hydrolysis—while both perturb biomarkers of cellular methylation capacity, the former act by limiting SAM (Zhang *et al*, 2013) and the latter act by increasing SAH amounts (Aury-Landas *et al*, 2019). The two types of SAM cycle inhibition could thereby exert distinct selection pressures on the virus and in particular on viral MTases. In order to study how the virus may adapt to the SCI-induced metabolic reprogramming, we propagated SARS-CoV-2 in the presence of either DMSO (control), FIDAS-5 (2.5 μM), or DZNep (1.25 μM) for 10 passages (Figs 5A and EV5A). We observed a consistent reduction in SARS-CoV-2 titer upon treatment with DZNep and FIDAS-5 at early passages (Fig EV5A). To monitor the potential gradual adaptation of the virus to DZNep and pinpoint potentially affected viral proteins, we sequenced virus isolates at every passage. This analysis revealed acquisition of mutations that are associated with adaptation to cell culture conditions (e.g., Spike R685H; Sasaki *et al*, 2021) and an overall comparable number of mutations in all conditions, suggesting that the SCIs do not affect overall viral mutation rates (Fig EV5B–D and Dataset EV5). While we identified substitutions that correlated with increased virus titer upon cultivation (Fig EV5E), we did not observe mutations in the viral proteins associated with methylation processes (i.e., NSP10, NSP14, and NSP16). To directly compare the fitness of individual virus isolates, we performed virus competition experiments in the presence of SCIs using parental (P0) and passage 10 (P10) isolates (Fig 5A). DMSO-adapted control viruses and viruses propagated in the presence of DZNep (Fig 5B) or FIDAS-5 (Fig EV5F) grew similarly under most tested conditions, suggesting no adaptation of viruses propagated in the presence of SCIs (Fig EV5G and Dataset EV6). In contrast, the growth of DMSO-adapted control virus outcompeted growth of the P0 isolate (Figs 5B and EV5F), which likely reflects the adaptation of SARS-CoV-2 to *in vitro* cultivation. The lack of adaptive mutations in viral MTases and the lack of increased fitness upon propagation of SARS-CoV-2 in the presence of SCIs underline the challenge for SARS-CoV-2 to adapt to SCI treatments. These findings further support the suitability of host-directed SCIs to impair virus growth for therapeutic purposes.

Synergistic potential of DZNep and its antiviral activity in a murine infection model

We next evaluated antiviral efficacy of DZNep in co-treatment with currently known COVID-19 drug candidates. In particular, we used dexamethasone (Carvalho *et al*, 2021; immunomodulatory corticosteroid), chloroquine (Carvalho *et al*, 2021; inhibitor of autophagy), ipatasertib (Stukalov *et al*, 2021; AKT kinase inhibitor), marimastat and prinomastat (Stukalov *et al*, 2021; hydroxamic acid-based broad-spectrum matrix metalloprotease inhibitors), remdesivir (Carvalho *et al*, 2021; an antiviral nucleoside analog), and IFN-α. Toward this, we pretreated A549-ACE2 cells with DZNep and known antiviral compounds and monitored growth of the SARS-CoV-2-GFP. Under the tested conditions, DZNep did not impair, and was not impaired by, any of the tested drugs (Appendix Fig S1A–D). Cap 2'O-ribose methylation is often required by the viruses, including coronaviruses (Menachery *et al*, 2014, 2017), to evade cell-intrinsic immunity, specifically from being sensed by the cellular pattern recognition receptors RIG-I (Schuberth-Wagner *et al*, 2015) and MDA5 (Züst *et al*, 2011) and restricted by the IFN-induced protein IFIT1 (Daffis *et al*, 2010; Habjan *et al*, 2013; Abbas *et al*, 2017). Insufficiency in cap 2'O-ribose methylation of viral or host RNA could thereby promote and potentiate cell-intrinsic antiviral mechanisms to further restrict virus replication. In line with this hypothesis, we demonstrate synergistic potential between antiviral activities of DZNep and IFN-α *in vitro* (Figs 5C and EV5H). In coronavirus infections, SAM facilitates the association of viral MTase NSP16 with its allosteric activator NSP10 (Aouadi *et al*, 2017). Interestingly, besides with NSP16, NSP10 also interacts with NSP14 through an overlapping interface to greatly stimulate its ExoN (Bouvet *et al*, 2014; Ma *et al*, 2015) but not MTase activity (Bouvet *et al*, 2010, 2012). It is possible that the interaction between NSP14 and NSP10 is in a similar manner facilitated by SAM binding. SCIs could, in this respect, affect the resistance of SARS-CoV-2 to incorporable nucleoside analogs such as Remdesivir, activity of which is reduced by 4.5-fold through ExoN activity of NSP14 (Shannon *et al*, 2020). Notably, we demonstrate synergistic functions between DZNep and remdesivir *in vitro* (Figs 5D and EV5I). While the molecular mechanism behind these observations is yet to be explored, they suggest that modulating SAM cycle metabolite levels by SCIs may influence the ExoN activity of NSP14 of SARS-CoV-2.

DZNep was studied as an antitumor drug, and in rodents, it exhibits favorable pharmacokinetics for treating acute pulmonary infections (Bray *et al*, 2000; Peer *et al*, 2013; Sun *et al*, 2015). It has also been shown to support tissue regeneration (Xiao *et al*, 2016; Zeybel *et al*, 2017; Mimura *et al*, 2018), which is essential to mitigate virus-associated long-term complications. In order to test whether DZNep treatment is antiviral against SARS-CoV-2 *in vivo*, we infected C57BL/6 mice with SARS-CoV-2 beta variant (B.1.351, 250 pfu intranasal) and treated the animals at the day (day 0) and 1 day after infection (day 1) with DZNep (10 μg, intranasal application; Fig 5E). At day 2 post-infection, which represented the early acute stage of infection, the animals were sacrificed and lungs were harvested to quantify the viral load. We observed a significant reduction in the infectious viral load (Fig 5F), as well as diminished abundance of virus-derived mRNAs (Figs 5G and EV5J) in the lungs of DZNep-treated animals relative to the controls in the absence of any indication of toxicity (Fig 5H).

Taken together, we discovered a surprising relationship between SARS-CoV-2 NSP16 and cellular MTr1, which influences considerations on therapeutic approaches against COVID-19. We show that broad targeting of MTases involved in the viral life cycle by host-directed antivirals may be favorable over highly specific directly acting antivirals. Moreover, we show that the multispecific and metabolic MTase inhibitors, such as DZNep, are yet unexplored treatment options against COVID-19 (Fig 5I).

© 2022 The Authors

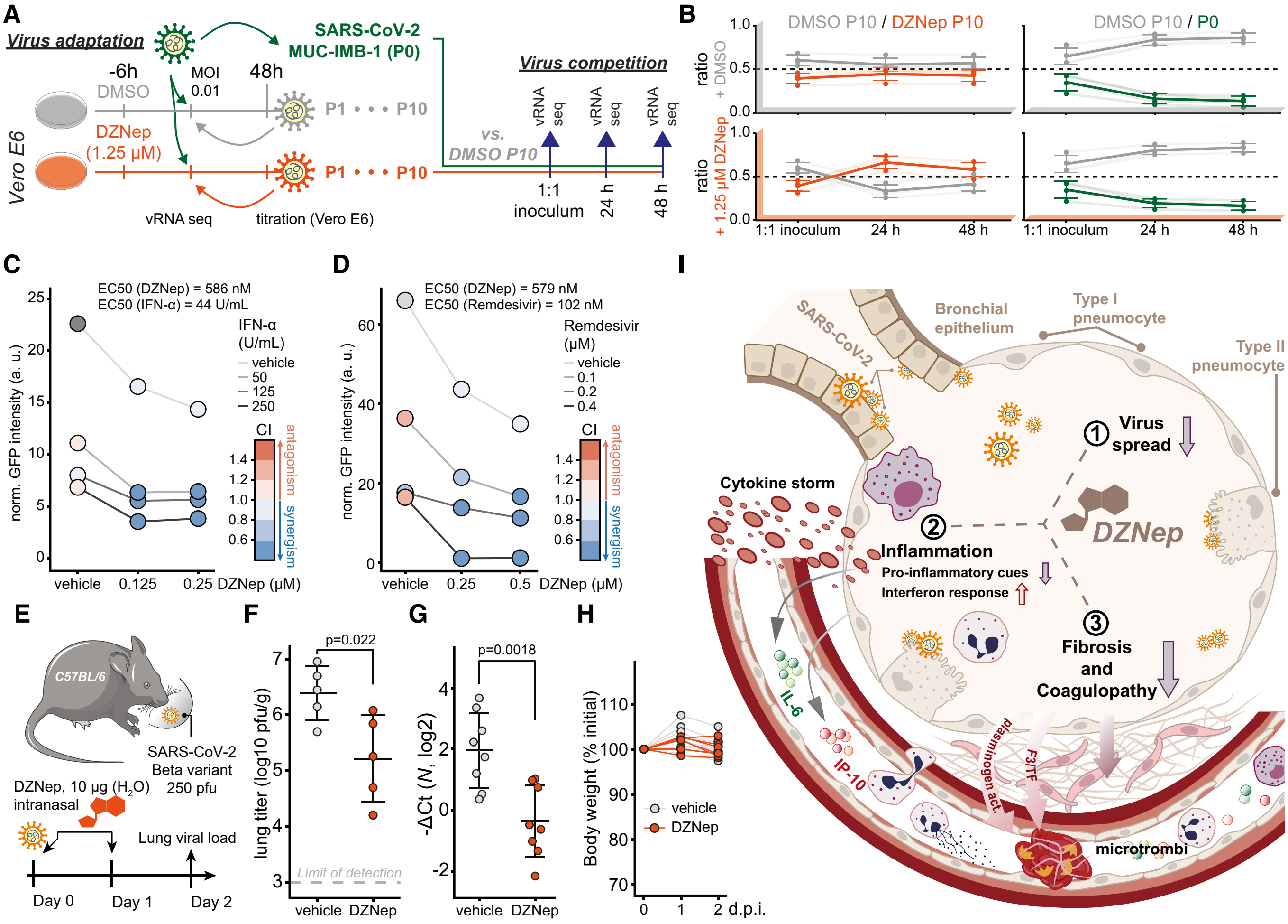

Figure 5. DZNep treatment does not lead to virus adaptation, exhibits synergism with remdesivir and IFN-α, and is antiviral *in vivo*.

A Schematic representation of the virus adaptation and subsequent pairwise competition experiments employing control (DMSO) and DZNep treatments.

B Ratio of indicated pairs of viral isolates in 1:1 inocula and 24 and 48 h post-infection of Vero E6 cells undergoing treatments as annotated. Four individual variations were used for ratio calculation (Fig EV5G, full list is available in Dataset EV6) and are shown alongside means ± SD.

C A549-ACE2 cells were pretreated for 6 h with indicated concentrations of IFN-α and DZNep and infected with SARS-CoV-2-GFP at MOI 1. Means of normalized integrated GFP intensities of six independently infected wells are shown as a measure of the reporter virus growth at 24 h post-infection alongside the combination index (CI) (Chou & Talalay, 1984) as a measure of treatments' synergy.

D A549-nRFP-ACE2 cells were pretreated for 6 h with indicated concentrations of remdesivir and DZNep and infected with SARS-CoV-2-GFP at MOI 1. Means of normalized integrated GFP intensities of five independently infected wells are shown as a measure of the reporter virus growth at 24 h post-infection alongside the combination index (CI) (Chou & Talalay, 1984) as a measure of treatments' synergy. The presented data are representative of three independent repeats.

E Schematic representation of the *in vivo* antiviral assay employing a murine infection model.

F, G C57BL/6 mice were infected with SARS-CoV-2 beta variant (250 pfu, intranasal) and treated at D0 and D1 with DZNep (10 µg, intranasal). Forty-eight hours post-infection, lungs of infected mice were isolated. (F) Lung infectious viral load was quantified by titration of lung homogenate supernatants on Vero E6 cells and expressed as log10 plaque-forming units per unit mass alongside mean ± SD ($n = 5$ animals per condition). Statistics were calculated using Student's two-sided *t*-test as indicated. (G) Abundance of viral transcript encoding SARS-CoV-2 *N* was quantified in the lung samples by RT–qPCR. The graph shows negative ΔCt values, as normalized to *18S rRNA*, and respective mean ± SD ($n = 8$ animals per condition). Statistics were calculated using Student's two-sided *t*-test as indicated.

H Animal body weight measured at indicated times post-infection, depicted as percentage of initial weight.

I Schematic representation of the proposed disease-relevant functions of DZNep in the context of COVID-19.

Data information: Data shown in (G, H) were pooled from two independent experiments.
Source data are available online for this figure.

Discussion

Here, we showed that robust antiviral effect against SARS-CoV-2 via cap 2'-O-ribose MTase inhibition requires concomitant targeting of both host (MTr1) and viral (NSP16) MTases. While the molecular mechanism behind the MTr1 involvement in the viral life cycle is yet to be clearly delineated, given its analogous function in host mRNA maturation, it is likely that it adds a degree of redundancy to the NSP16-facilitated viral RNA methylation. One may question why SARS-CoV-2 is not entirely relying on the activity of MTr1 given space constraints in viral genomes. A possible explanation may be the suboptimal localization of MTr1 from the viral perspective.

Alternatively, the readily available methylation capacity conferred by MTr1 may not be sufficient to facilitate rapid viral RNA buildup in the early stage of infection. Moreover, expression of MTr1 is induced by IFNs (Bélanger *et al*, 2010) but IFN expression is heavily inhibited by SARS-CoV-2. Collectively, the surprising synergy observed between NSP16 and MTr1 indicates that methylation of viral RNA is a rate-limiting step in the viral life cycle that cooperatively leverages the activities of both cellular and viral factors. The engagement of MTr1 seems to be specific for SARS-CoV-2 and has, to our knowledge, not been reported for any other virus that employs *de novo* RNA maturation. Indeed, cap 2’O-ribose methyltransferase activity-deficient YFV replicated similarly in MTr1-deficient cells, suggesting that the cellular RNA methyltransferase is not promiscuously active on viral RNAs. This novel conceptual advancement has direct implications for antiviral drug design and facilitated the discovery of two novel classes of antivirals active against SARS-CoV-2 that synergistically influence both host and viral factors.

Using *in silico* docking validated by *in vitro* MTase activity assays, we show that tubercidin is a broad-spectrum MTase inhibitor active against both NSP16 and MTr1. Tubercidin has been studied for antiviral (Olsen *et al*, 2004; Vittori *et al*, 2006) and anticancer properties (Grage *et al*, 1970), but its therapeutic value was hampered by unfavorable *in vivo* pharmacologic properties. As an alternative approach, we envisioned to target the SAM cycle through SCIs, which would indirectly hamper the activities of both NSP16 and MTr1. In contrast to tubercidin, the SCI DZNep is a well-tolerated drug that competitively inhibits AHCY at picomolar concentrations (Glazer *et al*, 1986) and that was also studied as an anticancer drug (Bray *et al*, 2000; Peer *et al*, 2013; Sun *et al*, 2015). In rats, SCI DZNep exhibits a favorable lung-to-plasma ratio of 3, its no-observed-adverse-effects level (NOAEL) was 10 mg/kg (Sun *et al*, 2015), and it is rapidly eliminated through renal secretion (Peer *et al*, 2013; Sun *et al*, 2015). Despite this, a single dose of DZNep was highly efficacious against Ebola (Bray *et al*, 2000, 2002) and vesicular stomatitis virus infections (De Clercq *et al*, 1989) in mice. In rats, liposome packaging of DZNep was shown to increase the area under the plasma concentration curve by 138-fold (Sun *et al*, 2012), potentially offering a major reduction in treatment doses. DZNep was previously shown to have antiviral activity against some viruses but not against others (Tseng *et al*, 1989; Chen *et al*, 2013; Arbuckle *et al*, 2017). In particular, it was shown to be antiviral against Ebola virus in mice (Bray *et al*, 2000, 2002), which could be explained by a combination of interferon induction and impeded viral RNA maturation. DZNep was also shown to impair viral mRNA cap methylation in the context of vesicular stomatitis virus infection and reduce viral mRNA translation (Gibbons *et al*, 2021). Recently, DZNep was reported to be antiviral against SARS-CoV-2 *in vitro* and *in ovo* (Kumar *et al*, 2022), leading to viral RNA m6A methylation and cap maturation defects and consequently to reduced viral protein production and inhibition of virus replication (Kumar *et al*, 2022). Overall, the above-mentioned independent work offers further evidence and supports findings presented herein toward demonstrating the treatment potential of SCIs against COVID-19.

The broad activity of DZNep on individual potentially antiviral pathways (IFNs, host or viral RNA methylation, histone methylation, etc.) complicates the identification of a dominant antiviral mechanism. Disregarding the potential contribution of inhibiting NSP14, the concomitant inhibition of NSP16 and MTr1 through drug-induced SAM starvation and SAH-based product inhibition may on its own restrict SARS-CoV-2 proliferation. Supportive of this hypothesis, it was previously shown that SAM facilitates the association of MERS-CoV NSP16 with its allosteric activator NSP10, and that SAH inhibits the MTase activity of NSP10/16 *in vitro* (Aouadi *et al*, 2017). Activity of NSP16 was also shown to be required for IFN resistance and virulence of related SARS and MERS coronaviruses (Menachery *et al*, 2014, 2017). Hypomethylation of viral mRNA at cap-proximal ribose moieties could promote antiviral innate immune activation (Züst *et al*, 2011; Schuberth-*Wagner et al*, 2015) and sensitize the virus towards translational repression by the innate immune effector protein IFIT1 (Daffis *et al*, 2010; Habjan *et al*, 2013; Abbas *et al*, 2017). Collectively, these effects could in part explain the DZNep-induced amplification of antiviral signaling that we observed *ex vivo* (Figs 4D and E, and EV4E and F), and synergism of DZNep with IFN-α co-treatment observed *in vitro* (Fig 5C), which induces expression of IFIT1, as well as shed light on selective antiviral efficacy of DZNep against SARS-CoV-2 as opposed to less IFN-sensitive SARS-CoV (Lokugamage *et al*, 2020). However, DZNep was active in a STAT1-independent manner (Fig EV3A and H), suggesting that innate immune signaling only partially contributes to anti-SARS-CoV-2 activity of SCIs.

Beyond suppressing virus growth, COVID-19 has numerous pulmonary and extrapulmonary manifestations requiring separate pharmaceutical interventions (Gupta *et al*, 2020). Coagulopathy, characterized by elevated von Willebrand factor, fibrinogen, and D-dimers and leading to excessive thrombin production, inhibition of fibrinolysis, and complement activation, has been associated with infection-mediated endothelialitis and endothelial injury (Gupta *et al*, 2020; Varga *et al*, 2020). We show that in primary human lung cells, SARS-CoV-2 and to a lesser extent SARS-CoV infections influenced abundance of proteins involved in blood coagulation such as PLAT (t-PA), PLAU (u-PA), PLAUR (u-PAR), F3 (TF), and SERPINE1 (PAI1), as well as components of the complement system such as C3, C4A/B, CD46, and CD55 (Fig 4D). Notably, DZNep treatment reduced the infection-induced deregulation of the above-mentioned factors. In most cases, the effect of DZNep treatment was also observed in uninfected settings, suggesting that this activity is unrelated to repression of virus growth and thus depends on inhibition of a yet unidentified host MTase. Crosstalk between fibrinolysis and organ fibrosis is mediated through protease antiprotease balance that further dictates tissue remodeling and cytokine activation (Mercer & Chambers, 2013). Using primary human lung cells, we show that SARS-CoV-2, and to a lesser degree SARS-CoV, perturbs abundance of pulmonary fibrosis-related proteins such as SERPINE1/PAI1, FN1, and HSPG2 (Fig 4D). Furthermore, we show that DZNep treatment alone or in context of SARS-CoV or SARS-CoV-2 infections reduces abundance of pulmonary fibrosis markers (e.g., SERPINE1, MMP14, and COL4A1) and increases levels of factors with antifibrotic activity (e.g., HOPX, PI3/ELAFIN, and SLPI; Fig 4D). These observations are in line with previous reports describing antifibrotic activity of DZNep in lungs (Xiao *et al*, 2016), liver (Zeybel *et al*, 2017), and kidneys (Mimura *et al*, 2018), which was linked to drug-induced inhibition of EZH2. Similar modulation of fibrosis-related proteins may be induced by other SCIs beyond DZNep, which may also perturb EZH2 activity in a metabolite-mediated manner.

© 2022 The Authors

The hallmark immunological characteristic of severe COVID-19 is the cytokine imbalance, whereby strong pro-inflammatory cues (e.g., mediated by elevated IL-6) are accompanied by only minor activation of innate antiviral defenses (e.g., mediated by type I IFNs) leading to deleterious systemic response (Blanco-Melo *et al*, 2020). It was shown that the type I IFN response is highly antiviral against SARS-CoV-2 (Mantlo *et al*, 2020). For this reason, interferons were considered as therapeutic options for COVID-19, but are as of yet not clinically used (Alavi Darazam *et al*, 2021). On the contrary, suppression of overshooting pro-inflammatory cues by, e.g., dexamethasone limits inflammation-mediated lung injury and is widely used for the treatment of COVID-19 (The RECOVERY Collaborative Group, 2021). Numerous biologicals (e.g., anti-IL-6 receptor (The REMAP-CAP Investigators, 2021) or anti-GM-CSF (De Luca *et al*, 2020)) were proposed to be used in a similar manner. We show that DZNep treatment is sufficient to prime and boost the cell-intrinsic antiviral response *ex vivo*, evidenced by upregulation of immunity-related genes (e.g., GBP1, IL-1RN; Fig 4D) and cytokines (IP-10; Fig 4E) in both uninfected and infected settings. In contrast, DZNep treatment of primary human lung cells led to upregulation of TNFAIP3/A20 (Fig 4D) and reduced SARS-CoV-2-induced secretion of NF-kB-dependent cytokine IL-6 (Fig 4F). In line with our observations, DZNep treatment was previously shown to inhibit EZH2 and invoke depletion of H3K27 trimethylation (Tan *et al*, 2007; Miranda *et al*, 2009), lifting the epigenetic suppression of the antiviral interferon signaling (Bray *et al*, 2002; Wee *et al*, 2014; Tiffen *et al*, 2020), as well as leading to upregulation of the NF-kB inhibitor TNFAIP3/A20 (Loong, 2013) and subsequent inhibition of NF-kB signaling (Loong, 2013). Specific inhibitors of EZH2, such as tazemetostat, may thus be effective co-treatment options along antivirals used in treatment of COVID-19 and other infectious diseases. The critical reliance on viral or host MTases and labile nature against intrinsic antiviral responses are common themes across the spectrum of pathogenic viral families. Supported by previous reports of its antiviral efficacy against diverse viral pathogens, the combined activities of DZNep and potentially SCIs in general make them unique candidate broad-spectrum antivirals that could curb multiple aspects of disease progression beyond COVID-19.

Herein, we leveraged both direct-acting and host-directed antiviral drug repurposing to explore the antiviral potential of pharmaceutical inhibition of SARS-CoV-2 cap 2’-O-ribose methyltransferase NSP16. We demonstrate that robust antiviral effect against SARS-CoV-2 critically requires concomitant inhibition of both viral MTase NSP16 and a novel host factor MTr1. Collectively, presented findings emphasize the potential of developing cross-functional host-directed antivirals, wherein the state-of-the-art knowledge of both virus and host biology is leveraged for applied antiviral research. Notably, we showed that host-directed therapies acting on the virus–host metabolic interface and targeting the SAM cycle can possess both antiviral and host-preserving functions. To our knowledge, no single-drug therapies against COVID-19 that would also tackle potentially long-term lung damage and fibrosis are currently available (Chitalia & Munawar, 2020; George *et al*, 2020; Feuillet *et al*, 2021). Most notably, DZNep is unparalleled in combining these activities by repressing viral load, limiting the hyperinflammatory response and promoting cell-intrinsic tissue repair programs, making it and similarly acting SCIs excellent treatment candidates against COVID-19.

Materials and Methods

Cell lines and reagents

HEK293T, A549 (kindly provided by Takashi Fujita, Kyoto University, Kyoto, Japan), A549-ACE2, and Vero E6 (CRL-1586, ATCC) cell lines, and their respective culturing conditions, were described previously (Stukalov *et al*, 2021). NHBE cells (CC-2540, Thermo Fisher Scientific) were cultured as described previously (Zissler *et al*, 2016); in short, the cells were grown until reaching 80% confluence. To avoid gene expression changes or influence on virus growth induced by growth factors in the BEGM (Lonza), cells were rested in basal medium (BEBM, Lonza) for 24 h before the start of the experiment. Baby hamster kidney cells (BHK-21/J), kindly provided by Charles M. Rice, Rockefeller University, New York, NY, USA, were grown in MEM containing 7.5% FBS, 1% L-glutamine, and 1% non-essential amino acids at 37°C, with 5% CO_2. Calu-3 cells (kindly provided by Stephan Pöhlmann, Deutsches Primatenzentrum, Münster, Germany, and Stephan Ludwig, University of Münster, Münster, Germany) were maintained in Eagle’s Minimum Essential Medium (MEM), containing 1% non-essential amino acids (NEAA, Gibco 11140), 10% fetal bovine serum, 1 mM Na-pyruvate (Gibco, 11360), 100 U/ml penicillin, and 100 µg/ml streptomycin at 37°C, with 5% CO_2. A549-RFP-ACE2 cell line was generated through lentiviral transduction of A549-ACE2 cell line and blasticidin selection, leading to expression of nuclear localized mRFP—plasmid pHIV-H2BmRFP was a gift from Bryan Welm & Zena Werb (Addgene plasmid #18982; http://n2t.net/addgene:18982; RRID: Addgene_18982; Welm *et al*, 2008). In preparation of KO cell lines, the following sequences were used in a multiplexed manner for cloning of gRNA templates into pLentiCRISPRv2 plasmid: STAT1 (GGTGGCAAATGAAACATCAT; GAGGTCATGAAAACGGATGG; CAG GAGGTCATGAAAACGGA), NTC (Sanjana *et al*, 2014; AACCGGAT CGCCACGCGTCC; TCCGGAGCTTCTCCAGTCAA; TGCAAAGTTCA GGGTAATGG), AHCY (TTTCCTCCCGTAGCCGACAT; CCAGGCAGCC AGGCCGATGT; TCCCGTAGCCGACATCGGCC) and MAT2A (CTGG AATGATCCTTCTTGCT; TGGAATGATCCTTCTTGCTG; TGCTGTT GACTACCAGAAAG). pLentiCRISPRv2 was a gift from Feng Zhang (Addgene plasmid #52961; http://n2t.net/addgene:52961; RRID: Addgene_52961; Sanjana *et al*, 2014). Lentivirus production, transduction of cells, and antibiotic selection for KO preparation were performed as described previously (Stukalov *et al*, 2021). In brief, A549-ACE2 cells were transduced using puromycin resistance carrying lentiviruses encoding Cas9 and gRNAs and grown for 4 days using medium, supplemented with 3 µg/ml puromycin, before being used for further experiments. MTr1 KO cells (clone number: H1) were generated by transducing the parental A549 cells with plasmid encoding gRNA (CCTCAACGATGTCCTTCCGACCC), and Cas9 and mCherry (kindly provided by Martin Schlee). After FACS sorting for mCherry-positive cells, clonal colonies were isolated, expanded, and validated for the loss of MTr1 by Western blotting and genome sequencing (CTR cell line was selected from clones with intact MTr1 locus and expression). All cell lines were tested to be mycoplasma-free.

For the stimulation of cells, recombinant human IFN-α was a kind gift from Peter Stäheli. The following inhibitors were used: SAH (RayBiotech, 229–20003), sinefungin (Cayman Chemical Company, 13829), cladribine (Cayman Chemical Company, Cay12085-

© 2022 The Authors

50), clofarabine (Cayman Chemical Company, B2764-Cay14125-10), 2-fluoroadenosine (Sigma-Aldrich, 656402), fludarabine (Tocris, 3495), 2-aminoadenosine (Santa Cruz Biotechnology, sc-220693A), vidarabine (BLD Pharmatech, BD42581), 3-DZA (Cayman Chemical Company, 9000785), nebularine (Cayman Chemical Company, 31329), tubercidin (Sigma-Aldrich, T0642), 1-DZA (Tocris, 4488), ribavirin (Sigma-Aldrich, R9644), tecadenoson (BLD Pharmatech, BD00781750), ITU (Sigma-Aldrich, I100), GDP-D-mannose disodium salt (Sigma-Aldrich, 07508), 3-deazaneplanocin A (Sigma-Aldrich, 5060690001, and Biozol, SEL-S7120), D-eritadenine (Biomol, Cay21747-1), remdesivir (Hölzel Biotech, CS-0028115), FIDAS-5 (MAT2A Inhibitor II, FIDAS-5—Calbiochem, Sigma-Aldrich, 5041730001), MAT2A inhibitor 1 (Hölzel Diagnostika, HY-112131), PF-9366 (Hölzel Diagnostika, HY-107778), CBHcy (S- (4-Carboxybutyl)-D,L-homocysteine, BioTrend, AOB2142), tazemetostat (EPZ-6438, Biomol, Cay16174-1), dexamethasone (Sigma-Aldrich, D1756), marimastat (Sigma-Aldrich, M2699), prinomastat (Sigma-Aldrich, PZ0198), ipatasertib (GDC-0068, 18412, Cayman chemical), and chloroquine (Chloroquine diphosphate salt, Sigma-Aldrich, C6628).

For the detection of protein abundance by Western blotting, ACTB-HRP (Santa Cruz; sc-47778; 1:5,000 dilution), ACE2 (Abcam; ab15348; 1:1,000 dilution), Venus (Santa Cruz; sc-9996; 1:1,000 dilution), MTr1 (Novus bio; NBP1-83047; 1:1,000 dilution), hnRNPA1-HRP (Santa Cruz; sc-32301 HRP; 1:1,000 dilution), GAPDH-HRP (Cell Signaling; 3683S; 1:1,000 dilution), and SARS-CoV-2/SARS-CoV N protein (Sino Biological; 40143-MM05; 1:1,000 dilution) antibodies were used. Secondary antibody detecting mouse IgG (Cell Signaling; 7076; 1:5,000 dilution) was horseradish peroxidase (HRP)-coupled. Alexa Fluor 488-conjugated goat anti-mouse antibody (Abcam, ab150113) was used for protein abundance detection by immunofluorescence. WB imaging was performed as described previously (Stukalov *et al*, 2021).

Structure-based NSP16 inhibitor screening

Structure-based virtual screening for NSP16 inhibitors was conducted using molecular docking against 5,597 bioactive compounds, with molecular weights ranging from 200 to 800 Da, from the DrugBank database. Docking simulations were performed using the Glide (Friesner *et al*, 2004; Halgren *et al*, 2004) SP docking program (Schrödinger, LLC) with a grid box defined by the SAM-binding pocket from the crystal structure of SARS-CoV-2 NSP10/16 (PDB ID: 6W4H).

UMAP dimensionality reduction according to MACCS structural keys (chemicalchecker.org; Duran-Frigola *et al*, 2020) was performed in Python 3.8.5, package UMAP 0.5.1, using default parameters.

Methyltransferase assays

Cap0 RNA, the methyl group acceptor in methyltransferase assays, was synthesized using the HiScribe T7 Quick High Yield RNA Synthesis Kit (NEB, E2050S) with cap analog m^{7}G (5′)ppp (5′)A (NEB, S1405), according to the manufacturer's instructions. The annealed 5′-overhang dsDNA was used as a template (Sense: 5'-TAATAC GACTCACTATA-3′, Antisense: 5′-CACTTTCACTTCTCCCTTTCAG TTTCCCTATAGTGAGTCGTATTA-3′).

The reaction buffer (50 mM Tris–HCl (pH 8.0), 5 mM KCl, 1 mM $MgCl_2$, 1 mM DTT) was complemented with methyltransferases (5 U/μl VACV VP39 (NEB, M0366S) or 1.5 μM/0.7 μM SARS-CoV-2 Nsp10/16 (Biomol, BPS-100747-1)), 10 mM tubercidin (or DMSO as vehicle control), 17 μM m^{7}GpppApG (pN_{27}; cap0 RNA), and 1.2 μM (0.02 μCi/μl) SAM[^{3}H] (PerkinElmer, NET155V250UC). The reaction mixtures were incubated at 37°C overnight. The samples were purified using a mini Quick Oligo column (Roche, 11814397001) to remove free SAM[^{3}H]. The purified sample was diluted in ULTIMA GOLD (PerkinElmer, 6013329) and measured using a scintillation counter LS6500 (Beckman Coulter).

Virus strains, stock preparation, and *in vitro* infection

SARS-CoV-Frankfurt-1 (Pfefferle *et al*, 2009), SARS-CoV-2-MUC-IMB-1 (Thi Nhu Thao *et al*, 2020), SARS-CoV-2 Alpha (B.1.1.7; Coronaviridae Study Group of the International Committee on Taxonomy of Viruses, 2020), SARS-CoV-2 Delta (B.1.617.2; Mlcochova *et al*, 2021), and SARS-CoV-2-GFP (Stukalov *et al*, 2021) strains were produced as described previously (Stukalov *et al*, 2021). The SARS-CoV-2 beta variant (B.1.351) was isolated in Bonn from a throat swab of a patient on and propagated on Caco-2 cells cultured in DMEM (10% FCS, 100 μg/ml streptomycin, 100 U/ml penicillin, and 2.5 μg/ml amphotericin B). All experiments with SARS-CoV-2 were performed in BSL3 laboratories under the approval of the Regierung von Oberbayern, Germany (AZ: 55.1GT-8791.GT_2-365-10 and 55.1GT-8791.GT_2-365-20) and approval of the government of Cologne, Germany. For *in vivo* experiments, the virus was passaged once on Caco-2 cells in DMEM (10% FCS, 100 μg/ml streptomycin, and 100 U/ml penicillin) at an MOI of 0.001 and harvested at 3 days post-infection. Virus in the cleared supernatant (200 g, 10 min, 4°C) was stored at −80°C. Viral titers of the stocks were determined on Vero E6 cells using a carboxymethylcellulose overlay as described previously (Koenig *et al*, 2021). Recombinant SARS-CoV-2 NSP16mut virus was generated via plasmid pBeloCoV harboring the inactivating mutations D130A and K170A in the coding sequence of NSP16 (pBeloCoV-NSP16mut), which was cloned through Red recombination (manuscript by T. Gramberg in preparation). The virus was further amplified in CaCo-2 cells (1 passage, 72 h) and quantified in cleared and purified supernatants by RT–qPCR. Recombinant YFV 17D and YFV 17D NS5 E218A (YFV E218A) were generated via electroporation of an infectious cDNA clone-derived *in vitro* mRNA transcript into BHK-J cells and a single passage on BHK-J cells; titers were determined by plaque assays using BHK-J cells as described previously (Kümmerer & Rice, 2002). Recombinant vesicular stomatitis virus (VSV) Indiana strain encoding EGFP in position 5 of the genome (VSV-GFP) was recovered from BSR T7/5 cells infected with VACV WR vTF7.3 and transfected with pVSV1 (+) P5_EGFP, pL, pP, and pN as described previously (Whelan *et al*, 1995). It was further propagated in BSR T7/5 cells, and virus titers were determined by the plaque assay using Vero cells.

Cells were pretreated with inhibitors by medium (containing any indicated inhibitor) exchange at 6 h (unless stated otherwise) prior to the addition of infectious inoculum containing SARS-CoV-2 at MOI 3 (SARS-CoV-2-MUC-IMB-1, unless stated otherwise) with medium replacement 1 h post-infection where indicated. Infection with YFV 17D wt and YFV NS5 E218A was performed in PBS

© 2022 The Authors

containing 1% FBS for 1 h, followed by 2× PBS and 1× MEM wash and medium replacement.

At the time of sample harvest, the cells were washed once with 1× PBS buffer and lysed in LBP (Macherey-Nagel), 1× SSB lysis buffer (62.5 mM Tris–HCl, pH 6.8; 2% SDS; 10% glycerol; 50 mM DTT; and 0.01% bromophenol blue), or freshly prepared SDC buffer (100 mM Tris–HCl, pH 8.5; 4% SDC) for RT–qPCR, Western blot, or LC–MS/MS analyses, respectively. The samples were heat-inactivated and frozen at −80°C until further processing. Sampled supernatants were stored frozen at −80°C until further processing.

Antiviral assays using SARS-CoV-2-GFP

A549-ACE2 cells were seeded into 96-well plates in DMEM (10% FCS, 100 µg/ml streptomycin, 100 IU/ml penicillin) 1 day before infection. Six hours before infection, the medium was replaced with 125 µl of DMEM containing either the compound (s) of interest or their respective vehicle (s) as control. Infection was performed by adding 10 µl of SARS-CoV-2-GFP (MOI 3, unless otherwise stated) per well, and plates were placed in the IncuCyte S3 Live-Cell Analysis System where images of phase, green, and red (when using A549-RFP-ACE2 cell line) channels were captured at regular time intervals at 4× (whole-well) or 20× magnification. Cell viability was assessed as the cell confluence per well (phase area). Virus growth was assessed as GFP integrated intensity normalized to cell confluence per well (GFP integrated intensity/phase area) or GFP area normalized to cell confluence per well (GFP area/phase area) or GFP area normalized to RFP-positive nucleus count (when using A549-RFP-ACE2 cell line). Basic image analysis and image export were performed using the IncuCyte S3 software (Essen Bioscience; version 2019B Rev2). Statistical analysis and visualization were performed using R version 4.0.2. Three-parameter logistic function fitting was performed using R package drc (version 3.0-1).

Plaque assays

Confluent monolayers of Vero E6 cells were infected with serial five-fold dilutions of virus supernatants (from 1:100 to 1:7,812,500) for 1 h at 37°C. The inoculum was removed and replaced with serum-free MEM (Gibco, Life Technologies) containing 0.5% carboxymethylcellulose (Sigma-Aldrich). Two days post-infection, cells were fixed for 20 min at room temperature with formaldehyde directly added to the medium to a final concentration of 5%. Fixed cells were washed extensively with PBS before staining with H_2O containing 1% crystal violet and 10% ethanol for 20 min. After rinsing with PBS, the number of plaques was counted and the virus titer was calculated.

Quantification of gene expression in cell lines by RT–qPCR

Total cellular RNA, or RNA content of the supernatants, was harvested and isolated using MACHEREY-NAGEL NucleoSpin RNA mini kit according to the manufacturer's instructions. Reverse transcription was performed using the Takara PrimeScript RT Reagent kit with gDNA eraser according to the manufacturer's instructions.

RT–qPCR was performed using primers targeting SARS-CoV-2 N (fw: 5′-TTACAAACATTGGCCGCAAA-3′; rev: 5′-GCGCGACATTCCGAAGAA-3′), SARS-CoV-2 *E* (Figs 1C and I, and EV1D; fw: 5′-ACAGGTACGTTAATAGTTAATAGCGT-3′; rev: 5′-ATATTGCAGCAGTACGCACACA-3′), SARS-CoV-2 *E* (Fig EV1G) and MERS-CoV *N*, which were described previously (Matsuyama *et al*, 2020); SARS-CoV *N* as described previously (Corman *et al*, 2012); VSV N (fw: 5′-GGAGTATCGGATGCTTCCAGAACCA-3′; rev: 5′-ACGACCTTCTGGCACAAGAGGTT-3′), MAT2A (fw: 5′-CTTCGTAAGGCCACTTCCGC-3′; rev: 5′-TCTGGTAGCAACAGCAGCTC-3′), AHCY (fw: 5′-AACTGCCCTACAAAGTCGCC-3′; rev: 5′-ATGGTCCTGGGTGGAGAAGA-3′), and RPLP0 (unless stated otherwise the housekeeper control, fw: 5’-GGATCTGCTGCATCTGCTTG-3′; rev: 5′-GCGACCTGGAAGTCCAACTA-3′) using PowerUp SYBR Green (Thermo Fisher, A25778); and SARS-CoV-2 RdRp (fw: 5′-GTGAAATGGTCATGTGTGGCGG-3′; rev: 5′-CAAATGTTAAAAACACTATTAGCATA-3′; VIC-CAGGTGGAACCTCATCAGGAGATGC-BMN-Q535), Eukaryotic 18S rRNA (Hs99999901_s1, Applied Biosystems), human *IFNB1* (Hs01077958_s1, Applied Biosystems), human *IFIT1* (ISG56; Hs03027069_s1, Applied Biosystems), and human *MxA* (Hs00895608_m1, Applied Biosystems) using TaqMan Fast Advanced Master Mix (Applied Biosystems). QuantStudio 3 Real-Time PCR System (Thermo Fisher) or Step One Plus Real-Time PCR System (Applied Biosystems) was used. Ct values, obtained using QuantStudio Design and Analysis Software v1.4.3, were averaged across technical replicates and −ΔCt values as a measure of gene expression were calculated as Ct (RPLP0) − Ct (N). −ΔΔCt values as a measure of change in gene expression between distinct KOs and NTC were calculated as −ΔCt (KO) − (−ΔCt (NTC)). For display of highly divergent values, one replicate of vehicle-treated samples was assigned a relative expression value of 10^6. Viral RNA copy was calculated from the standard curve using serial diluted cDNA with known copy number. Statistical analysis and visualization were performed using R version 4.0.2.

Protein abundance quantification by Western blotting

At the time of sample harvest, the cells were washed with PBS and lysed in SSB buffer (62.5 mM Tris–HCl from 1 M stock solution with pH 6.8, 2% SDS, 10% glycerol, 50 mM DTT, and 0.01% Bromophenol Blue in distilled water), and protein concentrations were measured using Pierce 660-nm Protein Assay with an addition of Ionic Detergent Compatibility Kit (Thermo Fisher Scientific) according to the manufacturer's instructions. Protein concentrations were equalized, and up to 10 µg of proteins was loaded in NuPAGE Bis-Tris, 1 mm, 4–12% gels (Thermo Fisher Scientific). Protein separation was performed according to the gel manufacturer's instructions, and proteins were transferred to 0.22-µm nitrocellulose membrane (1 h at 100 V in 25 mM Trizma base, 0.192 M Glycine, pH 8.3). The membranes were blocked for 1 h in 5% skim milk in TBS-T buffer (0.25% Tween-20 in phosphate-buffered saline solution) with gentle agitation. The antibodies listed in the section above (cell lines and reagents) were diluted in 5% skim milk (TBS-T); the membranes were washed 5× for 5 min with TBS-T between and after incubations with primary and secondary antibodies. Western Lightning ECL Pro (PerkinElmer) was used for band detection according to the manufacturer's instructions. Normalization of band signals was performed using the Image Lab Software (Bio-Rad; version 6.0.1 build 34).

© 2022 The Authors

MTr1 detection in separated cellular fraction

Cytoplasmic and nuclear extracts were prepared as described previously (Bélanger *et al*, 2010). Briefly, A549 cells with or without overnight IFN-β 1a (PBL Assay Science, 11410-2) treatment (1,000 U/ml) were detached from cell culture dish and resuspended in 600 μl of cold lysis buffer (10 mM HEPES (pH 7.5), 10 mM KCl, 0.1 mM EDTA, 0.1 mM EGTA, 1 mM DTT, and 1 × Protease/phosphatase Inhibitor Cocktail (Cell Signaling Technology, 5872S)). The cell suspension was incubated on ice for 15 min before addition of NP-40 to the final concentration of 0.5% and 10-s vortexing. The resulting mixture was centrifuged at 2,000 × *g* for 30 s at 4°C before the supernatant (cytoplasmic fraction) was removed. The pellet was resuspended in 100 μl of nuclear extraction buffer (20 mM HEPES (pH7.5), 400 mM KCl, 1 mM DTT, and 1 × Protease/phosphatase Inhibitor Cocktail), incubated on a rotating wheel at 4°C for 15 min, and centrifuged at 14,000 × *g* for 15 min at 4°C. The supernatant (nuclear fraction) was further harvested and frozen at −20°C until further use.

Viral protein detection and quantification by immunofluorescence

For detection of viral protein expression using immunofluorescence, the cells were washed 3× with phosphate-buffered saline (PBS), fixed for 15 min with 4% formaldehyde in PBS, washed again, and permeabilized using 0.1% Triton-X in 4% BSA (PBS) for 15 min. They were further blocked for 1 h using 4% BSA in PBS. The antibodies listed in the section above (cell lines and reagents) were diluted in 4% BSA (PBS); the cells were washed 5× for 1 min with PBS between and after incubations with primary and secondary antibodies. Stained cells were imaged using IncuCyte S3 Live-Cell Analysis System. Whole-well images of GFP and Phase channels were captured at 4× magnification. Cell viability and virus growth were assessed as the cell confluence per well (phase area) and GFP integrated intensity normalized to cell confluence per well (GFP integrated intensity/phase area), respectively, using the IncuCyte S3 Software (Essen Bioscience; version 2019B Rev2). Analysis and visualization were performed using the R version 4.0.2.

Quantification of secreted cytokines by ELISA

For detection of human IL-6 and IP-10, commercially available ELISA kits were used (Human IL-6 ELISA Set, BD OptEIA, 555220; Human IP-10 ELISA Set, BD OptEIA, 550926) according to the manufacturer's instructions. Basal medium, used for NHBE culturing at time of treatment and infection, was used as blank control. Statistics (Fig 4E) were calculated using paired Student's two-sided *t*-test on log-transformed values between indicated conditions before donor-wise normalization to vehicle-treated mock controls.

Mass spectrometry sample preparation and analysis

For the determination of proteome changes, A549-ACE2 cells were pretreated for 6 h with vehicle (PBS) or 0.75 μM DZNep and infected with SARS-CoV-2 and SARS-CoV at MOI 3 for 24 h. Experiment involving tubercidin was performed and analyzed in an analogous manner with the following experimental modifications: 1 μM tubercidin was used with DMSO as vehicle, 3 h pretreatment, SARS-CoV-2 MOI 0.1, SARS-CoV MOI 0.01. Cells were then lysed in SDC lysis buffer (100 mM Tris–HCl pH 8.5; 4% SDC). The following conditions were considered: vehicle-treated uninfected (3 replicates, 4 in tubercidin treatment), DZNep-treated uninfected (4 replicates), vehicle-treated SARS-CoV-2-infected (4 replicates), DZNep-treated SARS-CoV-2-infected (4 replicates), vehicle-treated SARS-CoV-infected (4 replicates), and DZNep-treated SARS-CoV-infected (4 replicates) cells. For the determination of proteome changes in NHBEs, pretreated for 6 h with vehicle (PBS) or 1.5 μM DZNep and infected with SARS-CoV-2 and SARS-CoV at MOI 3 for 24 h, cells were lysed in SDC lysis buffer (100 mM Tris–HCl pH 8.5; 4% SDC). The following conditions were considered: vehicle-treated uninfected, DZNep-treated uninfected, vehicle-treated SARS-CoV-2-infected, DZNep-treated SARS-CoV-2-infected, vehicle-treated SARS-CoV-infected, and DZNep-treated SARS-CoV-infected cells. Cells from four distinct donors were used. Sample preparation was performed as described previously (Stukalov *et al*, 2021). In brief, protein concentrations of cleared lysates were normalized and 50 μg was used for further processing. To reduce and alkylate proteins, samples were incubated for 5 min at 45°C with TCEP (10 mM) and CAA (40 mM). Samples were digested overnight at 37°C using trypsin (1:100 w/w, enzyme/protein, Sigma-Aldrich) and LysC (1:100 w/w, enzyme/protein, Wako). Resulting peptide solutions were desalted using SDB-RPS StageTips (Empore). Samples were diluted with 1% TFA in isopropanol to a final volume of 200 μl and loaded onto StageTips, and subsequently washed with 200 μl of 1% TFA in isopropanol and 200 μl 0.2% TFA/ 2% ACN. Peptides were eluted with 75 μl of 1.25% ammonium hydroxide (NH_4OH) in 80% ACN and dried using a SpeedVac centrifuge (Eppendorf, Concentrator plus). Next, the peptides were reconstituted in buffer A* (0.2% TFA/ 2% ACN) prior to LC–MS/MS analysis. Peptide concentrations were measured optically at 280 nm (Nanodrop 2000, Thermo Scientific) and subsequently equalized using buffer A*. One microgram peptide was subjected to LC–MS/MS, and protein groups were quantified (MaxQuant version 1.6.10.43) with LFQ normalization (A549s) and without LFQ normalization (NHBEs) as described previously (Stukalov *et al*, 2021).

The analysis of MS datasets was performed using R version 4.0.2. LFQ values were $\log_2$-transformed, and protein groups only identified by site, reverse matches, and potential contaminants were excluded from the analysis. Additionally, protein groups quantified by a single peptide or not detected in all replicates of at least one condition were excluded from further analysis. In NHBE dataset, LFQ values were normalized for donor-specific effects on protein abundance. In short, the protein $\log_2$ intensities were compared across conditions in a donor-wise manner, and systematic deviations across conditions were subtracted in order to get normalized LFQ values.

The imputation of missing $\log_2$ intensity values was done similar to the method implemented in Perseus (Tyanova *et al*, 2016): The mean and the standard deviation of $\log_2$ intensities were calculated for each dataset, and missing values were replaced by sampling from the normal distribution with the following parameters: 0.3 * standard deviation, mean − 1.8 * standard deviation. In addition, effect scaling was performed using the Gaussian generalized linear modeling approach (core function glm) to allow for quantitative comparison between virus infections and treatments in different

© 2022 The Authors

contexts. In short, the following experiment design was used: norm. $\log_2$-LFQ ~ virus + virus:treatment, where virus refers to infection with mock, SARS-CoV, or SARS-CoV-2, and treatment refers to vehicle or DZNep treatment. Median absolute values of significant effects ($P < 0.01$) originating from virus and virus:treatment coefficients were calculated and divided by median of SARS-CoV-2 and mock:DZNep, respectively, resulting in coefficient 1 ± 0.15 that were used in downstream analysis as coefficients in experimental design matrix.

The following experiment design was used for LASSO-based differential protein abundance analysis: LFQ ~ virus + virus:treatment, where virus refers to infection with mock-, SARS-CoV, or SARS-CoV-2, and treatment refers to vehicle or DZNep treatment. The following effects were thus estimated: effect of SARS-CoV infection, effect of SARS-CoV-2 infection, effect of DZNep treatment of mock-infected cells, effect of DZNep treatment of SARS-CoV-infected cells, and the effect of DZNep treatment of SARS-CoV-2-infected cells. The estimation of LASSO model parameters was performed using R package glmnet (Friedman *et al*, 2010; Simon *et al*, 2011) (version 4.0.2) with thresh = 1e-28, maxit = 1e7, and nfolds = 11. The exact model coefficients and lambda value at cross-validation minimum (lambda.min) were extracted and used for P-value estimation by fixed-lambda LASSO inference using the R package selectiveInference (Lee *et al*, 2013), version 1.2.5. Default parameters were used with the following modifications: tol.beta = 0.025, alpha = 0.1, tailarea_rtol = 0.1, tol.kkt = 0.1, and bits = 100. The bits parameter was set to 300 or 500 if the convergence was not reached. The sigma was explicitly estimated using function estimateSigma from the same package. No multiple hypothesis P-value correction was performed since that is facilitated by the choice of lambda. The following thresholds were applied to LASSO analysis results to identify statistically significant effects ($\log_2$ fold changes): $P < 10^{-5}$ and abs ($\log_2$ fold change) > 0.5 for the NHBE data, and $P < 10^{-4}$ and abs ($\log_2$ fold change) > 0.2 for A549 data. If a protein reached significance in one infected condition, or one treated condition, and not others, the significance thresholds for the other conditions were relaxed to: $P < 10^{-2}$ and abs ($\log_2$ fold change) > 0.2, in order to avoid over-estimating differences among similar infections or drug treatments.

Protein GO-term annotations were retrieved using R package biomaRt (Durinck *et al*, 2009; version 2.45.5). Fisher's exact test was employed, and FDR-adjusted P-values were used to identify the terms that are significantly enriched among the changing proteins (threshold: $P < 10^{-2}$).

Proteins, significantly changing in the same direction (up- or downregulated) upon DZNep treatment of SARS-CoV- and SARS-CoV-2-infected NHBEs as determined by the above described analysis (marked in gray and dark-gray in Fig 4B), were used in network diffusion analysis. Network diffusion analysis was performed using ReactomeFI network v2019 (Wu *et al*, 2014). Random walk with restart kernel (R) was computed for this network in undirected manner, with restart probability of 0.4 according to the following equation: $R = alpha * (I - (1-alpha)*W)^{-1}$, where I is the identity matrix, and W is the weight matrix computed as $W = D^{-1} * A$, where D is degree diagonal matrix, and A is adjacency matrix for ReactomeFI graph. The diagonal values of the R matrix, representing restart and feedback flows, were excluded from subsequent analysis and set to 0. The significant hits from MS data analysis were mapped to genes in the ReactomeFI network by matching gene names or their synonyms (from the biomaRt_hsapiens gene ensemble dataset) with the gene names in ReactomeFI. Nodes with significant flows originating from nodes representing hits in individual analyses were estimated using a randomization-based approach. All hits and non-hits of the analysis were attributed equal weight (1 and 0, respectively) in subsequent statistical analysis. Flows to all nodes in the network were computed by multiplying the R matrix with the vector of hits described above. Furthermore, nodes in the network were assigned to 8 bins of approximately equal size according to the node degree. The same procedure of calculating inbound flows to all network nodes was repeated for 2,500 iterations, each time using the same number of randomly selected decoy hits from sets of nodes with 1 bin higher node degree (on per-hit basis). The P-values describing the significance of functional connectivity to input hits were computed for each node according to the following formula: $P = N$ (iteration with equal or higher inbound flux)/N (iterations). For visualization purposes, the ReactomeFI network was filtered for nodes that were either representing input proteins or proteins with $P < 0.005$ and further trimmed by removing non-hit nodes with degree equal to 1.

Virus adaptation and competition assays

Vero E6 cells were seeded in T-175 flasks at 15 million cells per flask 24 h before the standard culturing medium was exchanged to one including treatments of choice (0.025% DMSO, 1.25 μM DZNep or 2.5 μM FIDAS-5). Six hours post-treatment, the cultures were inoculated with SARS-CoV-2-MUC-IMB-1 (P0) at MOI 0.01. Forty-eight hours post-inoculation, the supernatant was harvested, spun at 1,000 *g* for 5 min, and further processed for RNA isolation and titration of infectious viral particle content as described above. Deduced titers were used to inoculate freshly prepared Vero E6 cells as described for P0. The process was repeated until reaching passage 10 and is schematically depicted in Fig 5A. Isolated viral genomic RNA was reverse-transcribed as described above and submitted for sequencing (described below).

For pairwise comparison of replication fitness (competition assay), Vero E6 cells were seeded in 12-well plate at a density of 0.2 million cells per well 24 h before the standard culturing medium was exchanged for one containing treatments of choice (0.025% DMSO, 1.25 μM DZNep or 2.5 μM FIDAS-5). Six hours post-treatment, the cultures were inoculated with 1 to 1 mixture (according to infectious particle content) of (i) DMSO P10 and DZNep P10, (ii) DMSO P10 and FIDAS-5 P10, and (iii) DMSO P10 and P0, at MOI 0.01. A part of the inoculum was saved for sequencing analysis. Forty-eight hours post-infection, the culture supernatant was harvested and its RNA content isolated, which was further reverse-transcribed as described above and submitted for sequencing (described below).

For sequencing, SARS-CoV-2 genomes were prepared from amplicon pools, generated with a balanced primer pool according to ARTICv3 protocol (DNA Pipelines R&D *et al*, 2020). Amplicons were converted to barcoded Illumina sequencing libraries with the Nextera XT kit (Illumina, San Diego, USA) in a miniaturized version using a Mantis dispenser (Formulatrix, Bedford, USA) and sequenced on an Illumina NextSeq1000. The obtained sequence reads were demultiplexed and aligned to the SARS-CoV-2 reference

© 2022 The Authors

genome (NC 045512.2) with BWA-MEM (preprint: Li, 2013). The read depth along the reference genome was calculated with samtools depth. Variants were called using Freebayes (Cingolani *et al*, 2012) using a ploidy of 1 (−p 1). The effects of genetic variants on amino acid sequences were predicted with SnpEff (Cingolani *et al*, 2012). The pileups files were generated using samtools (Li *et al*, 2009) and used for consensus sequence generation within the iVar (Grubaugh *et al*, 2019) package with default settings. Multiple sequence alignments of the consensus sequences were calculated using MAFFT (v7.475; Katoh & Standley, 2013), which were passed to IQ-TREE2 (v.2.1.2; Minh *et al*, 2020) to calculate the Newick tree.

Ratios between viral isolates in virus competition assay were calculated using mutations depicted in Fig EV5G according to the following formulas, assuming no adaptation events during the course of virus competition assay:

$$S_{vf} = X \times A_{vf} + Y \times B_{vf}$$

$$X + Y = 1,$$

where S_{vf}, A_{vf}, and B_{vf} are measured variation frequencies of particular mutation in sample of interest, isolate A used in inoculum, and isolate B used in inoculum, respectively. X and Y describe the ratios of isolate A and isolate B in the sample, respectively, and in sum equal to unity. X and Y can be deduced from equations above in the following manner:

$$X = \frac{S_{vf} - B_{vf}}{A_{vf} - B_{vf}}$$

$$Y = 1 - X$$

Quantitative analysis of co-treatments

Viral inhibition assays utilizing DZNep and remdesivir (or IFN-α) co-treatment and SARS-CoV-2-GFP virus were performed as described above. For remdesivir, A549-RFP-ACE2 cell line was used and a number of RFP-positive cell nuclei were used for normalization of virus reporter signal (instead of phase-based cell confluence used for IFN-α). The calculations of combination indexes for mutually exclusive drugs were performed as described previously (Chou & Talalay, 1984). In short, fractions of system affected and unaffected (f_a and f_u, respectively) were calculated for means of normalized GFP integrated intensities (NGII) originating from individual treatment conditions according to the following equation:

$$f_a = 1 - f_u = 1 - \frac{NGII\ (c_{DZNep}, c_{Remdesivir})}{NGII\ (vehicle, vehicle)}$$

Half-maximal effective concentrations (EC50) and Hill-type coefficients (m) were calculated by performing linear modeling of vehicle-co-treated data according to the following equations:

$$\log_2\left(\frac{f_a(c_{DZNep}, vehicle)}{1 - f_a(c_{DZNep}, vehicle)}\right) = m \times \log_2 c_{DZNep} - m \times \log_2 EC50_{DZNep}$$

$$\log_2\left(\frac{f_a(vehicle, c_{Remdesivir})}{1 - f_a(vehicle, c_{Remdesivir})}\right) = m \times \log_2 c_{Remdesivir} - m \times \log_2 EC50_{Remdesivir}$$

Combination index (CI) was further calculated according to the following equations:

$$D^t_{DZNep} = EC50_{DZNep} \times \left(\frac{f_a}{1 - f_a}\right)^{1/m_{DZNep}}$$

$$D^t_{Remdesivir} = EC50_{Remdesivir} \times \left(\frac{f_a}{1 - f_a}\right)^{1/m_{Remdesivir}}$$

$$IC = \frac{c_{DZNep}}{c^t_{DZNep}} + \frac{c_{Remdesivir}}{c^t_{Remdesivir}}$$

In vivo experiments

Eight- to 10-week-old female C57BL/6J mice were purchased from Charles River Laboratories. Mice were anesthetized with 90 mg/kg ketamine (WDT) and 9 mg/kg xylazine (Serumwerk Bernburg AG). Mice were inoculated intranasally with 2.5×10^2 pfu of SARS-CoV-2 beta variant (also known as B.1.351). Infected mice were intranasally treated with 25 µg of tubercidin or 10 µg of DZNep at 30–60 min and 24 h post-infection. All animal experiments using SARS-CoV-2 were performed in a biosafety level 3 facility at University Hospital Bonn according to institutional and governmental guidelines of animal welfare (animal experiment application number: 81-02.04.2019.A247).

Quantification of virus transcripts in mouse lung material by RT–qPCR

At 2 days post-infection, lungs of infected mice were harvested and homogenized in TRIzol (Invitrogen) using gentleMACS Octo Dissociator (Miltenyi Biotec). RNA was extracted from the homogenates following the manufacturer's protocol. cDNA was generated using High-Capacity cDNA Reverse Transcription Kit (Applied Biosystems). To quantify the viral RNA, real-time quantitative PCR was performed by Step One Plus Real-Time PCR System (Applied Biosystems) using Fast SYBR Green Master Mix (Applied Biosystems) and TaqMan Fast Advanced Master Mix (Applied Biosystems; for transcripts *M*, *E*, and *18s rRNA*), and by QuantStudio 3 Real-Time PCR system (Thermo Fisher) using PowerUp SYBR Green (Thermo Fisher; for transcripts *N* and *Actb*). RT–qPCR primers were designed for SARS-CoV-2 genes as below: 5′-TGTGACATCAAGGACCTGCC-3′ and 5′-CTGAGTCACCTGCTACACGC-3′ for SARS-CoV-2 M; 5′-ACAGGTACGTTAATAGTTAATAGCGT-3′ and 5′-ATATTGCAGCAGTACGCACACA-3′ for SARS-CoV-2 E; and 5′-TTACAAACATTGGCCGCAAA-3′ and 5′-GCGCGACATTCCGAAGAA-3′ for SARS-CoV-2 N. Levels of viral transcripts *M* and *E* were normalized with *18s rRNA* levels using the TaqMan probe for eukaryotic 18s rRNA (Hs99999901_s1, Applied Biosystems). Levels of viral transcript *N* were normalized with *Actb* levels (RT–qPCR primers: 5′-CTCTGGCTCCTAGCACCATGAAGA-3′ and 5′-GTAAAACGCAGCTCAGTAACAGTCCG-3′).

Quantification of viral load in mouse lung material by plaque assay

Thirty milligram of lungs was collected from infected mice at 2 days post-infection. Lungs were homogenized in 300 µl of PBS using Tissue Grinder Mixy Professional (NIPPON Genetics EUROPE, NG010). Homogenates were cleared by centrifugation twice (200 *g*, 5 min, 4°C; and 20,000 *g*, 5 min, 4°C), and the supernatants were stored at −80°C until further processing. The viral titers were determined by the plaque assay using Vero E6 cells as described above.

Data availability

The mass spectrometry proteomics data have been deposited to the ProteomeXchange Consortium via the PRIDE (Perez-Riverol *et al*, 2022) partner repository with the dataset identifier PXD034361 (http://www.ebi.ac.uk/pride/archive/projects/PXD034361).

Expanded View for this article is available online.

Acknowledgements

We thank Janett Wieseler, Dr. Yueyuan Hu, and Dr. Alexander Herrmann for excellent technical assistance and Volker Thiel for the SARS-CoV-2 GFP virus. We further acknowledge the Microscopy Core Facility (MCF) of the Medical Faculty at the University of Bonn and BayBioMS@MRI for support. This project was supported by the European Research Council (ERC-CoG, Grant nr. 817798), Bavarian State Ministry of Science and Arts (Bavarian Research Network FOR-COVID) and the Helmholtz Association‘s Initiative and Networking Fund (KA1-Co-02 “COVIPA”) to APic, the Federal Ministry for Education and Research (BMBF; COVINET to AP, TTU 01.810 to BMK), the German Research Foundation (DFG; Germany’s Excellence Strategy—EXC 2151—390873048 to HK; TRR237 Grant No. 369799452 to APic (A07), BMK (A04), and HK (B22); and TRR179 (TP11), PI 1084/4, PI 1084/5, and PI 1084/7 to APic), CAJ, MO, and CBS-W were supported by funding from the German Center of Lung Research (DZL). Open Access funding enabled and organized by ProjektDEAL.

Author contributions

Valter Bergant: Conceptualization; supervision; investigation. **Shintaro Yamada:** Investigation. **Vincent Grass:** Investigation. **Yuta Tsukamoto:** Investigation. **Teresa Lavacca:** Investigation. **Karsten Krey:** Investigation. **Maria-Teresa Mühlhofer:** Investigation. **Sabine Wittmann:** Investigation. **Armin Ensser:** Investigation. **Alexandra Herrmann:** Investigation. **Anja Vom Hemdt:** Investigation. **Yuriko Tomita:** Investigation. **Shutoku Matsuyama:** Resources. **Takatsugu Hirokawa:** Formal analysis; visualization. **Yiqi Huang:** Investigation. **Antonio Piras:** Investigation. **Constanze A Jakwerth:** Resources. **Madlen Oelsner:** Resources. **Susanne Thieme:** Formal analysis; visualization. **Alexander Graf:** Formal analysis; visualization. **Stefan Krebs:** Resources. **Helmut Blum:** Resources. **Beate M Kümmerer:** Resources. **Alexey Stukalov:** Formal analysis; visualization. **Carsten B Schmidt-Weber:** Resources. **Manabu Igarashi:** Formal analysis; visualization. **Thomas Gramberg:** Resources. **Andreas Pichlmair:** Conceptualization; supervision; funding acquisition; investigation. **Hiroki Kato:** Conceptualization; supervision; funding acquisition; investigation.

In addition to the CRediT author contributions listed above, the contributions in detail are:

HK, APic, and VB conceptualized, supervised, and investigated the study. HK and APic acquired funding. TH, MI, ST, AG, and AS performed formal analysis and visualized the study. SY, YTs, SW, AE, AH, AVH, YTo, VG, TL, KK, M-TM, YH, and APir investigated the study. SM, BMK, TG, CAJ, MO, SK, HB, and CBS-W provided resources.

Disclosure and competing interests statement

VB, VG, and APic are co-inventors on the patent application related to the content of this manuscript.

References

Abbas YM, Laudenbach BT, Martínez-Montero S, Cencic R, Habjan M, Pichlmair A, Damha MJ, Pelletier J, Nagar B (2017) Structure of human IFIT1 with capped RNA reveals adaptable mRNA binding and mechanisms for sensing N1 and N2 ribose 2′-O methylations. *Proc Natl Acad Sci USA* 114: E2106–E2115

Acharya D, Liu G, Gack MU (2020) Dysregulation of type I interferon responses in COVID-19. *Nat Rev Immunol* 20: 397–398

Ahmed-Belkacem R, Sutto-Ortiz P, Guiraud M, Canard B, Vasseur J-J, Decroly E, Debart F (2020) Synthesis of adenine dinucleosides SAM analogs as specific inhibitors of SARS-CoV nsp14 RNA cap guanine-N7-methyltransferase. *Eur J Med Chem* 201: 112557

Alavi Darazam I, Shokouhi S, Pourhoseingholi MA, Naghibi Irvani SS, Mokhtari M, Shabani M, Amirdosara M, Torabinavid P, Golmohammadi M, Hashemi SP *et al* (2021) Role of interferon therapy in severe COVID-19: the COVIFERON randomized controlled trial. *Sci Rep* 11: 8059

Aldahham BJM, Al-Khafaji K, Saleh MY, Abdelhakem AM, Alanazi AM, Islam MA (2020) Identification of naphthyridine and quinoline derivatives as potential Nsp16-Nsp10 inhibitors: a pharmacoinformatics study. *J Biomol Struct Dyn*: 1–8

Aouadi W, Blanjoie A, Vasseur J-J, Debart F, Canard B, Decroly E (2017) Binding of the methyl donor S-adenosyl-l-methionine to middle east respiratory syndrome coronavirus 2′-O-methyltransferase nsp16 promotes recruitment of the allosteric activator nsp10. *J Virol* 91: e02217-16

Arbuckle JH, Gardina PJ, Gordon DN, Hickman HD, Yewdell JW, Pierson TC, Myers TG, Kristie TM (2017) Inhibitors of the histone methyltransferases EZH2/1 induce a potent antiviral state and suppress infection by diverse viral pathogens. *mBio* 8: e01141-17

Aury-Landas J, Girard N, Lhuissier E, Adouane D, Delépée R, Boumediene K, Baugé C (2019) The antitumoral effect of the S-adenosylhomocysteine hydrolase inhibitor, 3-deazaneplanocin A, is independent of EZH2 but is correlated with EGFR downregulation in chondrosarcomas. *Cell Physiol Biochem* 53: 731–745

Barnard DL, Day CW, Bailey K, Heiner M, Montgomery R, Lauridsen L, Chan PKS, Sidwell RW (2006) Evaluation of immunomodulators, interferons and known in vitro SARS-coV inhibitors for inhibition of SARS-coV replication in BALB/c mice. *Antivir Chem Chemother* 17: 275–284

Bélanger F, Stepinski J, Darzynkiewicz E (2010) Characterization of hMTr1, a human Cap1 2′-O-ribose methyltransferase. *J Biol Chem* 285: 33037–33044

Blanco-Melo D, Nilsson-Payant BE, Liu W-C, Uhl S, Hoagland D, Møller R, Jordan TX, Oishi K, Panis M, Sachs D *et al* (2020) Imbalanced host response to SARS-CoV-2 drives development of COVID-19. *Cell* 181: 1036–1045

Bouvet M, Debarnot C, Imbert I, Selisko B, Snijder EJ, Canard B, Decroly E (2010) In vitro reconstitution of SARS-coronavirus mRNA cap methylation. *PLoS Pathog* 6: e1000863

Bouvet M, Imbert I, Subissi L, Gluais L, Canard B, Decroly E (2012) RNA 3’-end mismatch excision by the severe acute respiratory syndrome coronavirus

© 2022 The Authors

nonstructural protein nsp10/nsp14 exoribonuclease complex. *Proc Natl Acad Sci USA* 109: 9372–9377

Bouvet M, Lugari A, Posthuma CC, Zevenhoven JC, Bernard S, Betzi S, Imbert I, Canard B, Guillemot J-C, Lécine P *et al* (2014) Coronavirus Nsp10, a critical co-factor for activation of multiple replicative enzymes. *J Biol Chem* 289: 25783–25796

Bray M, Driscoll J, Huggins JW (2000) Treatment of lethal Ebola virus infection in mice with a single dose of an S-adenosyl-L-homocysteine hydrolase inhibitor. *Antiviral Res* 45: 135–147

Bray M, Raymond JL, Geisbert T, Baker RO (2002) 3-deazaneplanocin A induces massively increased interferon-alpha production in Ebola virus-infected mice. *Antiviral Res* 55: 151–159

Carvalho T, Krammer F, Iwasaki A (2021) The first 12 months of COVID-19: a timeline of immunological insights. *Nat Rev Immunol* 21: 245–256

Chen S, Sheng C, Liu D, Yao C, Gao S, Song L, Jiang W, Li J, Huang W (2013) Enhancer of zeste homolog 2 is a negative regulator of mitochondria-mediated innate immune responses. *J Immunol* 191: 2614–2623

Chen Y, Cai H, Pan J, Xiang N, Tien P, Ahola T, Guo D (2009) Functional screen reveals SARS coronavirus nonstructural protein nsp14 as a novel cap N7 methyltransferase. *Proc Natl Acad Sci USA* 106: 3484–3489

Chen Y, Su C, Ke M, Jin X, Xu L, Zhang Z, Wu A, Sun Y, Yang Z, Tien P *et al* (2011) Biochemical and structural insights into the mechanisms of SARS coronavirus RNA Ribose 2′-O-methylation by nsp16/nsp10 protein complex. *PLoS Pathog* 7: e1002294

Chitalia VC, Munawar AH (2020) A painful lesson from the COVID-19 pandemic: the need for broad-spectrum, host-directed antivirals. *J Transl Med* 18: 390

Chou TC, Talalay P (1984) Quantitative analysis of dose-effect relationships: the combined effects of multiple drugs or enzyme inhibitors. *Adv Enzyme Regul* 22: 27–55

Cingolani P, Platts A, Wang LL, Coon M, Nguyen T, Wang L, Land SJ, Lu X, Ruden DM (2012) A program for annotating and predicting the effects of single nucleotide polymorphisms, SnpEff: SNPs in the genome of *Drosophila melanogaster* strain w1118; iso-2; iso-3. *Fly* 6: 80–92

Collinsova M, Strakova J, Jiracek J, Garrow TA (2006) Inhibition of betaine-homocysteine S-methyltransferase causes hyperhomocysteinemia in mice. *J Nutr* 136: 1493–1497

Corman VM, Eckerle I, Bleicker T, Zaki A, Landt O, Eschbach-Bludau M, van Boheemen S, Gopal R, Ballhause M, Bestebroer TM *et al* (2012) Detection of a novel human coronavirus by real-time reverse-transcription polymerase chain reaction. *Euro Surveill* 17: 20285

Coronaviridae Study Group of the International Committee on Taxonomy of Viruses (2020) The species severe acute respiratory syndrome-related coronavirus: classifying 2019-nCoV and naming it SARS-CoV-2. *Nat Microbiol* 5: 536–544

Daffis S, Szretter KJ, Schriewer J, Li J, Youn S, Errett J, Lin TY, Schneller S, Zust R, Dong H *et al* (2010) 2′-O methylation of the viral mRNA cap evades host restriction by IFIT family members. *Nature* 468: 452–456

De Clercq E, Cools M, Balzarini J, Marquez VE, Borcherding DR, Borchardt RT, Drach JC, Kitaoka S, Konno T (1989) Broad-spectrum antiviral activities of neplanocin A, 3-deazaneplanocin A, and their 5'-nor derivatives. *Antimicrob Agents Chemother* 33: 1291–1297

Decroly E, Imbert I, Coutard B, Bouvet M, Selisko B, Alvarez K, Gorbalenya AE, Snijder EJ, Canard B (2008) Coronavirus nonstructural protein 16 is a cap-0 binding enzyme possessing (nucleoside-2'O)-methyltransferase activity. *J Virol* 82: 8071–8084

De Luca G, Cavalli G, Campochiaro C, Della-Torre E, Angelillo P, Tomelleri A, Boffini N, Tentori S, Mette F, Farina N *et al* (2020) GM-CSF blockade with mavrilimumab in severe COVID-19 pneumonia and systemic hyperinflammation: a single-centre, prospective cohort study. *Lancet Rheumatol* 2: e465–e473

DNA Pipelines R&D, Farr B, Rajan D, Betteridge E, Lesley S, Quail M, Park N, Redshaw N, Bronner IF, Aigrain L *et al* (2020) COVID-19 ARTIC v3 Illumina library construction and sequencing protocol V.5. *protocolos.io.* https://doi.org/10.17504/protocols.io.bibtkann

Duran-Frigola M, Pauls E, Guitart-Pla O, Bertoni M, Alcalde V, Amat D, Juan-Blanco T, Aloy P (2020) Extending the small-molecule similarity principle to all levels of biology with the Chemical Checker. *Nat Biotechnol* 38: 1087–1096

Durinck S, Spellman PT, Birney E, Huber W (2009) Mapping identifiers for the integration of genomic datasets with the R/ Bioconductor package biomaRt. *Nat Protoc* 4: 1184–1191

Feuillet V, Canard B, Trautmann A (2021) Combining antivirals and immunomodulators to fight COVID-19. *Trends Immunol* 42: 31–44

FitzGerald ES, Chen Y, Fitzgerald KA, Jamieson AM (2021) Lung epithelial cell transcriptional regulation as a factor in COVID-19–associated coagulopathies. *Am J Respir Cell Mol Biol* 64: 687–697

Friedman J, Hastie T, Tibshirani R (2010) Regularization paths for generalized linear models via coordinate descent. *Journal of Statistical Software*, 33. https://doi.org/10.18637/jss.v033.i01

Friesner RA, Banks JL, Murphy RB, Halgren TA, Klicic JJ, Mainz DT, Repasky MP, Knoll EH, Shelley M, Perry JK *et al* (2004) Glide: a new approach for rapid, accurate docking and scoring. 1. Method and assessment of docking accuracy. *J Med Chem* 47: 1739–1749

García-Serradilla M, Risco C, Pacheco B (2019) Drug repurposing for new, efficient, broad spectrum antivirals. *Virus Res* 264: 22–31

Gebhardt A, Bergant V, Schnepf D, Moser M, Meiler A, Togbe D, MacKowiak C, Reinert LS, Paludan SR, Ryffel B *et al* (2019) The alternative cap-binding complex is required for antiviral defense in vivo. *PLoS Pathog* 15: e1008155

George PM, Wells AU, Jenkins RG (2020) Pulmonary fibrosis and COVID-19: the potential role for antifibrotic therapy. *Lancet Respir Med* 8: 807–815

Gibbons JS, Khadka S, Williams CG, Wang L, Schneller SW, Liu C, Tufariello JM, Basler CF (2021) Mechanisms of anti-vesicular stomatitis virus activity of deazaneplanocin and its 3-brominated analogs. *Antiviral Research* 191: 105088. https://doi.org/10.1016/j.antiviral.2021.105088

Glazer RI, Hartman KD, Knode MC, Richard MM, Chiang PK, Tseng CK, Marquez VE (1986) 3-Deazaneplanocin: a new and potent inhibitor of S-adenosylhomocysteine hydrolase and its effects on human promyelocytic leukemia cell line HL-60. *Biochem Biophys Res Commun* 135: 688–694

Grage TB, Rochlin DB, Weiss AJ, Wilson WL (1970) Clinical studies with tubercidin administered after absorption into human erythrocytes. *Cancer Res* 30: 79–81

Grubaugh ND, Gangavarapu K, Quick J, Matteson NL, De Jesus JG, Main BJ, Tan AL, Paul LM, Brackney DE, Grewal S *et al* (2019) An amplicon-based sequencing framework for accurately measuring intrahost virus diversity using PrimalSeq and iVar. *Genome Biol* 20: 8

Gupta A, Madhavan MV, Sehgal K, Nair N, Mahajan S, Sehrawat TS, Bikdeli B, Ahluwalia N, Ausiello JC, Wan EY *et al* (2020) Extrapulmonary manifestations of COVID-19. *Nat Med* 26: 1017–1032

Habjan M, Hubel P, Lacerda L, Benda C, Holze C, Eberl CH, Mann A, Kindler E, Gil-Cruz C, Ziebuhr J *et al* (2013) Sequestration by IFIT1 impairs translation of 2'O-unmethylated capped RNA. *PLoS Pathog* 9: e1003663

Hadjadj J, Yatim N, Barnabei L, Corneau A, Boussier J, Smith N, Péré H, Charbit B, Bondet V, Chenevier-Gobeaux C *et al* (2020) Impaired type I interferon activity and inflammatory responses in severe COVID-19 patients. *Science* 369: 718–724

© 2022 The Authors

Halgren TA, Murphy RB, Friesner RA, Beard HS, Frye LL, Pollard WT, Banks JL (2004) Glide: a new approach for rapid, accurate docking and scoring. 2. Enrichment factors in database screening. *J Med Chem* 47: 1750–1759

Hasan T, Arora R, Bansal AK, Bhattacharya R, Sharma GS, Singh LR (2019) Disturbed homocysteine metabolism is associated with cancer. *Exp Mol Med* 51: 1–13

Hoffman DR, Marion DW, Cornatzer WE, Duerre JA (1980) S-Adenosylmethionine and S-adenosylhomocystein metabolism in isolated rat liver. Effects of L-methionine, L-homocystein, and adenosine. *J Biol Chem* 255: 10822–10827

Jha PK, Vijay A, Halu A, Uchida S, Aikawa M (2021) Gene expression profiling reveals the shared and distinct transcriptional signatures in human lung epithelial cells infected with SARS-CoV-2, MERS-CoV, or SARS-CoV: potential implications in cardiovascular complications of COVID-19. *Front Cardiovasc Med* 7: 623012

Jiracek J, Collinsova M, Rosenberg I, Budesinsky M, Protivinska E, Netusilova H, Garrow TA (2006) S-alkylated homocysteine derivatives: new inhibitors of human betaine-homocysteine S-methyltransferase. *J Med Chem* 49: 3982–3989

Katoh K, Standley DM (2013) MAFFT multiple sequence alignment software version 7: improvements in performance and usability. *Mol Biol Evol* 30: 772–780

Kaufmann SHE, Dorhoi A, Hotchkiss RS, Bartenschlager R (2018) Host-directed therapies for bacterial and viral infections. *Nat Rev Drug Discov* 17: 35–56

Kawase M, Shirato K, van der Hoek L, Taguchi F, Matsuyama S (2012) Simultaneous treatment of human bronchial epithelial cells with serine and cysteine protease inhibitors prevents severe acute respiratory syndrome coronavirus entry. *J Virol* 86: 6537–6545

Knutson SK, Kawano S, Minoshima Y, Warholic NM, Huang K-C, Xiao Y, Kadowaki T, Uesugi M, Kuznetsov G, Kumar N *et al* (2014) Selective inhibition of EZH2 by EPZ-6438 leads to potent antitumor activity in EZH2-mutant non-Hodgkin lymphoma. *Mol Cancer Ther* 13: 842–854

Konteatis Z, Travins J, Gross S, Marjon K, Barnett A, Mandley E, Nicolay B, Nagaraja R, Chen Y, Sun Y *et al* (2021) Discovery of AG-270, a first-in-class oral MAT2A inhibitor for the treatment of tumors with homozygous MTAP deletion. *J Med Chem* 64: 4430–4449

Krafcikova P, Silhan J, Nencka R, Boura E (2020) Structural analysis of the SARS-CoV-2 methyltransferase complex involved in RNA cap creation bound to sinefungin. *Nat Commun* 11: 3717

Kumar R, Khandelwal N, Chander Y, Nagori H, Verma A, Barua A, Godara B, Pal Y, Gulati BR, Tripathi BN *et al* (2022) S-adenosylmethionine-dependent methyltransferase inhibitor DZNep blocks transcription and translation of SARS-CoV-2 genome with a low tendency to select for drug-resistant viral variants. *Antiviral Res* 197: 105232

Kümmerer BM, Rice CM (2002) Mutations in the yellow fever virus nonstructural protein NS2A selectively block production of infectious particles. *J Virol* 76: 4773–4784

Lainšček D, Fink T, Forstnerič V, Hafner-Bratkovič I, Orehek S, Strmšek Ž, Manček-Keber M, Pečan P, Esih H, Malenšek Š *et al* (2021) A nanoscaffolded spike-RBD vaccine provides protection against SARS-CoV-2 with minimal anti-scaffold response. *Vaccines (Basel)* 9: 431

Lee JD, Sun DL, Sun Y, Taylor JE (2013) Exact post-selection inference, with application to the lasso. *Ann Stat* 44: 907–927

Leisman DE, Ronner L, Pinotti R, Taylor MD, Sinha P, Calfee CS, Hirayama AV, Mastroiani F, Turtle CJ, Harhay MO *et al* (2020) Cytokine elevation in severe and critical COVID-19: a rapid systematic review, meta-analysis, and comparison with other inflammatory syndromes. *Lancet Respir Med* 8: 1233–1244

Li H (2013) Aligning sequence reads, clone sequences and assembly contigs with BWA-MEM. *arXiv* https://doi.org/10.48550/arXiv.1303.3997 [PREPRINT]

Li H, Handsaker B, Wysoker A, Fennell T, Ruan J, Homer N, Marth G, Abecasis G, Durbin R (2009) The sequence Alignment/Map format and SAMtools. *Bioinformatics* 25: 2078–2079

Lokugamage KG, Hage A, de Vries M, Valero-Jimenez AM, Schindewolf C, Dittmann M, Rajsbaum R, Menachery VD (2020) Type I interferon susceptibility distinguishes SARS-CoV-2 from SARS-CoV. *J Virol* 94: e01410-20

Loong KT (2013) EZH2 mediates resistance to apoptosis in Nktl by activating Nfkb signaling through repression of TNFAIP3/A20 by H3K27 trimethylation. *Blood* 122: 1278

Mantlo E, Bukreyeva N, Maruyama J, Paessler S, Huang C (2020) Antiviral activities of type I interferons to SARS-CoV-2 infection. *Antiviral Res* 179: 104811

Markland W, McQuaid TJ, Jain J, Kwong AD (2000) Broad-spectrum antiviral activity of the IMP dehydrogenase inhibitor VX-497: a comparison with ribavirin and demonstration of antiviral additivity with alpha interferon. *Antimicrob Agents Chemother* 44: 859–866

Matsuyama S, Kawase M, Nao N, Shirato K, Ujike M, Kamitani W, Shimojima M, Fukushi S (2020) The inhaled steroid ciclesonide blocks SARS-CoV-2 RNA replication by targeting the viral replication-transcription complex in cultured cells. *J Virol* 95: e01648-20

Ma Y, Wu L, Shaw N, Gao Y, Wang J, Sun Y, Lou Z, Yan L, Zhang R, Rao Z (2015) Structural basis and functional analysis of the SARS coronavirus nsp14-nsp10 complex. *Proc Natl Acad Sci USA* 112: 9436–9441

Menachery VD, Gralinski LE, Mitchell HD, Dinnon KH, Leist SR, Yount BL, Graham RL, McAnarney ET, Stratton KG, Cockrell AS *et al* (2017) Middle east respiratory syndrome coronavirus nonstructural protein 16 is necessary for interferon resistance and viral pathogenesis. *mSphere* 2: e00346-17

Menachery VD, Yount BL Jr, Josset L, Gralinski LE, Scobey T, Agnihothram S, Katze MG, Baric RS (2014) Attenuation and restoration of severe acute respiratory syndrome coronavirus mutant lacking 2’-o-methyltransferase activity. *J Virol* 88: 4251–4264

Mercer PF, Chambers RC (2013) Coagulation and coagulation signalling in fibrosis. *Biochim Biophys Acta* 1832: 1018–1027

Mimura I, Hirakawa Y, Kanki Y, Nakaki R, Suzuki Y, Tanaka T, Aburatani H, Nangaku M (2018) Genome-wide analysis revealed that DZNep reduces tubulointerstitial fibrosis via down-regulation of pro-fibrotic genes. *Sci Rep* 8: 3779

Minh BQ, Schmidt HA, Chernomor O, Schrempf D, Woodhams MD, von Haeseler A, Lanfear R (2020) IQ-TREE 2: New Models and Efficient Methods for Phylogenetic Inference in the Genomic Era. *Mol Biol Evol* 37: 1530–1534

Miorin L, Kehrer T, Sanchez-Aparicio MT, Zhang K, Cohen P, Patel RS, Cupic A, Makio T, Mei M, Moreno E *et al* (2020) SARS-CoV-2 Orf6 hijacks Nup98 to block STAT nuclear import and antagonize interferon signaling. *Proc Natl Acad Sci USA* 117: 28344–28354

Miranda TB, Cortez CC, Yoo CB, Liang G, Abe M, Kelly TK, Marquez VE, Jones PA (2009) DZNep is a global histone methylation inhibitor that reactivates developmental genes not silenced by DNA methylation. *Mol Cancer Ther* 8: 1579–1588

Mlcochova P, Kemp SA, Dhar MS, Papa G, Meng B, Ferreira IATM, Datir R, Collier DA, Albecka A, Singh S *et al* (2021) SARS-CoV-2 B.1.617.2 Delta variant replication and immune evasion. *Nature* 599: 114–119

Morel KL, Sheahan AV, Burkhart DL, Baca SC, Boufaied N, Liu Y, Qiu X, Cañadas I, Roehle K, Heckler M *et al* (2021) EZH2 inhibition activates a dsRNA–STING–interferon stress axis that potentiates response to PD-1 checkpoint blockade in prostate cancer. *Nat Cancer* 2: 444–456

Muthukrishnan S, Moss B, Cooper JA, Maxwell ES (1978) Influence of 5'-terminal cap structure on the initiation of translation of vaccinia virus mRNA. *J Biol Chem* 253: 1710–1715

Olsen DB, Eldrup AB, Bartholomew L, Bhat B, Bosserman MR, Ceccacci A, Colwell LF, Fay JF, Flores OA, Getty KL *et al* (2004) A 7-deaza-adenosine analog is a potent and selective inhibitor of hepatitis C virus replication with excellent pharmacokinetic properties. *Antimicrob Agents Chemother* 48: 3944–3953

O'Sullivan JM, Gonagle DM, Ward SE, Preston RJS, O'Donnell JS (2020) Endothelial cells orchestrate COVID-19 coagulopathy. *Lancet Haematol* 7: e553–e555

Koenig P-A, Das H, Liu H, Kümmerer BM, Gohr FN, Jenster L-M, Schiffelers LDJ, Tesfamariam YM, Uchima M, Wuerth JD *et al* (2021) Structure-guided multivalent nanobodies block SARS-CoV-2 infection and suppress mutational escape. *Science* 371: eabe6230

Peer CJ, Rao M, Spencer SD, Shahbazi S, Steeg PS, Schrump DS, Figg WD (2013) A rapid ultra HPLC-MS/MS method for the quantitation and pharmacokinetic analysis of 3-deazaneplanocin A in mice. *J Chromatogr B Analyt Technol Biomed Life Sci* 927: 142–146

Perez-Riverol Y, Bai J, Bandla C, Hewapathirana S, García-Seisdedos D, Kamatchinathan S, Kundu D, Prakash A, Frericks-Zipper A, Eisenacher M *et al* (2022) The PRIDE database resources in 2022: A Hub for mass spectrometry-based proteomics evidences. *Nucleic Acids Res* 50: D543–D552

Pfefferle S, Krähling V, Ditt V, Grywna K, Mühlberger E, Drosten C (2009) Reverse genetic characterization of the natural genomic deletion in SARS-Coronavirus strain Frankfurt-1 open reading frame 7b reveals an attenuating function of the 7b protein in-vitro and in-vivo. *Virol J* 6: 131

Quinlan CL, Kaiser SE, Bolaños B, Nowlin D, Grantner R, Karlicek-Bryant S, Feng JL, Jenkinson S, Freeman-Cook K, Dann SG *et al* (2017) Targeting S-adenosylmethionine biosynthesis with a novel allosteric inhibitor of Mat2A. *Nat Chem Biol* 13: 785–792

REMAP-CAP Investigators (2021) Interleukin-6 receptor antagonists in critically ill patients with Covid-19. *N Engl J Med* 384: 1491–1502

Rosas-Lemus M, Minasov G, Shuvalova L, Inniss NL, Kiryukhina O, Brunzelle J, Satchell KJF (2020) High-resolution structures of the SARS-CoV-2 2'-O-methyltransferase reveal strategies for structure-based inhibitor design. *Sci Signal* 13: eabe1202

Sanjana NE, Shalem O, Zhang F (2014) Improved vectors and genome-wide libraries for CRISPR screening. *Nat Methods* 11: 783–784

Sasaki M, Uemura K, Sato A, Toba S, Sanaki T, Maenaka K, Hall WW, Orba Y, Sawa H (2021) SARS-CoV-2 variants with mutations at the S1/S2 cleavage site are generated in vitro during propagation in TMPRSS2-deficient cells. *PLoS Pathog* 17: e1009233

Schanche JS, Schanche T, Ueland PM, Holý A, Votruba I (1984) The effect of aliphatic adenine analogues on S-adenosylhomocysteine and S-adenosylhomocysteine hydrolase in intact rat hepatocytes. *Mol Pharmacol* 26: 553–558

Schuberth-Wagner C, Ludwig J, Bruder AK, Herzner A-M, Zillinger T, Goldeck M, Schmidt T, Schmid-Burgk JL, Kerber R, Wolter S *et al* (2015) A conserved histidine in the RNA sensor RIG-I controls immune tolerance to N1-2'O-methylated self RNA. *Immunity* 43: 41–51

Schultz DC, Johnson RM, Ayyanathan K, Miller J, Whig K, Kamalia B, Dittmar M, Weston S, Hammond HL, Dillen C *et al* (2022) Pyrimidine inhibitors synergize with nucleoside analogues to block SARS-CoV-2. *Nature* 604: 134–140

Shannon A, Le NT-T, Selisko B, Eydoux C, Alvarez K, Guillemot J-C, Decroly E, Peersen O, Ferron F, Canard B (2020) Remdesivir and SARS-CoV-2: structural requirements at both nsp12 RdRp and nsp14 Exonuclease active-sites. *Antiviral Res* 178: 104793

Simon N, Friedman J, Hastie T, Tibshirani R (2011) Regularization paths for Cox's proportional hazards model via coordinate descent. *Journal of Statistical Software*, 39. https://doi.org/10.18637/jss.v039.i05

Strakova J, Gupta S, Kruger WD, Dilger RN, Tryon K, Li L, Garrow TA (2011) Inhibition of betaine-homocysteine S-methyltransferase in rats causes hyperhomocysteinemia and reduces liver cystathionine β-synthase activity and methylation capacity. *Nutr Res* 31: 563–571

Stukalov A, Girault V, Grass V, Karayel O, Bergant V, Urban C, Haas DA, Huang Y, Oubraham L, Wang A *et al* (2021) Multilevel proteomics reveals host perturbations by SARS-CoV-2 and SARS-CoV. *Nature* 594: 246–252

Sun F, Lee L, Zhang Z, Wang X, Yu Q, Duan X, Chan E (2015) Preclinical pharmacokinetic studies of 3-deazaneplanocin A, a potent epigenetic anticancer agent, and its human pharmacokinetic prediction using GastroPlus^{TM}. *Eur J Pharm Sci* 77: 290–302

Sun F, Li J, Yu Q, Chan E (2012) Loading 3-deazaneplanocin A into pegylated unilamellar liposomes by forming transient phenylboronic acid-drug complex and its pharmacokinetic features in Sprague-Dawley rats. *Eur J Pharm Biopharm* 80: 323–331

Sviripa VM, Zhang W, Balia AG, Tsodikov OV, Nickell JR, Gizard F, Yu T, Lee EY, Dwoskin LP, Liu C *et al* (2014) 2',6'-Dihalostyrylanilines, pyridines, and pyrimidines for the inhibition of the catalytic subunit of methionine S-adenosyltransferase-2. *J Med Chem* 57: 6083–6091

Szemiel AM, Merits A, Orton RJ, MacLean OA, Pinto RM, Wickenhagen A, Lieber G, Turnbull ML, Wang S, Furnon W *et al* (2021) In vitro selection of Remdesivir resistance suggests evolutionary predictability of SARS-CoV-2. *PLoS Pathog* 17: e1009929

Tan J, Yang X, Zhuang L, Jiang X, Chen W, Lee PL, Karuturi RKM, Tan PBO, Liu ET, Yu Q (2007) Pharmacologic disruption of Polycomb-repressive complex 2-mediated gene repression selectively induces apoptosis in cancer cells. *Genes Dev* 21: 1050–1063

The RECOVERY Collaborative Group (2021) Dexamethasone in hospitalized patients with Covid-19. *N Engl J Med* 384: 693–704

Thi Nhu Thao T, Labroussaa F, Ebert N, V'kovski P, Stalder H, Portmann J, Kelly J, Steiner S, Holwerda M, Kratzel A *et al* (2020) Rapid reconstruction of SARS-CoV-2 using a synthetic genomics platform. *Nature* 582: 561–565

Tiffen J, Gallagher SJ, Filipp F, Gunatilake D, Emran AA, Cullinane C, Dutton-Register K, Aoude L, Hayward N, Chatterjee A *et al* (2020) EZH2 cooperates with DNA methylation to downregulate key tumor suppressors and IFN gene signatures in melanoma. *J Invest Dermatol* 140: 2442–2454

Tseng CK, Marquez VE, Fuller RW, Goldstein BM, Haines DR, McPherson H, Parsons JL, Shannon WM, Arnett G, Hollingshead M (1989) Synthesis of 3-deazaneplanocin A, a powerful inhibitor of S-adenosylhomocysteine hydrolase with potent and selective in vitro and in vivo antiviral activities. *J Med Chem* 32: 1442–1446

Tyanova S, Temu T, Sinitcyn P, Carlson A, Hein MY, Geiger T, Mann M, Cox J (2016) The Perseus computational platform for comprehensive analysis of (prote)omics data. *Nat Methods* 13: 731–740

Uchiyama N, Dougan DR, Lawson JD, Kimura H, Matsumoto S-I, Tanaka Y, Kawamoto T (2017) Identification of AHCY inhibitors using novel high-throughput mass spectrometry. *Biochem Biophys Res Commun* 491: 1–7

Varga Z, Flammer AJ, Steiger P, Haberecker M, Andermatt R, Zinkernagel AS, Mehra MR, Schuepbach RA, Ruschitzka F, Moch H (2020) Endothelial cell infection and endotheliitis in COVID-19. *Lancet* 395: 1417–1418

© 2022 The Authors

Vijayan V, Pant P, Vikram N, Kaur P, Singh TP, Sharma S, Sharma P (2020) Identification of promising drug candidates against NSP16 of SARS-CoV-2 through computational drug repurposing study. *J Biomol Struct Dyn* 39: 6713–6727

Vittori S, Dal Ben D, Lambertucci C, Marucci G, Volpini R, Cristalli G (2006) Antiviral properties of deazaadenine nucleoside derivatives. *Curr Med Chem* 13: 3529–3552

Wee ZN, Li Z, Lee PL, Lee ST, Lim YP, Yu Q (2014) EZH2-mediated inactivation of IFN-γ-JAK-STAT1 signaling is an effective therapeutic target in MYC-driven prostate cancer. *Cell Rep* 8: 204–216

Welm BE, Dijkgraaf GJP, Bledau AS, Welm AL, Werb Z (2008) Lentiviral transduction of mammary stem cells for analysis of gene function during development and cancer. *Cell Stem Cell* 2: 90–102

Whelan SP, Ball LA, Barr JN, Wertz GT (1995) Efficient recovery of infectious vesicular stomatitis virus entirely from cDNA clones. *Proc Natl Acad Sci USA* 92: 8388–8392

Williams GD, Gokhale NS, Snider DL, Horner SM (2020) The mRNA Cap 2'-O-Methyltransferase CMTR1 Regulates the Expression of Certain Interferon-Stimulated Genes. *mSphere* 5: e00202-20

Wu G, Dawson E, Duong A, Haw R, Stein L (2014) ReactomeFIViz: a Cytoscape app for pathway and network-based data analysis. *F1000Res* 3: 146

Xiao X, Senavirathna LK, Gou X, Huang C, Liang Y, Liu L (2016) EZH2 enhances the differentiation of fibroblasts into myofibroblasts in idiopathic pulmonary fibrosis. *Physiol Rep* 4: e12915

Yang WS, Kim JH, Jeong D, Hong YH, Park SH, Yang Y, Jang Y-J, Kim J-H, Cho JY (2020) 3-Deazaadenosine, an S-adenosylhomocysteine hydrolase inhibitor, attenuates lipopolysaccharide-induced inflammatory responses via inhibition of AP-1 and NF-κB signaling. *Biochem Pharmacol* 182: 114264

Yan L, Yang Y, Li M, Zhang Y, Zheng L, Ge J, Huang YC, Liu Z, Wang T, Gao S *et al* (2021) Coupling of N7-methyltransferase and 3′-5′ exoribonuclease with SARS-CoV-2 polymerase reveals mechanisms for capping and proofreading. *Cell* 184: 3474–3485

Konteatis ZD, Sui Z, Travins JM, Zhixiong YE (2018) Inhibitors of cellular metabolic processes. World Patent

Zeybel M, Luli S, Sabater L, Hardy T, Oakley F, Leslie J, Page A, Moran Salvador E, Sharkey V, Tsukamoto H *et al* (2017) A proof-of-concept for epigenetic therapy of tissue fibrosis: inhibition of liver fibrosis progression by 3-deazaneplanocin A. *Mol Ther* 25: 218–231

Zhang W, Sviripa V, Chen X, Shi J, Yu T, Hamza A, Ward ND, Kril LM, Vander Kooi CW, Zhan C-G *et al* (2013) Fluorinated N,N-dialkylaminostilbenes repress colon cancer by targeting methionine S-adenosyltransferase 2A. *ACS Chem Biol* 8: 796–803

Zhou Y, Ray D, Zhao Y, Dong H, Ren S, Li Z, Guo Y, Bernard KA, Shi P-Y, Li H (2007) Structure and function of Flavivirus NS5 methyltransferase. *J Virol* 81: 3891–3903

Zissler UM, Chaker AM, Effner R, Ulrich M, Guerth F, Piontek G, Dietz K, Regn M, Knapp B, Theis FJ *et al* (2016) Interleukin-4 and interferon-γ orchestrate an epithelial polarization in the airways. *Mucosal Immunol* 9: 917–926

Züst R, Cervantes-Barragan L, Habjan M, Maier R, Neuman BW, Ziebuhr J, Szretter KJ, Baker SC, Barchet W, Diamond MS *et al* (2011) Ribose 2′-O-methylation provides a molecular signature for the distinction of self and non-self mRNA dependent on the RNA sensor Mda5. *Nat Immunol* 12: 137–143

License: This is an open access article under the terms of the Creative Commons Attribution License, which permits use, distribution and reproduction in any medium, provided the original work is properly cited.

Multilevel proteomics reveals host perturbations by SARS-CoV-2 and SARS-CoV

https://doi.org/10.1038/s41586-021-03493-4

Received: 12 June 2020

Accepted: 25 March 2021

Published online: 12 April 2021

Check for updates

Alexey Stukalov[1,15], Virginie Girault[1,15], Vincent Grass[1,15], Ozge Karayel[2,15], Valter Bergant[1,15], Christian Urban[1,15], Darya A. Haas[1,15], Yiqi Huang[1,15], Lila Oubraham[1], Anqi Wang[1], M. Sabri Hamad[1], Antonio Piras[1], Fynn M. Hansen[2], Maria C. Tanzer[2], Igor Paron[2], Luca Zinzula[3], Thomas Engleitner[4], Maria Reinecke[5,6,7], Teresa M. Lavacca[1], Rosina Ehmann[8,9], Roman Wölfel[8,9], Jörg Jores[10], Bernhard Kuster[5,6,7], Ulrike Protzer[1,9], Roland Rad[4], John Ziebuhr[11], Volker Thiel[12,13], Pietro Scaturro[1,14], Matthias Mann[2] & Andreas Pichlmair[1,9] ✉

The emergence and global spread of SARS-CoV-2 has resulted in the urgent need for an in-depth understanding of molecular functions of viral proteins and their interactions with the host proteome. Several individual omics studies have extended our knowledge of COVID-19 pathophysiology[1–10]. Integration of such datasets to obtain a holistic view of virus–host interactions and to define the pathogenic properties of SARS-CoV-2 is limited by the heterogeneity of the experimental systems. Here we report a concurrent multi-omics study of SARS-CoV-2 and SARS-CoV. Using state-of-the-art proteomics, we profiled the interactomes of both viruses, as well as their influence on the transcriptome, proteome, ubiquitinome and phosphoproteome of a lung-derived human cell line. Projecting these data onto the global network of cellular interactions revealed crosstalk between the perturbations taking place upon infection with SARS-CoV-2 and SARS-CoV at different levels and enabled identification of distinct and common molecular mechanisms of these closely related coronaviruses. The TGF-β pathway, known for its involvement in tissue fibrosis, was specifically dysregulated by SARS-CoV-2 ORF8 and autophagy was specifically dysregulated by SARS-CoV-2 ORF3. The extensive dataset (available at https://covinet.innatelab.org) highlights many hotspots that could be targeted by existing drugs and may be used to guide rational design of virus- and host-directed therapies, which we exemplify by identifying inhibitors of kinases and matrix metalloproteases with potent antiviral effects against SARS-CoV-2.

To identify protein–protein interactions of SARS-CoV-2 and SARS-CoV and cellular proteins, we transduced A549 lung carcinoma cells with lentiviruses expressing individual haemagglutinin-tagged viral proteins (Fig. 1a, Extended Data Fig. 1a, Supplementary Table 1). Statistical modelling of quantitative data from affinity purification followed by mass spectrometry (AP–MS) analysis identified 1,801 interactions between 1,086 cellular proteins and 24 SARS-CoV-2 and 27 SARS-CoV bait proteins (Fig. 1b, Extended Data Fig. 1b, Supplementary Table 2), substantially increasing the number of reported interactions of SARS-CoV-2 and SARS-CoV[1,2,5,6,10,11] (Supplementary Table 10). The resulting virus–host interaction network revealed a wide range of cellular activities intercepted by SARS-CoV-2 and SARS-CoV (Fig. 1b, Extended Data Table 1, Supplementary Table 2). In particular, we observed that SARS-CoV-2 targets a number of key innate immunity regulators (ORF7b–MAVS and ORF7b–UNC93B1), stress response components (N–HSPA1A) and DNA damage response mediators (ORF7a–ATM and ORF7a–ATR) (Fig. 1b, Extended Data Fig. 1c–e). Additionally, SARS-CoV-2 proteins interact with molecular complexes involved in intracellular trafficking (for example, endoplasmic reticulum–Golgi trafficking) and transport (for example, solute carriers and ion transport by ATPases) as well as cellular metabolism (for example, mitochondrial respiratory chain and glycolysis) (Fig. 1b, Extended Data Table 1, Supplementary Table 2). Comparing the AP–MS data of homologous SARS-CoV-2 and SARS-CoV proteins identified differences in the enrichment of individual host targets, highlighting potential virus-specific interactions (Fig. 1b (edge colour), c, Extended Data Figs. 1f, 2a, b, Supplementary Table 2). For instance, we recapitulated the known interactions between SARS-CoV NSP2 and prohibitins[12] (PHB and PHB2), but this interaction was not

---

[1]Technical University of Munich, School of Medicine, Institute of Virology, Munich, Germany. [2]Department of Proteomics and Signal Transduction, Max-Planck Institute of Biochemistry, Martinsried, Germany. [3]Department of Molecular Structural Biology, Max-Planck Institute of Biochemistry, Martinsried, Germany. [4]Institute of Molecular Oncology and Functional Genomics and Department of Medicine II, School of Medicine, Technical University of Munich, Munich, Germany. [5]Chair of Proteomics and Bioanalytics, Technical University of Munich, Freising, Germany. [6]German Cancer Consortium (DKTK), Munich Partner Site, Munich, Germany. [7]German Cancer Research Center (DKFZ), Heidelberg, Germany. [8]Bundeswehr Institute of Microbiology, Munich, Germany. [9]German Center for Infection Research (DZIF), Munich Partner Site, Munich, Germany. [10]Institute of Veterinary Bacteriology, Department of Infectious Diseases and Pathobiology, University of Bern, Bern, Switzerland. [11]Justus Liebig University Giessen, Institute of Medical Virology, Giessen, Germany. [12]Institute of Virology and Immunology (IVI), Bern, Switzerland. [13]Department of Infectious Diseases and Pathobiology, University of Bern, Bern, Switzerland. [14]Leibniz Institute for Experimental Virology, Hamburg, Germany. [15]These authors contributed equally: Alexey Stukalov, Virginie Girault, Vincent Grass, Ozge Karayel, Valter Bergant, Christian Urban, Darya A. Haas, Yiqi Huang. ✉e-mail: andreas.pichlmair@tum.de

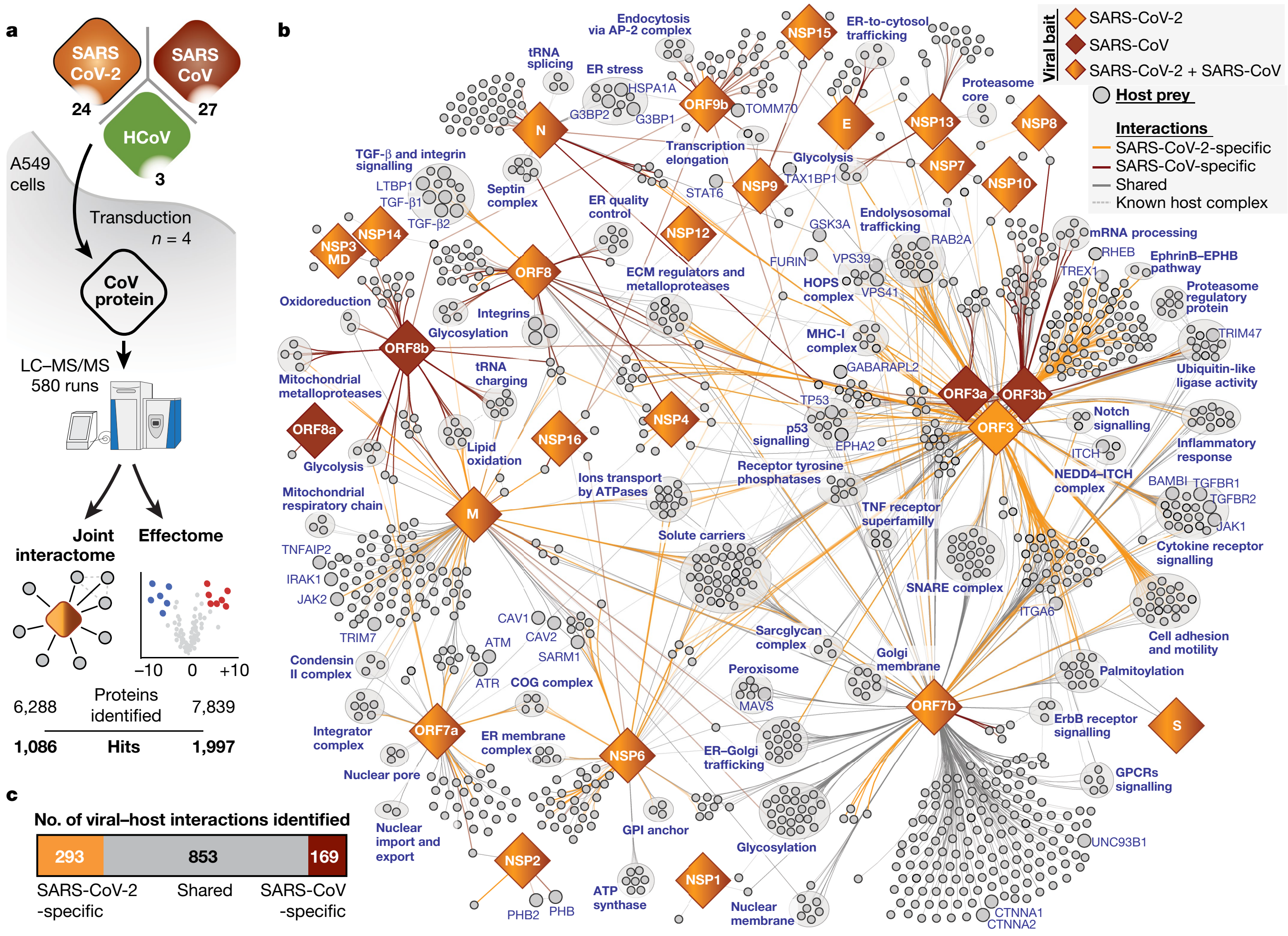

Fig. 1 | Joint analysis of SARS-CoV-2 and SARS-CoV virus–host protein–protein interactomes. a, Systematic comparison of interactomes and host proteome changes (effectomes) of the 24 SARS-CoV-2 and 27 SARS-CoV viral proteins, using 3 homologues from human coronaviruses (HCoV-NL63 and HCoV-229E) as reference for pan-coronavirus specificity. **b**, Combined virus–host protein-interaction network of SARS-CoV-2 and SARS-CoV measured by AP–MS. Homologous viral proteins are displayed as a single node. Shared and virus-specific interactions are denoted by the edge colour. The edge intensity reflects the *P*-value for the interaction (with the smallest *P*-value represented by solid edges and the highest *P*-value (<0.001) represented by faded edges). ECM, extracellular matrix; ER, endoplasmic reticulum; GPCR, G-protein-coupled receptor; HOPS, homotypic fusion and protein-sorting; MHC, major histocompatibility complex; SNARE, soluble *N*-ethylmaleimide-sensitive factor attachment protein receptor; COG, conserved oligomeric Golgi. **c**, The numbers of unique and shared host interactions between the homologous proteins of SARS-CoV-2 and SARS-CoV.

conserved with SARS-CoV-2 NSP2, suggesting that the two viruses differ in their ability to modulate mitochondrial function and homeostasis through NSP2 (Extended Data Fig. 2a). The exclusive interaction of SARS-CoV-2 ORF8 with the TGF-β1–LTBP1 complex is another interaction that potentially explains the differences in pathogenicity of the two viruses (Extended Data Figs. 1f, 2b). Notably, disbalanced TGF-β signalling has been linked to lung fibrosis and oedema, a common complication of severe pulmonary diseases including COVID-19[13–16].

To map the virus–host interactions to the functions of viral proteins, we conducted a study of total proteomes of A549 cells expressing 54 individual viral proteins comprising the 'effectome' (Fig. 1a, Supplementary Table 3). This dataset provides clear links between changes in protein expression and virus–host interactions, as exemplified by ORF9b, which leads to a dysregulation of mitochondrial functions and binds to TOMM70, a known regulator of mitophagy[2,17] (Fig. 1b, Supplementary Tables 2, 3). Global pathway-enrichment analysis of the effectome dataset confirmed that ORF9b of both viruses led to mitochondrial dysregulation[2,18] (Extended Data Fig. 2c, Supplementary Table 3) and further highlighted virus-specific effects, as exemplified by the upregulation of proteins involved in cholesterol metabolism (CYP51A1, DHCR7, IDI1 and SQLE) by SARS-CoV-2 NSP6 but not by SARS-CoV NSP6. Of note, cholesterol metabolism was recently shown to be implicated in SARS-CoV-2 replication and has been suggested as a promising target for drug development[19–21]. Besides perturbations at the pathway level, viral proteins also specifically modulated single host proteins, possibly explaining more specific molecular mechanisms involved in viral protein function. Focusing on the 180 most affected host proteins, we identified RCOR3, a putative transcriptional corepressor, as strongly upregulated by NSP4 of both viruses (Extended Data Figs. 2d, 3a). Notably, apolipoprotein B (APOB) was substantially regulated by ORF3 and NSP1 of SARS-CoV-2, suggesting that it has an important role in SARS-CoV-2 biology (Extended Data Fig. 3b).

Multi-omics profiling of virus infection

Although the interactome and the effectome provide in-depth information on the activity of individual viral proteins, we aimed to directly study their combined activities in the context of viral infection. To this end, we infected A549 cells expressing angiotensin-converting enzyme 2 (ACE2) (A549-ACE2 cells) (Extended Data Fig. 4a, b) with SARS-CoV-2

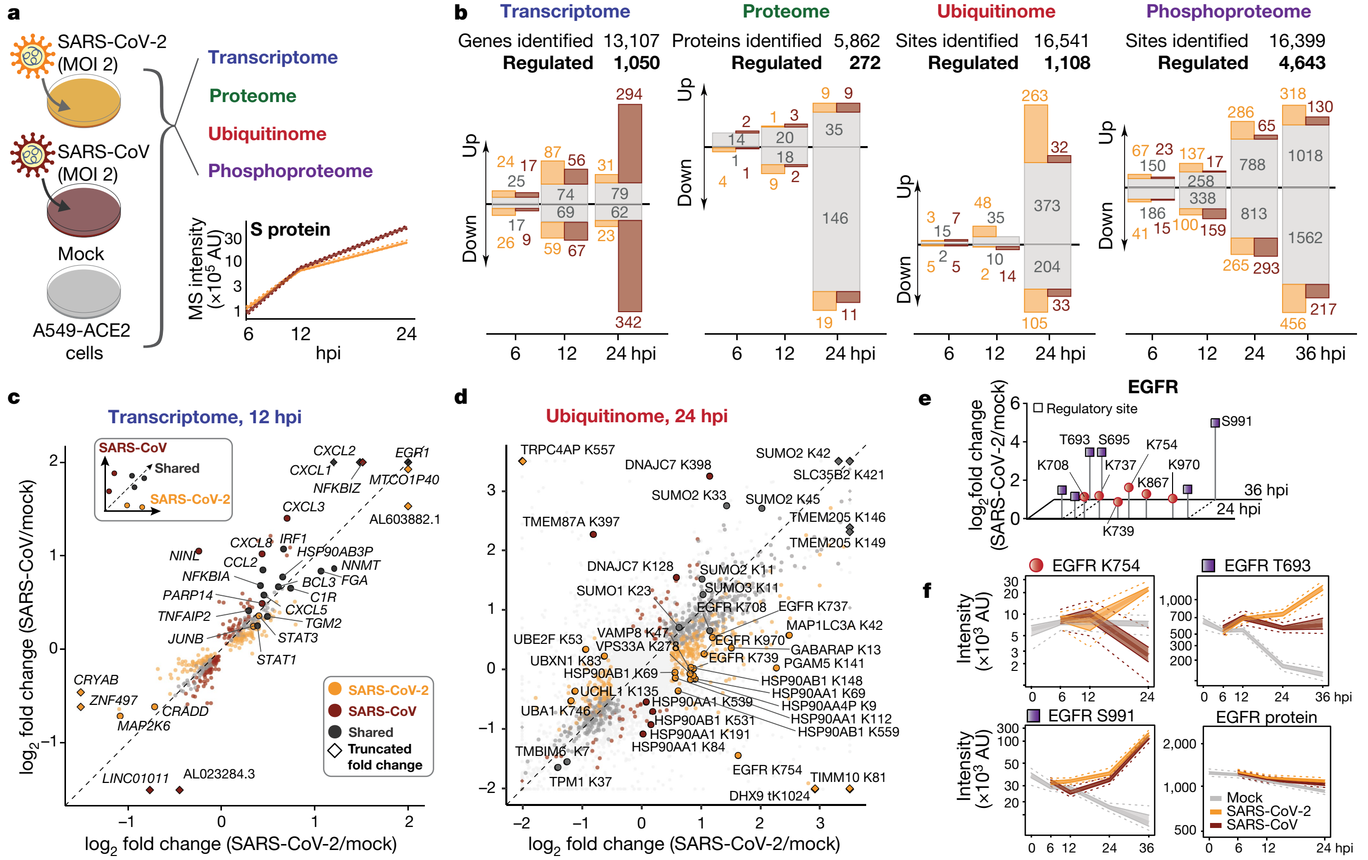

Fig. 2 | Multi-level profiling of SARS-CoV-2 and SARS-CoV infection. **a**, Time-resolved profiling of parallel SARS-CoV-2 and SARS-CoV infection by multiple omics methods. The plot shows the mass spectroscopy (MS) intensity estimates for spike proteins of SARS-CoV-2 and SARS-CoV over time ($n = 4$ independent experiments). MOI, multiplicity of infection. **b**, The numbers of distinct transcripts, proteins, ubiquitination and phosphorylation sites that are significantly up- or downregulated at given time points after infection (relative to mock infection at the same time point). Transcripts, proteins or sites that are regulated similarly by SARS-CoV-2 and SARS-CoV infection are shown in grey, those regulated specifically by SARS-CoV-2 are in orange and those regulated by SARS-CoV are in brown. **c**, **d**, Comparison of host transcriptome 12 h (**c**) and ubiquitinome 24 h (**d**) after infection (hpi) with SARS-CoV-2 (*x*-axis) or SARS-CoV (*y*-axis) (log$_2$ fold change in comparison to the mock infection samples at the same time point). Significantly regulated transcripts by moderated *t*-test with false discovery rate-corrected two-sided *P*-value ≤0.05 (**c**) and significantly regulated sites by Bayesian linear model-based unadjusted two-sided *P*-value $\leq 10^{-3}$, |log$_2$ fold change| ≥0.5 (**d**) are coloured according to specificity as indicated. Diamonds indicate that the actual log$_2$ fold change was truncated to fit into the plot. $n = 3$ independent experiments. **e**, Phosphorylation (purple squares) and ubiquitination (red circles) sites on EGFR that are regulated upon SARS-CoV-2 infection. The plot shows median log$_2$ fold change of abundance compared with mock infection at 24 and 36 hpi. All identified phosphorylation sites have known regulatory function. **f**, Profile plots of time-resolved EGFR K754 ubiquitination, EGFR T693 and S991 phosphorylation, and total EGFR protein levels in A549-ACE2 cells infected with SARS-CoV-2 or SARS-CoV with indicated median (line), 50% (shaded region) and 95% (dotted line) confidence intervals. $n = 3$ (ubiquitination) or 4 (phosphorylation and total protein) independent experiments.

or SARS-CoV, and profiled the effects of viral infection on mRNA expression, protein abundance, ubiquitination and phosphorylation in a time-resolved manner (Fig. 2a-b).

In line with previous reports[9,22], we found that both SARS-CoV-2 and SARS-CoV can downregulate the type I interferon response and activate a pro-inflammatory signature at transcriptome and proteome levels (Fig. 2a–c, Extended Data Fig. 4c–f, i, Supplementary Tables 4, 8, Supplementary Discussion 1). However, SARS-CoV elicited a more pronounced activation of the NF-κB pathway, correlating with its higher replication rate and potentially explaining the lower severity of pulmonary disease in cases of SARS-CoV-2 infection[23] (Supplementary Tables 4, 5). By contrast, SARS-CoV-2 infection led to higher expression of FN1 and SERPINE1, which may be linked to the specific recruitment of TGF-β factors (Fig. 1b), supporting regulation of TGF-β signalling by SARS-CoV-2.

To better understand the mechanisms underlying perturbation of cellular signalling, we performed comparative ubiquitination and phosphorylation profiling following infection with SARS-CoV-2 or SARS-CoV. This analysis showed that 1,108 of 16,541 detected ubiquitination sites were differentially regulated by infection with SARS-CoV-2 or SARS-CoV (Fig. 2a, b, d, Extended Data Fig. 5a, Supplementary Table 6). More than half of the significant sites were regulated in a similar manner by both viruses. These included sites on SLC35 and SUMO family proteins, indicating possible regulation of sialic acid transport and the SUMO activity. SARS-CoV-2 specifically increased ubiquitination on autophagy-related factors (MAP1LC3A, GABARAP, VPS33A and VAMP8) as well as specific sites on EGFR (for example, K739, K754 and K970). In some cases, the two viruses targeted distinct sites on the same cellular protein, as exemplified by HSP90 family members (for example, K84, K191 and K539 on HSP90AA1) (Fig. 2d). Notably, a number of proteins (for example, ALCAM, ALDH3B1, CTNNA1, EDF1 and SLC12A2) exhibited concomitant ubiquitination and a decrease at the protein level after infection, pointing to ubiquitination-mediated protein degradation (Fig. 2d, Extended Data Figs. 4f, 5a, Supplementary Tables 5, 6). Among these downregulated proteins, EDF1 has a pivotal role in the maintenance of endothelial integrity and may be a link to endothelial dysfunctions

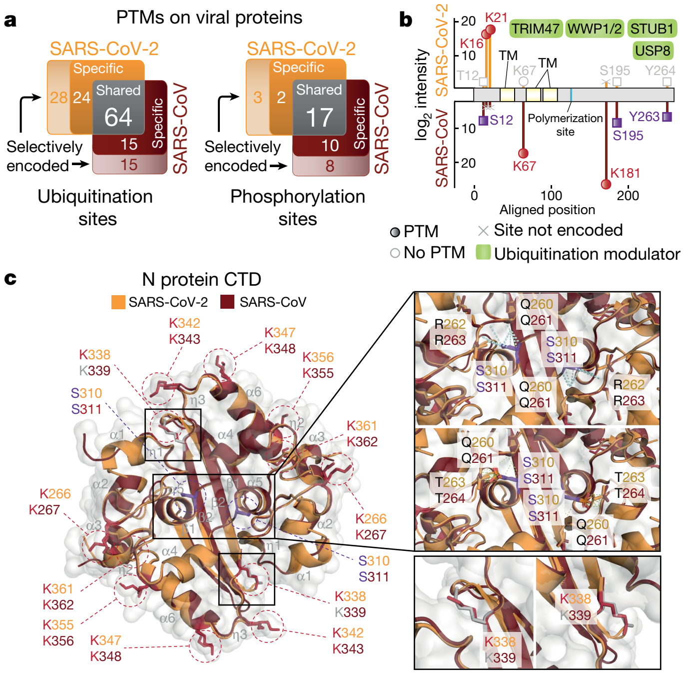

Fig. 3 | Phosphorylation and ubiquitination of SARS-CoV-2 and SARS-CoV viral proteins. a, Distribution of identified shared, differentially regulated and selectively encoded (sequence-specific) ubiquitination and phosphorylation sites on SARS-CoV-2 and SARS-CoV homologous proteins after infection of A549-ACE2 cells. PTM, post-translational modification. **b**, Mapping of the ubiquitination (red circles) and phosphorylation (purple squares) sites on an alignment of SARS-CoV-2 ORF3 and SARS-CoV ORF3a proteins, showing median $\log_2$ intensities in virus-infected A549-ACE2 cells at 24 hpi. Functional (blue) and topological (yellow) domains are mapped on each sequence. Ubiquitin-modifying enzymes binding to ORF3 and ORF3a as identified in our AP–MS experiments (Extended Data Fig. 1b) are indicated (green). TM, transmembrane domain. **c**, Surface and ribbon representation of superimposed SARS-CoV (Protein Data Bank (PDB) ID: 2CJR, brown) and SARS-CoV-2 (PDB ID: 6YUN, orange) N protein CTD dimers (r.m.s.d. values of 0.492 Å for 108 matching Cα atoms). Secondary structures are numbered in grey (prefixed with α for α-helix, β for β-strand and η for non-structured regions). Side chains are colour coded depending on whether they are in ubiquitinated (red), phosphorylated (purple) or unmodified (grey) sites. The K338 ubiquitination site unique to SARS-CoV-2 is shown as a close-up for both monomers (bottom right). Close-ups of inter-chain residue interactions established by non-phosphorylated (top right) and phosphorylated (middle right) SARS-CoV-2 S310 or SARS-CoV S311.

described for COVID-19[24,25]. Profound regulation of cellular signalling pathways was also observed at the phosphoproteomic level: among 16,399 total quantified phosphorylation sites, 4,643 showed significant changes after infection with SARS-CoV-2 or SARS-CoV (Extended Data Fig. 5b, c, Supplementary Table 7). Highly regulated sites were identified for the proteins of the MAPK pathways (for example, MAPKAPK2, MAP2K1, JUN and SRC), and proteins involved in autophagy signalling (for example, DEPTOR, RICTOR, OPTN, SQSTM1 and LAMTOR1) and viral entry (for example, ACE2 and RAB7A) (Extended Data Fig. 5b, d). Notably, RAB7A was recently shown to be an important host factor for SARS-CoV-2 infection that assists endosomal trafficking of ACE2 to the plasma membrane[26]. We observed higher phosphorylation at S72 of RAB7A in SARS-CoV-2 infection compared with SARS-CoV or mock infection; this site is implicated in RAB7A intracellular localization and molecular association[27]. The regulation of known phosphorylation sites suggests an involvement of central kinases (cyclin dependent kinases, AKT, MAPKs, ATM, and CHEK1) linked to cell survival, cell cycle progression, cell growth and motility, stress responses and the DNA damage response; this was also supported by the analysis of enriched motifs (Extended Data Fig. 5e, f, Supplementary Tables 7, 8). Notably, SARS-CoV-2 infection, but not SARS-CoV infection, led to phosphorylation of the antiviral kinase EIF2AK2 (also known as PKR) at the critical regulatory residue S33[28]. This differential activation of EIF2AK2 could contribute to the difference in the growth kinetics of the two viruses (Supplementary Table 4, 5).

Our data clearly point to an interplay of phosphorylation and ubiquitination patterns on individual host proteins. For instance, EGFR showed increased ubiquitination on 6 lysine residues at 24 h post-infection (hpi) accompanied by increased phosphorylation of T693, S695 and S991 at 24 and 36 hpi (Fig. 2e, f). Ubiquitination of all six lysine residues on EGFR was more pronounced following infection with SARS-CoV-2 than with SARS-CoV. Moreover, vimentin, a central co-factor for coronavirus entry[29] and pathogenicity[30,31], displayed distinct phosphorylation and ubiquitination patterns on several sites early (for example, S420) or late (for example, S56, S72 and K334) in infection (Extended Data Fig. 6a, b). These findings underscore the value of testing different post-translational modifications simultaneously and suggest a concerted engagement of regulatory machineries to modify target protein functions and abundance.

Post-translational modification of viral proteins

The majority of viral proteins were also post-translationally modified. Of the 27 detected SARS coronavirus proteins, 21 were ubiquitinated. Nucleocapsid (N), spike (S), NSP2 and NSP3 were the most heavily modified proteins in both viruses (Extended Data Fig. 6c, Supplementary Table 6). Many ubiquitination sites were common to both viruses. Around half of the sites that were exclusively ubiquitinated in either virus were conserved between SARS-CoV and SARS-CoV-2. The remaining specifically regulated ubiquitination sites were unique to each virus, indicating that these acquired adaptations can be post-translationally modified and may recruit cellular proteins with distinct functions (Fig. 3a). Our interactome data identified several host E3 ligases (for example, we identified interactions between SARS-CoV-2 ORF3 and TRIM47, WWP1, WWP2 and STUB1; and between SARS-CoV-2 M and TRIM7) and deubiquitinating enzymes (for example, interactions between SARS-CoV-2 ORF3 and USP8; SARS-CoV-2 ORF7a and USP34; and SARS-CoV N and USP9X), suggesting crosstalk between ubiquitination and viral protein functions (Fig. 1b, Extended Data Fig. 6d, Supplementary Table 2). Of particular interest are extensive ubiquitination events on the S protein of both viruses (K97, K528, K825, K835, K921 and K947), which are distributed on functional domains (N-terminal domain, C-terminal domain (CTD), fusion peptide and heptad repeat 1 domain), potentially indicating critical regulatory functions that are conserved between the two viruses (Extended Data Fig. 6e). We observed phosphorylation of 5 SARS-CoV-2 proteins (M, N, S, NSP3 and ORF9b) and 8 SARS-CoV proteins (M, N, S, NSP1, NSP2, NSP3, ORF3 and ORF9b) (Extended Data Fig. 6f, Supplementary Table 7), on sites corresponding to known recognition motifs. In particular, CAMK4 and MAPKAPK2 potentially phosphorylate sites on S and N, respectively. Phosphorylation of cellular proteins suggested that the activities of these kinases were enriched in cells infected with SARS-CoV-2 or SARS-CoV (Extended Data Figs. 5e, f, 6e, g). Moreover, N proteins of both SARS-CoV-2 and SARS-CoV recruit GSK3, which could potentially be linked to phosphorylation events on these viral proteins (Fig. 1b, Extended Data Fig. 6g, Supplementary Table 7). Notably, we identified novel post-translationally modified sites located at functional domains of viral proteins; we detected ubiquitination at SARS-CoV-2 N K338 and phosphorylation on SARS-CoV-2 and SARS-CoV N S310 and S311 (Extended Data Fig. 6g). Mapping these sites to the atomic structure of the CTD[32,33] highlights critical positions for the function of the protein (Fig. 3c, Extended Data Fig. 6h, Supplementary Discussion 2). Collectively, while the identification of differentially regulated sites

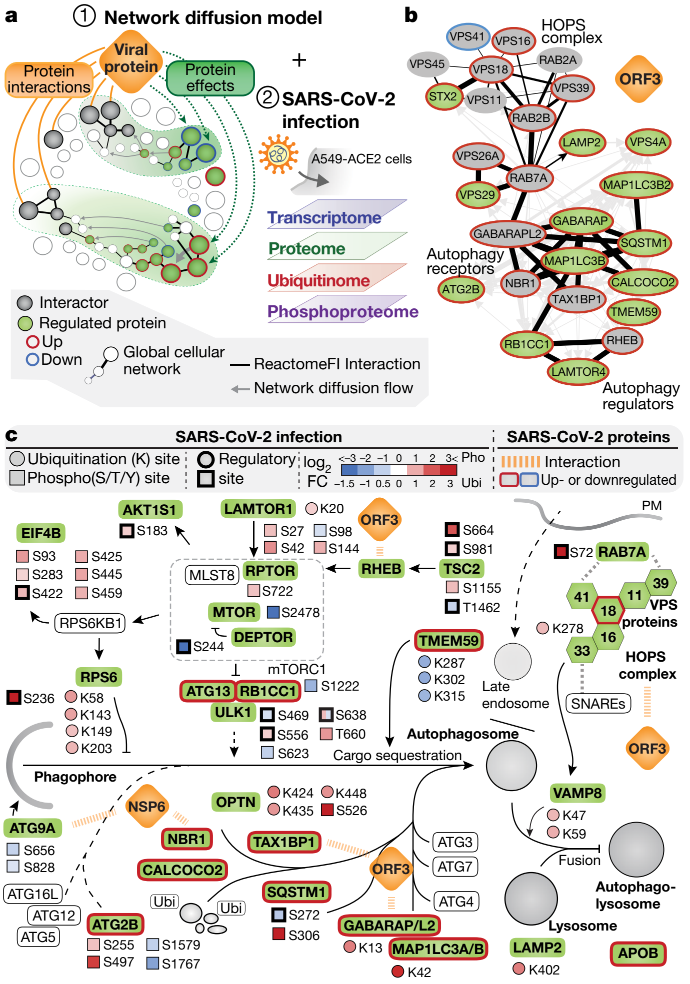

Fig. 4 | A network diffusion approach enables identification of molecular pathways linking protein–protein interactions with downstream changes in the host proteome. a, The network diffusion approach to identify functional connections between the host targets of a viral protein and downstream proteome changes. The results of network diffusion are integrated with omics datasets of SARS coronavirus infection to streamline the identification of affected host pathways. **b**, Subnetworks of the network diffusion linking host targets of SARS-CoV-2 ORF3 to factors involved in autophagy. The thickness of directed edges is proportional to the random-walk transition probability. Black edges denote connections present in ReactomeFI. **c**, Overview of perturbations to host-cell autophagy induced by SARS-CoV-2. The pathway regulation is derived from the network diffusion model for SARS-CoV-2 ORF3 and NSP6 and is overlaid with the changes in protein levels, ubiquitination (Ubi) and phosphorylation (Pho) induced by SARS-CoV-2 infection. FC, fold change; PM, plasma membrane.

may indicate pathogen-specific functions, insights from conserved post-translational modifications may also provide useful knowledge for the development of targeted pan-antiviral therapies.

Viral perturbation of key cellular pathways

Our unified experimental design in a syngeneic system enabled direct time-resolved comparison of SARS-CoV-2 and SARS-CoV infection across different levels. Integrative pathway-enrichment analysis demonstrated that both viruses largely perturb the same cellular processes at multiple levels, albeit with distinct temporal patterns (Extended Data Fig. 7a). For instance, transcriptional downregulation of proteins involved in tau protein kinase activity and Fe ion sequestration at 6 hpi was followed by a decrease in protein abundance after 12 hpi (Supplementary Table 8). RHO GTPase activation, mRNA processing and the role of ABL in ROBO–SLIT signalling appeared to be regulated mostly through phosphorylation (Extended Data Fig. 7a). By contrast, processes connected to cellular integrity such as the formation of senescence-associated heterochromatin foci, apoptosis-induced DNA fragmentation and amino acid transport across the plasma membrane were modulated through concomitant phosphorylation and ubiquitination events, suggesting molecular links between these post-translational modifications. Ion transporters, especially the SLC12 family of cation-coupled chloride cotransporters—previously identified as cellular factors in pulmonary inflammation[34]—were also regulated at multiple levels, evidenced by reduced protein abundance as well as differential post-translational modifications (Extended Data Fig. 7a).

The pathway-enrichment analysis provided a global and comprehensive picture of how SARS-CoV-2 and SARS-CoV affect the host. We next applied an automated approach to systematically explore the underlying molecular mechanisms contained in the viral interactome and effectome data. We mapped the measured interactions and effects of each viral protein onto the global network of cellular interactions[35] and applied a network diffusion approach[36] (Fig. 4a). This type of analysis uses known cellular protein–protein interactions, signalling and regulation events to identify connection points between cellular proteins that interact with viral proteins and the proteins affected by the expression of these viral proteins (Extended Data Figs. 1b, 2d, Supplementary Tables 2, 3). The connections inferred from the real data were significantly shorter than for randomized data, validating the relevance of the approach and the quality of the data (Extended Data Fig. 8a, b). The findings from this approach include the potential mechanisms by which ORF3 and NSP6 may regulate autophagy, the modulation of innate immunity by M, ORF3 and ORF7b, and the perturbation of integrin–TGF-β–EGFR–receptor tyrosine kinase signalling by ORF8 of SARS-CoV-2 (Fig. 4b, Extended Data Fig. 8c, d). Enriching these subnetworks with data on SARS-CoV-2 infection-dependent mRNA abundance, protein abundance, phosphorylation and ubiquitination (Fig. 4a) provided insights into the regulatory mechanisms activated by SARS-CoV-2. For instance, the analysis confirmed a role of NSP6 in both SARS-CoV-2- and SARS-CoV-induced autophagy[37] and revealed the SARS-CoV-2 specific inhibition of autophagic flux by ORF3 protein, leading to the accumulation of autophagy receptors (SQSTM1, GABARAPL2, NBR1, CALCOCO2, MAP1LC3A, MAP1LC3B and TAX1BP1), consistent with the accumulation of MAP1LC3B protein observed in cells infected with SARS-CoV-2 (Fig. 4c, Extended Data Fig. 8e, f). This inhibition may be a result of the interaction of the ORF3 protein with the HOPS complex (VPS11, VPS16, VPS18, VPS39 and VPS41), which is essential for autophagosome–lysosome fusion, as well as the differential phosphorylation of regulatory sites (for example, on TSC2, mTORC1 complex, ULK1, RPS6 and SQSTM1) and ubiquitination of key components (MAP1LC3A, GABARAPL2, VPS33A and VAMP8) (Fig. 4c, Extended Data Fig. 8g). This inhibition of autophagosome function may have direct consequences for protein degradation. The abundance of APOB, a protein that is degraded via autophagy[38], was selectively increased after SARS-CoV-2 infection or expression of SARS-CoV-2 ORF3 (Extended Data Fig. 3b, 8h). Accumulating APOB levels could increase the risk of arterial thrombosis[39], one of the main complications contributing to lung, heart and kidney failure in patients with COVID-19[40]. The inhibition of the interferon (IFN)-α and IFN-β response observed at transcriptional and proteome levels was similarly explained by the network diffusion analysis (Extended Data Fig. 8i), which implicated multiple proteins of SARS-CoV-2 in the disruption of antiviral immunity. Further experiments functionally corroborated the inhibition of IFN-α and IFN-β induction or signalling by ORF3, ORF6, ORF7a, ORF7b and ORF9b (Extended Data Fig. 8j). Upon virus infection, we observed the regulation of TGF-β and EGFR pathways modulating cell survival, motility and innate immune responses (Extended Data Fig. 9a–d). Specifically, our network diffusion analysis revealed a connection between

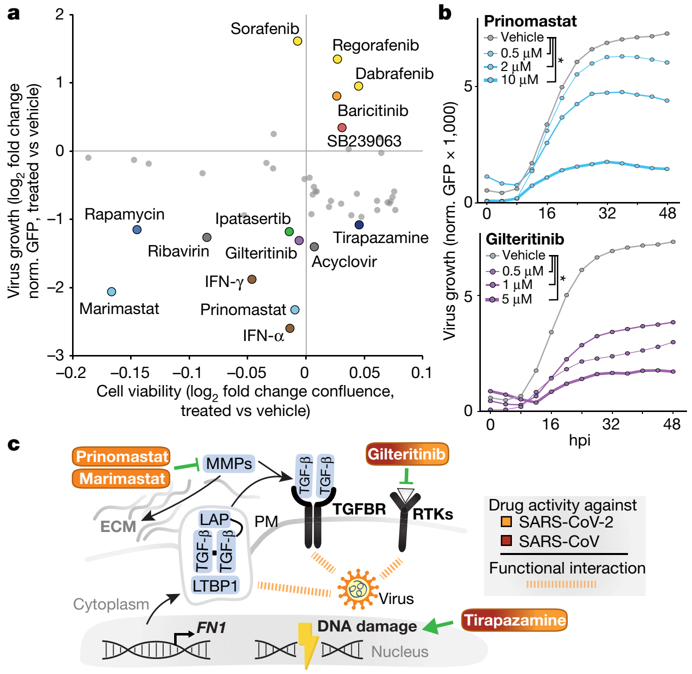

Fig. 5 | Identification of pathways targeted by SARS-CoV-2 using a multi-omics profiling approach enables systematic testing of candidate antiviral therapies. a, **b**, A549-ACE2 cells were treated with the indicated drugs 6 h before infection with SARS-CoV-2-GFP (MOI of 3). Changes in cell viability and virus growth (**a**) in drug-treated cells compared with untreated A549-ACE2 cells at 48 hpi. A confluence cut-off of −0.2 $\log_2$ fold change was applied to remove cytotoxic compounds. **b**, Time courses of virus replication after pre-treatment of cells with prinomastat or gilteritinib. $n = 4$ independent experiments; $^*P \leq 0.01$ compared with control treatment, unadjusted two-sided Wilcoxon test. Norm., normalized. **c**, Drugs potentially targeting pathways identified in our study. Colour indicates antiviral activity against SARS-CoV-2 or SARS-CoV (brown–orange gradient) or SARS-CoV-2 specifically (orange), as inferred from in vitro experiments.

the binding of the ORF8 and ORF3 proteins to TGF-β-associated factors (TGF-β1, TGF-β2, LTBP1, TGFBR2, FURIN and BAMBI), the differential expression of extracellular matrix regulators (FERMT2 and CDH1) and the virus-induced upregulation of fibrinogens (FGA, FGB), fibronectin (FN1) and SERPINE1[41] (Extended Data Fig. 9a, b). The increased phosphorylation of proteins involved in MAPK signalling (for example, SHC1 (on S139), SOS1 (S1134/S1229), JUN (S63/S73), MAPKAPK2 (T334) and p38 (T180/Y182)) and receptor tyrosine kinase signalling (for example, phosphorylation of PI3K complex members PDPK1 (S241) and RPS6KA1 (S380)) as well as a higher expression of JUN, FOS and EGR1 are further indications of regulation of TGF-β and EGFR pathways (Extended Data Fig. 9a, c, d). In turn, TGF-β and EGFR signalling are known to be potentiated by integrin signalling and activation of YAP-dependent transcription[42], which we observed to be regulated in a time-dependent manner upon SARS-CoV-2 infection (Extended Data Fig. 9a). As well as promoting virus replication, activation of these pathways has been implicated in fibrosis[13–15], one of the hallmarks of COVID-19[16].

Data-guided drug identification and testing

Together, the viral protein–host protein interactions and regulation of pathways observed at multiple levels identify potential points for targeting SARS-CoV and SARS-CoV-2 using well-characterized selective antiviral drugs. To test antiviral efficacy, we used time-lapse fluorescent microscopy of infection with a GFP reporter SARS-CoV-2[43]. Inhibition of virus replication by treatment with IFN-α corroborated previous conclusions that efficient SARS-CoV-2 replication involves the inactivation of this pathway at an early step[9,44] and confirmed the reliability of this screening approach (Extended Data Fig. 10a). We tested a panel of 48 drugs that modulate the pathways perturbed by the virus for their effects on SARS-CoV-2 replication (Fig. 5a, Supplementary Table 9). Of note, inhibitors of B-RAF (sorafenib, regorafenib and dabrafenib), JAK1/2 (baricitinib) and MAPK (SB239063), which are commonly used to treat cancer and autoimmune diseases[45–47], significantly increased virus growth in an in vitro model of infection (Fig. 5a, Extended Data Fig. 10b, Supplementary Table 9). By contrast, inducers of DNA damage (tirapazamine and rabusertib) or an mTOR inhibitor (rapamycin) suppressed virus growth. The highest antiviral activity was observed for gilteritinib (a designated inhibitor of FLT3 and AXL), ipatasertib (an AKT inhibitor), prinomastat and marimastat (matrix metalloprotease (MMP) inhibitors) (Fig. 5a, b, Extended Data Fig. 10c, Supplementary Table 9). These compounds profoundly inhibited replication of SARS-CoV-2 while having no effects or minor effects on cell growth (Extended Data Fig. 10b, Supplementary Table 9). Quantitative PCR analysis indicated antiviral activities for gilteritinib and tirapazamine against SARS-CoV-2 and SARS-CoV (Fig. 5c, Extended Data Fig. 10d, e). Notably, prinomastat and marimastat, specific inhibitors of MMP2 and MMP9, showed selective activity against SARS-CoV-2 but not against SARS-CoV (Fig. 5c, Extended Data Fig. 10f, g). Activities of MMPs have been linked to TGF-β activation and pleural effusions, alveolar damage and neuroinflammation (for example, Kawasaki disease), all of which are characteristic of COVID-19[23,48–51].

This drug screen demonstrates the value of our combined dataset, which profiles SARS-CoV-2 infection at multiple levels. We expect that further exploration of these rich data by the scientific community and additional studies of the interplay between different omics levels will substantially advance our molecular understanding of coronavirus biology, including the pathogenicity associated with specific human coronaviruses, such as SARS-CoV-2 and SARS-CoV. Moreover, this resource, together with complementary approaches[26,52–54], will streamline the search for antiviral compounds and serve as a base for rational design of combination therapies that target the virus from multiple synergistic angles, thus potentiating the effect of individual drugs while minimizing potential side effects on healthy tissues.

Online content

Any methods, additional references, Nature Research reporting summaries, source data, extended data, supplementary information, acknowledgements, peer review information; details of author contributions and competing interests; and statements of data and code availability are available at https://doi.org/10.1038/s41586-021-03493-4.

1. Gordon, D. E. et al. A SARS-CoV-2 protein interaction map reveals targets for drug repurposing. *Nature* **583**, 459–468 (2020).
2. Gordon, D. E. et al. Comparative host–coronavirus protein interaction networks reveal pan-viral disease mechanisms. *Science* **370**, eabe9403 (2020).
3. Bojkova, D. et al. Proteomics of SARS-CoV-2-infected host cells reveals therapy targets. *Nature* **583**, 469–472 (2020).
4. Messner, C. B. et al. Ultra-high-throughput clinical proteomics reveals classifiers of COVID-19 infection. *Cell Syst.* **11**, 11–24.e4 (2020).
5. Samavarchi-Tehrani, P. et al. A SARS-CoV-2–host proximity interactome. Preprint at https://doi.org/10.1101/2020.09.03.282103 (2020).
6. Laurent, E. M. N. et al. Global BioID-based SARS-CoV-2 proteins proximal interactome unveils novel ties between viral polypeptides and host factors involved in multiple COVID19-associated mechanisms. Preprint at https://doi.org/10.1101/2020.08.28.272955 (2020).
7. Klann, K. et al. Growth factor receptor signaling inhibition prevents SARS-CoV-2 replication. *Mol. Cell* **80**, 164–174.e4 (2020).
8. Huang, J. et al. SARS-CoV-2 infection of pluripotent stem cell-derived human lung alveolar type 2 cells elicits a rapid epithelial-intrinsic inflammatory response. *Cell Stem Cell* **27**, 962–973.e7 (2020).
9. Blanco-Melo, D. et al. Imbalanced host response to SARS-CoV-2 drives development of COVID-19. *Cell* **181**, 1036–1045.e9 (2020).
10. Li, J. et al. Virus–host interactome and proteomic survey reveal potential virulence factors influencing SARS-CoV-2 pathogenesis. *Med* **2**, 99–112.e7 (2021).
11. von Brunn, A. et al. Analysis of intraviral protein–protein interactions of the SARS coronavirus ORFeome. *PLoS ONE* **2**, e459 (2007).

12. Cornillez-Ty, C. T., Liao, L., Yates, J. R., III, Kuhn, P. & Buchmeier, M. J. Severe acute respiratory syndrome coronavirus nonstructural protein 2 interacts with a host protein complex involved in mitochondrial biogenesis and intracellular signaling. *J. Virol*. **83**, 10314–10318 (2009).
13. Andrianifahanana, M. et al. ERBB receptor activation is required for profibrotic responses to transforming growth factor β. *Cancer Res*. **70**, 7421–7430 (2010).
14. Pittet, J.-F. et al. TGF-β is a critical mediator of acute lung injury. *J. Clin. Invest*. **107**, 1537–1544 (2001).
15. George, P. M., Wells, A. U. & Jenkins, R. G. Pulmonary fibrosis and COVID-19: the potential role for antifibrotic therapy. *Lancet Respir. Med*. **8**, 807–815 (2020).
16. Mo, X. et al. Abnormal pulmonary function in COVID-19 patients at time of hospital discharge. *Eur. Respir. J*. **55**, 2001217 (2020).
17. Heo, J.-M. et al. Integrated proteogenetic analysis reveals the landscape of a mitochondrial-autophagosome synapse during PARK2-dependent mitophagy. *Sci. Adv*. **5**, eaay4624 (2019).
18. Shi, C.-S. et al. SARS-coronavirus open reading frame-9b suppresses innate immunity by targeting mitochondria and the MAVS/TRAF3/TRAF6 signalosome. *J. Immunol*. **193**, 3080–3089 (2014).
19. Hoagland, D. A. et al. Modulating the transcriptional landscape of SARS-CoV-2 as an effective method for developing antiviral compounds. Preprint at https://doi.org/10.1101/2020.07.12.199687 (2020).
20. Castiglione, V., Chiriacò, M., Emdin, M., Taddei, S. & Vergaro, G. Statin therapy in COVID-19 infection. *Eur. Heart J. Cardiovasc. Pharmacother*. **6**, 258–259 (2020).
21. Radenkovic, D., Chawla, S., Pirro, M., Sahebkar, A. & Banach, M. Cholesterol in relation to COVID-19: should we care about it? *J. Clin. Med*. **9**, 1909 (2020).
22. Chu, H. et al. Comparative replication and immune activation profiles of SARS-CoV-2 and SARS-CoV in human lungs: an ex vivo study with implications for the pathogenesis of COVID-19. *Clin. Infect. Dis*. **71**, 1400–1409 (2020).
23. Zhu, Z. et al. From SARS and MERS to COVID-19: a brief summary and comparison of severe acute respiratory infections caused by three highly pathogenic human coronaviruses. *Respir. Res*. **21**, 224 (2020).
24. Cazzaniga, A., Locatelli, L., Castiglioni, S. & Maier, J. The contribution of EDF1 to PPARγ transcriptional activation in VEGF-treated human endothelial cells. *Int. J. Mol. Sci*. **19**, 1830 (2018).
25. Gavriilaki, E. et al. Endothelial dysfunction in COVID-19: lessons learned from coronaviruses. *Curr. Hypertens. Rep*. **22**, 63 (2020).
26. Daniloski, Z. et al. Identification of required host factors for SARS-CoV-2 infection in human cells. *Cell* **184**, 92–105 (2021).
27. Shinde, S. R. & Maddika, S. PTEN modulates EGFR late endocytic trafficking and degradation by dephosphorylating Rab7. *Nat. Commun*. **7**, 10689 (2016).
28. Wang, D. et al. Auto-phosphorylation represses protein kinase R activity. *Sci. Rep*. **7**, 44340 (2017).
29. Yu, Y. T.-C. et al. Surface vimentin is critical for the cell entry of SARS-CoV. *J. Biomed. Sci*. **23**, 14 (2016).
30. dos Santos, G. et al. Vimentin regulates activation of the NLRP3 inflammasome. *Nat. Commun*. **6**, 6574 (2015).
31. Ramos, I., Stamatakis, K., Oeste, C. L. & Pérez-Sala, D. Vimentin as a multifaceted player and potential therapeutic target in viral infections. *Int. J. Mol. Sci*. **21**, 4675 (2020).
32. Zinzula, L. et al. High-resolution structure and biophysical characterization of the nucleocapsid phosphoprotein dimerization domain from the Covid-19 severe acute respiratory syndrome coronavirus 2. *Biochem. Biophys. Res. Commun*. **538**, 54–62 (2021).
33. Chen, C.-Y. et al. Structure of the SARS coronavirus nucleocapsid protein RNA-binding dimerization domain suggests a mechanism for helical packaging of viral RNA. *J. Mol. Biol*. **368**, 1075–1086 (2007).
34. Perry, J. S. A. et al. Interpreting an apoptotic corpse as anti-inflammatory involves a chloride sensing pathway. *Nat. Cell Biol*. **21**, 1532–1543 (2019).
35. Wu, G., Dawson, E., Duong, A., Haw, R. & Stein, L. ReactomeFIViz: a Cytoscape app for pathway and network-based data analysis. *F1000Res*. **3**, 146 (2014).
36. Reyna, M. A., Leiserson, M. D. M. & Raphael, B. J. Hierarchical HotNet: identifying hierarchies of altered subnetworks. *Bioinformatics* **34**, i972–i980 (2018).
37. Cottam, E. M., Whelband, M. C. & Wileman, T. Coronavirus NSP6 restricts autophagosome expansion. *Autophagy* **10**, 1426–1441 (2014).
38. Ohsaki, Y., Cheng, J., Fujita, A., Tokumoto, T. & Fujimoto, T. Cytoplasmic lipid droplets are sites of convergence of proteasomal and autophagic degradation of apolipoprotein B. *Mol. Biol. Cell* **17**, 2674–2683 (2006).
39. Khalil, M. F., Wagner, W. D. & Goldberg, I. J. Molecular interactions leading to lipoprotein retention and the initiation of atherosclerosis. *Arterioscler. Thromb. Vasc. Biol*. **24**, 2211–2218 (2004).
40. Nicolai, L. et al. Immunothrombotic dysregulation in COVID-19 pneumonia is associated with respiratory failure and coagulopathy. *Circulation* **142**, 1176–1189 (2020).
41. Zavadil, J. et al. Genetic programs of epithelial cell plasticity directed by transforming growth factor-β. *Proc. Natl Acad. Sci. USA* **98**, 6686–6691 (2001).
42. Qin, Z., Xia, W., Fisher, G. J., Voorhees, J. J. & Quan, T. YAP/TAZ regulates TGF-β/Smad3 signaling by induction of Smad7 via AP-1 in human skin dermal fibroblasts. *Cell Commun. Signal*. **16**, 18 (2018).
43. Thi Nhu Thao, T. et al. Rapid reconstruction of SARS-CoV-2 using a synthetic genomics platform. *Nature* **582**, 561–565 (2020).
44. Mantlo, E., Bukreyeva, N., Maruyama, J., Paessler, S. & Huang, C. Antiviral activities of type I interferons to SARS-CoV-2 infection. *Antiviral Res*. **179**, 104811 (2020).
45. Seebacher, N. A., Stacy, A. E., Porter, G. M. & Merlot, A. M. Clinical development of targeted and immune based anti-cancer therapies. *J. Exp. Clin. Cancer Res*. **38**, 156 (2019).
46. O'Shea, J. J., Kontzias, A., Yamaoka, K., Tanaka, Y. & Laurence, A. Janus kinase inhibitors in autoimmune diseases. *Ann. Rheum. Dis*. **72** (Suppl 2), ii111–ii115 (2013).
47. Yong, H.-Y., Koh, M.-S. & Moon, A. The p38 MAPK inhibitors for the treatment of inflammatory diseases and cancer. *Expert Opin. Investig. Drugs* **18**, 1893–1905 (2009).
48. Hsieh, W.-Y. et al. ACE/ACE2 ratio and MMP-9 activity as potential biomarkers in tuberculous pleural effusions. *Int. J. Biol. Sci*. **8**, 1197–1205 (2012).
49. Ueland, T. et al. Distinct and early increase in circulating MMP-9 in COVID-19 patients with respiratory failure. *J. Infect*. **81**, e41–e43 (2020).
50. Villalta, P. C., Rocic, P. & Townsley, M. I. Role of MMP2 and MMP9 in TRPV4-induced lung injury. *Am. J. Physiol. Lung Cell. Mol. Physiol*. **307**, L652–L659 (2014).
51. Marten, N. W. & Zhou, J. in *Experimental Models of Multiple Sclerosis* (eds Lavi, E. & Constantinescu, C. S.) 839–848 (Springer, 2005).
52. Zhang, J.-Y. et al. Single-cell landscape of immunological responses in patients with COVID-19. *Nat. Immunol*. **21**, 1107–1118 (2020).
53. Ellinghaus, D. et al. Genomewide association study of severe Covid-19 with respiratory failure. *N. Engl. J. Med*. **383**, 1522–1534 (2020).
54. Ali, A. & Vijayan, R. Dynamics of the ACE2–SARS-CoV-2/SARS-CoV spike protein interface reveal unique mechanisms. *Sci. Rep*. **10**, 14214 (2020).

Publisher's note Springer Nature remains neutral with regard to jurisdictional claims in published maps and institutional affiliations.

© The Author(s), under exclusive licence to Springer Nature Limited 2021

Methods

No statistical methods were used to predetermine sample size. The experiments were not randomized. The investigators were not blinded to allocation during experiments and outcome assessment.

Cell lines and reagents

HEK293T, A549, Vero E6 and HEK293-R1 cells were authentified by PCR-single-locus-technology and their respective culturing conditions were described previously[55]. All cell lines were tested to be mycoplasma free. Expression constructs for C-terminal HA-tagged viral open reading frames were synthesized (Twist Bioscience and BioCat) and cloned into pWPI vector as described previously[56] with the following modifications: a starting ATG codon was added, internal canonical splicing sites were replaced with synonymous mutations and a C-terminal HA-tag, followed by an amber stop codon, was added to individual viral open reading frames. A C-terminally HA-tagged ACE2 sequence was amplified from an ACE2 expression vector (provided by S. Pöhlmann)[57] into the lentiviral vector pWPI-puro. A549 cells were transduced twice, and A549-ACE2 cells were selected with puromycin. Lentivirus production, transduction of cells and antibiotic selection were performed as described previously[52]. RNA isolation (Macherey–Nagel NucleoSpin RNA plus), reverse transcription (TaKaRa Bio PrimeScript RT with gDNA eraser) and quantitative PCR with reverse transcription (RT–qPCR) (Thermo-Fisher Scientific PowerUp SYBR green) were performed as described previously[54]. RNA isolation for next generation sequencing applications was performed according to the manufacturer's protocol (Qiagen RNeasy mini kit, RNase free DNase set). For detection of protein abundance by western blotting, HA–horseradish peroxidase (HRP) (Sigma-Aldrich; H6533; 1:2,500 dilution), ACTB–HRP (Santa Cruz; sc-47778; 1:5,000 dilution), MAP1LC3B (Cell Signaling; 3868; 1:1,000 dilution), MAVS (Cell Signaling; 3993; 1:1,000 dilution), HSPA1A (Cell Signaling; 4873; 1:1,000 dilution), TGF-β (Cell Signaling; 3711; 1:1,000 dilution), phospho-p38 (T180/Y182) (Cell Signaling; 4511; 1:1,000 dilution), p38 (Cell Signaling; 8690; 1:1,000 dilution) and SARS-CoV-2 or SARS-CoV N protein (Sino Biological; 40143-MM05; 1:1,000 dilution) antibodies were used. Secondary antibodies detecting mouse (Cell Signaling; 7076; 1:5,000 dilution; Jackson ImmunoResearch; 115-035-003; 1:5,000 dilution), rat (Invitrogen; 31470; 1:5,000 dilution), and rabbit IgG (Cell Signaling; 7074; 1:5,000 dilution) were coupled to HRP. For AP–MS and affinity purification–western blotting applications, HA beads (Sigma-Aldrich and Thermo Fisher Scientific) and Streptactin II beads (IBA Lifesciences) were used. Imaging of western blots was performed as described[58]. Recombinant human IFN-α used for stimulation of cells in the reporter assay was a gift from P. Stäheli (Institute of Virology, University of Freiburg), recombinant human IFN-γ was purchased from PeproTech, and IVT4 was produced as described before[59]. All compounds tested in the viral inhibitor assay are listed in Supplementary Table 9.

Virus strains, stock preparation, plaque assay and in vitro infection

SARS-CoV-Frankfurt-1, SARS-CoV-2-MUC-IMB-1 and SARS-CoV-2-GFP strains[43] were produced by infecting Vero E6 cells cultured in DMEM medium (10% FCS, 100 μg ml^{-1} Streptomycin, 100 IU ml^{-1} penicillin) for 2 days (MOI of 0.01). Viral stock was collected and spun twice (1,000*g* for 10 min) before storage at −80 °C. Titre of viral stock was determined by plaque assay. Confluent monolayers of Vero E6 cells were infected with serial fivefold dilutions of virus supernatants for 1 h at 37 °C. The inoculum was removed and replaced with serum-free MEM (Gibco, Life Technologies) containing 0.5% carboxymethylcellulose (Sigma-Aldrich). Two days after infection, cells were fixed for 20 min at room temperature with formaldehyde added directly to the medium to a final concentration of 5%. Fixed cells were washed extensively with PBS before staining with water containing 1% crystal violet and 10% ethanol for 20 min. After rinsing with PBS, the number of plaques was counted and the virus titre was calculated.

A549-ACE2 cells were infected with either SARS-CoV-Frankfurt-1 or SARS-CoV-2-MUC-IMB-1 strains (MOI of 2) for the subsequent experiments. At each time point, the samples were washed once with 1× TBS buffer and collected in sodium deoxycholate (SDC) lysis buffer (100 mM Tris HCl pH 8.5; 4% SDC) for proteome-phosphoproteome-ubiquitinome analysis, sodium dodecyl sulfate (SDS) lysis buffer (62.5 mM Tris HCl pH 6.8; 2% SDS; 10% glycerol; 50 mM DTT; 0.01% bromophenol blue) for western blot, or buffer RLT (Qiagen) for transcriptome analysis. The samples were heat-inactivated and frozen at −80 °C until further processing.

Affinity purification and mass spectrometric analyses of SARS-CoV-2, SARS-CoV, HCoV-229E and HCoV-NL63 proteins expressed in A549 cells

To determine the interactomes of SARS-CoV-2 and SARS-CoV and the interactomes of an accessory protein (encoded by ORF4 or ORF4a of HCoV-229E or ORF3 of HCoV-NL63) that presumably represents a homologue of the ORF3 and ORF3a proteins of SARS-CoV-2 and SARS-CoV, respectively, four replicate affinity purifications were performed for each HA-tagged viral protein. A549 cells (6×10^6 cells per 15-cm dish) were transduced with lentiviral vectors encoding HA-tagged SARS-CoV-2, SARS-CoV or HCoV-229E/NL63 proteins and protein lysates were prepared from cells collected 3 days after transduction. Cell pellets from two 15-cm dishes were lysed in lysis buffer (50 mM Tris-HCl pH 7.5, 100 mM NaCl, 1.5 mM $MgCl_2$, 0.2% (v/v) NP-40, 5% (v/v) glycerol, cOmplete protease inhibitor cocktail (Roche), 0.5% (v/v) 750 U/μl Sm DNase) and sonicated (5 min, 4 °C, 30 s on, 30 s off, low settings; Bioruptor, Diagenode). Following normalization of protein concentrations of cleared lysates, virus protein-bound host proteins were enriched by adding 50 μl anti-HA-agarose slurry (Sigma-Aldrich, A2095) with constant agitation for 3 h at 4 °C. Non-specifically bound proteins were removed by four subsequent washes with lysis buffer followed by three detergent-removal steps with washing buffer (50 mM Tris-HCl pH 7.5, 100 mM NaCl, 1.5 mM $MgCl_2$, 5% (v/v) glycerol). Enriched proteins were denatured, reduced, alkylated and digested by addition of 200 μl digestion buffer (0.6 M guanidinium chloride, 1 mM tris(2-carboxyethyl)phosphine (TCEP), 4 mM chloroacetamide (CAA), 100 mM Tris-HCl pH 8, 0.5 μg LysC (WAKO Chemicals) and 0.5 μg trypsin (Promega) at 30 °C overnight. Peptide purification on StageTips with three layers of C18 Empore filter discs (3M) and subsequent mass spectrometry analysis was performed as described previously[55,56]. In brief, purified peptides were loaded onto a 20-cm reverse-phase analytical column (75 μm diameter; ReproSil-Pur C18-AQ 1.9 μm resin; Dr Maisch) and separated using an EASY-nLC 1200 system (Thermo Fisher Scientific). A binary buffer system consisting of buffer A (0.1% formic acid (FA) in H_2O) and buffer B (80% acetonitrile (ACN), 0.1% FA in H_2O) with a 90-min gradient (5–30% buffer B (65 min), 30–95% buffer B (10 min), wash out at 95% buffer B (5 min), decreased to 5% buffer B (5 min), and 5% buffer B (5 min)) was used at a flow rate of 300 nl per min. Eluting peptides were directly analysed on a Q-Exactive HF mass spectrometer (Thermo Fisher Scientific). Data-dependent acquisition included repeating cycles of one MS1 full scan (300–1650 *m*/*z*, R = 60,000 at 200 *m*/*z*) at an ion target of 3×10^6, followed by 15 MS2 scans of the highest abundant isolated and higher-energy collisional dissociation (HCD) fragmented peptide precursors (R = 15,000 at 200 *m*/*z*). For MS2 scans, collection of isolated peptide precursors was limited by an ion target of 1×10^5 and a maximum injection time of 25 ms. Isolation and fragmentation of the same peptide precursor was eliminated by dynamic exclusion for 20 s. The isolation window of the quadrupole was set to 1.4 *m*/*z* and HCD was set to a normalized collision energy of 27%.

Proteome analyses of cells expressing SARS-CoV-2, SARS-CoV, HCoV-229E or HCoV-NL63 proteins

For the determination of proteome changes in A549 cells expressing SARS-CoV-2, SARS-CoV, HCoV-229E or HCoV-NL63 proteins, a fraction of

1 × 10^6 lentivirus-transduced cells from the affinity purification samples were lysed in guanidinium chloride buffer (6 M guanidinium chloride, 10 mM TCEP, 40 mM CAA, 100 mM Tris-HCl pH 8), boiled at 95 °C for 8 min and sonicated (10 min, 4 °C, 30 s on, 30 s off, high settings). Protein concentrations of cleared lysates were normalized to 50 µg, and proteins were pre-digested with 1 µg LysC at 37 °C for 1 h followed by a 1:10 dilution (100 mM Tris-HCl pH 8) and overnight digestion with 1 µg trypsin at 30 °C. Peptide purification on StageTips with three layers of C18 Empore filter discs (3M) and subsequent mass spectrometry analysis was performed as described previously[55,56]. In brief, 300 ng of purified peptides were loaded onto a 50-cm reversed-phase column (75 µm inner diameter, packed in house with ReproSil-Pur C18-AQ 1.9 µm resin (Dr Maisch)). The column temperature was maintained at 60 °C using a homemade column oven. A binary buffer system, consisting of buffer A (0.1% FA) and buffer B (80% ACN, 0.1% FA), was used for peptide separation, at a flow rate of 300 nl min^{-1}. An EASY-nLC 1200 system (Thermo Fisher Scientific), directly coupled online with the mass spectrometer (Q Exactive HF-X, Thermo Fisher Scientific) via a nano-electrospray source, was employed for nano-flow liquid chromatography. Peptides were eluted by a linear 80 min gradient from 5% to 30% buffer B (0.1% v/v FA, 80% v/v ACN), followed by a 4 min increase to 60% B, a further 4 min increase to 95% B, a 4 min plateau phase at 95% B, a 4 min decrease to 5% B and a 4 min wash phase of 5% B. To acquire MS data, the data-independent acquisition (DIA) scan mode operated by the XCalibur software (Thermo Fisher) was used. DIA was performed with one full MS event followed by 33 MS/MS windows in one cycle resulting in a cycle time of 2.7 s. The full MS settings included an ion target value of 3 × 10^6 charges in the 300–1,650 *m/z* range with a maximum injection time of 60 ms and a resolution of 120,000 at *m/z* 200. DIA precursor windows ranged from 300.5 *m/z* (lower boundary of first window) to 1,649.5 *m/z* (upper boundary of 33rd window). MS/MS settings included an ion target value of 3 × 10^6 charges for the precursor window with an Xcalibur-automated maximum injection time and a resolution of 30,000 at *m/z* 200.

To generate the proteome library for DIA measurements purified peptides from the first and the fourth replicates of all samples were pooled separately and 25 µg of peptides from each pool were fractionated into 24 fractions by high pH reversed-phase chromatography as described earlier[60]. During each separation, fractions were concatenated automatically by shifting the collection tube every 120 s. In total 48 fractions were dried in a vacuum centrifuge, resuspended in buffer A* (0.2% trifluoroacetic acid (TFA), 2% ACN) and subsequently analysed by a top-12 data-dependent acquisition (DDA) scan mode using the same LC gradient and settings. The mass spectrometer was operated by the XCalibur software (Thermo Fisher). DDA scan settings on full MS level included an ion target value of 3 × 10^6 charges in the 300–1,650 *m/z* range with a maximum injection time of 20 ms and a resolution of 60,000 at *m/z* 200. At the MS/MS level the target value was 10^5 charges with a maximum injection time of 60 ms and a resolution of 15,000 at *m/z* 200. For MS/MS events only, precursor ions with 2–5 charges that were not on the 20-s dynamic exclusion list were isolated in a 1.4 *m/z* window. Fragmentation was performed by higher-energy C-trap dissociation with a normalized collision energy of 27 eV.

Infected time-course proteome–phosphoproteome–diGly proteome sample preparation

Frozen lysates of infected A549-ACE2 cells collected at 6, 12 and 24 hpi (and 36 hpi for the phosphoproteomics study) were thawed on ice, boiled for 5 min at 95 °C and sonicated for 15 min (Branson Sonifierer). Protein concentrations were estimated by tryptophan assay[61]. To reduce and alkylate proteins, samples were incubated for 5 min at 45 °C with TCEP (10 mM) and CAA (40 mM). Samples were digested overnight at 37 °C using trypsin (1:100 w/w, enzyme/protein, Sigma-Aldrich) and LysC (1:100 w/w, enzyme/protein, Wako).

For proteome analysis, 10 µg of peptide material were desalted using SDB-RPS StageTips (Empore)[61]. In brief, samples were diluted with 1% TFA in isopropanol to a final volume of 200 µl and loaded onto StageTips, subsequently washed with 200 µl of 1% TFA in isopropanol and 200 µl 0.2% TFA/ 2% ACN. Peptides were eluted with 75 µl of 1.25% ammonium hydroxide (NH_4OH) in 80% ACN and dried using a SpeedVac centrifuge (Eppendorf, Concentrator Plus). They were resuspended in buffer A* (0.2% TFA, 2% ACN) before LC–MS/MS analysis. Peptide concentrations were measured optically at 280 nm (Nanodrop 2000, Thermo Scientific) and subsequently equalized using buffer A*. One microgram of peptide was analysed by LC–MS/MS.

The rest of the samples were diluted fourfold with 1% TFA in isopropanol and loaded onto SDB-RPS cartridges (Strata-X-C, 30 mg per 3 ml, Phenomenex), pre-equilibrated with 4 ml 30% MeOH/1% TFA and washed with 4 ml 0.2% TFA. Samples were washed twice with 4 ml 1% TFA in isopropanol, once with 0.2% TFA/2% ACN and eluted twice with 2 ml 1.25% NH_4OH/80% ACN. Eluted peptides were diluted with ddH_2O to a final ACN concentration of 35%, snap frozen and lyophilized.

For phosphopeptide enrichment, lyophilized peptides were resuspended in 105 µl of equilibration buffer (1% TFA/80% ACN) and the peptide concentration was measured optically at 280 nm (Nanodrop 2000, Thermo Scientific) and subsequently equalized using equilibration buffer. The AssayMAP Bravo robot (Agilent) performed the enrichment for phosphopeptides (150 µg) by priming AssayMAP cartridges (packed with 5 µl Fe^{3+}-NTA) with 0.1% TFA in 99% ACN followed by equilibration in equilibration buffer and loading of peptides. Enriched phosphopeptides were eluted with 1% ammonium hydroxide, which was evaporated using a Speedvac for 20 min. Dried peptides were resuspended in 6 µl buffer A* and 5 µl was analysed by LC–MS/MS.

For diGly peptide enrichment, lyophilized peptides were reconstituted in IAP buffer (50 mM MOPS, pH 7.2, 10 mM Na_2HPO_4, 50 mM NaCl) and the peptide concentration was estimated by tryptophan assay. K-ε-GG remnant containing peptides were enriched using the PTMScan Ubiquitin Remnant Motif (K-ε-GG) Kit (Cell Signaling Technology). Cross-linking of antibodies to beads and subsequent immunopurification was performed with slight modifications as previously described[62]. In brief, two vials of cross-linked beads were combined and equally split into 16 tubes (~31 µg of antibody per tube). Equal peptide amounts (600 µg) were added to cross-linked beads, and the volume was adjusted with IAP buffer to 1 ml. After 1 h of incubation at 4 °C and gentle agitation, beads were washed twice with cold IAP and 5 times with cold ddH_2O. Thereafter, peptides were eluted twice with 50 µl 0.15% TFA. Eluted peptides were desalted and dried as described for proteome analysis with the difference that 0.2% TFA instead of 1%TFA in isopropanol was used for the first wash. Eluted peptides were resuspended in 9 µl buffer A* and 4 µl was subjected to LC–MS/MS analysis.

DIA measurements

Samples were loaded onto a 50-cm reversed-phase column (75 µm inner diameter, packed in house with ReproSil-Pur C18-AQ 1.9 µm resin (Dr Maisch)). The column temperature was maintained at 60 °C using a homemade column oven. A binary buffer system, consisting of buffer A (0.1% FA) and buffer B (80% ACN plus 0.1% FA) was used for peptide separation, at a flow rate of 300 nl min^{-1}. An EASY-nLC 1200 system (Thermo Fisher Scientific), directly coupled online with the mass spectrometer (Orbitrap Exploris 480, Thermo Fisher Scientific) via a nano-electrospray source, was employed for nano-flow liquid chromatography. The FAIMS device was placed between the nanoelectrospray source and the mass spectrometer and was used for measurements of the proteome and the PTM-library samples. Spray voltage was set to 2,650 V, RF level to 40 and heated capillary temperature to 275 °C.

For proteome measurements we used a 100 min gradient starting at 5% buffer B followed by a stepwise increase to 30% in 80 min, 60% in 4 min and 95% in 4 min. The buffer B concentration stayed at 95% for 4 min, decreased to 5% in 4 min and stayed there for 4 min. The mass spectrometer was operated in data-independent mode (DIA) with a full scan range of 350–1,650 *m/z* at 120,000 resolution at 200 *m/z*, normalized automatic gain control (AGC) target of 300% and a maximum fill time of 28 ms. One full scan was followed by 22 windows with a resolution of 15,000, normalized AGC target of 1,000% and a maximum fill time of 25 ms in profile mode using positive polarity. Precursor ions were fragmented by HCD (NCE 30%). Each of the selected compensation voltage (CV) (−40, −55 and −70 V) was applied to sequential survey scans and MS/MS scans; the MS/MS CV was always paired with the appropriate CV from the corresponding survey scan.

For phosphopeptide samples, 5 µl were loaded and eluted with a 70-min gradient starting at 3% buffer B followed by a stepwise increase to 19% in 40 min, 41% in 20 min, 90% in 5 min and 95% in 5 min. The mass spectrometer was operated in DIA mode with a full scan range of 300–1,400 m/z at 120,000 resolution at 200 m/z and a maximum fill time of 60 ms. One full scan was followed by 32 windows with a resolution of 30,000. Normalized AGC target and maximum fill time were set to 1,000% and 54 ms, respectively, in profile mode using positive polarity. Precursor ions were fragmented by HCD (NCE stepped 25–27.5–30%). For the library generation, we enriched A549 cell lysates for phosphopeptides and measured them with 7 different CV settings (−30, −40, −50, −60, −70, −80 or −90 V) using the same DIA method. The noted CVs were applied to the FAIMS electrodes throughout the analysis.

For the analysis of K-ε-GG peptide samples, half of the samples were loaded. We used a 120-min gradient starting at 3% buffer B followed by a stepwise increase to 7% in 6 min, 20% in 49 min, 36% in 39 min, 45% in 10 min and 95% in 4 min. The buffer B concentration stayed at 95% for 4 min, decreased to 5% in 4 min and stayed there for 4 min. The mass spectrometer was operated in DIA mode with a full scan range of 300–1,350 m/z at 120,000 resolution at m/z 200, normalized AGC target of 300% and a maximum fill time of 20 ms. One full scan was followed by 46 windows with a resolution of 30,000. Normalized AGC target and maximum fill time were set to 1,000% and 54 ms, respectively, in profile mode using positive polarity. Precursor ions were fragmented by HCD (NCE 28%). For K-ε-GG peptide library, we mixed the first replicate of each sample and measured them with eight different CV setting (−35, −40, −45, −50, −55, −60, −70 or −80 V) using the same DIA method.

Processing of raw MS data

AP–MS data. Raw MS data files of AP–MS experiments conducted in DDA mode were processed with MaxQuant (version 1.6.14) using the standard settings and label-free quantification (LFQ) enabled (LFQ min ratio count 1, normalization type none, stabilize large LFQ ratios disabled). Spectra were searched against forward and reverse sequences of the reviewed human proteome including isoforms (UniprotKB, release 2019.10) and C-terminally HA-tagged SARS-CoV-2, SARS-CoV and HCoV proteins by the built-in Andromeda search engine[63].

In-house Julia scripts (https://doi.org/10.5281/zenodo.4541090) were used to define alternative protein groups: only the peptides identified in AP–MS samples were considered for being protein group-specific, protein groups that differed by the single specific peptide or had less than 25% different specific peptides were merged to extend the set of peptides used for protein group quantitation and reduce the number of protein isoform-specific interactions.

Viral protein overexpression and DIA MS data. Spectronaut version 13 (Biognosys) with the default settings was used to generate the proteome libraries from DDA runs by combining files of respective fractionations using the human fasta file (Uniprot, 2019.10, 42 431 entries) and viral bait sequences. Proteome DIA files were analysed using the proteome library with the default settings and disabled cross run normalization.

SARS-CoV-2/SARS-CoV-infected proteome/PTM DIA MS data. Spectronaut version 14 (Biognosys)[64] was used to generate the libraries and analyse all DIA files using the human fasta file (UniprotKB, release 2019.10) and sequences of SARS-CoV-2/SARS-CoV proteins (UniProt, release 2020.08). Orf1a polyprotein sequences were split into separate protein chains according to the cleavage positions specified in the UniProt. For the generation of the PTM-specific libraries, the DIA single CV runs were combined with the actual DIA runs and either phosphorylation at serine, threonine or tyrosine, or GlyGly at lysine, was added as variable modification to default settings. The maximum number of fragment ions per peptide was increased to 25. The proteome DIA files were analysed using direct DIA approach with default settings and disabled cross run normalization. All post-translational modification DIA files were analysed using their respective hybrid library and either phosphorylation at Serine/Threonine/Tyrosine or GlyGly at Lysine was added as an additional variable modification to default settings with LOESS normalization and disabled PTM localization filter.

A collection of in-house Julia scripts(https://doi.org/10.5281/zenodo.4541090) were used to process the elution group (EG) -level Spectronaut reports, identify PTMs and assign EG-level measurements to PTMs. The PTM was considered if at least once it was detected with ≥0.75 localization probability in EG with q-value $\leq 10^{-3}$. For further analysis of given PTM, only the measurements with ≥0.5 localization probability and EG q-value $\leq 10^{-2}$ were used.

Bioinformatic analysis

Unless otherwise specified, the bioinformatic analysis was done in R (version 3.6), Julia (version 1.5) and Python (version 3.8) using a collection of in-house scripts (https://doi.org/10.5281/zenodo.4541090 and https://doi.org/10.5281/zenodo.4541082).

Datasets. The following public datasets were used in the study: Gene Ontology and Reactome annotations (http://download.baderlab.org/EM_Genesets/April_01_2019/Human/UniProt/Human_GO_AllPathways_with_GO_iea_April_01_2019_UniProt.gmt); IntAct Protein Interactions (https://www.ebi.ac.uk/intact/, v2019.12); IntAct Protein Complexes (https://www.ebi.ac.uk/complexportal/home, v2019.12); CORUM Protein Complexes (http://mips.helmholtz-muenchen.de/corum/download/allComplexes.xml.zip, v2018.3); Reactome Functional Interactions (https://reactome.org/download/tools/ReatomeFIs/FIsInGene_020720_with_annotations.txt.zip); Human (v2019.10), Human-CoV, SARS-CoV-2 and SARS-CoV (v2020.08) protein sequences: https://uniprot.org.

Statistical analysis of MS data. MaxQuant and Spectronaut output files were imported into R using in-house maxquantUtils R package (https://doi.org/10.5281/zenodo.4536603). For all MS datasets, the Bayesian linear random effects models were used to define how the abundances of proteins change between the conditions. To specify and fit the models we used the msglm R package (https://doi.org/10.5281/zenodo.4536605), which uses the rstan package (version 2.19)[65] for inferring the posterior distribution of the model parameters. In all the models, the effects corresponding to the experimental conditions have regularized horseshoe+ priors[66], whereas the batch effects have normally distributed priors. Laplacian distribution was used to model the instrumental error of MS intensities. For each MS instrument used, the heteroscedastic intensities noise model was calibrated with the technical replicate MS data of the instrument. These data were also used to calibrate the logit-based model of missing MS data (the probability that the MS instrument will fail to identify the protein given its expected abundance in the sample). The model was fit using unnormalized MS intensities data. Instead of transforming the data by normalization, the inferred protein abundances were scaled by the normalization multiplier of each individual MS sample to match the expected MS intensity of that sample. This allows taking the signal-to-noise variation between the samples into account when fitting the model. Due to high computational intensity, the model was applied to each protein group separately. For all the models, 4,000 iterations (2,000 warmup + 2,000 sampling) of the no-U-turn Markov Chain Monte Carlo were performed in 7 or 8 independent chains, every 4th sample was collected for posterior distribution of the model parameters. For estimating the statistical significance of protein abundance changes between the two experimental conditions, the *P*-value was defined as the probability that a random sample from the posterior distribution of the first condition would be smaller (or larger) than a random sample drawn from the second condition. No-multiple hypothesis testing corrections were applied, since this is handled by the choice of the model priors.

Statistical analysis of AP–MS data and filtering for specific interactions. The statistical model was applied directly to the MS1 intensities of protein group-specific LC peaks (evidence.txt table of MaxQuant output). In R GLM formula language, the model could be specified as

$$\log(\text{Intensity}) \approx 1 + \text{APMS} + \text{Bait} + \text{Bait} : \text{Virus} + \text{MS1peak} + \text{MSbatch},$$

where the APMS effect models the average shift of intensities in AP–MS data in comparison to full proteome samples, Bait is the average enrichment of a protein in AP–MS experiments of homologous proteins of both SARS-CoV and SARS-CoV-2, and Bait:Virus corresponds to the virus-specific changes in protein enrichment. MS1peak is the log ratio between the intensity of a given peak and the total protein abundance (the peak is defined by its peptide sequence, PTMs and the charge; it is assumed that the peak ratios do not depend on experimental conditions[67]), and MSbatch accounts for batch-specific variations of protein intensity. APMS, Bait and Bait:Virus effects were used to reconstruct the batch effect-free abundance of the protein in AP–MS samples.

The modelling provided the enrichment estimates for each protein in each AP experiment. Specific AP–MS interactions had to pass the two tests. In the first test, the enrichment of the candidate protein in a given bait AP was compared against the background, which was dynamically defined for each interaction to contain the data from all other baits, where the abundance of the candidate was within 50–90% percentile range (excluding top 10% baits from the background allowed the protein to be shared by a few baits in the resulting AP–MS network). The non-targeting control and Gaussian luciferase baits were always preserved in the background. Similarly, to filter out any potential side-effects of very high bait protein expression, the ORF3 homologues were always present in the background of M interactors and vice versa. To rule out the influence of the batch effects, the second test was applied. It was defined similarly to the first one, but the background was constrained to the baits of the same batch, and 40–80% percentile range was used. In both tests, the protein has to be fourfold enriched over the background (16 fold for highly expressed baits: ORF3, M, NSP13, NSP5, NSP6, ORF3a, ORF7b, ORF8b and HCoV-229E ORF4a) with $P\text{-value} \leq 10^{-3}$.

Additionally, we excluded the proteins that, in the viral protein expression data, have shown upregulation, and their enrichment in AP–MS data was less than 16 times stronger than observed upregulation effects. Finally, to exclude the carryover of material between the samples sequentially analysed by MS, we removed the putative interactors, which were also enriched at higher levels in the samples of the preceding bait, or the one before it.

For the analysis of interaction specificity between the homologous viral proteins, we estimated the significance of interaction enrichment difference (corrected by the average difference between the enrichment of the shared interactors to adjust for the bait expression variation). Specific interactions have to be fourfold enriched in comparison to the homologue with $P\text{-value} \leq 10^{-3}$.

Statistical analysis of DIA proteome effects upon viral protein overexpression. The statistical model of the viral protein overexpression dataset was similar to AP–MS data, except that protein-level intensities provided by Spectronaut were used. The PCA analysis of the protein intensities has identified that the second principal component is associated with the batch-dependent variations between the samples. To exclude their influence, this principal component was added to the experimental design matrix as an additional batch effect.

As with AP–MS data, the two statistical tests were used to identify the significantly regulated proteins (column 'is_change' in Supplementary Table 3). First, the absolute value of median $\log_2$-fold change of the protein abundance upon overexpression of a given viral protein in comparison to the background had to be above 1.0 with $P\text{-value} \leq 10^{-3}$. The background was individually defined for each analysed protein. It was composed of experiments, where the abundance of given protein was within the 20–80% percentile range of all measured samples. Second, the protein had to be significantly regulated (same median $\log_2$-fold change and *P*-value thresholds applied) against the batch-specific background (defined similarly to the global background, but using only the samples of the same batch).

An additional stringent criterion was applied to select the most significant changes (column 'is_top_change' in Supplementary Table 3; Extended Data Fig. 1i).

For each protein we classified bait-induced changes as: 'high' when $|\text{median} \log_2 \text{fold-change}| \geq 1$ and $P\text{-value} \leq 10^{-10}$ both in background and batch comparisons; 'medium' if $10^{-10} < P\text{-value} \leq 10^{-4}$ with same fold-change requirement; and 'low' if $10^{-4} < P\text{-value} \leq 10^{-2}$ with the same fold-change requirement. All other changes were considered non-significant.

We then required that 'shared' top-regulated proteins should have exactly one pair of SARS-CoV-2 and SARS-CoV high- or medium-significant homologous baits among the baits with either up- or down-regulated changes and no other baits with significant changes of the same type.

We further defined 'SARS-CoV-2-specific' or 'SARS-CoV-specific' top-regulated proteins to be the ones with exactly one high-significant change, and no other significant changes of the same sign. For 'specific' hits we additionally required that in the comparison of high-significant bait to its homologue $|\text{median} \log_2 \text{fold-change}| \geq 1$ and $P\text{-value} \leq 10^{-3}$. When the homologous bait was missing (SARS-CoV-2 NSP1, SARS-CoV ORF8a and SARS-CoV ORF8b), we instead required that in the comparison of the high-significant change to the background $|\text{median} \log_2 \text{fold-change}| \geq 1.5$.

The resulting network of most affected proteins was imported and prepared for publication in Cytoscape v.3.8.1[68].

Statistical analysis of DIA proteomic data of SARS-CoV-2 and SARS-CoV-infected A549-ACE2 cells. Similarly to the AP–MS DDA data, the linear Bayesian model was applied to the EG-level intensities. To model the protein intensity, the following linear model (in R notation) was used:

$$\log(\text{Intensity}(t)) \sim 1 + \sum_{t_i \leq t} (\text{after}(t_i) + (\text{infection } \pm \text{CoV2}) : \text{after}(t_i)) + \text{EG},$$

where the after(t_i) effect corresponds to the protein abundance changes in mock-infected samples that happened between t_{i-1} and t_i after infection and it is applied to the modelled intensity at all time points starting from t_i; infection:after(t_i) ($t_i = 6, 12, 24$) is the common effect of SARS-CoV-2 and SARS-CoV infections occurring between t_{i-1} and t_i; CoV2:after(t_i) is the virus-specific effect within t_{i-1} and t_i hpi that is added to the log intensity for SARS-CoV-2-infected samples and subtracted from the intensity for SARS-CoV ones; EG is the elution group-specific shift in the measured log-intensities.

The absolute value of median $\log_2$ fold change between the conditions above 0.25 and the corresponding unadjusted $P\text{-value} \leq 10^{-3}$ were used to define the significant changes at a given time point in comparison to mock infection. We also required that the protein group is quantified in at least two replicates of at least one of the compared conditions. Additionally, if for one of the viruses (for example, SARS-CoV-2) only the less stringent condition (|median $\log_2$ fold-change| ≥ 0.125, P-value $\leq 10^{-2}$) was fulfilled, but the change was significant in the infection of the other virus (SARS-CoV), and the difference between the viruses was not significant, the observed changes were considered significant for both viruses.

Statistical analysis of DIA phosphoproteome and ubiquitinome data of SARS-CoV-2 and SARS-CoV infections. The data from single-double- and triple-modified peptides were analysed separately and, for a given PTM, the most significant result was reported.

The data were analysed with the same Bayesian linear model as proteome SARS-CoV and SARS-CoV-2 infection data. In addition to the intensities normalization, for each replicate sample the scale of the effects in the experimental design matrix was adjusted, so that on average the correlation between log fold changes of the replicates was 1:1. The same logic as for the proteome analysis, was applied to identify significant changes, but the median $\log_2$ fold change had to be larger than 0.5, or 0.25 for the less stringent test. We additionally required that the PTM peptides are quantified in at least two replicates of at least one of the compared conditions. To ignore the changes in PTM site intensities that are due to proteome-level regulation, we excluded PTM sites on significantly regulated proteins if the directions of protein and PTM site changes were the same and the difference between their median $\log_2$ fold changes was less than two. Phosphoproteomics data were further analysed with Ingenuity Pathway Analysis software (Qiagen; https://www.qiagenbioinformatics.com/products/ingenuity-pathway-analysis)

Transcriptomic analysis of SARS-CoV-2 and SARS-CoV infected A549-ACE2 cells. For the analysis of the transcriptome data, Gencode gene annotations v28 and the human reference genome GRCh38 were derived from the Gencode homepage (EMBL-EBI). Viral genomes were derived from GenBank (SARS-CoV-2 - LR824570.1, and SARS-CoV - AY291315.1). Dropseq tool v1.12 was used for mapping raw sequencing data to the reference genome. The resulting UMI filtered count matrix was imported into R v3.4.4. CPM (counts per million) values were calculated for the raw data and genes having a mean cpm value less than 1 were removed from the dataset. A dummy variable combining the covariates infection status (mock, SARS-CoV, SARS-CoV-2) and time point was used for modelling the data within Limma (v3.46.0)[69].

Data were transformed with the Voom method[69] followed by quantile normalization. Differential testing was performed between infection states at individual time points by calculating moderated t-statistics and P-values for each host gene. A gene was considered to be significantly regulated if the false discovery rate-adjusted P-value was below 0.05.

Gene set enrichment analysis. We used Gene Ontology, Reactome and other EnrichmentMap gene sets of human proteins (version 2020.10)[70] as well as protein complexes annotations from IntAct Complex Portal (version 2019.11)[71] and CORUM (version 2019)[72]. PhosphoSitePlus (version 2020.08) was used for known kinase-substrate and regulatory sites annotations, Perseus (version 1.6.14.0)[73] was used for annotation of known kinase motifs. For transcription factor enrichment analysis (Extended Data Fig. 2e) the significantly regulated transcripts were submitted to ChEA3 web-based application[74] and ENCODE data on transcription factor–target gene associations were used[75].

To find the non-redundant collection of annotations describing the unique and shared features of multiple experiments in a dataset (Fig. 1d, Extended Data Fig. 2l, m), we used in-house Julia package OptEnrichedSetCover.jl (https://doi.org/10.5281/zenodo.4536596), which employs evolutionary multi-objective optimization technique to find a collection of annotation terms that have both significant enrichments in the individual experiments and minimal pairwise overlaps.

The resulting set of terms was further filtered by requiring that the annotation term has to be significant with the specified unadjusted Fisher's exact test P-value cut-off in at least one of the experiments or comparisons (the specific cut-off value is indicated in the figure legend of the corresponding enrichment analysis).

The generation of diagonally-split heat maps was done with the VegaLite.jl package (https://github.com/queryverse/VegaLite.jl).

Viral PTMs alignment. For matching the PTMs of SARS-CoV-2 and SARS-CoV the protein sequences were aligned using the BioAlignments.jl Julia package (v.2.0; https://github.com/BioJulia/BioAlignments.jl) with the Needleman–Wunsch algorithm using BLOSUM80 substitution matrix, and applying −5 and −3 penalties for the gap and extension, respectively.

For the cellular proteins, we required that the viral phosphorylation or ubiquitination site is observed with q-value $\leq 10^{-3}$ and localization probability ≥ 0.75. For the PTMs with lower confidence (q-value $\leq 10^{-2}$ and localization probability ≥ 0.5) we required that the same site is observed with high confidence at the matching position of the orthologous protein of the other virus.

Network diffusion analysis. To systematically detect functional interactions, which may connect the cellular targets of each viral protein (interactome dataset) with the downstream changes it induces on proteome level (effectome dataset), we have used the network diffusion-based HierarchicalHotNet method[36] as implemented in Julia package HierarchicalHotNet.jl (https://doi.org/10.5281/zenodo.4536590). Specifically, for network diffusion with restart, we used the ReactomeFI network (version 2019)[35] of cellular functional interactions, reversing the direction of functional interaction (for example, replacing kinase→substrate interaction with substrate→kinase). The proteins with significant abundance changes upon bait overexpression (|median($\log_2$ fold change)| ≥ 0.25, $P \leq 10^{-2}$ both in the comparison against the controls and against the baits of the same batch) were used as the sources of signal diffusion with weights set to $w_i = \sqrt{|\text{median}\log_2(\text{fold change})| \cdot |\log_{10} P\text{-value}|}$, otherwise the node weight was set to zero. The weight of the edge $g_i \rightarrow g_j$ was set to $w_{i,j} = 1 + w_j$. The restart probability was set to 0.4, as suggested in the original publication, so that the probability of the random walk to stay in the direct neighbourhood of the node is the same as the probability to visit more distant nodes. To find the optimal cutting threshold of the resulting hierarchical tree of strongly connected components (SCCs) of the weighted graph corresponding to the stationary distribution of signal diffusion and to confirm the relevance of predicted functional connections, the same procedure was applied to 1,000 random permutations of vertex weights as described in Reyna et al.[36] (vertex weights are randomly shuffled between the vertices with similar in and out degrees). Since cutting the tree of SCCs at any threshold t (keeping only the edges with weights above t) and collapsing each resulting SCC into a single node produces the directed acyclic graph of connections between SCCs, it allowed efficient enumeration of the paths from the 'source' nodes (proteins strongly perturbed by viral protein expression with vertex weight w, $w \geq 1.5$) to the 'sink' nodes (interactors of the viral protein). At each threshold t, the average inverse of the path length from source to sink nodes was calculated as:

$$L_{\text{avg}}^{-1}(t) = \frac{1}{N_{\text{source}} \cdot N_{\text{sink}}} \sum_{p} L_{\text{SCC}}^{-1}(p),$$

where N_{source} is the number of sources, N_{sink} is the number of sinks, $L_{\text{SCC}}(p)$ is the number of SCCs that the given path p from source to sink goes through, and the sum is for all paths from sources to sinks. The metric changes from 1 (all sources and sinks in the same SCC) to 0 (no or infinitely long paths between sources and sinks). For the generation of the diffusion networks we were using the t_{opt} threshold that maximized the difference between $L_{\text{avg}}^{-1}(t)$ for the real data and the third quartile of $L_{\text{avg}}^{-1}(t)$ for randomly shuffled data.

In the generated SCC networks, the direction of the edges was reverted back, and the results were exported as GraphML files using in-house Julia scripts (https://doi.org/10.5281/zenodo.4541090). The catalogue of the networks for each viral bait is available as Supplementary Data 1.

To assess the significance of edges in the resulting network, we calculated the *P*-value of the edge $g_i \to g_j$ as the probability that the transition probability between the given pair of genes based on permuted data is higher than the transition probability based on the real data:

$$P(w_{\mathrm{real}}(g_i, g_j) \le w_{\mathrm{perm}}(g_i, g_j)).$$

This *P*-value was stored as the 'prob_perm_walkweight_greater' edge attribute of GraphML output. The specific subnetworks predicted by the network diffusion (Fig. 4b–d) were filtered for edges with $P \le 0.05$.

When the $g_i \to g_j$ connection was not present in the ReactomeFI network, to recover the potential short pathways connecting g_i and g_j, ReactomeFI was searched for intermediate g_k nodes, such that the edges $g_i \to g_k$ and $g_k \to g_j$ are present in ReactomeFI. The list of these short pathways is provided as the 'flowpaths' edge attribute in GraphML output.

The GraphML output of network diffusion was prepared for publication using yEd (v.3.20; https://www.yworks.com).

Intersection with other SARS coronavirus datasets. The intersection between the data generated by this study and other publicly available datasets was done using the information from respective supplementary tables. When multiple viruses were used in a study, only the comparisons with SARS-CoV and SARS-CoV-2 were included. For time-resolved data, all time points up to 24 hpi were considered. The dataset coverage was defined as the number of reported distinct protein groups for proteomic studies and genes for transcriptomic studies. Confident interactions or significant regulations were filtered according to the criteria specified in the original study. A hit was considered as 'confirmed' when it was significant both in the present study and the external data and showed the same trend.

qRT–PCR analysis

RNA isolation from SARS-CoV and SARS-CoV-2 infected A549-ACE2 cells was performed as described above (Qiagen). Five hundred nanograms total RNA was used for reverse transcription with PrimeScript RT with gDNA eraser (Takara). For relative transcript quantification PowerUp SYBR Green (Applied Biosystems) was used. Primer sequences can be provided upon request.

Co-immunoprecipitation and western blot analysis

HEK293T cells were transfected with pWPI plasmid encoding single HA-tagged viral proteins, alone or together with pTO-SII-HA expressing host factor of interest. 48 h after transfection, cells were washed in PBS, flash frozen in liquid nitrogen and kept at −80 °C until further processing. Co-immunoprecipitation experiments were performed as described previously[55,56]. In brief, cells were lysed in lysis buffer (50 mM Tris-HCl pH 7.5, 100 mM NaCl, 1.5 mM $MgCl_2$, 0.2% (v/v) NP-40, 5% (v/v) glycerol, cOmplete protease inhibitor cocktail (Roche), 0.5% (v/v) 750 U μl^{-1} Sm DNase) and sonicated (5 min, 4 °C, 30 s on, 30 s off, low settings; Bioruptor, Diagenode SA). HA or Streptactin beads were added to cleared lysates and samples were incubated for 3 h at 4 °C under constant rotation. Beads were washed six times in the lysis buffer and resuspended in 1× SDS sample buffer 62.5 mM Tris-HCl pH 6.8, 2% SDS, 10% glycerol, 50 mM DTT, 0.01% bromophenol blue). After boiling for 5 min at 95 °C, a fraction of the input lysate and elution were loaded on NuPAGE Novex 4–12% Bis-Tris (Invitrogen), and further submitted to western blotting using Amersham Protran nitrocellulose membranes. Imaging was performed by HRP luminescence (ECL, Perkin Elmer).

SARS-CoV-2 infected A549-ACE2 cell lysates were sonicated (10 min, 4 °C, 30 s on, 30 s off, low settings; Bioruptor, Diagenode). Protein concentration was adjusted based on Pierce660 assay supplemented with ionic detergent compatibility reagent. After boiling for 5 min at 95 °C and brief centrifugation at maximum speed, the samples were loaded on NuPAGE Novex 4–12% Bis-Tris (Invitrogen), and blotted onto 0.22 μm Amersham Protran nitrocellulose membranes (Merck). Primary and secondary antibody stainings were performed according to the manufacturer's recommendations. Imaging was performed by HRP luminescence using Femto kit (ThermoFischer Scientific) or Western Lightning PlusECL kit (Perkin Elmer).

Mapping of post-translational modification sites on the N CTD structure

N CTD dimers of SARS-CoV-2 (PDB: 6YUN) and SARS-CoV (PDB: 2CJR) were superimposed by aligning the α-carbons backbone over 111 residues (from position 253/254 to position 364/365 following SARS-CoV-2/SARS-CoV numbering) by using the tool MatchMaker[76] as implemented in the Chimera software[77]. Ubiquitination sites were visually inspected and mapped by using the PyMOL software (https://pymol.org). Phosphorylation on Ser310/311 was simulated in silico by using the PyTMs plugin as implemented in PyMOL[78]. Inter-chain residue contacts, dimer interface area, free energy and complex stability were comparatively analysed between non-phosphorylated and phosphorylated SARS-CoV-2 and SARS-CoV N CTD by using the PDBePISA server[79]. Poisson–Boltzmann electrostatic surface potential of native and post-translationally modified N CTD was calculated by using the PBEQ Solver tool on the CHARMM-GUI server by preserving existing hydrogen bonds[80]. Molecular graphics depictions were produced with the PyMOL software.

Reporter assay and IFN bioassay

The following reporter constructs were used in this study: pISRE-luc was purchased from Stratagene, EF1-α-ren was obtained from E. Gürlevik (Department of Gastroenterology, Hepatology and Endocrinology, Hannover Medical School, Germany), pCAGGS-Flag-RIG-I was obtained from C. Basler (Department of Microbiology, Mount Sinai School of Medicine, USA), pIRF1-GAS-ff-luc, pWPI-SMN1-flag and pWPI-NS5 (ZIKV)-HA was described previously[56,81].

For the reporter assay, HEK293-R1 cells were plated in 24-well plates 24 h before transfection. Firefly reporter and *Renilla* transfection control were transfected together with plasmids expressing viral proteins using polyethylenimine (PEI, Polysciences) for untreated and treated conditions. In 18 h cells were stimulated for 8 h with a corresponding inducer and collected in the passive lysis buffer (Promega). Luminescence of Firefly and *Renilla* luciferases was measured using dual-luciferase-reporter assay (Promega) according to the manufacturer's instructions in a microplate reader (Tecan).

Total amounts of IFN-α and IFN-β in cell supernatants were measured by using 293T cells stably expressing the firefly luciferase gene under the control of the mouse Mx1 promoter (Mx1-luc reporter cells)[82]. In brief, HEK293-R1 cells were seeded, transfected with pCAGGS-flag-RIG-I plus viral protein constructs and stimulated as described above. Cell supernatants were collected in 8 h. Mx1-luc reporter cells were seeded into 96-well plates in triplicates and were treated 24 h later with supernatants. At 16 h after incubation, cells were lysed in the passive lysis buffer (Promega), and luminescence was measured with a microplate reader (Tecan). The assay sensitivity was determined by a standard curve.

Viral inhibitor assay

A549-ACE2 cells were seeded into 96-well plates in DMEM medium (10% FCS, 100 μg ml^{-1} streptomycin, 100 IU ml^{-1} penicillin) one day before infection. Six hours before infection, or at the time of infection, the medium was replaced with 100 μl of DMEM medium containing either the compounds of interest or DMSO as a control. Infection was performed by adding 10 μl of SARS-CoV-2-GFP (MOI of 3) per well and plates were placed in the IncuCyte S3 Live-Cell Analysis System (Essen

Bioscience), where whole well real-time images of mock (phase channel) and infected (GFP and phase channel) cells were captured every 4 h for 48 h. Cell viability (mock) and virus growth (mock and infected) were assessed as the cell confluence per well (phase area) and GFP area normalized by cell confluence per well (GFP area/phase area) respectively using IncuCyte S3 Software (Essen Bioscience; version 2019B rev2).

For comparative analysis of antiviral treatment activity against SARS-CoV and SARS-CoV-2, A549-ACE2 cells were seeded in 24-well plates, as previously described. Treatment was performed for 6 h with 0.5 ml of DMEM medium containing either the compounds of interest or DMSO as a control, and infected with SARS-CoV-Frankfurt-1 or SARS-CoV-2-MUC-IMB-1 (MOI of 1) for 24 h. Total cellular RNA was collected and analysed by RT–qPCR, as previously described.

Reporting summary

Further information on research design is available in the Nature Research Reporting Summary linked to this paper.

Data availability

The raw sequencing data for this study have been deposited with the ENA at EMBL-EBI under accession number PRJEB38744. The mass spectrometry proteomics data have been deposited to the ProteomeXchange Consortium via the PRIDE[83] partner repository with the dataset identifiers PXD022282, PXD020461 and PXD020222. Protein interactions identified in this study have been submitted to the IMEx (https://www.imexconsortium.org) consortium through IntAct[84] with the identifier IM-28109. The data and analysis results are accessible online via the interactive web interface at https://covinet.innatelab.org.

Code availability

In-house R and Julia packages and scripts used for the bioinformatics analysis of the data have been deposited to public GitHub repositories: https://doi.org/10.5281/zenodo.4536605, https://doi.org/10.5281/zenodo.4536603, https://doi.org/10.5281/zenodo.4536590, https://doi.org/10.5281/zenodo.4536596, https://doi.org/10.5281/zenodo.4541090 and https://doi.org/10.5281/zenodo.4541082.

55. Hubel, P. et al. A protein-interaction network of interferon-stimulated genes extends the innate immune system landscape. *Nat. Immunol*. **20**, 493–502 (2019).
56. Scaturro, P. et al. An orthogonal proteomic survey uncovers novel Zika virus host factors. *Nature* **561**, 253–257 (2018).
57. Hoffmann, M. et al. SARS-CoV-2 cell entry depends on ACE2 and TMPRSS2 and is blocked by a clinically proven protease inhibitor. *Cell* **181**, 271–280.e8 (2020).
58. Gebhardt, A. et al. The alternative cap-binding complex is required for antiviral defense in vivo. *PLoS Pathog*. **15**, e1008155 (2019).
59. Goldeck, M., Schlee, M., Hartmann, G. & Hornung, V. Enzymatic synthesis and purification of a defined RIG-I ligand. *Methods Mol. Biol*. **1169**, 15–25 (2014).
60. Kulak, N. A., Geyer, P. E. & Mann, M. Loss-less nano-fractionator for high sensitivity, high coverage proteomics. *Mol. Cell. Proteomics* **16**, 694–705 (2017).
61. Kulak, N. A., Pichler, G., Paron, I., Nagaraj, N. & Mann, M. Minimal, encapsulated proteomic-sample processing applied to copy-number estimation in eukaryotic cells. *Nat. Methods* **11**, 319–324 (2014).
62. Udeshi, N. D., Mertins, P., Svinkina, T. & Carr, S. A. Large-scale identification of ubiquitination sites by mass spectrometry. *Nat. Protoc*. **8**, 1950–1960 (2013).
63. Tyanova, S., Temu, T. & Cox, J. The MaxQuant computational platform for mass spectrometry-based shotgun proteomics. *Nat. Protoc*. **11**, 2301–2319 (2016).
64. Bober, M. & Miladinovic, S. General guidelines for validation of decoy models for HRM/DIA/SWATH as exemplified using Spectronaut. *F1000posters* https://f1000research.com/posters/1097512 (2015).
65. Carpenter, B. et al. Stan: a probabilistic programming language. *J. Stat. Softw*. **76**, 1–32 (2017).
66. Bhadra, A., Datta, J., Polson, N. G. & Willard, B. The Horseshoe+ estimator of ultra-sparse signals. *Bayesian Anal*. **12**, 1105–1131 (2017).
67. Goeminne, L. J. E., Gevaert, K. & Clement, L. Peptide-level robust ridge regression improves estimation, sensitivity, and specificity in data-dependent quantitative label-free shotgun proteomics. *Mol. Cell. Proteomics* **15**, 657–668 (2016).
68. Shannon, P. et al. Cytoscape: a software environment for integrated models of biomolecular interaction networks. *Genome Res*. **13**, 2498–2504 (2003).
69. Ritchie, M. E. et al. limma powers differential expression analyses for RNA-sequencing and microarray studies. *Nucleic Acids Res*. **43**, e47 (2015).
70. Merico, D., Isserlin, R., Stueker, O., Emili, A. & Bader, G. D. Enrichment map: a network-based method for gene-set enrichment visualization and interpretation. *PLoS ONE* **5**, e13984 (2010).
71. Meldal, B. H. M. et al. Complex Portal 2018: extended content and enhanced visualization tools for macromolecular complexes. *Nucleic Acids Res*. **47** (D1), D550–D558 (2019).
72. Giurgiu, M. et al. CORUM: the comprehensive resource of mammalian protein complexes-2019. *Nucleic Acids Res*. **47** (D1), D559–D563 (2019).
73. Tyanova, S. et al. The Perseus computational platform for comprehensive analysis of (prote)omics data. *Nat. Methods* **13**, 731–740 (2016).
74. Keenan, A. B. et al. ChEA3: transcription factor enrichment analysis by orthogonal omics integration. *Nucleic Acids Res*. **47** (W1), W212–W224 (2019).
75. Landt, S. G. et al. ChIP-seq guidelines and practices of the ENCODE and modENCODE consortia. *Genome Res*. **22**, 1813–1831 (2012).
76. Meng, E. C., Pettersen, E. F., Couch, G. S., Huang, C. C. & Ferrin, T. E. Tools for integrated sequence-structure analysis with UCSF Chimera. *BMC Bioinformatics* **7**, 339 (2006).
77. Pettersen, E. F. et al. UCSF Chimera–a visualization system for exploratory research and analysis. *J. Comput. Chem*. **25**, 1605–1612 (2004).
78. Warnecke, A., Sandalova, T., Achour, A. & Harris, R. A. PyTMs: a useful PyMOL plugin for modeling common post-translational modifications. *BMC Bioinformatics* **15**, 370 (2014).
79. Paxman, J. J. & Heras, B. Bioinformatics tools and resources for analyzing protein structures. *Methods Mol. Biol*. **1549**, 209–220 (2017).
80. Jo, S., Vargyas, M., Vasko-Szedlar, J., Roux, B. & Im, W. PBEQ-Solver for online visualization of electrostatic potential of biomolecules. *Nucleic Acids Res*. **36**, W270–W275 (2008).
81. Vogt, C. et al. The interferon antagonist ML protein of thogoto virus targets general transcription factor IIB. *J. Virol*. **82**, 11446–11453 (2008).
82. Jorns, C. et al. Rapid and simple detection of IFN-neutralizing antibodies in chronic hepatitis C non-responsive to IFN-alpha. *J. Med. Virol*. **78**, 74–82 (2006).
83. Perez-Riverol, Y. et al. The PRIDE database and related tools and resources in 2019: improving support for quantification data. *Nucleic Acids Res*. **47** (D1), D442–D450 (2019).
84. Orchard, S. et al. The MIntAct project–IntAct as a common curation platform for 11 molecular interaction databases. *Nucleic Acids Res*. **42**, D358–D363 (2014).

Acknowledgements We thank S. Pöhlmann for sharing ACE2 plasmids and R. Baier for technical assistance, M. Trojan for advice on drugs, J. Pancorbo and J. Albert-von der Gönna from the Leibniz Supercomputing Centre (https://www.lrz.de) for technical assistance. We further thank the Karl Max von Bauernfeind–Verein for support for the screening microscope. Work in the authors' laboratories was supported by an ERC consolidator grant (ERC-CoG ProDAP, 817798), the German Research Foundation (PI 1084/3, PI 1084/4, PI 1084/5, TRR179/TP11, TRR237/A07), the Bavarian State Ministry of Science and Arts (Bavarian Research Network FOR-COVID) and the German Federal Ministry of Education and Research (COVINET) to A. Pichlmair. This work was also supported by the German Federal Ministry of Education and Research (CLINSPECT-M) to B.K. A.W. was supported by the China Scholarship Council (CSC). The work of J.Z. was supported by the German Research Foundation (SFB1021, A01 and B01; KFO309, P3), the State of Hessen through the LOEWE Program (DRUID, B02) and the German Ministry for Education and Research (COVINET, RAPID). The work of P.S. is supported by the Free and Hanseatic City of Hamburg and the German Research Foundation (SC 314/1-1). We thank R. Polakiewicz, F. Gnad and Cell Signaling Technology for the gift of the PTMScan Ubiquitin Remnant Motif (K-ε-GG) Kits.

Author contributions Conceptualization: A.S., V. Girault, V. Grass, O.K., V.B., C.U., D.A.H., Y.H., J.Z., P.S., M.M. and A. Pichlmair. Investigation: V. Girault, V. Grass, O.K., V.B., C.U., D.A.H., Y.H., L.O., A.W., A. Piras, F.M.H., M.C.T., I.P., T.M.L., R.E., J.J. and P.S. Data analysis: A.S., V. Girault, V. Grass, V.B., O.K., C.U., D.A.H., Y.H., M.S.H., F.M.H., M.C.T., L.Z., T.E. and M.R. Funding acquisition: R.W., B.K., U.P., R.R., J.Z., V.T., M.M. and A. Pichlmair. Supervision: M.M., R.R. and A. Pichlmair. Writing: A.S., V. Girault, V. Grass, O.K., V.B., C.U., D.A.H., Y.H., L.Z., M.M. and A. Pichlmair.

Competing interests The authors declare no competing interests.

Additional information

Supplementary information The online version contains supplementary material available at https://doi.org/10.1038/s41586-021-03493-4.

Correspondence and requests for materials should be addressed to A.P.

Peer review information *Nature* thanks Ivan Dikic, Trey Ideker, Michael Weekes, and the other, anonymous, reviewer(s) for their contribution to the peer review of this work. Peer reviewer reports are available.

Reprints and permissions information is available at http://www.nature.com/reprints.

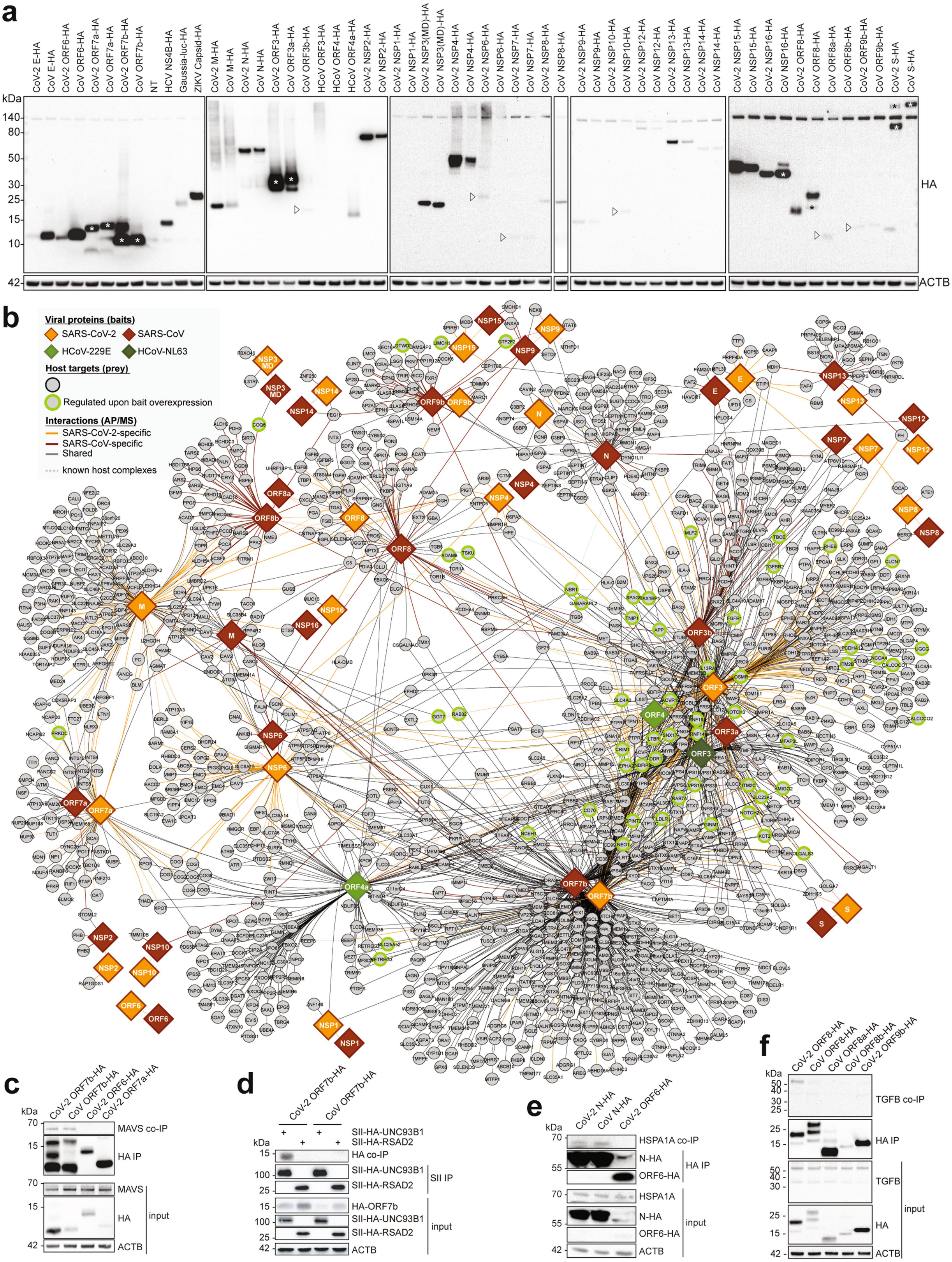

Extended Data Fig. 1 | See next page for caption.

Extended Data Fig. 1 | SARS-CoV-2 and SARS-CoV proteins expressed in A549 cells target host proteins. a, Expression of HA-tagged viral proteins in stably transduced A549 cells, used in AP–MS and proteome expression measurements. When several bands are present in a single lane, * or ► mark the band with the expected molecular weight (*n* = 4 independent experiments). For gel source data, see Supplementary Fig. 1. **b**, Extended version of the virus-host protein–protein interaction network with 24 SARS-CoV-2 and 27 SARS-CoV proteins, as well as ORF3 of HCoV-NL63 and ORF4 and ORF4a of HCoV-229E, used as baits. Host targets regulated upon viral protein overexpression are highlighted (see the in-plot legend). **c**–**f**, Co-precipitation experiments in HEK293T cells showing a specific enrichment of endogenous MAVS co-precipitated with C-terminal HA-tagged ORF7b of SARS-CoV-2 and SARS-CoV (negative controls: SARS-CoV-2 ORF6-HA, ORF7a-HA) (**c**), ORF7b-HA of SARS-CoV-2 and SARS-CoV co-precipitated with SII-HA-UNC93B1 (control precipitation: SII-HA-RSAD2) (**d**), endogenous HSPA1A co-precipitated with N-HA of SARS-CoV-2 and SARS-CoV (control: SARS-CoV-2 ORF6-HA) (**e**) and endogenous TGF-β with ORF8-HA of SARS-CoV-2 vs ORF8-HA, ORF8a-HA, ORF8b-HA of SARS-CoV or ORF9b-HA of SARS-CoV-2 (**f**), (*n* = 2 independent experiments). For gel source data, see Supplementary Fig. 1. AP–MS: affinity-purification coupled to mass spectrometry; MD: Macro domain; NSP: Non-structural protein.

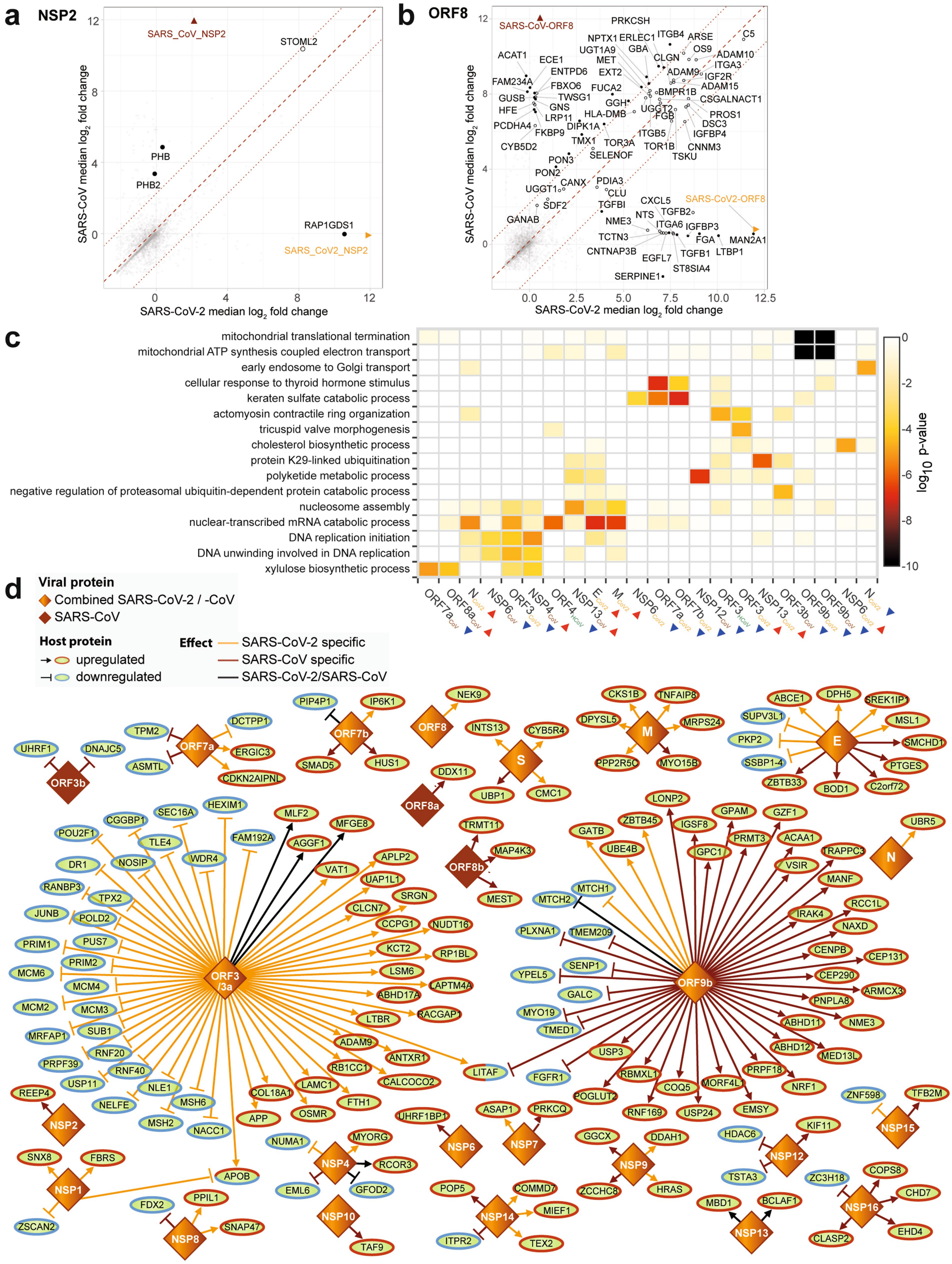

Extended Data Fig. 2 | SARS-CoV-2 and SARS-CoV proteins trigger shared and specific interactions with host factors, and induce changes to the host proteome. a, **b**, Differential enrichment of proteins in NSP2 (**a**) and ORF8 (**b**) of SARS-CoV-2 (*x*-axis) vs SARS-CoV (*y*-axis) AP–MS experiments (*n* = 4 independent experiments). **c**, Gene Ontology Biological Processes enriched among the cellular proteins that are up- (red arrow) or down- (blue arrow) regulated upon overexpression of individual viral proteins. **d**, The most affected proteins from the effectome data of protein changes upon viral bait overexpression in A549 cells (see materials and methods for the exact protein selection criteria). Homologous viral proteins are displayed as a single node. Shared and virus-specific effects are denoted by the edge colour. NSP: Non-structural protein.

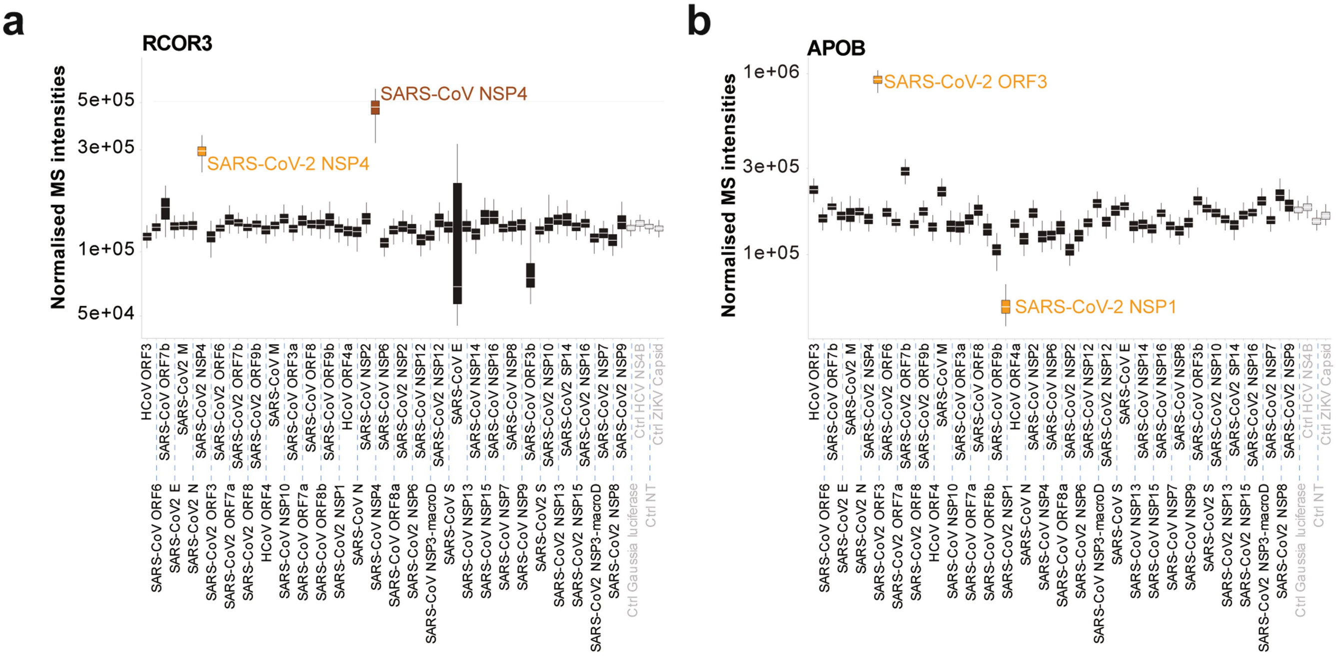

Extended Data Fig. 3 | RCOR3 and APOB regulation upon SARS-CoV-2 and SARS-CoV protein overexpression. a, **b**, Normalized intensities of selected candidates specifically perturbed by individual viral proteins: RCOR3 was upregulated both by SARS-CoV-2 and SARS-CoV NSP4 proteins (**a**), APOB was upregulated by ORF3 and downregulated by NSP1 specifically to SARS-CoV-2 (**b**). The box and the whiskers represent 50% and 95% confidence intervals, and the white line corresponds to the median of the $\log_2$ fold change upon viral protein overexpression ($n = 4$ independent experiments).

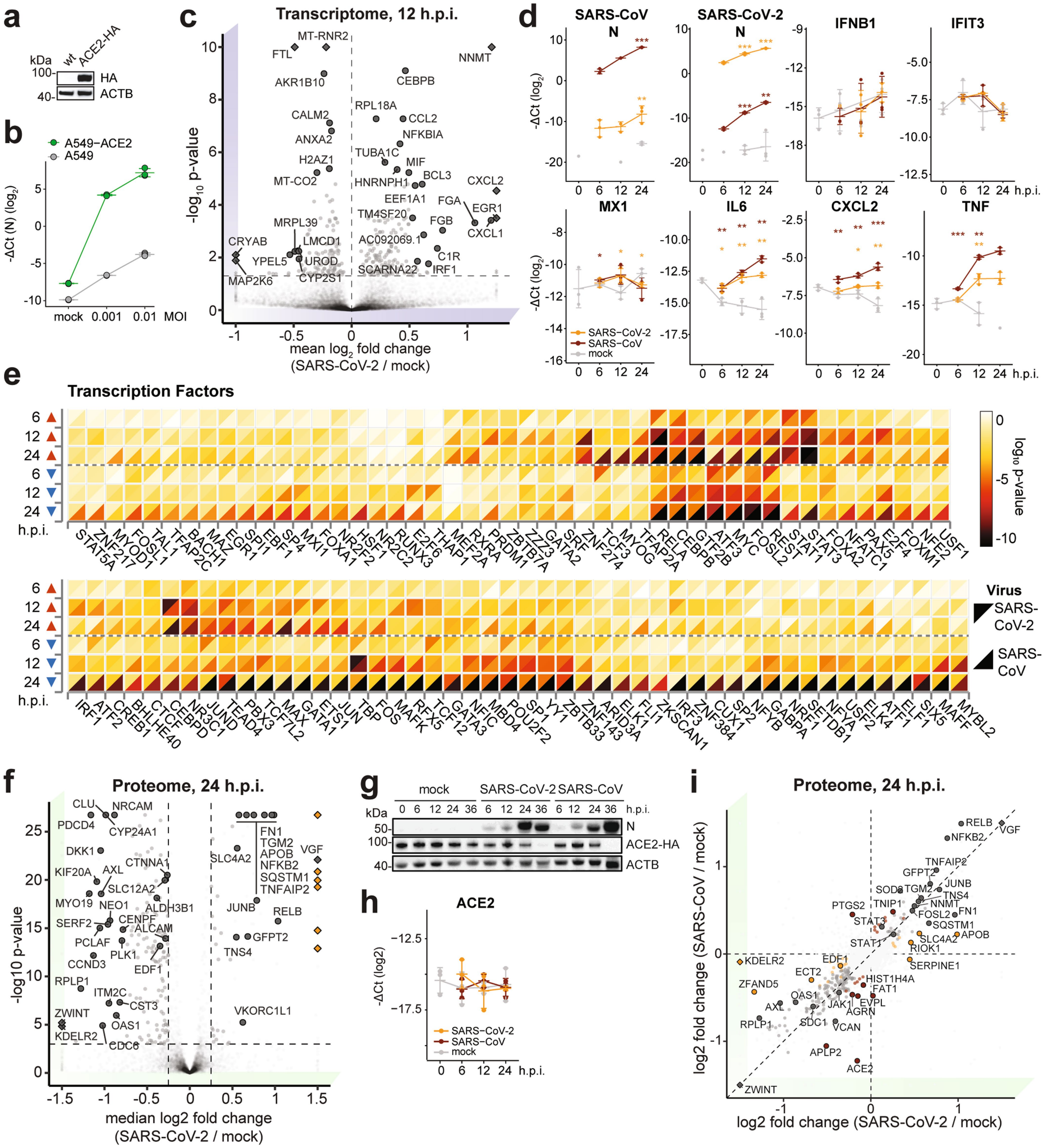

Extended Data Fig. 4 | See next page for caption.

Extended Data Fig. 4 | Tracking of virus-specific changes in infected A549-ACE2 cells by transcriptomics and proteomics. a, Western blot showing ACE2-HA expression levels in A549 cells untransduced (wild-type) or transduced with ACE2-HA-encoding lentivirus (*n* = 2 independent experiments). For gel source data, see Supplementary Fig. 1. **b**, mRNA expression levels of SARS-CoV-2 *N* relative to *RPLPO* as measured by qRT–PCR upon infection of wild-type A549 and A549-ACE2 cells at the indicated MOIs. Error bars represent mean and standard deviation (*n* = 3 independent experiments). **c**, Volcano plot of mRNA expression changes of A549-ACE2 cells, infected with SARS-CoV-2 at an MOI of 2 in comparison to mock infection at 12 hpi. Significant hits are highlighted in grey (moderated *t*-test fasle discovery rate-corrected two-sided *P*-value, *n* = 3 independent experiments). Diamonds indicate that the actual $\log_2$ fold change or *P*-value were truncated to fit into the plot. **d**, Expression levels, as measured by qRT–PCR, of SARS-CoV-2/SARS-CoV *N* and host transcripts relative to *RPLPO* in infected (MOI of 2) A549-ACE2 cells with SARS-CoV-2 (orange) and SARS-CoV (brown) at indicated time points. Error bars correspond to mean and standard deviation (Two-sided student *t*-test, unadjusted *P*-value, *n* = 3 independent experiments). **P*-value ≤ 0.05; ***P*-value ≤ 0.01; ****P*-value ≤ 10^{-3}. **e**, Analysis of transcription factors, whose targets are significantly enriched among up- (red arrow) and down- (blue arrow) regulated genes of A549-ACE2 cells infected with SARS-CoV-2 (upper triangle) and SARS-CoV (lower triangle) for indicated time points (Fisher's exact test unadjusted one-sided *P*-value ≤ 10^{-4}). **f**, Volcano plot of SARS-CoV-2-induced protein abundance changes at 24 hpi in comparison to mock. Viral proteins are highlighted in orange, selected significant hits are marked in black (Bayesian linear model-based unadjusted two-sided *P*-value ≤ 10^{-3}, |median $\log_2$ fold change| ≥ 0.25, *n* = 4 independent experiments). Diamonds indicate that the actual $\log_2$ fold change was truncated to fit into the plot. **g**, Western blot showing the total levels of ACE2-HA protein at 6, 12, 24 and 36 hpi (mock, SARS-CoV-2 and SARS-CoV infections); N viral protein as infection and ACTB as loading controls (*n* = 3 independent experiments). For gel source data, see Supplementary Fig. 1. **h**, Stable expression of *ACE2* mRNA transcript relative to *RPLPO*, as measured by qRT–PCR, after SARS-CoV-2 and SARS-CoV infections (MOI of 2) of A549-ACE2 cells at indicated hpi (error bars show mean and standard deviation, *n* = 3 independent experiments). **i**, Scatter plots comparing the host proteome of SARS-CoV-2 (*x*-axis) and SARS-CoV (*y*-axis) infection at 24 hpi ($\log_2$ fold change in comparison to the mock infection samples at the same time point). Significantly regulated proteins (Bayesian linear model-based unadjusted two-sided *P*-value ≤ 10^{-3}, |$\log_2$ fold change| ≥ 0.25, *n* = 4 independent experiments), are colored according to their specificity in both infections. Diamonds indicate that the actual $\log_2$ fold change was truncated to fit into the plot.

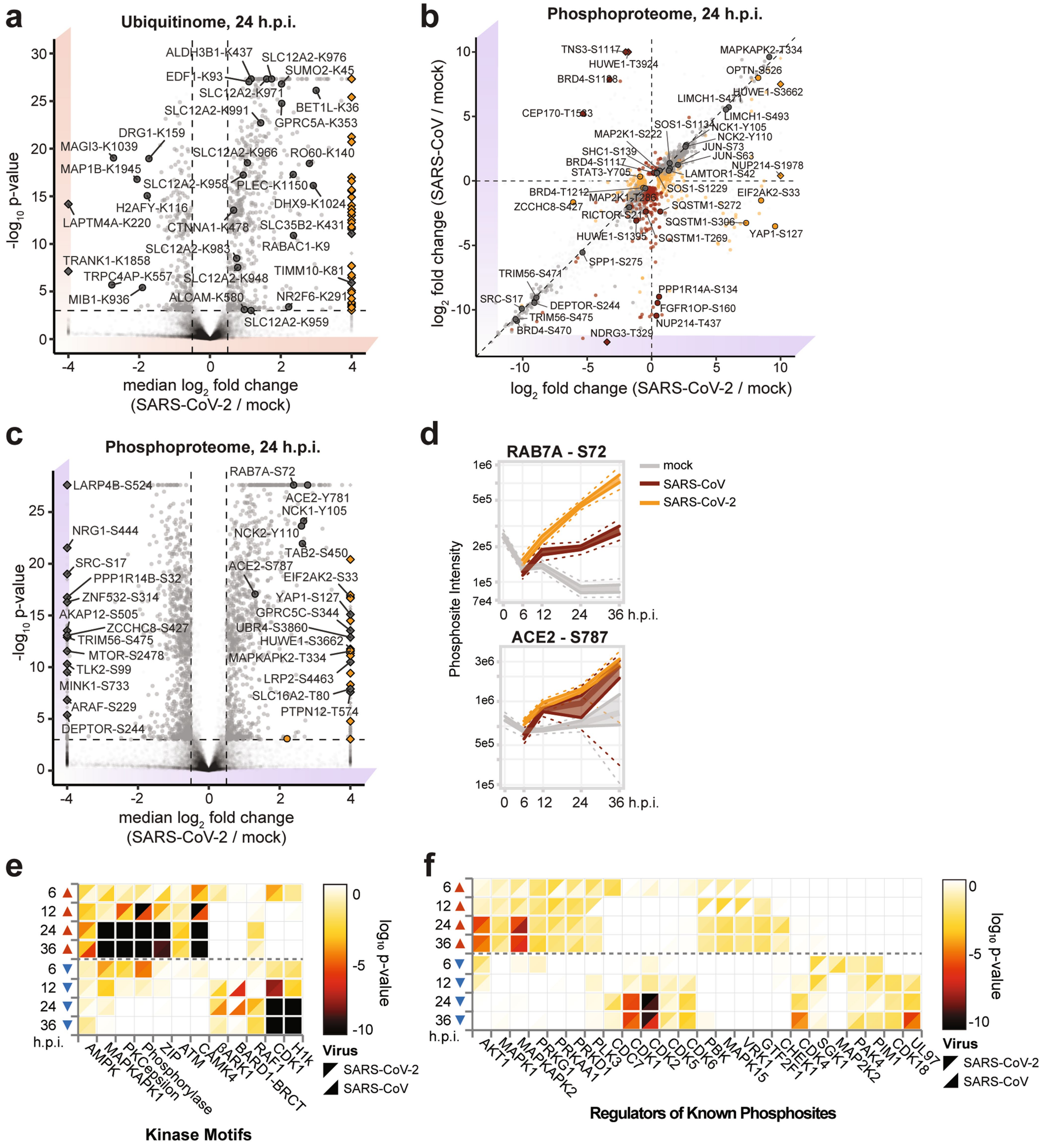

Extended Data Fig. 5 | Post-translational modifications modulated during SARS-CoV-2 or SARS-CoV infection. a, Volcano plots of SARS-CoV-2-induced ubiquitination changes at 24 hpi in comparison to mock. The viral PTM sites are highlighted in orange and selected significant hits in black. **b**, Scatter plots comparing the host phosphoproteome of SARS-CoV-2 (*x*-axis) and SARS-CoV (*y*-axis) infection at 24 hpi ($\log_2$ fold change in comparison to the mock infection samples at the same time point). Significantly regulated sites are colored according to their specificity in both infections. **c**, Volcano plots of SARS-CoV-2-induced phosphorylation changes at 24 hpi in comparison to mock. The viral PTM sites are highlighted in orange and selected significant hits in black. For **a**–**c**, a change is defined significant if its Bayesian linear model-based unadjusted two-sided *P*-value $\leq 10^{-3}$ and $|\log_2 \text{fold change}| \geq 0.5$, $n = 3$ independent experiments for ubiquitination and $n = 4$ independent experiments for phosphorylation data. Diamonds in **a**–**c** indicate that the actual median $\log_2$ fold change was truncated to fit into the plot. **d**, Profile plots showing the time-resolved phosphorylation of ACE2 (S787) and RAB7A (S72) with indicated median, 50% and 95% confidence intervals, $n = 4$ independent experiments. **e**, The enrichment of host kinase motifs among the significantly regulated phosphorylation sites of SARS-CoV-2 (upper triangle) and SARS-CoV-infected (lower triangle) A549-ACE2 cells (MOI of 2) at the indicated time points (Fisher's exact test, unadjusted one-sided *P*-value $\leq 10^{-3}$). **f**, The enrichment of specific kinases among the ones known to phosphorylate significantly regulated sites at the indicated time points and annotated in PhosphoSitePlus database (Fisher's exact test, unadjusted one-sided *P*-value $\leq 10^{-2}$).

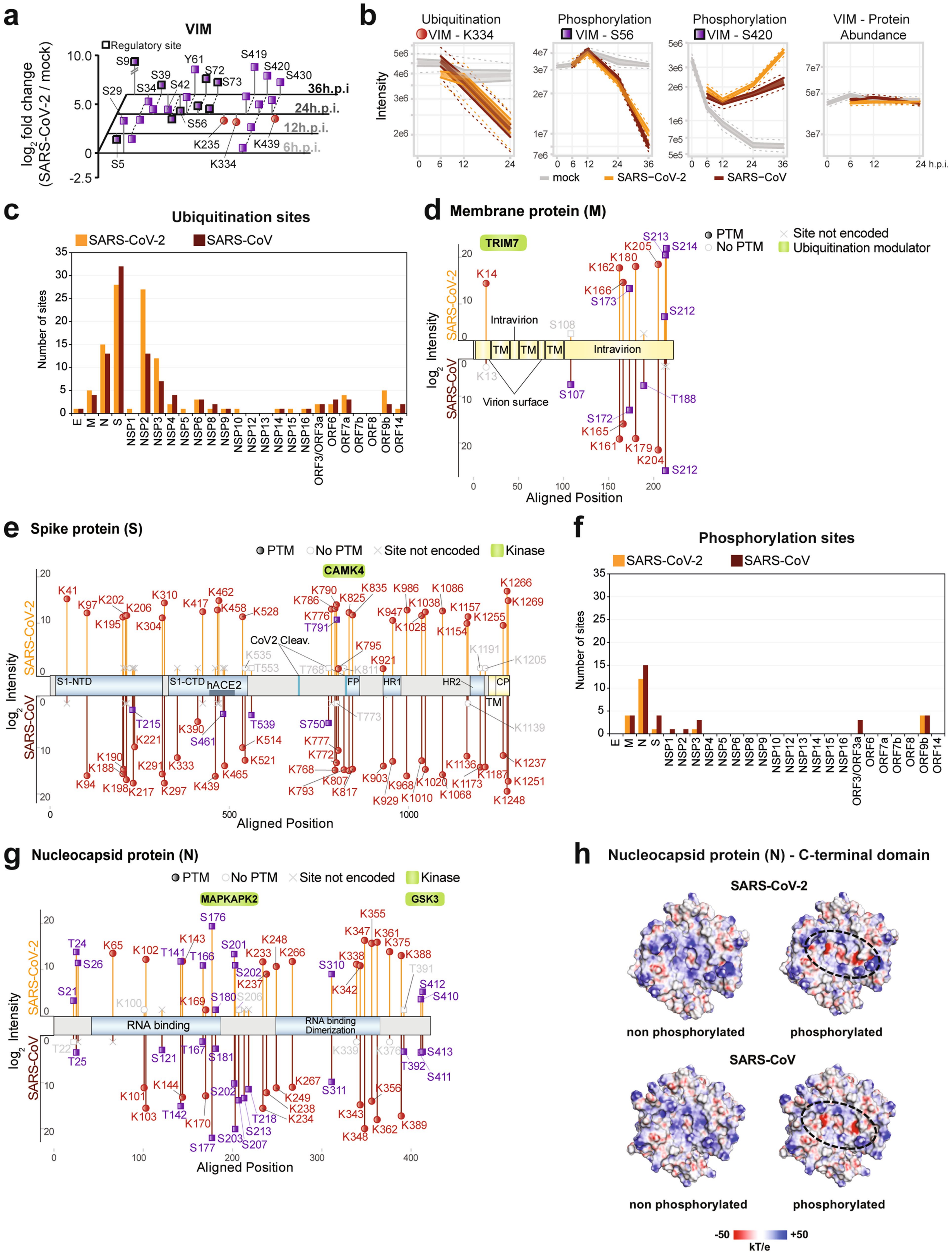

Extended Data Fig. 6 | See next page for caption.

Extended Data Fig. 6 | Integration of multi-omics data from SARS-CoV-2 and SARS-CoV infection identified co-regulation of host and viral factors. **a**, Phosphorylation (purple square) and ubiquitination (red circles) sites on vimentin (VIM) regulated upon SARS-CoV-2 infection. The plot shows the medians of $\log_2$ fold changes compared to mock at 6, 12, 24 and 36 hpi, regulatory sites are indicated with a thick black border. **b**, Profile plots of VIM K334 ubiquitination, S56 and S72 phosphorylation, and total protein levels in SARS-CoV-2 or SARS-CoV infected A549-ACE2 cells at indicated times after infection, with indicated median, 50% and 95% confidence intervals, $n = 3$ (ubiquitination) or $n = 4$ (total protein levels, phosphorylation) independent experiments. **c**, Number of ubiquitination sites identified on each SARS-CoV-2 or SARS-CoV proteins in infected A549-ACE2 cells. **d**, **e**, Mapping the ubiquitination and phosphorylation sites of SARS-CoV-2/SARS-CoV M and S proteins on their aligned sequence showing median $\log_2$ intensities in infected A549-ACE2 cells at 24 hpi ($n = 4$ independent experiments for phosphorylation and $n = 3$ independent experiments for ubiquitination data) with functional (blue) and topological (yellow) domains highlighted. Ubiquitin modifying enzymes binding to both M proteins and the host kinases that potentially recognize motifs associated with the reported sites and overrepresented among cellular motifs enriched upon infection (Extended Data Fig. 5e, f) or interacting with given viral protein (Extended Data Fig. 1b) are indicated (green). **f**, Number of phosphorylation sites identified on each SARS-CoV-2 or SARS-CoV proteins in infected A549-ACE2 cells. **g**, Mapping the ubiquitination (red circle) and phosphorylation (purple square) sites of SARS-CoV-2/SARS-CoV N protein on their aligned sequence showing median $\log_2$ intensities in A549-ACE2 cells infected with the respective virus at 24 hpi ($n = 4$ independent experiments) with functional domains highlighted in blue. The host kinases that potentially recognize motifs associated with the reported sites and overrepresented among cellular motifs enriched upon infection (Extended Data Fig. 5e, f) or interacting with given viral protein (Extended Data Fig. 1b) (green). **h**, Electrostatic surface potential analysis of non-phosphorylated and phosphorylated SARS-CoV and SARS-CoV-2 N CTD dimers; red, white and blue regions represent areas with negative, neutral and positive electrostatic potential, respectively (scale from −50 to +50 kT e^{-1}). NTD, N-terminal domain; hACE2, binding site of human ACE2; FP, fusion peptide; HR1/2, Heptad region 1/2; CP, cytoplasmic region. CoV2 Cleav., SARS-CoV-2 cleavage sites.

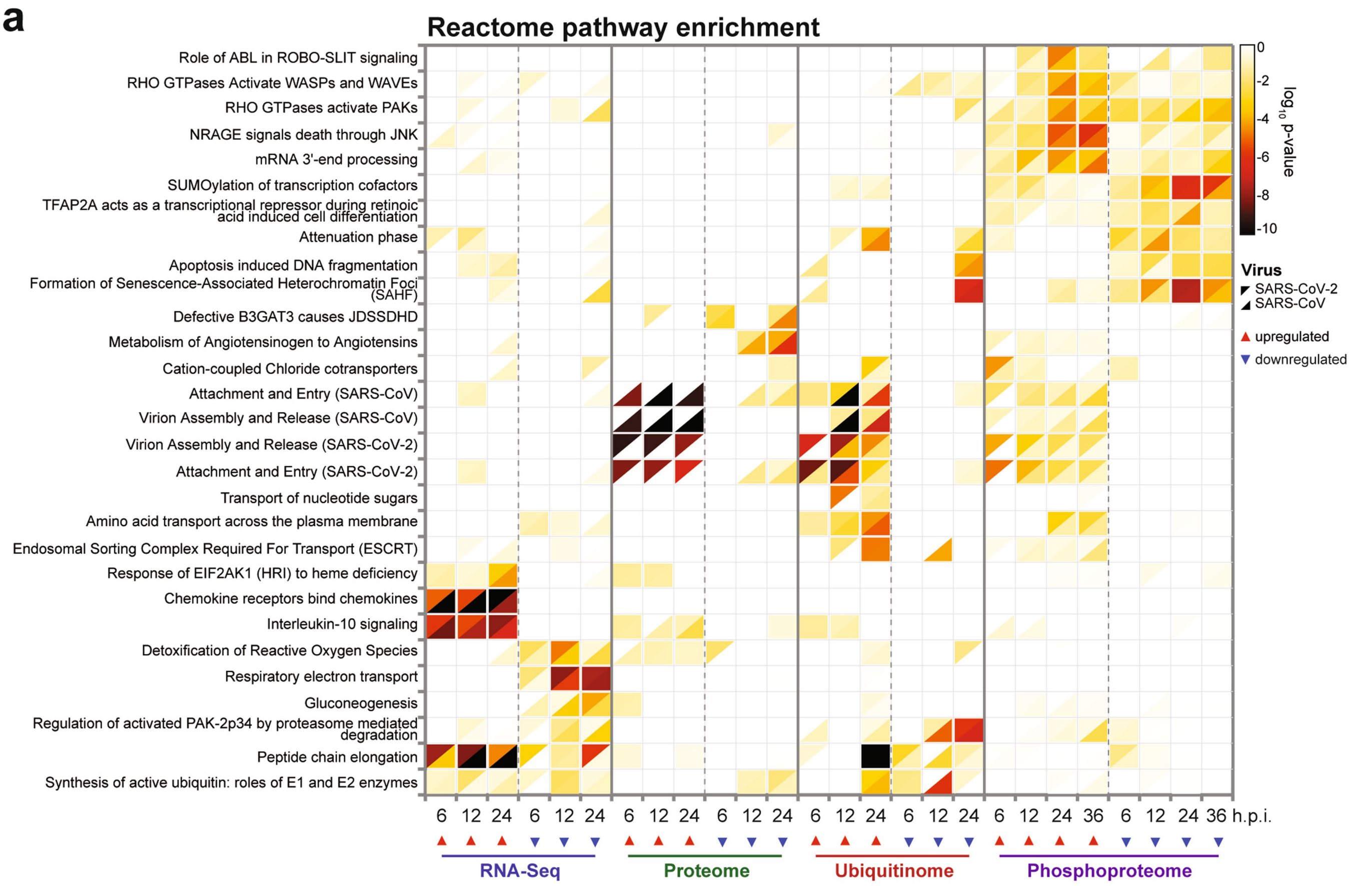

Extended Data Fig. 7 | Reactome pathways enrichment in multi-omics data of SARS-CoV-2 and SARS-CoV infection. a, Reactome pathways enriched in up- (red arrow) or downregulated (blue arrow) transcripts, proteins, ubiquitination and phosphorylation sites (Fisher's exact test unadjusted *P*-value $\leq 10^{-4}$) in SARS-CoV-2 or SARS-CoV-infected A549-ACE2 cells at indicated times after infection.

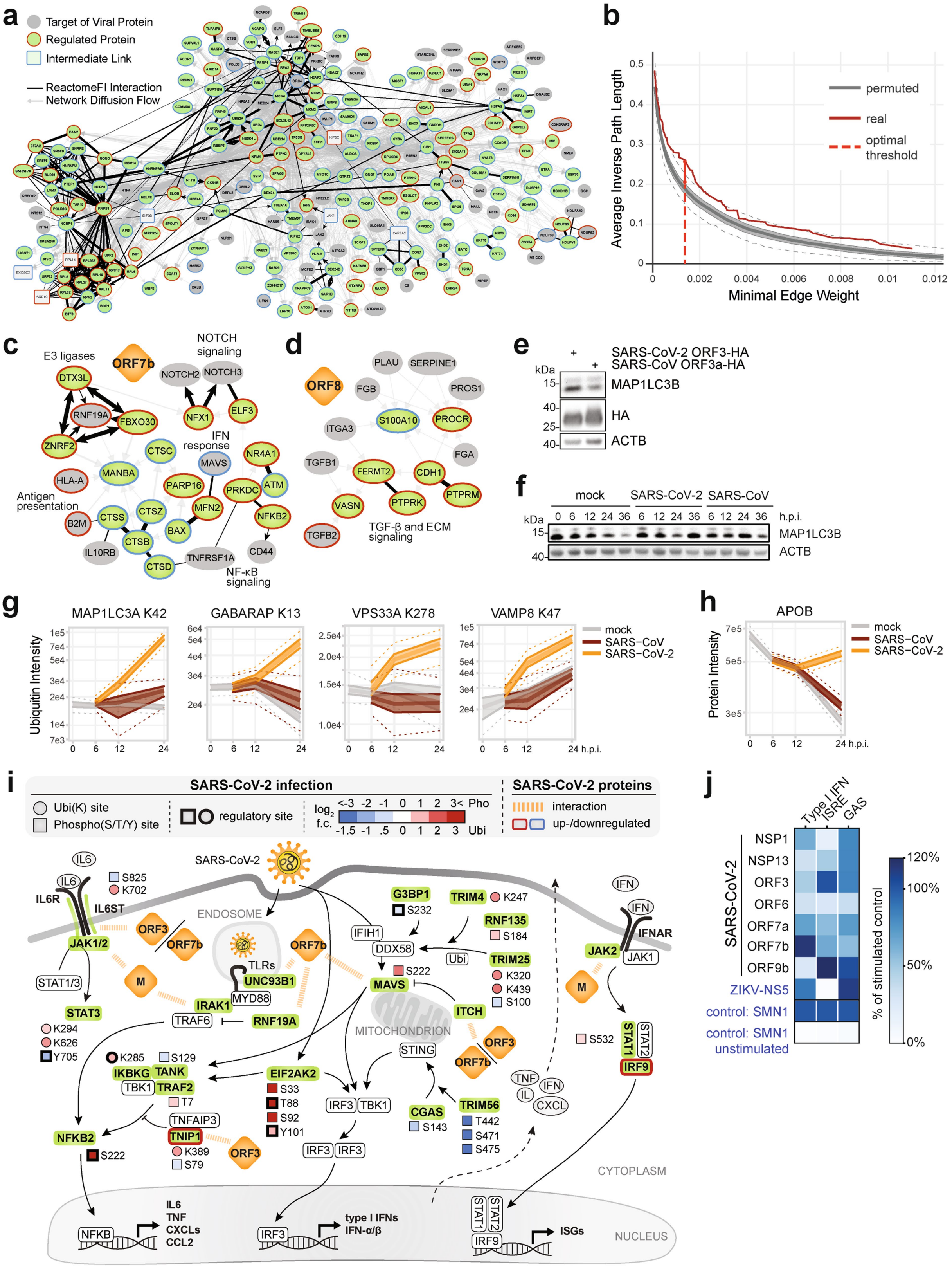

Extended Data Fig. 8 | See next page for caption.

Extended Data Fig. 8 | SARS-CoV-2 uses a multi-pronged approach to perturb host-pathways at several levels. a, The host subnetwork perturbed by SARS-CoV-2 M predicted by the network diffusion approach. Edge thickness reflects the transition probability in random walk with restart, directed edges represent the walk direction, and ReactomeFI connections are highlighted in black. **b**, Selection of the optimal threshold for the network diffusion model of SARS-CoV-2 M-induced proteome changes. The plot shows the relationship between the minimal allowed edge weight of the random walk graph (*x*-axis) and the mean inverse length of the path from the regulated proteins to the host targets of the viral protein along the edges of the resulting filtered subnetwork (*y*-axis). The red curve represents the metric for the network diffusion analysis of the actual data. The grey band shows 50% confidence interval, and dashed lines correspond to 95% confidence interval for the average inverse path length distribution for 1,000 randomized datasets. Optimal edge weight threshold that maximizes the difference between the metric based on the real data and its 3rd quartile based on randomized data are highlighted by the red vertical line. **c**, **d**, Subnetworks of the network diffusion predictions linking host targets of SARS-CoV-2 ORF7b (**c**) to the factors involved in innate immunity and ORF8 (**d**) to the factors involved in TGF-β signalling. **e**, **f**, Western blot showing the accumulation of the autophagy-associated factor MAP1LC3B upon SARS-CoV-2 ORF3 expression in HEK293-R1 cells (*n* = 3 independent experiments) (**e**) and SARS-CoV-2/SARS-CoV infection of A549-ACE2 cells (*n* = 3 independent experiments) (**f**). For gel source data, see Supplementary Fig. 1. **g**, **h**, Profile plots showing the time-resolved ubiquitination of the autophagy regulators MAP1LC3A, GABARAP, VPS33A and VAMP8 (*n* = 3 independent experiments) (**g**), as well as an increase in total protein abundance of APOB with indicated median, 50% and 95% confidence intervals (*n* = 4 independent experiments) (**h**). **i**, Overview of perturbations to host-cell innate immunity-related pathways, induced by distinct proteins of SARS-CoV-2, derived from the network diffusion model and overlaid with transcriptional, ubiquitination and phosphorylation changes upon SARS-CoV-2 infection. **j**, Heat map showing the effects of the indicated SARS-CoV-2 proteins on type-I IFN expression levels, ISRE and GAS promoter activation in HEK293-R1. Accumulation of type-I IFN in the supernatant was evaluated by testing supernatants of PPP-RNA (IVT4) stimulated cells on MX1-luciferase reporter cells, ISRE promoter activation—by luciferase assay after IFN-α stimulation, and GAS promoter activation—by luciferase assay after IFN-γ stimulation in cells expressing SARS-CoV-2 proteins as compared to the controls (ZIKV NS5 and SMN1) (*n* = 3 independent experiments).

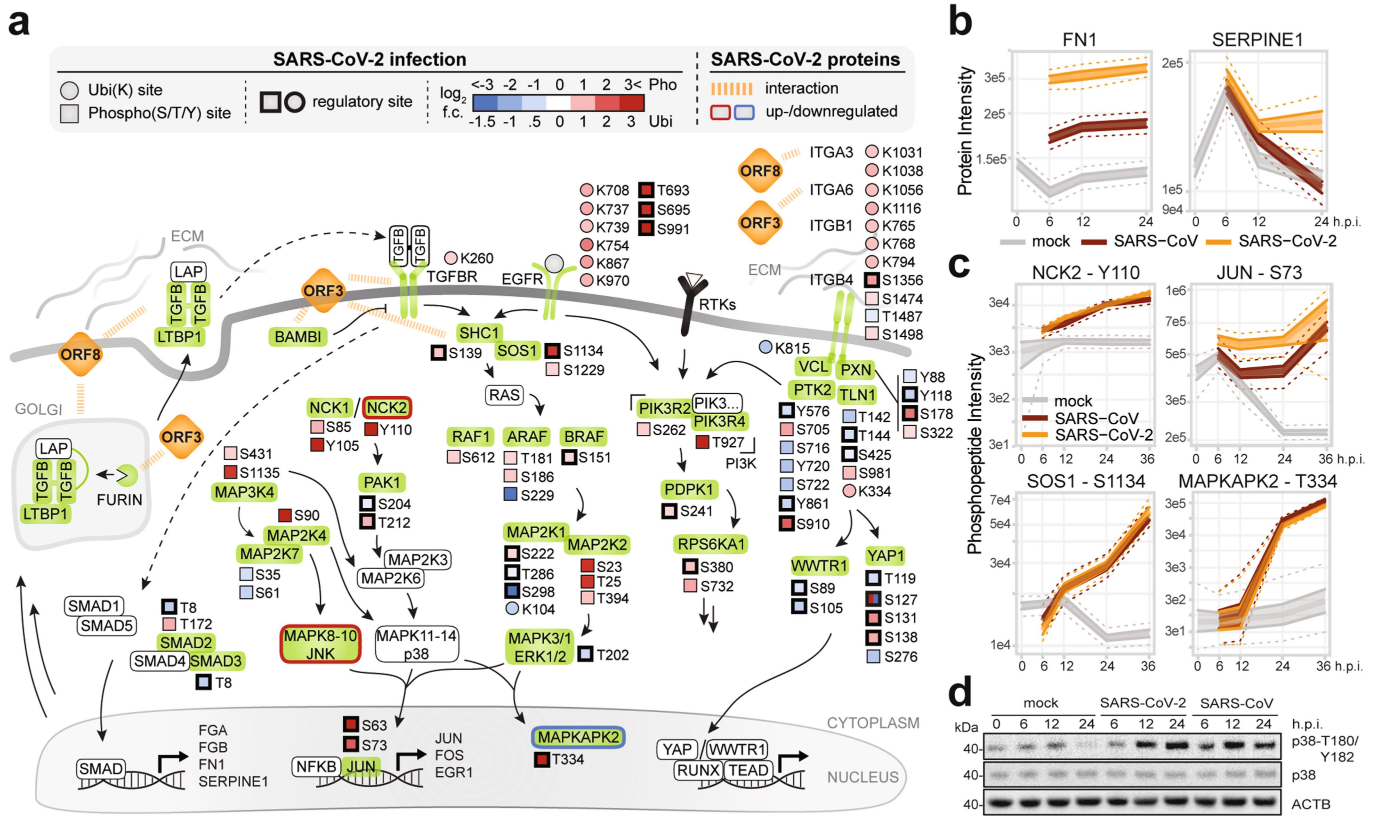

Extended Data Fig. 9 | Perturbation of host integrin-TGF-β-EGFR-receptor tyrosine kinase signalling by SARS-CoV-2. a, Overview of perturbations to host-cell Integrin-TGF-β-EGFR-receptor tyrosine kinase signalling, induced by distinct proteins of SARS-CoV-2, derived from the network diffusion model and overlaid with transcriptional, ubiquitination and phosphorylation changes upon SARS-CoV-2 infection. **b**, Profile plots of total protein levels of SERPINE1 and FN1 in SARS-CoV-2 or SARS-CoV-infected A549-ACE2 cells at 6, 12, and 24 hpi, with indicated median, 50% and 95% confidence intervals (*n* = 4 independent experiments). **c**, Profile plots showing intensities of indicated phosphosites on NCK2, JUN, SOS1 and MAPKAPK2 in SARS-CoV-2 or SARS-CoV-infected A549-ACE2 cells at 6, 12, 24 and 36 hpi, with indicated median, 50% and 95% confidence intervals (*n* = 4 independent experiments). **d**, Western blot showing phosphorylated (T180/Y182) and total protein levels of p38 in SARS-CoV-2 or SARS-CoV infected A549-ACE2 cells (*n* = 3 independent experiments). For gel source data, see Supplementary Fig. 1.

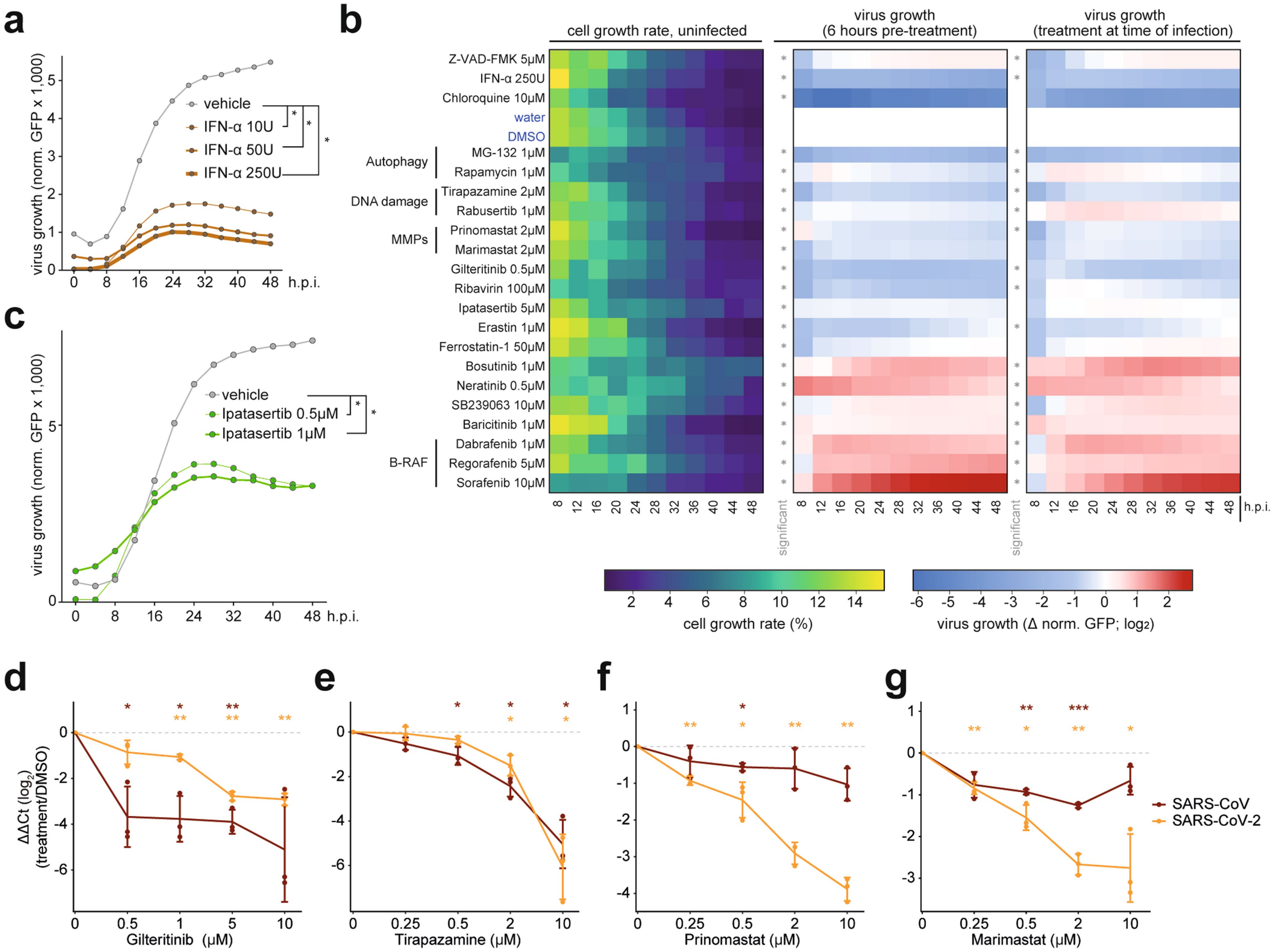

Extended Data Fig. 10 | Drug repurposing screen, focusing on pathways perturbed by SARS-CoV-2, reveals potential candidates for use in antiviral therapy. a, A549-ACE2 cells exposed for 6 h to the specified concentrations of IFN-α and infected with SARS-CoV-2-GFP reporter virus (MOI of 3). GFP signal and cell confluency were analysed by live-cell imaging for 48 hpi. Time-courses show virus growth over time as the mean of GFP-positive area normalized to the total cell area ($n = 4$ independent experiments). **b**, A549-ACE2 cells were pre-treated for 6 h or treated at the time of infection with SARS-CoV-2-GFP reporter virus (MOI of 3). GFP signal and cell growth were tracked for 48 hpi by live-cell imaging using an Incucyte S3 platform. Left heat map: the cell growth rate (defined as the change of cell confluence between t_i and t_{i-1} timepoints divided by cell confluence at t_{i-1}) over time in drug-treated uninfected conditions. Middle (6 h of pre-treatment) and right (treatment at the time of infection) heat maps: treatment-induced changes in virus growth over time (GFP signal normalized to total cell confluence $\log_2$ fold change between the treated and control (water, DMSO) conditions). Only non-cytotoxic treatments with significant effects on SARS-CoV-2-GFP are shown. Asterisks indicate significance of the difference to the control treatment (Wilcoxon test; unadjusted two-sided P-value ≤ 0.05, $n = 4$ independent experiments). **c**, A549-ACE2 cells exposed for 6 h to the specified concentrations of ipatasertib and infected with SARS-CoV-2-GFP reporter virus (MOI of 3). GFP signal and cell confluency were analysed by live-cell imaging for 48 hpi. Time-courses show virus growth over time as the mean of GFP-positive area normalized to the total cell area ($n = 4$ independent experiments). **d**–**g**, mRNA expression levels at 24 hpi of SARS-CoV-2 (orange) and SARS-CoV (brown) *N* relative to *RPLP0*, compared to DMSO-treated cells, as measured by qRT–PCR in infected A549-ACE2 cells (MOI of 1) pre-treated for 6 h with gilteritinib (**d**), tirapazamine (**e**), prinomastat (**f**) or marimastat (**g**). Error bars represent mean and standard deviation (Student *t*-test, two-sided, unadjusted P-value, $n = 3$ independent experiments). * P-value ≤ 0.05; ** P-value ≤ 0.01; *** P-value $\leq 10^{-3}$.

Extended Data Table 1 | Functional annotations of the protein–protein interaction network of SARS-CoV-2 and SARS-CoV (AP–MS)

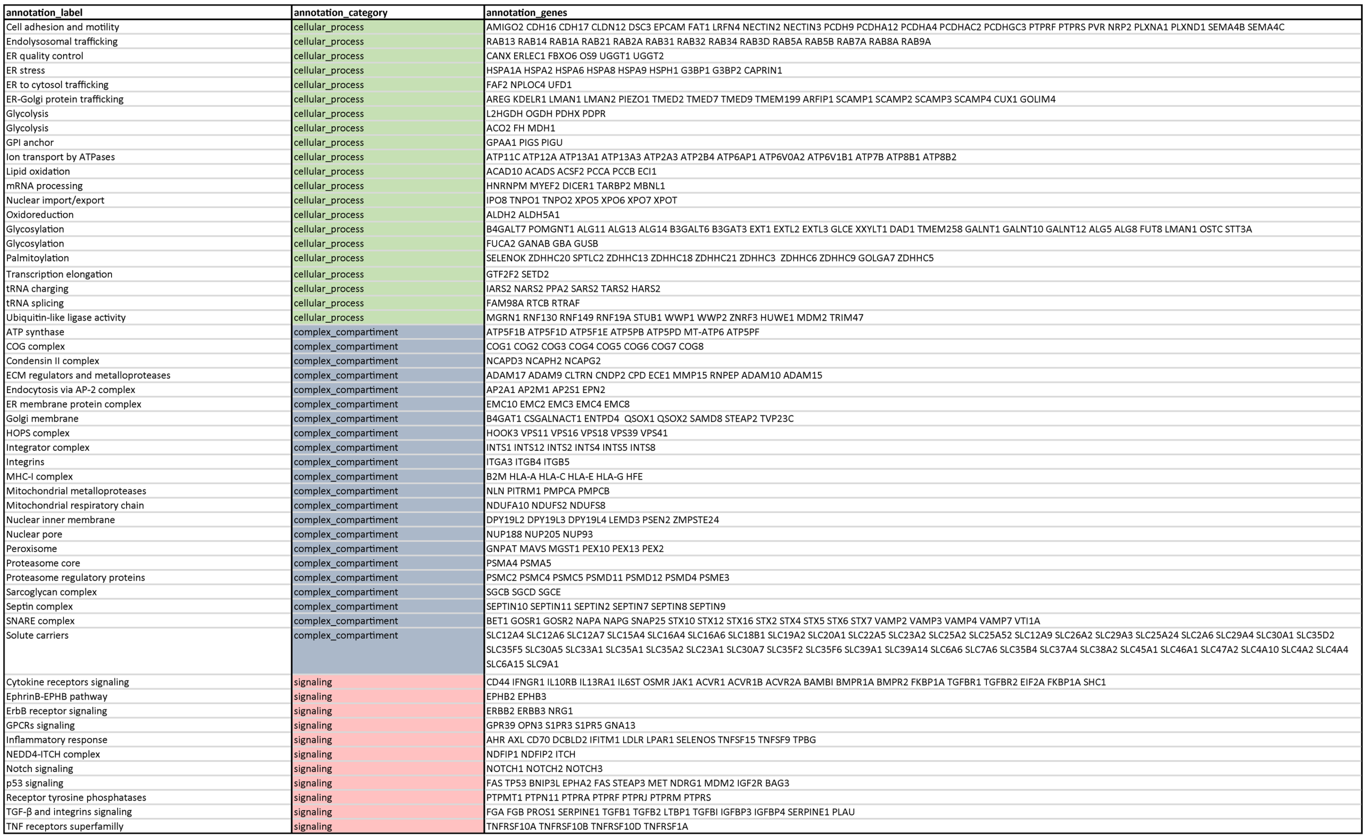

annotation_label	annotation_category	annotation_genes
Cell adhesion and motility	cellular_process	AMIGO2 CDH16 CDH17 CLDN12 DSC3 EPCAM FAT1 LRFN4 NECTIN2 NECTIN3 PCDH9 PCDHA12 PCDHA4 PCDHAC2 PCDHGC3 PTPRF PTPRS PVR NRP2 PLXNA1 PLXND1 SEMA4B SEMA4C
Endolysosomal trafficking	cellular_process	RAB13 RAB14 RAB1A RAB21 RAB2A RAB31 RAB32 RAB34 RAB3D RAB5A RAB5B RAB7A RAB8A RAB9A
ER quality control	cellular_process	CANX ERLEC1 FBXO6 OS9 UGGT1 UGGT2
ER stress	cellular_process	HSPA1A HSPA2 HSPA6 HSPA8 HSPA9 HSPH1 G3BP1 G3BP2 CAPRIN1
ER to cytosol trafficking	cellular_process	FAF2 NPLOC4 UFD1
ER-Golgi protein trafficking	cellular_process	AREG KDELR1 LMAN1 LMAN2 PIEZO1 TMED2 TMED7 TMED9 TMEM199 ARFIP1 SCAMP1 SCAMP2 SCAMP3 SCAMP4 CUX1 GOLIM4
Glycolysis	cellular_process	L2HGDH OGDH PDHX PDPR
Glycolysis	cellular_process	ACO2 FH MDH1
GPI anchor	cellular_process	GPAA1 PIGS PIGU
Ion transport by ATPases	cellular_process	ATP11C ATP12A ATP13A1 ATP13A3 ATP2A3 ATP2B4 ATP6AP1 ATP6V0A2 ATP6V1B1 ATP7B ATP8B1 ATP8B2
Lipid oxidation	cellular_process	ACAD10 ACADS ACSF2 PCCA PCCB ECI1
mRNA processing	cellular_process	HNRNPM MYEF2 DICER1 TARBP2 MBNL1
Nuclear import/export	cellular_process	IPO8 TNPO1 TNPO2 XPO5 XPO6 XPO7 XPOT
Oxidoreduction	cellular_process	ALDH2 ALDH5A1
Glycosylation	cellular_process	B4GALT7 POMGNT1 ALG11 ALG13 ALG14 B3GALT6 B3GAT3 EXT1 EXTL2 EXTL3 GLCE XXYLT1 DAD1 TMEM258 GALNT1 GALNT10 GALNT12 ALG5 ALG8 FUT8 LMAN1 OSTC STT3A
Glycosylation	cellular_process	FUCA2 GANAB GBA GUSB
Palmitoylation	cellular_process	SELENOK ZDHHC20 SPTLC2 ZDHHC13 ZDHHC18 ZDHHC21 ZDHHC3 ZDHHC6 ZDHHC9 GOLGA7 ZDHHC5
Transcription elongation	cellular_process	GTF2F2 SETD2
tRNA charging	cellular_process	IARS2 NARS2 PPA2 SARS2 TARS2 HARS2
tRNA splicing	cellular_process	FAM98A RTCB RTRAF
Ubiquitin-like ligase activity	cellular_process	MGRN1 RNF130 RNF149 RNF19A STUB1 WWP1 WWP2 ZNRF3 HUWE1 MDM2 TRIM47
ATP synthase	complex_compartiment	ATP5F1B ATP5F1D ATP5F1E ATP5PB ATP5PD MT-ATP6 ATP5PF
COG complex	complex_compartiment	COG1 COG2 COG3 COG4 COG5 COG6 COG7 COG8
Condensin II complex	complex_compartiment	NCAPD3 NCAPH2 NCAPG2
ECM regulators and metalloproteases	complex_compartiment	ADAM17 ADAM9 CLTRN CNDP2 CPD ECE1 MMP15 RNPEP ADAM10 ADAM15
Endocytosis via AP-2 complex	complex_compartiment	AP2A1 AP2M1 AP2S1 EPN2
ER membrane protein complex	complex_compartiment	EMC10 EMC2 EMC3 EMC4 EMC8
Golgi membrane	complex_compartiment	B4GAT1 CSGALNACT1 ENTPD4 QSOX1 QSOX2 SAMD8 STEAP2 TVP23C
HOPS complex	complex_compartiment	HOOK3 VPS11 VPS16 VPS18 VPS39 VPS41
Integrator complex	complex_compartiment	INTS1 INTS12 INTS2 INTS4 INTS5 INTS8
Integrins	complex_compartiment	ITGA3 ITGB4 ITGB5
MHC-I complex	complex_compartiment	B2M HLA-A HLA-C HLA-E HLA-G HFE
Mitochondrial metalloproteases	complex_compartiment	NLN PITRM1 PMPCA PMPCB
Mitochondrial respiratory chain	complex_compartiment	NDUFA10 NDUFS2 NDUFS8
Nuclear inner membrane	complex_compartiment	DPY19L2 DPY19L3 DPY19L4 LEMD3 PSEN2 ZMPSTE24
Nuclear pore	complex_compartiment	NUP188 NUP205 NUP93
Peroxisome	complex_compartiment	GNPAT MAVS MGST1 PEX10 PEX13 PEX2
Proteasome core	complex_compartiment	PSMA4 PSMA5
Proteasome regulatory proteins	complex_compartiment	PSMC2 PSMC4 PSMC5 PSMD11 PSMD12 PSMD4 PSME3
Sarcoglycan complex	complex_compartiment	SGCB SGCD SGCE
Septin complex	complex_compartiment	SEPTIN10 SEPTIN11 SEPTIN2 SEPTIN7 SEPTIN8 SEPTIN9
SNARE complex	complex_compartiment	BET1 GOSR1 GOSR2 NAPA NAPG SNAP25 STX10 STX12 STX16 STX2 STX4 STX5 STX6 STX7 VAMP2 VAMP3 VAMP4 VAMP7 VTI1A
Solute carriers	complex_compartiment	SLC12A4 SLC12A6 SLC12A7 SLC15A4 SLC16A4 SLC16A6 SLC18B1 SLC19A2 SLC20A1 SLC22A5 SLC23A2 SLC25A2 SLC25A52 SLC12A9 SLC26A2 SLC29A3 SLC25A24 SLC2A6 SLC29A4 SLC30A1 SLC35D2 SLC35F5 SLC30A5 SLC33A1 SLC35A1 SLC35A2 SLC23A1 SLC30A7 SLC35F2 SLC35F6 SLC39A1 SLC39A14 SLC6A6 SLC7A6 SLC35B4 SLC37A4 SLC38A2 SLC45A1 SLC46A1 SLC47A2 SLC4A10 SLC4A2 SLC4A4 SLC6A15 SLC9A1
Cytokine receptors signaling	signaling	CD44 IFNGR1 IL10RB IL13RA1 IL6ST OSMR JAK1 ACVR1 ACVR1B ACVR2A BAMBI BMPR1A BMPR2 FKBP1A TGFBR1 TGFBR2 EIF2A FKBP1A SHC1
EphrinB-EPHB pathway	signaling	EPHB2 EPHB3
ErbB receptor signaling	signaling	ERBB2 ERBB3 NRG1
GPCRs signaling	signaling	GPR39 OPN3 S1PR3 S1PR5 GNA13
Inflammatory response	signaling	AHR AXL CD70 DCBLD2 IFITM1 LDLR LPAR1 SELENOS TNFSF15 TNFSF9 TPBG
NEDD4-ITCH complex	signaling	NDFIP1 NDFIP2 ITCH
Notch signaling	signaling	NOTCH1 NOTCH2 NOTCH3
p53 signaling	signaling	FAS TP53 BNIP3L EPHA2 FAS STEAP3 MET NDRG1 MDM2 IGF2R BAG3
Receptor tyrosine phosphatases	signaling	PTPMT1 PTPN11 PTPRA PTPRF PTPRJ PTPRM PTPRS
TGF-β and integrins signaling	signaling	FGA FGB PROS1 SERPINE1 TGFB1 TGFB2 LTBP1 TGFBI IGFBP3 IGFBP4 SERPINE1 PLAU
TNF receptors superfamilly	signaling	TNFRSF10A TNFRSF10B TNFRSF10D TNFRSF1A

Proteins identified as SARS-CoV-2 and/or SARS-CoV host binders via AP–MS (Fig. 1b) grouped based on functional enrichment analysis of GOBP, GPCC, GPMF and Reactome terms (Supplementary Table 2).